# Dispersion in photonic crystals

Thesis by

Jeremy Witzens

In Partial Fulfillment of the Requirements
for the Degree of
Doctor of Philosophy


California Institute of Technology
Pasadena, California

2005
(Defended May 10, 2005)

To my parents,

Peter and Sabine.

# Acknowledgements

I would like to thank Professor Axel Scherer for his guidance and support, and for providing me with the opportunity and resources to complete my Ph.D. Caltech has been a wonderful environment for promoting creativity and learning. In particular I would like to thank Joerg Schilling, Brett Maune and Tobias Kippenberg, not only for their friendship and for stimulating scientific discussions that enriched my own work, but also for their trust and their readiness to discuss their own projects. I would like to thank Michael Hochberg for his feedback on semiconductor fabrication techniques, Thomas Baehr-Jones for sharing the simulation software he wrote and Christopher Walker for sharing his measurement setup.

I would also like to thank Luxtera Inc. for the knowledge I acquired there from very bright, knowledgeable and well-rounded individuals such as Maxime Rattier, Thierry Pinguet, Giovanni Capellini and Cary Gunn.

I'd like to acknowledge the other friends I have made in California for their moral support, in particular Nivalda Pinguet, Matthieu Liger, David Barsic, George Maltezos, Hareem Tariq and Suzy Lee who each in their own way have helped keep me grounded and have made my stay at Caltech an enjoyable experience.

Last but not least I would like to thank my parents, Peter and Sabine Witzens, not only for offering me the shelter of a loving family, but also for fostering my intellectual curiosity throughout the years, for the education they provided me with and for laying the groundwork that ultimately led me to where I am today.

# List of Publications


[1] J. Witzens, M. Lončar, and A. Scherer, "Self-Collimation in Planar Photonic Crystals", IEEE J. Sel. Top. Quant. Electron. **8**, 1246-1257 (2002).

[2] J. Witzens and A. Scherer, "Efficient excitation of self-collimated beams and single Bloch modes in planar photonic crystals", J. Opt. Soc. Am. A **20**, 935-940 (2003).

[3] J. Witzens, T. Baehr-Jones, M. Hochberg, M. Lončar, and A. Scherer, "Photonic crystal waveguide-mode orthogonality conditions and computation of intrinsic waveguide losses", J. Opt. Soc. Am. A **20**, 1963-1968 (2003).

[4] J. Witzens, M. Hochberg, T. Baehr-Jones, and A. Scherer, "Mode matching interface for efficient coupling of light into planar photonic crystals", Phys. Rev. E **69**, 046609 1-12 (2004).

[5] B. Maune, M. Lončar, J. Witzens, M. Hochberg, T. Baehr-Jones, D. Psaltis, Y. Qiu, and A. Scherer, "Liquid-crystal electric tuning of a photonic crystal laser", Appl. Phys. Lett. **85**, 360-362 (2004).

[6] L. C. Gunn, T. J. Pinguet, M. J. Rattier, J. Witzens, "Polarization Splitting Grating Coupler", United States Patent Application (2004).

[7] J. Witzens, T. Baehr-Jones, and A. Scherer, "Hybrid superprism with low insertion losses and suppressed cross-talk", Phys. Rev. E **71**, 026604 1-9 (2005).

[8] J. Witzens, G. Pickrell, D. Louderback, P. Guilfoyle, and A. Scherer, "Monolithic integration of vertical-cavity surface-emitting lasers with in-plane waveguides", Appl. Phys. Lett. **86**, 101105 1-101105 3 (2005).

[9] T. Baehr-Jones, M. Hochberg, C. Walker, J. Witzens, L. Gunn, and A. Scherer, "Segmented Waveguides in thin Silicon-on-Insulator", J. Opt. Soc. Am. B (2005).

[10] B. Maune, J. Witzens, T. Baehr-Jones, M. Kolodrubetz, H. Atwater, R. Hagen, Y. Qiu, and A. Scherer, "An optically triggered Q-switched photonic crystal laser", *in review.*

[11] J. Witzens, T. J. Kippenberg, C. Walker, K. J. Vahala, and A. Scherer, "Scattering in ring resonators", *in review.*

[12] T. Baehr-Jones, M. Hochberg, J. Witzens, A. Scherer, "Segmented Waveguides in Thin Silicon on Insulator", United States Patent Application (2005).

[13] J. Witzens, "Grating Coupler with Defect Mode", United States Patent Application (2005).

# Abstract

Investigations on the dispersive properties of photonic crystals, modified scattering in ring-resonators, monolithic integration of vertical-cavity surface-emitting lasers and advanced data processing techniques for the finite-difference time-domain method are presented.

Photonic crystals are periodic mesoscopic arrays of scatterers that modify the propagation properties of electromagnetic waves in a similar way as "natural" crystals modify the properties of electrons in solid-state physics. In this thesis photonic crystals are implemented as planar photonic crystals, i.e., optically thin semiconductor films with periodic arrays of holes etched into them, with a hole-to-hole spacing of the order of the wavelength of light in the dielectric media. Photonic crystals can feature forbidden frequency ranges (the band-gaps) in which light cannot propagate. Even though most work on photonic crystals has focused on these band-gaps for application such as confinement and guiding of light, this thesis focuses on the allowed frequency regions (the photonic bands) and investigates how the propagation of light is modified by the crystal lattice. In particular the guiding of light in bulk photonic crystals in the absence of lattice defects (the self-collimation effect) and the angular steering of light in photonic crystals (the superprism effect) are investigated. The latter is used to design a planar lightwave circuit for frequency domain demultiplexion. Difficulties such as efficient insertion of light into the crystal are resolved and previously predicted limitations on the resolution are circumvented. The demultiplexer is also fabricated and characterized.

Monolithic integration of vertical-cavity surface-emitting lasers by means of resonantly enhanced grating couplers is investigated. The grating coupler is designed to bend light through a ninety degree angle and is characterized with the finite-difference

time-domain method. The vertical-cavity surface-emitting lasers are fabricated and characterized.

A purely theoretical section of the thesis investigates advanced data processing techniques for the finite-difference time-domain method. In particular it is shown that an inner product can be used to filter out specific photonic crystal modes or photonic crystal waveguide modes (Bloch-modes). However it is also shown that the numerical accuracy of this inner product severely worsens for Bloch modes with very low group velocities. Analytical functions of the bounds of these inaccuracies are formally derived.

# Contents

# List of Figures

# Glossary of Acronyms

**ABC** Absorbing boundary condition

**BBC** Bloch boundary condition

**DBR** Distributed Bragg reflector

**EFC** Equi-frequency contour

**FDTD** Finite-difference time-domain computation

**GC** Grating coupler

**GVD** Group velocity dispersion

**ICPRIE** Inductively coupled plasma reactive ion etch

**MBE** Molecular beam epitaxy

**MLG** Multi layered grating

**PBG** Photonic band-gap

**PC** Photonic crystal

**PCW** Photonic crystal waveguide

**PMMA** Polymethylmethacrylate

**PPC** Planar photonic crystal

**PR** Photoresist

**QW** Quantum well

**RIE** Reactive ion etch

**SEM** Scanning electron microscope

**SP** Superprism

**TE** Transverse electric

**TM** Transverse magnetic

**VCSEL** Vertical-cavity surface-emitting laser

**WGM** Whispering gallery mode

# Chapter 1

# Introduction

Photonic crystals (PCs) are artificial metamaterials formed by a mesoscopic periodic array of scatterers [1,2]. They have attracted a lot of attention due to their ability to control the flow of light on a very small length scale [3–17] and due to their ability to modify spontaneous emission of emitters such as atoms or quantum dots [1,18–23]. More recently their diverse dispersive properties have also led to applications such as self-collimation of light [25–30] or compact planar demultiplexers [31–41]. Inside photonic crystals, distributed Bragg reflection induced by the periodic array of scattering sites can create frequency regions in which light cannot propagate inside the crystal—the photonic band-gap (PBG)—in analogy to the electronic band-gap in semi-conductor crystals [2].

Due to their artificial nature, the properties of PCs can be tailored to satisfy specific needs. Line defects and point defects in the crystal lattice can define waveguides [3–5] and cavities [6–8] on a micron scale. These optical elements can be coupled to form complex optical systems [16, 17].

Photonic crystal point defects have been used to fabricate micro-lasers in the near [9–13] or far infrared [14, 15]. More recently, additional functionalization has resulted from the integration of photonic crystal lasers with liquids [42], liquid crystals [43] and photo-addressable polymers [44]. Electrical tunability of the lasing wavelength [43] and active switching of the laser polarization [44] have been achieved this way.

However, the bulk properties of PCs are also of interest [24–41]. Their anisotropic nature leads to modified, anisotropic spatial dispersion that can be tailored for specific engineering applications. In certain crystallographic directions the beam broadening is inhibited so that light stays collimated within the crystal even in the absence of waveguiding (self-collimation) [25–30]. On the other hand the dispersion is enhanced in other crystallographic directions. The latter can be used to achieve frequency domain demultiplexion, with an effect dubbed the superprism effect [31–41] due to its similarity to the conventional dielectric prism. However, the achievable frequency resolution per device size is much higher for the superprism (SP) due to the enhanced, tailored dispersion. This makes the SP a promising device for integrated micro-optics, although difficulties such as insertion losses [39–41] and beam-broadening within the crystal [38, 41] have to be overcome.

In its most general form a photonic crystal can be any type of mesoscopic periodic structure, i.e., the dimensionality of the periodicity can be one, two or three. Three dimensional photonic crystals (3D PC) [18,19,45–50] offer the advantage of a completely depleted density of states inside the PBG, which is particularly important for applications such as suppression of spontaneous emission. Many advances have been made in the fabrication of such structures in the form of inverted self-assembled opals [18, 19], square spiral photonic crystals [47], 3D structures formed by photo-electro-chemical etching [48], holographic lithography [49] or two-photon absorption lithography [50]. However, another type of photonic crystals, the planar photonic crystal (PPC) [51], represents a promising structure for integrated optics, since its fabrication is compatible with conventional microelectronics patterning techniques. A PPC is an optically thin dielectric slab perforated with a two-dimensional (2D) lattice of holes. Light is confined in the slab in the vertical direction by means of total internal reflection and in the lateral direction by means of distributed Bragg reflection induced by the 2D lattice of holes [52, 53]. This technology has certain drawbacks as the PBG is only complete for modes that are bound to the slab. Although the optical density of states is reduced inside the PBG, it stays finite due to radiative free space modes.

Most of this thesis (chapters 2 to 7) is dedicated to dispersive properties of PCs, with a particular emphasis on the superprism effect [40,41]. However, the self-collimation effect [27,28] is also investigated in the third chapter. A large fraction focuses on insertion of light at the interface between the PCs and other optical elements, and coupling mechanisms are proposed both for the self-collimation effect [28] (chapter 4) and for the superprism [40,41] (chapter 5). The coupling difficulties are shown to be related to the Bloch mode structure (chapter 5), which is first derived from high-level concepts such as band-folding and then substantiated with a numerical analysis. Several coupling schemes are presented, such as evanescent coupling between the PPC and a dielectric waveguide located above the PPC (chapter 4), efficient butt-coupling between the slab waveguide and the PPC with help of a mode matching interface composed of a series of cascaded diffraction gratings (chapter 5), and finally an adiabatic transition of the hole size at the onset of the PPC. The latter operates a similar mode conversion to the multilayered grating but does not rely on resonant mechanisms and has a wider angular and spectral passband (chapter 5).

The propagation properties of light inside the PC are also investigated. In particular we show how limitations of self-collimation can give rise to beating profiles in beams propagated for distances of the order of or longer than $\sim$ 100 $\mu$m in the case of the implemented PPC (chapter 3). We also show how negative index of refraction [54–56] in PCs [57–59] can be used to suppress cross-talk inside the SP (chapter 6). Limits on the resolution that have been previously predicted in the literature [38] are overcome in this way and the scaling law of the resolution is improved to a linear dependency (resolution versus device size). Finally a superprism incorporating several of these improvements is designed, fabricated and characterized (chapter 7).

At several points in this thesis an inner product [60] is applied to field cross-sections obtained by finite-difference time-domain computations (FDTD) [61] in order to filter out specific modes. This inner-product is introduced in the appendix. A short proof of its applicability to Bloch modes is provided. As an example of possible applications it is used to compute intrinsic photonic waveguide losses. We show that by using this inner product to analyze data generated by FDTD, the size of computational domains can be significantly reduced while maintaining the accuracy of the obtained results. However it is also shown that the numerical accuracy of this method breaks down when applied to Bloch modes with very low group velocity. The origin and bounds of the numerical accuracy are formally derived.

The tool box used to analyze the dispersion in PCs increases in complexity throughout the first 6 chapters. Chapter 2 briefly introduces the general concepts that are used in the following chapters, such as group velocity in photonic crystals, the generalized Snell's law used at the interface of the superprism, etc... Chapter 3 is dedicated to self-collimation and analyzes propagation of light *inside* the photonic crystal. Chapters 4 and 5 then investigate the *coupling* of light in and out of PCs. Chapter 6 further investigates how the interaction between the dispersive properties of a PPC and conventional waveguide based integrated optics [62–65] can lead to dramatic improvements in device performance. One of the recurrent tools used throughout this thesis is the equi-frequency contour (EFC) introduced in chapter 2. The results derived in chapter 3, i.e., both the emergence of self-collimation and its limitations, can be entirely derived from the shape of the EFC restricted to the 1$^{st}$ Brillouin zone (BZ). However in order to understand coupling of light into PCs, and the interaction of PCs with the surrounding optics, the structure of Bloch modes also has to be carefully analyzed (chapter 5), and coupling conditions have to be derived in extended Fourier space. Chapter 7 combines all these techniques to optimize a planar demultiplexer that is subsequently fabricated and characterized.

Chapter 8 is independent from the rest of the thesis. It introduces a resonantly enhanced grating coupler (GC) that couples light around a 90 degree angle and is used to monolithically integrate vertical-cavity surface-emitting lasers (VCSELs) to on-chip waveguides [66]. In particular the VCSELs are coupled to planar waveguides without the need to place the GC inside the laser cavity such as in previous designs [68]. Rather, the GC is etched in the topmost epitaxial layer of the chip and does not necessitate regrowth after etching. However, in order to achieve good coupling efficiencies around a 90 degree angle a resonant mechanism has to be used. This is solved by introducing a defect into the grating. Electrically pumped VCSELs are fabricated in an aluminum-gallium-arsenide (AlGaAs) based material system and subsequently characterized.

# Chapter 2

# Engineered dispersion in photonic crystals

The dispersion characteristics of PCs can be engineered for practical applications such as guiding of light with the self-collimation effect [25–30], wavelength demultiplexion with the superprism effect [31–41], spot size conversion [24] or superlensing with negative index of refraction [54–59]. In this chapter we will introduce the basic concepts related to these effects. The first section introduces general concepts such as the Bloch theorem, the Brillouin zones (BZs), photonic crystal bands, the light cone, equi-frequency contours (EFCs) and the group velocity in PCs. The second, third and fourth sections are brief introductions to self-collimation, negative index of refraction, superlensing and the superprism (SP) effect. The fifth section relates the dispersion properties of PCs as well as the Bloch mode structure to band-folding. A more indepth version of this analysis can be found at the beginning of chapter 5.

## 2.1 Basic concepts

A planar photonic crystal (PPC) [51–53] is a thin dielectric slab in which a periodic array of scattering sites has been introduced. In the following the PCs are implemented as a periodic lattice of holes lithographically defined in a silicon film. The silicon film is clad on both sides by silicon dioxide, and the holes are backfilled with silicon dioxide. The fabrication process is described in section 7.2. The lattice of holes is generated from its unit cell by two primitive lattice vectors $\vec{e}_1$ and $\vec{e}_2$ (figure 2.1). The unit cell is defined as the smallest piece of the PPC from which the full crystal can be reconstructed with a periodic tiling.

Unlike a slab waveguide a PPC does not have a continuous translation symmetry. However, it has discrete translation symmetries generated by the unit lattice vectors. Due to these discrete

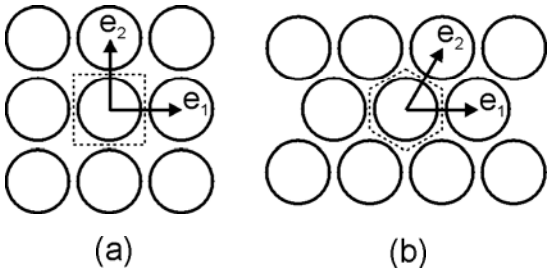


Figure 2.1: Schematic of (a) a square lattice PPC and (b) a triangular lattice PPC. The unit cell is delimited by a dashed line, and the lattice vectors are shown by arrows.

symmetries, light propagating in PCs can be described by modes $\psi = (\vec{E}, \vec{B})$ that verify

$$E(\vec{r}) = \bar{E}(\vec{r})e^{i\vec{k}\cdot\vec{r}} \tag{2.1}$$

$$B(\vec{r}) = \bar{B}(\vec{r})e^{i\vec{k}\cdot\vec{r}} \tag{2.2}$$

where $\vec{r}$ is the position-vector and $\bar{E}$, $\bar{B}$ are functions that have the same periodicity as the PC. In other words $\bar{E}(\vec{r} + m\vec{e}_1 + n\vec{e}_2) = \bar{E}(\vec{r})$, where $m$ and $n$ are integers. This property is known as the **Bloch theorem**, and PC modes are called Bloch modes [2].

By operating a Fourier transform, equation 2.1 can also be cast into the form

$$E(\vec{r}) = \sum_{m,n} \tilde{E}(m,n)e^{i(\vec{k}+m\vec{K}_1+n\vec{K}_2)\cdot\vec{r}} \tag{2.3}$$

$$B(\vec{r}) = \sum_{m,n} \tilde{B}(m,n)e^{i(\vec{k}+m\vec{K}_1+n\vec{K}_2)\cdot\vec{r}} \tag{2.4}$$

where $m$ and $n$ are integers and $\vec{K}_1$ and $\vec{K}_2$ are the inverse lattice vectors (so called because they belong to reciprocal k-space). They verify

$$\vec{e}_i \cdot \vec{K}_j = 2\pi\delta_{ij} \tag{2.5}$$

where $i, j \in \{1, 2\}$. In other words a Bloch mode can be described as a superposition of plane waves, where the relative phase and amplitude of the plane waves are linked by the Bloch mode structure. The term "plane wave" has to be taken with caution in this context as each individual component is not a solution of Maxwell's equations on its own. They are referred to as plane waves due to the fact that they feature planar wavefronts.

The vector $\vec{k}$ in equation 2.3 is not uniquely determined for a given Bloch mode; it is only determined modulo the inverse lattice vectors. In fact, replacing $\vec{k}$ by $\vec{k} + m\vec{K}_1 + n\vec{K}_2$ would only lead to a renumbering of the terms inside the sum 2.3. However there is only one possible choice of $\vec{k}$ inside a region of reciprocal k-space called the $\mathbf{1}^{\text{st}}$ **Brillouin zone** (BZ). It is defined as the

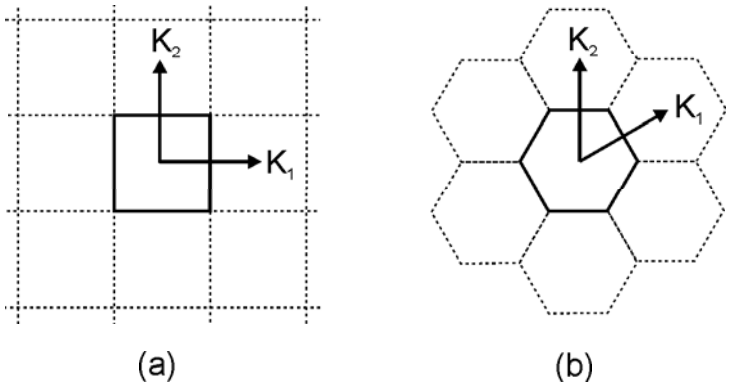


Figure 2.2: Schematic of reciprocal Fourier space for (a) a square lattice and (b) a triangular lattice. The inverse lattice vectors $\vec{K}_1$ and $\vec{K}_2$ are represented by arrows, and the 1st BZ is shown with a continuous line. Each of the cells delimited by the dashed line contains a single Fourier component of the Bloch mode. The inverse lattice vectors in the case of the triangular lattice are rotated by 30° relative to the lattice vectors in order to satisfy equation 2.5. Furthermore the magnitude of $\vec{K}_{1/2}$ is $2\pi/a$ in the case of the square lattice crystal and $4\pi/(\sqrt{3}a)$ in the case of the triangular lattice crystal, where $a$ is the lattice constant of the PC.

region of k-space delimited by the lines bisecting the inverse lattice vectors (figure 2.2). $\vec{k}$ is then called the reduced k-vector and will be noted as $\vec{k}_0$.

When photonic crystal Bloch modes are plotted as a function of their frequency and of their reduced k-vector, they form continuous surfaces called **photonic bands** [2]. A Bloch mode is uniquely determined by its band and its reduced k-vector. The first two photonic bands of a square lattice PPC are represented in such a manner in figure 2.3. The radiative modes of the cladding are also represented by a conical surface in the diagram. The set of all the cladding modes is delimited by that surface and is called the **light cone**[1]. Due to the isotropic nature of the cladding, the light cone has a cylindrical symmetry (that is the frequency does not depend on the in-plane orientation of the k-vector). If the cladding is assumed to be dispersion-free—which in the case of a real material such as silicon dioxide is an approximation—the light cone is truly a cone. In that case the k-vector is given by $2\pi n/\lambda$, where $n$ is the refractive index of the cladding (1.46 in the case of $SiO_2$) and $\lambda$ is the free space wavelength. Cladding modes located on the surface of the light cone correspond to light propagating parallel to the plane of the PPC, while modes inside the light cone propagate with a finite angle relative to the plane of the PPC. The PPC has a discrete translation symmetry so that the in-plane component of the k-vector is conserved modulo the inverse lattice vectors (in

[1]Band diagrams are often represented as 2D plots instead of the 3D *full* band diagrams. In that case the bands are only represented along the lines linking the high symmetry points, ΓM, MX and XΓ. The light cone is then represented as a line and is called the **light line**. The modes above the light line are the modes inside the light cone and are thus the lossy ones. In this thesis most band diagrams are full band diagrams in order to derive the dispersive properties of the crystal; thus we use the light cone nomenclature.

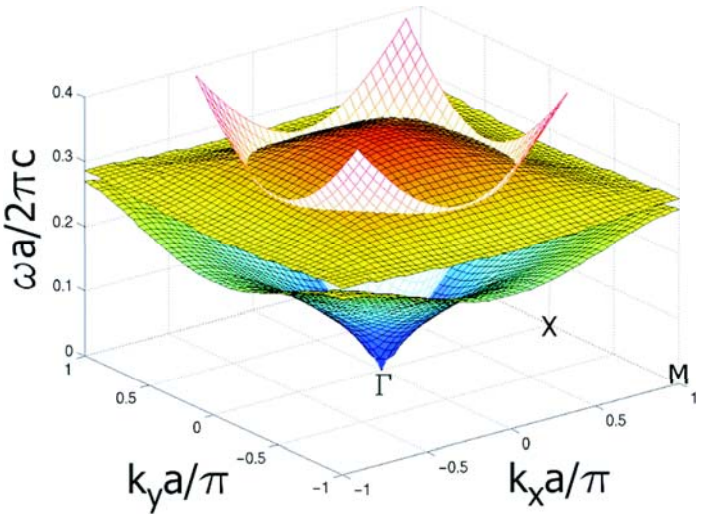


Figure 2.3: This figure shows the normalized frequency of the first two photonic bands of a square lattice PPC as a function of the normalized in-plane k-vector ($\omega a/2\pi c = a/\lambda$, where $\omega$ is the angular frequency and $\lambda$ the wavelength). The light cone is also shown. The PPC is a square lattice crystal with lattice constant $a$ and is etched into a silicon membrane of thickness $t = 0.57a$. It is cladd by air, and the radius of the holes is $r = 0.3a$.

other words the reduced k-vector is conserved). Thus PPC modes located outside the light cone cannot couple to the cladding and are lossless in an ideal crystal (that is in the absence of material absorption and fabrication imperfections). Only Bloch modes outside the light cone are truly bound eigenmodes of the PPC, while "modes" inside the light cone are lossy resonances of the PPC.

The set of all the reduced k-vectors of Bloch modes belonging to the same band, and corresponding to the same frequency, forms a continuous contour called an **equi-frequency contour** (EFC). It is the equivalent of the Fermi surface in solid state physics. In figure 2.3 this would correspond to the intersection of the bands with a horizontal plane (such contours are shown in figure 2.4). In general, the direction of propagation of a wave-packet is given by the **group velocity** $\vec{v}_g = \vec{\nabla}_k(\omega)$, where $\omega$ is the angular frequency. This also holds for Bloch modes, in that case $\vec{\nabla}_k$ is replaced by $\vec{\nabla}_{k_0}$, where $k_0$ is the reduced k-vector. The group velocity is perpendicular to the EFCs (the gradient of $\omega$ is perpendicular to contours of constant $\omega$) so that the direction of propagation of Bloch modes can be derived in a trivial way from the EFC. This makes the EFC a very powerful tool for the analysis of PCs. In the following sections it will be used to explain the self-collimation effect and the superprism (SP) effect.

## 2.2 Self-collimation

The anisotropic shape of the EFCs in PCs fundamentally modifies the propagation of light inside the slab. In particular, modes centered on the corners of the contour propagate in a very different

manner than modes located on the sides of the contour. The corners or other sharp features of the contour are also referred to as "**cusps**" in the following pages (this nomenclature makes particular sense in the case of triangular crystals where the EFCs can take the form of a six-branched star or of a hexagon). In this section, we will show how broadening of a finite cross-section beam can be suppressed to a large extent inside PPCs. This guiding mechanism is called self-collimation. We will start with a quick derivation of the beam-broadening in planar waveguides. We will then show how this diffraction is modified in PCs.

In a plain dielectric slab, an initially collimated beam broadens while propagating through the slab. The spatial Fourier transform of its finite cross-section also has a finite width. The individual components of the Fourier transform propagate in different directions so that the beam broadening can be related to the spatial Fourier spectrum. In turn, the width of that spectrum can be related to the width of the beam cross-section. The standard deviation (std) of the lateral k-vector component $\delta_{k_x}$ and the std of the field intensity distribution along the cross-section $\delta_x$ verify the inequality

$$\delta_x \delta_{k_x} \quad \geq \quad 1/2 \tag{2.6}$$

where $\delta_x$ and $\delta_{k_x}$ are given by

$$\delta_x \quad = \quad \sqrt{\frac{\int I(x) x^2 dx}{\int I(x) dx}} \tag{2.7}$$

$$\delta_{k_x} \quad = \quad \sqrt{\frac{\int \tilde{I}(k_x) {k_x}^2 dk_x}{\int \tilde{I}(k_x) dk_x}} \tag{2.8}$$

where $I(x)$ is the field intensity along the cross-section and $\tilde{I}(k_x)$ the field intensity distribution in k-space. The beam is assumed to be centered on $x = 0$ and to propagate in the y-direction. For a transform limited Gaussian beam the inequality turns into an equality, i.e., a Gaussian beam minimizes the width of the k-vector distribution for a given beam width, provided the widths are measured with the std[2]. In the case of a Gaussian beam the local beam width follows a hyperbolic dependence. The amplitude of the beam is given by $A(y)e^{-x^2/\sigma_x(y)^2}$ where $W(y) = 2\sigma_x(y)$ is the

[2]When the widths are measured with another metric, other functional forms might have a lower $\delta_x \cdot \delta_k$ product. For example if the full width at half maximum (FWHM) is used to evaluate the beam width, a hyperbolic secant $1/\cosh(x/x0)$ transform limited beam profile leads to $\Delta_k \cdot \Delta_x > 0.315 \cdot 2\pi$ while a Gaussian beam leads to $\Delta_k \cdot \Delta_x > 0.441 \cdot 2\pi$.

local beam width and is given by [71]

$$W(y) = W_0[1+(\frac{y}{y_0})^2]^{1/2} \tag{2.9}$$

$$y_0 = \frac{\pi W_0^2 n}{4\lambda} \tag{2.10}$$

$$\alpha_0 = \frac{2\lambda}{n\pi W_0} \tag{2.11}$$

where $n$ is the effective index of the slab, $y_0$ the Rayleigh range defined as the length after which the beam width is broadened by a factor $\sqrt{2}$ and $\alpha_0$ is the diffraction angle. The Fourier transform of a Gaussian beam also has a Gaussian functional dependence $exp(-k_x^2/\sigma_k^2)$. Equation 2.6 then turns into an equality *at the beam waist* and can be expressed in terms of $\sigma_x$ and $\sigma_k$ as

$$\sigma_x \cdot \sigma_k = 2 \tag{2.12}$$

Finally the FWHM of the Gaussian beam can be expressed as $\sqrt{2\log(2)}\sigma_x$. These expressions will be used in chapter 7 to evaluate design parameters for the superprism.

In PCs this situation is modified due to their anisotropic nature. The EFCs are no longer circles, but have features such as flat sides and cusps (figure 2.4). Along a flat side, the direction of the group velocity is constant, even if the k-vector is varied, so that diffraction is suppressed. On the other hand in the vicinity of a cusp, the direction of the group velocity undergoes sharper changes than what would be expected in the case of a circular contour of similar size. Thus, in a PC the diffraction is unevenly distributed in k-space. The propagation of light inside the PC is strongly dependent on the coupling conditions as they determine whether the k-vector distribution of the beam is located in the strong diffraction region or in the suppressed diffraction region (figure 2.5). It is relatively straightforward to see how a different crystal orientation can lead to self-collimation and suppressed diffraction, or to enhanced diffraction (figure 2.5).

## 2.3 Negative index refraction

This section is dedicated to negative index of refraction in PCs. First, we will introduce negative index on a high level—that is, we will describe the properties of negative index of refraction by taking the material properties as granted and show how a Gaussian beam can be refocused. We will then proceed by showing how these properties can be implemented with a PPC.

We first consider a Gaussian beam propagating from a material with refractive index $n_1 > 0$ to a material with refractive index $n_2 = -n_1$. In this case the Gaussian beam will refocus in the second material. In fact, the EFC is a circle of identical radius in both materials, but the group velocity points outside the contour in the first material and inside the contour in the second material. The

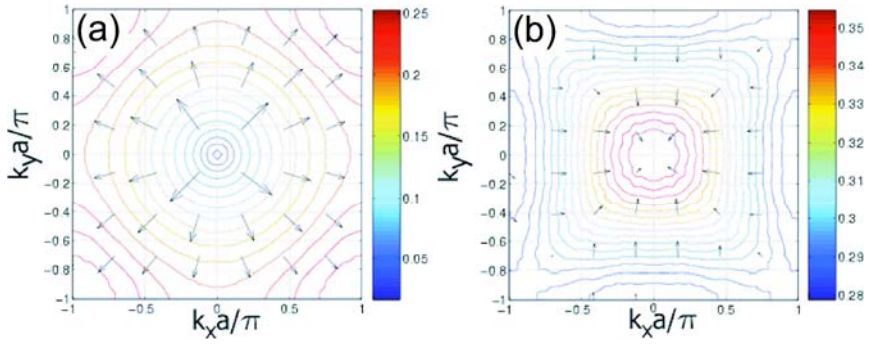


Figure 2.4: This figure shows EFCs for the 1st (a) and 2nd (b) bands of the square lattice PPC already introduced in figure 2.3. It can be seen that the contours are not circles as in an unpatterned slab. The group velocity is perpendicular to the contour and is indicated by arrows. It is pointing inside the contour rather than outside the contour in the case of the second band (section 2.5).

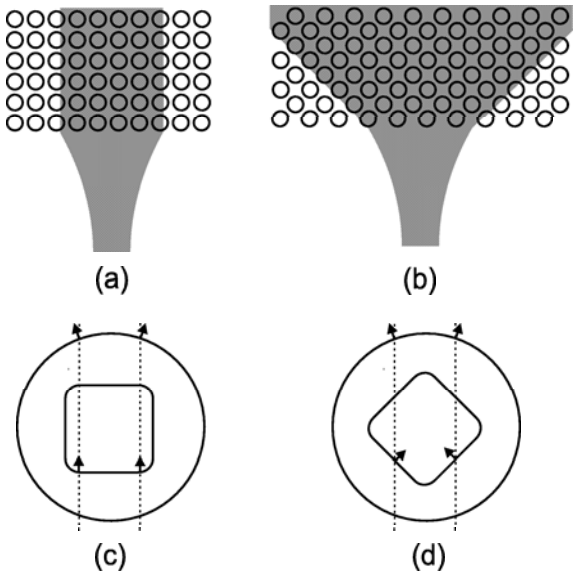


Figure 2.5: This figure illustrates how two different coupling conditions can lead to self-collimation, or conversely to very strong beam broadening inside the PC. In (a) and (b) a Gaussian beam is coupled from an unpatterned slab into a PPC. In (b) the lattice of the PPC is rotated by 45° relative to (a). While in (a) the beam stays collimated inside the crystal, in (b) the beam undergoes very strong broadening. (c) and (d) show the corresponding Fourier space diagrams. The projection of the k-vector onto the PPC boundary is conserved modulo $2\pi/a$ in (a) and modulo $2\pi/\sqrt{2}a$ in (b). The projection from the circular EFC of the unpatterned slab onto the squarish EFC of the PPC is visualized by the dashed lines. The EFCs are shown with a continuous line. The resulting group velocities are represented by arrows. It can be seen that in (c) beam-broadening is actually suppressed inside the PPC, while in (d) it is enhanced.

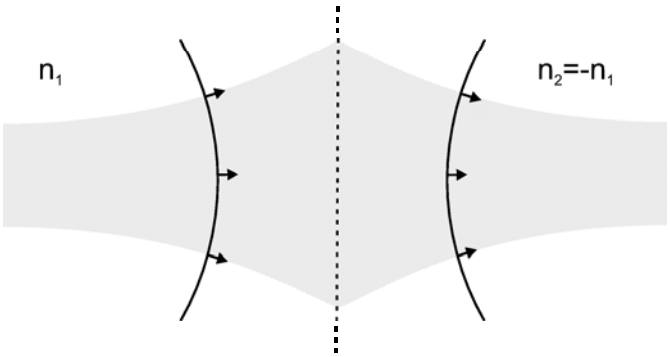


Figure 2.6: This figure illustrates the propagation of a Gaussian beam when coupled from a material with refractive index $n_1$ to a material with refractive index $-n_1$. The dashed line shows the boundary between the two materials. The circles show the EFCs in the materials, and the group velocities are indicated by arrows.

consequence is that for a given $k_x$, the angle of propagation in the second material $\alpha_2$ is the exact opposite of the angle in the first material $\alpha_1$; it is then easy to see in a ray-approximation that the beam reconverges (figure 2.6). The situation is more complicated when $n_2$ is not the exact opposite of $n_1$. In that case $\tan(\alpha_2) \simeq -n_1/|n_2|\tan(\alpha_1)$ only holds asymptotically around $k_x = 0$ so that the beam reconverges imperfectly inside the negative index material, at the distance $d|n_2|/n_1$ from the interface, where $d$ is the distance between the waist of the beam in the first material and the interface.

Negative index of refraction in metamaterials has attracted a lot of attention due to the fact that in a "left-handed" material, that is an artificial material with both a negative permittivity and a negative permeability, sub-diffraction-limit imaging (sometimes referred to as **superlensing**) is achievable. Such materials have the property of reamplifying evanescent waves that were exponentially decreasing in the positive index material. The emission profile of a light source or scatterer is composed of evanescent waves and propagative waves. The evanescent waves decay, and the corresponding information is lost. The propagative waves can be refocused, but the resolution is then limited by the diffraction limit $\lambda/2$. However if the evanescent waves can be reamplified and refocused this limitation does not apply anymore [54]. These properties have been shown in metallic left-handed metamaterials in the microwave regime [55, 56]. These materials are also the first to have been characterized with a negative refractive index. There has been originally some controversy over whether superlensing is achievable with photonic crystals; however, sub-diffraction-limit imaging has since been demonstrated in dielectric PCs [57,58]. However, in the following we only use negative index to refocus Gaussian beams. Thus we have not verified if and under which conditions superlensing occurs for the particular PPC used in chapters 6 and 7; this is why we sometimes refer to it as quasi negative index.

As already mentioned, the group velocity of modes belonging to the second band points inside

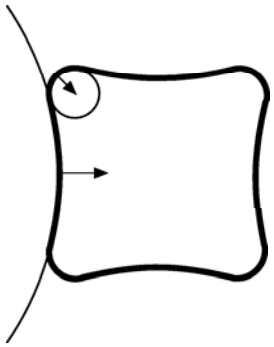

Figure 2.7: Negative index of refraction can be achieved if the group velocity points inside the tangent circle determined by the local curvature of the EFC. Even though the group velocity points inside the EFC for the second band, the curvature of the sides can be concave rather than convex so that the side of the EFC corresponds to a (very large) positive index. However, the corner region corresponds to a (small) negative index. Conversely, the EFC of the first band can be locally approximated by a negative index in certain cases (chapter 7), even though the group velocity points outside the EFC *when represented inside the first BZ.*

the EFC. Indeed the slope of the second band is negative, so that $\vec{\nabla}_{\vec{k}}(\omega)$ points inward. This is also related to the fact that the contour is folded back inside the first BZ (section 2.5). Furthermore, the EFC takes a circular shape near the high symmetry points so that an effective index can be unambiguously defined in these regions [72]. This can be seen in figure 2.4 where the contours take a circular shape around $\vec{k} = 0$ ($\Gamma$ point)[3]. Under these conditions, i.e., a circular EFC with the group velocity pointing inside the circle, the diffraction inside the photonic crystal can be described by a negative index of refraction. This is why negative refraction in PCs is often associated to the second band.

While the effective index approximation is straightforward for circular EFCs, it is not limited to them. In the case of contours with more general shapes, an effective index cannot describe the overall behavior of light. However, it is possible to associate an effective index to the *local* curvature of the EFC. Propagation of light can then be described by this index provided the k-vector distribution of the beam is limited to the region of the contour approximated by the tangent circle (figure 2.7) [41, 58]. For example in figure 2.5(d) the corner of the EFC has a rounded shape. If the lateral k-vector distribution $\{k_x\}$ were confined to that region the propagation of light could be described by an index $-n_{eff}$, where the radius of curvature of the rounded corner is $2\pi n_{eff}/\lambda$. This will be used in chapter 6 to refocus a beam exciting a SP. However, when the local curvature is used to derive an effective index, that index is not automatically positive for the first band and negative for the second band, as the tangent circle can be outside or inside the contour. In fact it doesn't matter

[3]This effective index is not constrained by $|n| > 1$; in fact the radius of the contour vanishes while approaching the high symmetry point. However in the immediate vicinity of the high symmetry point, the group velocity also tends to zero, and dispersion becomes very high [27] which leads to broadening of pulses in the time domain and to high insertion losses.

whether the group velocity points inside or outside the contour, but rather whether it points inside or outside the tangent circle determined by the local curvature of the EFC. Indeed in chapter 7 we use quasi negative index in the first band, while there can be regions of the second band where the effective index is positive (figure 2.7).

## 2.4 Superprism effect

The dispersive properties of PPCs can also be used to build planar wavelength demultiplexers. The most common configuration is known as the "superprisms" (SP). Figure 2.8 shows the general setup of such a device. An angled waveguide terminates at the boundary of the PPC. Depending on the frequency, light propagates in different directions inside the PPC and is guided to various waveguides at the output of the prism. The SP is similar to the conventional prism in that light is deflected at the boundary of the prism. In the case of the conventional prism the deflection of light can be derived from Snell's law, and the frequency dependence is linked to the chromatic dispersion of the dielectric, while in the SP a **generalized Snell's law** has to be applied. It consists in the conservation of the reduced k-vector component parallel to the interface. In the configuration shown in figure 2.8, the waveguide needs necessarily to be angled to achieve demultiplexion due to the orientation of the PC (the normal to the interface is a symmetry axis of the crystal lattice). Otherwise light would be coupled to modes on the ΓM axis that all propagate in the same direction, perpendicular to the interface, regardless of the frequency. Due to the fact the ΓM axis is a **symmetry axis** of the crystal, the group velocity has to be on ΓM when $k_0$ is on ΓM.

Light does not need to be coupled to the PC through Fourier components located inside the 1st BZ, but can also be coupled through components in higher order BZs. Equation 2.3 shows that a Bloch mode with a reduced k-vector $\vec{k}_0$ can also have components in **extended Fourier space** at k-vectors $\vec{k}_0 + m\vec{K}_1 + n\vec{K}_2$. Thus we represent the EFCs as a tiled pattern in extended Fourier-space, where the contours are offset by $m\vec{K}_1 + n\vec{K}_2$. Figure 2.9 illustrates one way to use a square lattice crystal as a SP; light is coupled to higher order BZs in order to couple to the cusp of the EFC while maintaining a large incident waveguide angle. The k-vector corresponding to light propagating in the waveguide is labeled as $k_{\mathrm{WG}}$ and makes an angle $\theta$ in respect to the normal to the interface of the PPC ($\theta$ also corresponds to the waveguide orientation). $k_{\mathrm{WG}}$ is shown for three slightly different frequencies so that the magnitude of the vector changes. Vertical dashed lines show how $k_{\mathrm{WG}}$ projects onto the EFC. Due to the steep angle they do not project onto the EFC in the 1st BZ but in a higher order BZ. Figure 2.9 is simplified in that the shape of the EFC doesn't change. In reality it does, we only opted for that representation to avoid overwhelming the schematic with details. A rigorous analysis of the SP that takes this into account can be found in chapter 7 (equation 7.3). In fact we will show that in this particular case the deformation of the

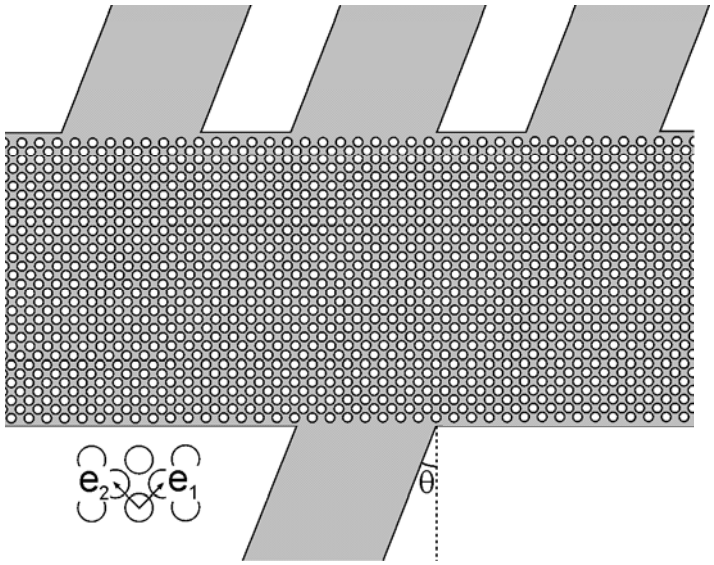


Figure 2.8: Schematic of a SP. A waveguide is terminated at one boundary of the PPC. Light propagates inside the PPC with a direction of propagation dependent on the wavelength. An array of waveguides collects the light at the other boundary of the PPC. The unit vectors $\vec{e}_1 = [1\ 0]$ and $\vec{e}_2 = [0\ 1]$ are represented. The orientation of the waveguides is given by $\theta$.

EFC actually reduces the resolution. Without going into a detailed analysis at this point, we can already see that for $\sin(\theta)k_{\mathrm{WG}} = 2\pi/(a\sqrt{2})$ light couples to the center of the cusp (on the higher BZ equivalent of the ΓM axis) and propagates strictly forward. For $\sin(\theta)k_{\mathrm{WG}} < 2\pi/(a\sqrt{2})$ light couples to the left of the center and propagates to the right, and for $\sin(\theta)k_{\mathrm{WG}} > 2\pi/(a\sqrt{2})$ light couples to the right of the center and propagates to the left.

There is another approximation in figure 2.9. The process is represented as if for each frequency light were coupled to a single point of the EFC. This only holds if the incoming light corresponds to a plane wave with infinite extent. However, when the incoming light is coupled from a waveguide, $k_{\mathrm{WG}}$ does not have a single well-defined value, but rather corresponds to a distribution whose width depends on the waveguide width (equation 2.6). The wider the waveguide, the more beam steering will be necessary to separate two frequencies (they need to be separated by the width of the waveguide or more if beam broadening occurs inside the PC), and thus the PPC needs to be wider. However, the wider the waveguide, the smaller the k-vector distribution corresponding to one frequency, and the smaller the overlap between the k-vector distributions of two distinct frequencies. The highest achievable frequency resolution will be higher for wider waveguides. Indeed for an infinitely large PPC, the frequency resolution would be uniquely limited by the overlap of the k-vector distributions. Thus there is a trade-off that determines the optimum waveguide width for a given PC size. The waveguides shown in figure 2.8 are represented as being fairly wide. There is actually a minimum

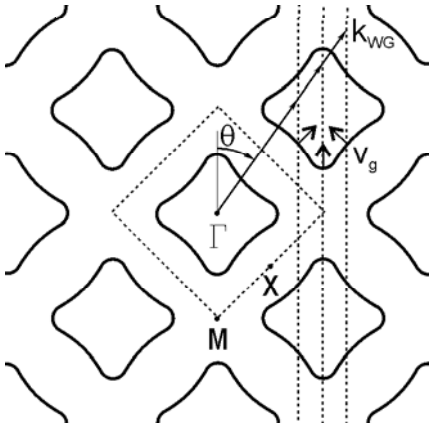


Figure 2.9: This Fourier space diagram illustrates a possible way to use a square lattice PPC as a SP. The first BZ is shown by a dashed square, and the EFC is shown both inside the 1st BZ and in higher order BZs. The orientation of the contours corresponds to the orientation of the PC in figure 2.8. The k-vector of the light inside the waveguide is labeled as $k_{\mathrm{WG}}$, and $\theta$ is the angle between the waveguide and the normal to the interface. The group velocity of light inside the crystal is labeled by $v_g$. The three high-symmetry points $\Gamma$, M and X are also shown. The projection of $k_{\mathrm{WG}}$ onto the contour is represented by dashed lines. $k_{\mathrm{WG}}$ and $v_g$ are shown for three different frequencies.

waveguide size that makes sense for demultiplexion, even if a very low resolution is targeted. If the waveguide is too thin, a situation as in figure 2.5(d) occurs, where most of the light gets coupled to the flat sides of the EFC (on both sides of the cusp) and propagates in the directions of self-collimation ($\pm 45^{\mathrm{o}}$ relative to the interface) regardless of the frequency. This analysis will be developed in details in chapter 6, and in chapter 7 an optimum waveguide width will be calculated for a specific design.

## 2.5 Band-folding and the shape of equi-frequency contours

The dispersive properties of PCs can be understood in terms of band-folding [40, 41]. Figure 2.10 illustrates this for the case of the second band of a square lattice crystal. We start with the EFC of the unperturbed slab (central circle). To the first order, the periodic lattice of holes generates other circular contours offset from the original one by an inverse lattice vector. These contours intersect in the first BZ (shown by the dashed square) and anti-cross, which gives rise to the rounded corners. Also the group velocity points outside of the circles, and thus inside the square contour. Of course the lattice of holes gives rise to higher order perturbations in the case of a finite hole size. In particular, the radius of the circles has to be modified from $2\pi n_{slab}/\lambda$ to $2\pi n_{eff}/\lambda$. Taking for $n_{eff}$ the weighted mean of the effective slab index $n_{slab}$ (weighted by $1-\pi(r/a)^2$) and the cladding index

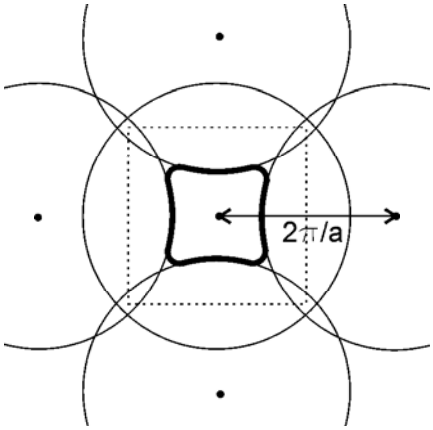


Figure 2.10: This figure illustrates how the EFC can be derived in terms of band-folding. The dashed square represents the first BZ. The central circle shows the EFC of the unperturbed slab, with a possible effective index correction. The 2D lattice of holes generates higher order contours offset by inverse lattice vectors (the center of the circles are indicated by black dots). Where they intersect, anti-crossing occurs giving rise to the rounded corners. The final contour is shown with the thicker line.

(weighted by $\pi(r/a)^2$) is a good first order correction (this is shown in section 5.1)[4]. The section of the circles located in the corners of the 1$^{\text{st}}$ BZ (i.e., the fractions of the circles inside the 1$^{\text{st}}$ BZ that do not belong to the squarish EFC of the 2$^{\text{nd}}$ band) would eventually give rise to the third band. However, due to the large splitting between the bands, there is a frequency region where only the second band is present. The large splitting is due to the fact that on the ΓM direction the second and the third bands have opposite symmetries in respect to $\vec{e}_1 + \vec{e}_2$. This leads to a higher overlap with the silicon for the second band and a higher overlap with the low index holes for the third band (section 5.1).

The Fourier structure of the modes—that is the relative intensity of the Fourier components for a given Bloch mode—can also be explained by this model. The dominant Fourier component is the one closest to the unfolded circle centered on the origin (the EFC of the unperturbed slab after correction for the effective index $n_{\text{slab}} \to n_{\text{PPC}}$). This can be visualized by progressively turning on the coupling induced by the lattice of holes. At zero coupling the dominant component contains 100% of the power. In figure 2.11 arrows indicate the correspondence between the EFC in the first

[4]The effective index of photonic crystals can be derived by homogenization theory in the limit of long wavelengths. In this limit the effective *dielectric constant* for the TM modes (E-field along the axis of the holes) of 2D photonic crystals is the weighted mean of the dielectric constants of the materials [73], while the *effective index* for TE modes seems to be the mean of the refractive indices of the materials. For a 2D square lattice photonic crystal with air pores of radius $r/a = 0.3$ etched into silicon, we calculated with FDTD the effective index to be 2.7453 in the limit of large wavelengths. The weighted mean of the refractive indices is 2.7429, which is the same number within the numerical accuracy of the calculations. In this thesis the crystals are PPCs, and the large wavelength condition is not verified; however, it seems that the weighted mean of the effective slab index and of the refractive index of the material filling the holes is a good approximation *before folding back into the* 1$^{\text{st}}$ *BZ*, as shown in section 5.1.

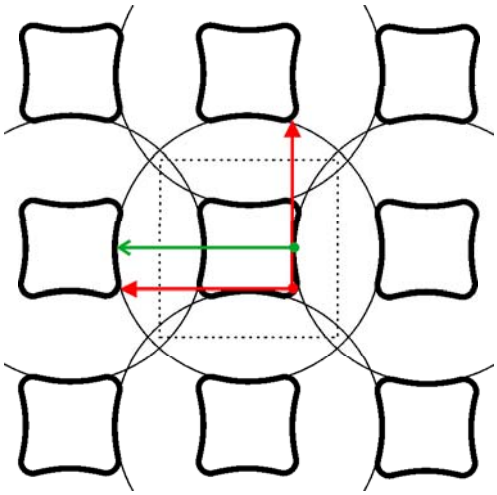

Figure 2.11: This figure illustrates the correspondence between the reduced k-vector located on the EFC in the 1st BZ and the dominant Fourier component(s) (shown by arrows). The dashed square shows the 1st BZ, and EFCs are shown by thick lines. The green arrow ("open" arrowhead) shows the correspondence between a mode located on the side of the EFC and its single dominant Fourier component. The red arrows (filled arrowheads) indicate the two dominant Fourier components of a mode located on the cusp of the EFC.

BZ and the dominant Fourier component(s). The modes on the corner of the EFC correspond to the anti-crossing region and have their power equally split between two dominant Fourier components.

The Bloch mode structure also gives some physical insight into how modes can propagate in the opposite direction than their reduced k-vector. The labeling of Bloch modes by their reduced k-vector is somewhat arbitrary from the point of view of the physics as it does not correspond to the dominant Fourier component in the case of the 2nd band. The k-vector of the dominant component is offset by $2\pi/a$ and is on the other side relative to the origin ($\Gamma$) so that it points in the same direction as the group velocity. Thus the relationship between the direction of the k-vector and the group velocity can be of a purely formal nature and misleading. The emergence of an actual physical phenomenon, negative refraction, is usually accompanied by strong coupling between Fourier components and complex mode structures, such as on the cusp of the EFC or in the vicinity of high-symmetry points.

Finally, the sharp change in direction of propagation at the cusp can also be correlated to the Bloch mode structure. In the corner-region of the contour the group velocity undergoes a drastic change in direction. However, at the same time the Bloch mode structure also undergoes a drastic change. On one side of the corner one component is dominant, while on the other side another component is dominant. The change in direction of propagation is due to a change in the relative weight of these two components. The coupling efficiency to and from the PPC is strongly dependent on the Bloch mode structure, which makes this analysis very important for the design of practical SP-based demultiplexers (chapter 5).

# Chapter 3

# Self-collimation and limitations

In chapter 2 the dispersive properties of PCs were introduced. In particular, it was shown that broadening of finite cross-section beams can be suppressed in bulk PCs without defining line-defects and without requiring non-linear effects [25]. This so-called self-collimation effect [25–30] will be numerically investigated in this chapter by means of square-lattice PPCs. In the first section self-collimation is introduced in detail. Also a specific PPC is investigated and shown to exhibit self-collimation without intrinsic radiation losses, provided the beam is coupled from free-space with an angle smaller than 54°. The second section explores the applicability of less computationally intensive 2D FDTD calculations. In the third section the group-velocity dispersion (GVD) for this PPC is investigated. A region in parameter space is given where group-velocity is maximized, GVD minimized and the self-collimation effect optimized. Group-velocity dispersion is expressed in terms of a generalized "$\beta_2$" ($\beta_2$ is taken from the optical fiber literature [74] and precisely defined in section 3). Self-collimation is not perfect due to the fact that the sides of the EFC are not perfectly flat. This leads to finite beam-broadening and to the emergence of beating patterns in the beam-profile [27]. They are investigated in section 4 by looking at the detailed shape of the EFC and by operating a Fourier analysis on the beam profiles. In the last section self-collimation in the first band is compared to self-collimation in the second band.

## 3.1 3D FDTD analysis of self-collimation in a square lattice planar photonic crystal

The structure that we are considering here is a silicon slab (refractive index $n_{Si} = 3.5$) of thickness $t = 0.57a$ and patterned with a 2D square lattice of holes of radius $r = 0.3a$, where $a$ is the periodicity of the lattice. The slab is surrounded by air on both sides. We have used a three-dimensional FDTD code [61] to analyze one unit cell of the structure by applying appropriate boundary conditions to the sides of the computational domain, as indicated in the Figure 3.1(a). The discretization

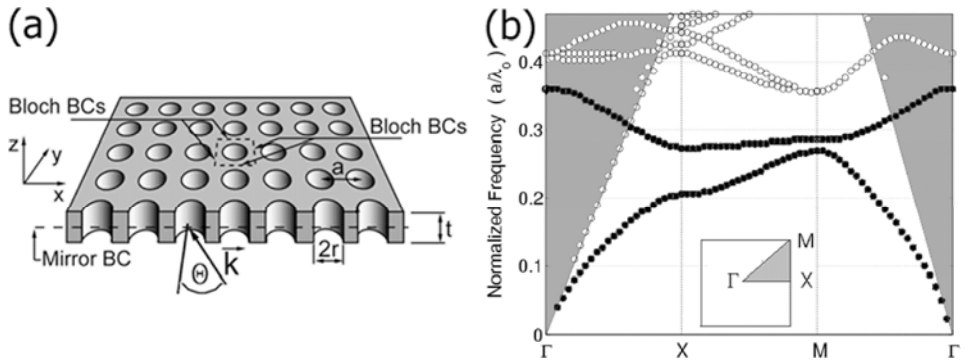


Figure 3.1: (a) Schematic view of the Si slab patterned with a 2D square lattice of holes. External light is incident on the slab at an angle $\theta$. The unit cell of the PC, with boundary conditions used in the 3D FDTD calculation, is also indicated. (b) Band diagram for TE-like modes (vertically even) of the square lattice PPC. The gray region represents the light cone. The inset shows the high symmetry points in the 1$^{st}$ BZ.

used in our 3D FDTD algorithm was 30 computation points per lattice period. By applying the mirror boundary condition at the center of the slab it was possible to reduce by half the size of the computational domain (the slab half thickness was $t/2 = 8$ computational points). Choosing the type of mirror symmetry (even or odd) we could select between TE-like (vertically even) or TM-like (vertically odd) eigenmodes of the PPC. Mur's absorbing boundary conditions [61] were applied at 100 computational points away from the surface of the slab, yielding a computational domain of $30 \cdot 30 \cdot 108$ cubic cells. More details on the band diagram analysis of PPCs using the FDTD method can be found in the literature [3].

The starting point for the investigation of any PPC based device is the calculation of a dispersion diagram of the modes supported by the PPC. In Figure 3.1(b) we show such a band diagram for the case of a square lattice PPC, obtained by using 3D FDTD. The band diagram is calculated only along the high symmetry directions in the first Brillouin zone (1$^{st}$ BZ), and the light cone is represented by the gray region. Only the modes that lie outside the light cone (below the light line) are guided in the PPC by total internal reflection, i.e., without any losses other than absorption, scattering and imperfect lithography. In other words, only modes outside the light cone are lossless in the ideal PPC (chapter 2). We can see that this structure has a small PBG. However, the width of the PBG is not what concerns us here. We instead hope to find unusual phenomena associated with the difference between the dispersion diagram of this structure and the dispersion diagram of an unpatterned slab. In order to do so, we have to calculate the *full* band diagram for *all* k-vectors in the 1$^{st}$ BZ and not only along the ΓX, XM and ΓM directions.

Figure 3.2(a) shows such a dispersion diagram for the first two bands [black circles in figure 3.1(b)] for *all* $k$-vectors in the 1$^{st}$ BZ. The band diagram was calculated from 325 equally spaced points in 1/8 of the 1$^{st}$ BZ [shaded region in the inset of figure 3.1(b)], the data were then fitted

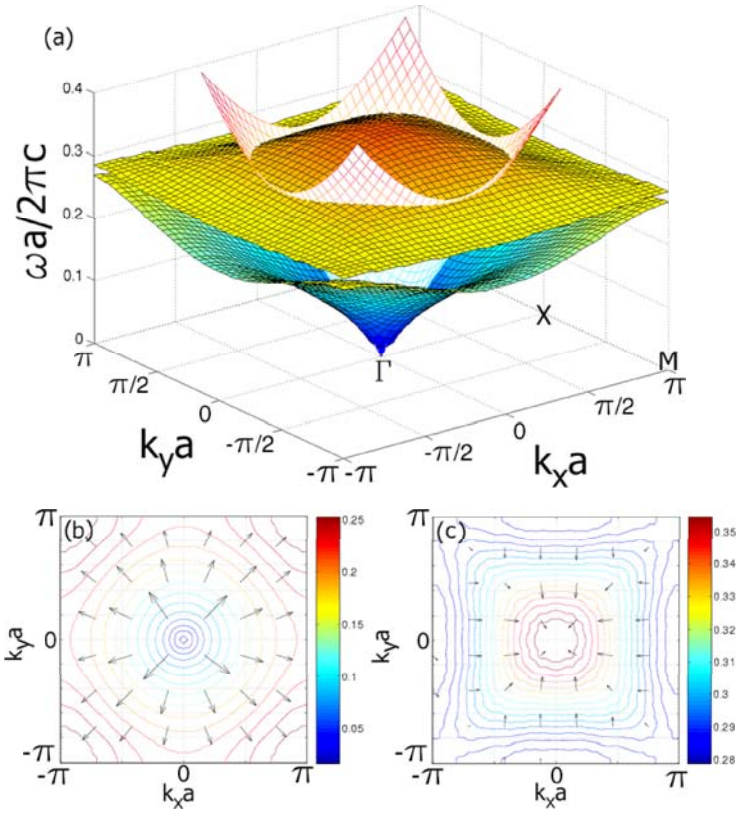


Figure 3.2: (a) Full band diagrams for the first two bands of the PPC. $\omega(k)$ is calculated for all $k$-vectors in the 1$^{st}$ BZ. The light cone is also represented. The EFCs for the first and second band are respectively shown in (b) and (c). The color code corresponds to the normalized frequency ($a/\lambda$). The vectors represent the group velocity.

with a polynomial of the fifth order and finally were mapped into the entire 1$^{st}$ BZ. The light cone is represented by the unshaded mesh. From figure 3.2(a) we conclude that the 1$^{st}$ band is entirely outside the light cone (guided), while the 2$^{nd}$ band is guided only for normalized frequencies $a/\lambda < 0.306$. In Figure 3.2(b) and (c) we plot the EFCs of the 1$^{st}$ and 2$^{nd}$ bands. The group velocity $\vec{\nabla}_{\vec{k}}\omega$ is indicated by vectors along the EFCs. In the case of the 2$^{nd}$ band the group velocity points inside the contour, an indication that the band is folded back into the first BZ. In addition, EFCs of the 2$^{nd}$ band are almost perfect squares in the frequency range where the 2$^{nd}$ band is guided. This is very different from the unpatterned Si slab, where EFCs of the guided modes are circles [Figure 3.3]. This modification of the EFCs from circles to squares leads to collimation-like effects in privileged directions (ΓX). This collimation effect is intrinsic to PPCs in that it does not require defects or non-linear effects. It is called self-collimation.

In Figure 3.4(a) we again show EFCs of the 2$^{nd}$ band of the square lattice PPC but this time only for frequencies that lie outside the light cone ($a/\lambda \in (0.273, 0.306)$). The light cone is represented by a dashed circle for $a/\lambda = 0.306$ (for higher frequencies part of the EFC is inside the light cone due

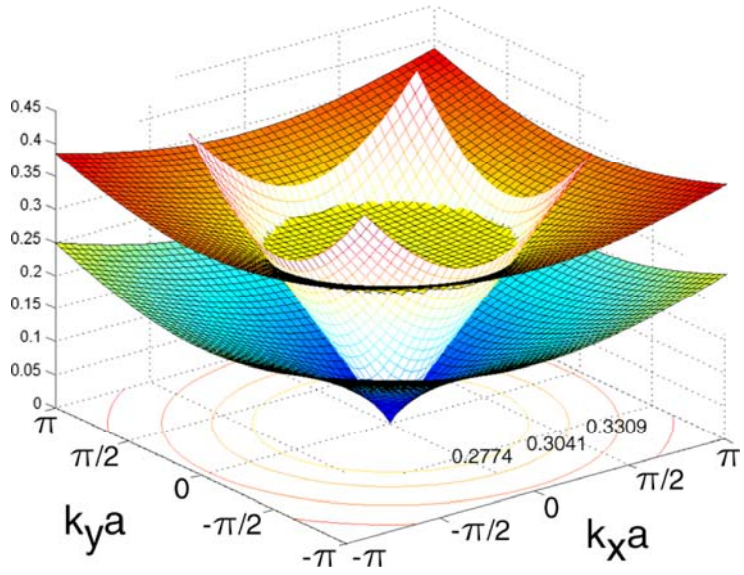


Figure 3.3: The dispersion of the first two bands supported in the unpatterned Si slab. The light cone is represented as an unshaded mesh. The EFCs are circles since all in-plane directions are equivalent.

to the fact that the EFC becomes smaller but the cross-section of the light cone becomes larger). It can be seen that the EFCs can be approximated by squares for $a/\lambda \in (0.295, 0.306)$. The energy propagation of the excited mode is given by the group velocity that can be calculated as

$$\vec{v}_g = \nabla_k \omega(k) = \hat{x} \cdot \frac{\partial}{\partial k_x} \omega(k_x, k_y) + \hat{y} \cdot \frac{\partial}{\partial k_y} \omega(k_x, k_y) \tag{3.1}$$

It is useful to reformulate this equation in terms of the normalized frequency $a/\lambda$ and the normalized $k$-vector ($a \cdot \vec{k}$), as band-diagrams are usually shown in those dimensionless units. $\vec{v}_g = 2\pi c \vec{\nabla}_{\vec{k} \cdot a}(a/\lambda)$. The direction of propagation is perpendicular to the EFC. Therefore, if we consider light incoming from an unpatterned slab onto a PPC with a range of $k$-vectors so that their projection onto the interface ($k_x$) is comprised between $-k_0$ and $k_0$ [Figure 3.4(a)], light in the PPC will propagate along the y-axis direction ($\Gamma$X). This is indicated by the gray color in Figure 3.4(a). In other words, the light beam in the PPC can be self-collimated. This property of square PPCs is entirely due to the fact that EFCs for the 2$^{\text{nd}}$ band look like squares. In contrast to the PPC case, EFCs of an unpatterned Si slab are circles [Figure 3.4(b)]. When such a slab is excited with a range of $k_x$ components, light in the slab diverges as schematically indicated by the gray region in Figure 3.4(b).

We consider a PPC with a cleaved edge along the xOz plane and a light beam incident on the edge with an angle $\theta$ [Figure 3.1(a)]. In order for the beam to be self-collimated, the x-component of the k-vector inside the PC ($k_x$) has to be within the approximately flat side of the EFC [Figure 3.4(a)]. However, $k_x$ is determined by the wavelength of the incident light as well as the angle of

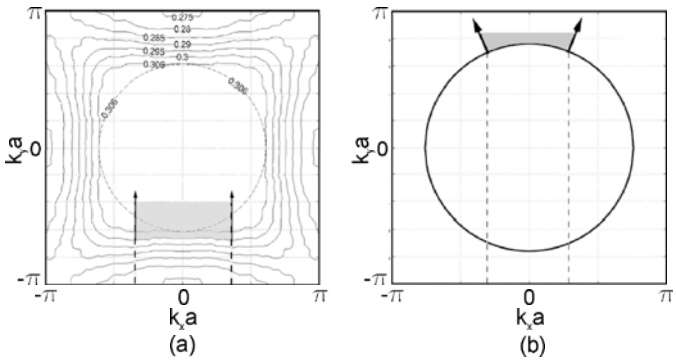


Figure 3.4: (a) The EFCs of the 2nd band of a square lattice PPC. Only the region outside of the light cone is shown $[a/\lambda \in (0.273, 0.306)]$. The light cone is represented for $a/\lambda = 0.306$ by the dashed circle. Light coupled to the side of the EFC is self-collimated and propagates in the direction indicated by the gray color. (b) EFCs of the unpatterned Si slab are circles, and beam broadening occurs.

incidence $\theta$ [Figure 3.1(a)]. Therefore, self-collimation might occur only for a restricted range of $\theta$s. The x-component of the reduced k-vector is conserved at the interface of the PC. This is due to the fact that both the slab and the PC verify the same discrete translation symmetry along the interface. $k_x$ can be expressed as $k_x = (2\pi/\lambda) \cdot \sin(\theta)$. In order for $k_x$ to belong to the flat side of the EFC it has to satisfy $\mid k_x \mid \leq k_0$, where $2 \cdot (k_0 \cdot a)$ is the normalized width of the side minus the rounded corners and is a function of normalized frequency. Combining these two expressions we get

$$\frac{(k_0 \cdot a)}{(a/\lambda) \cdot 2\pi} \geq \mid \sin(\theta) \mid \tag{3.2}$$

It can be easily verified that if the EFCs were perfect squares, inequality 3.2 would be verified for all EFCs outside the light cone. It is the most stringent at the highest frequency for which the EFC is still below the light cone. At that frequency the light cone is the inscribed circle of the squarish EFC so that $k_0$ is also the radius of the light cone $2\pi/\lambda$ provided the EFC is a perfect square. The left hand side of equation 3.2 then turns to 1 so that the equation is satisfied for any angle $\theta$. However, since the equi-frequency squares are rounded at the corners, we have to assume a more conservative value $k_0 \cdot a = 1.502$ for $a/\lambda = 0.306$ [Figure 3.4(a)]. Then, the left hand side of (3.2) becomes

$$\frac{(k_0 \cdot a)}{(a/\lambda) \cdot 2\pi} = 0.817 \tag{3.3}$$

and $\mid \theta \mid \leq \arcsin(0.817) \approx 54^{\circ}$. Therefore, the square lattice PPC acts as a self-collimator for incident angles $\mid \theta \mid \leq 54^{\circ}$ and $a/\lambda \in (0.295, 0.306)$. The group velocity of a PPC Bloch mode depends both on the normalized frequency and on the $k$-vector, and is calculated to be in the range $v_g \in (0.16, 0.25) \cdot c_0$ ($c_0$ is the speed of light in vacuum) for $a/\lambda \in (0.295, 0.306)$ and $\mid \theta \mid \leq 54^{\circ}$.

In order to verify the predictions that self-collimation is possible in a square lattice PPC we have

used 3D FDTD modeling on such a structure. Figure 3.1 shows the field evolution ($B_z$ component) in an unpatterned (a) and patterned (b, c) Si slab. The structures were excited with a dipole source placed at the center of the slab. In the case of the unpatterned slab, the characteristic dipole radiation, with spherical wavefronts, is observed [Figure 3.1(a)]. The PPC structure shown in figure 3.1(b) was excited with a dipole source with a frequency ($a/\lambda = 0.295$) chosen to be in the frequency region of the 2$^{\text{nd}}$ band where EFCs are squares [Figure 3.4(a)]. Because of that, it is expected that light is radiated predominantly in the four ΓX directions that are perpendicular to the four sides of the EFC. Indeed, the 3D FDTD simulation of the structure [Figure 3.1(b)] shows such a behavior. Therefore, we conclude that the square lattice PPC has modified the radiation pattern of the dipole source in the way predicted by the above analysis of EFCs. It is also important to notice that this interesting phenomenon is taking place outside the light cone. Thus, the light is self-collimated as it propagates in the ideal PPC without any intrinsic losses. Self-collimation can also be obtained by exciting the 1$^{\text{st}}$ band; this time light propagates in the ΓM direction, as shown in Figure 3.1(c). This figure has been rotated by 45$^{\text{o}}$ and rescaled by $1/\sqrt{2}$ in order to show structural similarities between self-collimation in the 1$^{\text{st}}$ and in the 2$^{\text{nd}}$ bands (section 3.5).

In summary, based on a 3D FDTD analysis, we have found a PPC geometry as well as a range of parameters, frequency and incident angle of light for which self-collimation can be observed. The next sections are dedicated to phenomena that require more intensive computations. First, we briefly investigate the difference between 2D and 3D calculations and their applicability to self-collimation in PPCs. We then proceed with a more detailed analysis of EFCs and validate our conclusions with corresponding 2D FDTD simulations.

## 3.2 Applicability of a 2D FDTD analysis to planar photonic crystals

In the following several properties relating to self-collimation, such as group velocity dispersion (GVD), the emergence of beating patterns and structural similarities between self-collimation in the first and in the second photonic bands are investigated. Real space simulation of large PCs are performed in order to demonstrate these properties. Due to limitations of the available computational power we reverted to use 2D FDTD. In this section we briefly investigate the difference between 2D and 3D calculations as far as self-collimation is concerned. It is by no means an exhaustive analysis but it provides some useful insights.

In order to accurately predict the frequencies of the bands of 3D PPC structures using 2D calculations, it might seem a good approach to replace the index of the slab material by the effective index of the slab [Figure 3.6(a)]. In fact, by reducing the slab index from 3.5 (the index assumed in the 3D FDTD computations) to 2.7 it was possible to get a better overall overlap between the

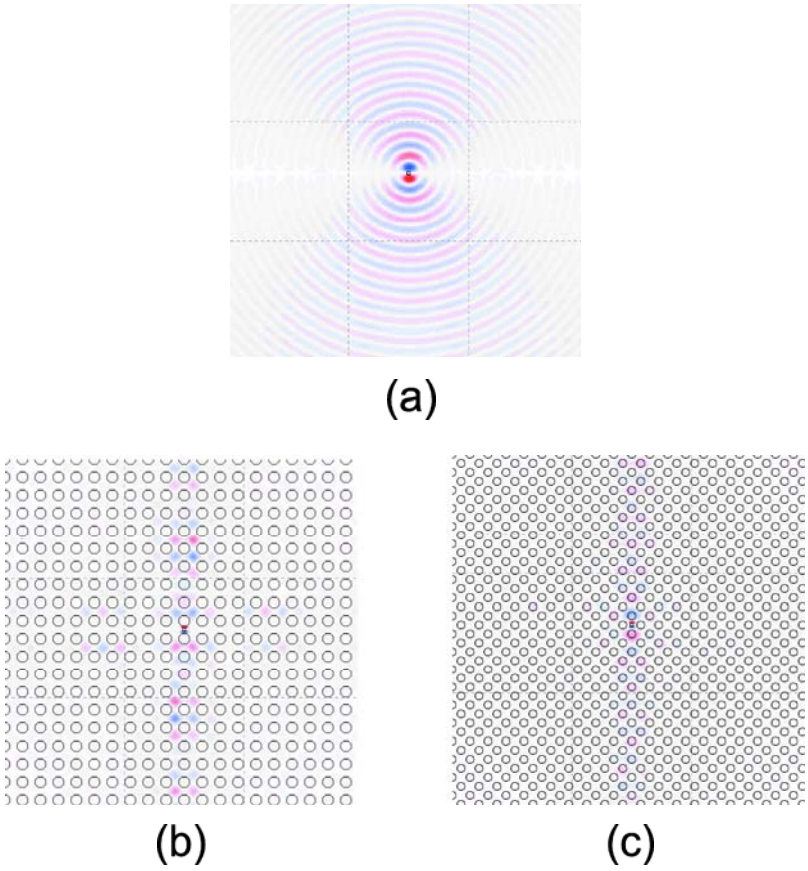


Figure 3.5: Evolution of the out of plane component of the B-field in (a) the unpatterned slab and (b,c) the slab patterned with a square lattice PPC. The structures were excited with a dipole source at frequencies (a) $a/\lambda = 0.295$, (b) $a/\lambda = 0.295$ and (c) $a/\lambda = 0.2086/\sqrt{2}$. (b) corresponds to self-collimation in the second band. In this case, light is radiated predominantly along ΓX directions. (c) corresponds to self-collimation in the first band. (c) has been rotated by 45° and rescaled by $\sqrt{2}$ to show structural similarities in the emission patterns that will be elaborated on in section 3.5.

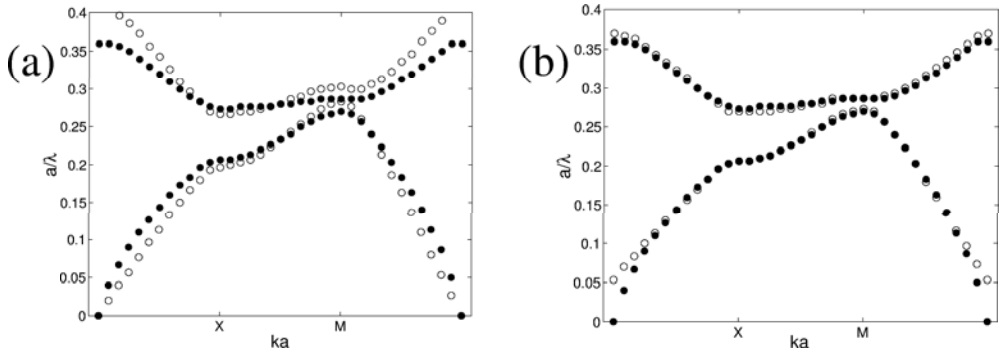


Figure 3.6: The band-diagram for TE-like (vertically even) modes of the square lattice PPC as calculated by 3D FDTD is shown by dots in (a) and (b). In (a), circles show the bands calculated for a 2D square lattice PC with an index of 2.7 assumed for the slab. In (b), a slab index of 3.5 (same index as in the 3D calculation) has been assumed and a constant normalized frequency offset was added (0.0533).

calculated bands in the 2D and in the 3D cases. However this comes with the price of a significant distortion of the bands. We found that calculating the band diagram with 2D FDTD with the original index and subsequently adding a fixed frequency offset to the bands yielded a much better overlap [Figure 3.6(b)]. For the particular PPC investigated in this chapter a constant normalized frequency offset of 0.0533 results in the best overlap between 2D and 3D calculations. For normalized frequencies between 0.15 and 0.35 there is a very close overlap. This includes the useful frequency range for self-collimation. In the following 2D FDTD simulations, this frequency offset must be added to all reported frequencies in order for them to apply to the 3D PPC .

## 3.3 Group velocity, group velocity dispersion

The maximum group velocity in the second band is calculated to be 0.276 times the speed of light and is reached in the region of strong self-collimation, where the EFCs are squares with maximally flat sides [Figure 3.7]. This region also corresponds to a local minimum of the GVD, as the derivative of the group velocity is zero at its maximum. Thus, a self-collimated beam in that regime (minimum spatial pulse dispersion) would also have maximum group velocity and minimum GVD (temporal pulse dispersion). This occurs at the normalized frequency $a/\lambda = 0.261$ and at a normalized $k$-vector $k \cdot a = 1.795$ in the $\Gamma$X direction. It corresponds to an effective index of $1.096 > 1$[1] and would thus correspond to a non-leaky mode had this been a 3D calculation. However, in the case of the 3D PPC, the normalized frequency is shifted up by 0.0533. This mode is then situated inside the light cone and is leaky. That is why in the 3D analysis the maximum $v_g$ for non-leaky modes was found to be 0.25 instead of 0.276 predicted by the 2D calculation. In other words, in order to avoid radiative losses we have to settle with a slightly sub-optimum mode as far as group velocity and GVD are concerned.

In the fiber optics literature, the GVD is given by $\beta_2$ [74]

$$\beta_2 = \frac{\partial}{\partial\omega}\left(\frac{1}{v_g}\right) = -\frac{1}{v_g^2}\frac{\partial v_g}{\partial\omega} \tag{3.4}$$

After propagating an initially transform-limited pulse for a length $L$ through a fiber characterized

[1] "Effective index" is not used in the same way here as in section 2.3. In the latter the refractive index is related to the local curvature of the EFC; however, the center of the tangent circle is not the $\Gamma$ point. This is a good approach to predict beam propagation, but not to evaluate whether a beam is inside or outside the light cone. Here the effective index is related to the reduced k-vector, that is, to the distance between the $\Gamma$ point and the $1^{st}$ BZ Fourier component. It is not suitable to predict propagation properties (the EFC is not a circle with the reduced k-vector as radius; in fact beams are self-collimated); however, with the latter definition $n_{\text{eff}} > n_{\text{clad}}$ is a good criterion to verify whether light is outside the light cone. $n_{\text{clad}}$ is the refractive index of the cladding.

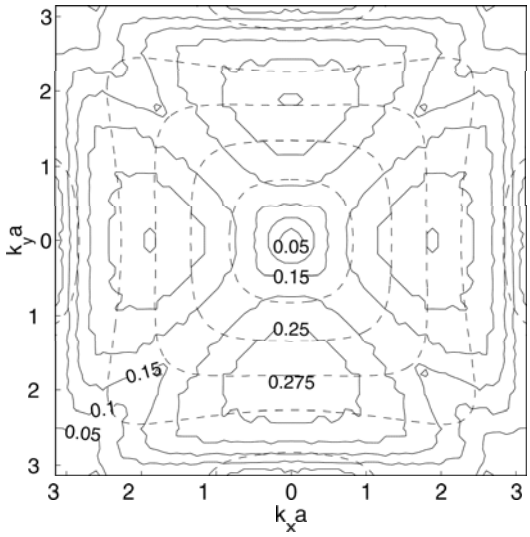


Figure 3.7: The EFCs of the second TE-like band (dashed lines) and the group velocity isocurves (continuous line). The group velocity is given as a fraction of the vacuum speed of light. The contours of constant group velocity are ragged because the numerical differentiation amplifies the numerical inaccuracies of the raw data.

by $\beta_2$, the temporal pulse width would become

$$\mid \beta_2 \mid \cdot L \cdot \Delta\omega \tag{3.5}$$

where $\Delta\omega$ is the spectral pulse width. $\beta_2$ is unambiguously defined in a fiber because $v_g$ is a function of $\omega$. However, in a PC $v_g$ depends both on $\omega$ and on the specific $k$-vector. For a specific frequency, the k-vector is constrained to be on the EFC, but this still leaves a degree of freedom. In the following we use a generalized $\beta_2$ to estimate beam broadening in a PC.

$$\beta_2 = \frac{\| \vec{\nabla}_k(v_g) \|}{v_g^3} \tag{3.6}$$

In a 2D crystal the group velocity for a given normalized frequency is independent of the lattice constant $a$ (the formula for the group velocity in terms of normalized frequency and normalized k-vector is given at the beginning of this chapter). However $\vec{\nabla}_k = a\vec{\nabla}_{a\cdot k}$ is proportional to $a$. Thus $\beta_2$ is dependant on the scaling of the PC, but $\beta_2/a$ is independent of a [Figure 3.8].

## 3.4 Beating patterns

Due to the fact that the EFC is a square with approximately flat sides, beam broadening is suppressed to a large extent. However the sides of the contour are not perfectly flat so that a small amount of beam broadening is still present. In this section we will show that beam broadening can also lead to

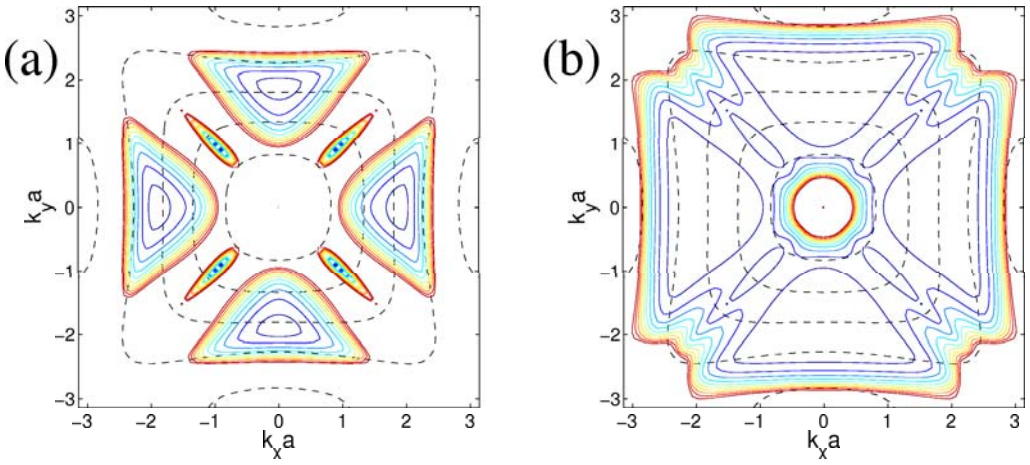


Figure 3.8: Isocurves for $\beta_2/a \cdot c_0^2$ (dimensionless normalized units) for the second band of a square lattice PC with $r/a = 0.3$. The group velocity calculated previously was smoothed before further differentiation. (a) Isocurves for $\beta_2/a \cdot c_0^2$ from 0 to 10 and (b) isocurves for $\beta_2/a \cdot c_0^2$ from 10 to 100.

the emergence of beating patterns. Due to the slightly concave shape of the side and to the convex shape of the corners, there are only three points along each side with the group velocity exactly aligned along $\Gamma X$ [Figure 3.9]. If we propagate a self-collimated beam for a long distance we expect these three components to become dominant. In fact we will show that these three components can give rise to a beating pattern in the self-collimated beam once they become dominant. The emergence of this beating pattern is dependant on the initial conditions with which the beam is launched. Indeed if the initial k-vector distribution is thin enough to contain only one of the three points the beam will simply broaden and no beating pattern will appear, while if at least two of the points are in the initial k-vector distribution the beating will appear.

We took the spatial Fourier transform of a beam propagated for 400 periods. The Fourier transform was operated on a region of $15 \cdot 15$ periods, centered on the self-collimated beam ($a/\lambda = 0.2596$). Three distinct components are strongly dominant in the spatial Fourier spectrum [Figure 3.4].

The beating pattern along the direction of propagation will depend on $\delta k_y$ [Figure 3.4]. $\delta k_y$ is very small, and the beating length is thus long. We propagated a self-collimated beam of normalized frequency 0.2596 (distributed 2D FDTD) and observed a beating pattern along the center of the beam. The beating length is about 1000 lattice periods. This corresponds to $a\delta k_y = 2 \cdot \pi/1000 = 0.0063$ and is relatively close to the $a\delta k_y$ extracted from the EFC (0.0093). In order to confirm that the beating length can be related to $\delta k_y$, we propagated a self-collimated beam corresponding to a different frequency ($a/\lambda = 0.25$) with a larger $\delta k_y$. We found the beating length to be 133 periods. This corresponds to $a\delta k_y = 2 \cdot \pi/133 = 0.047$ and is very close to the $a\delta k_y$ extracted from the EFC (0.057).

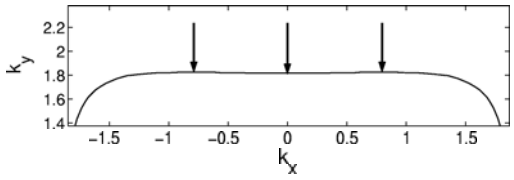


Figure 3.9: Zoom of one of the sides of the EFC at normalized frequency 0.2596. The arrows indicate the $k$-vectors for which the group velocity is perfectly aligned to the y axis.

We also observed in both cases the emergence of side lobes. This transverse interference pattern is due to the different $k_x$ of the three perfectly collimated components. The transverse interference pattern can only be seen if the self-collimated beam is wide enough, after significant broadening. As the continuum of Bloch-modes decays to the superposition of three discrete modes (or more precisely three narrow k-vector distributions), the beam broadens ($\delta k_x \cdot \delta x \geq 1/2$, see chapter 2) and an interference pattern emerges. This interference pattern has a beating length of $2\pi/1.16 = 5.4a$ in the case of $a/\lambda = 0.2596$ and of $2\pi/1.38 = 4.5a$ in the case of $a/\lambda = 0.25$.

A tiling pattern is generated by the simultaneous effect of longitudinal and lateral beating. Because $\delta k_y << \delta k_x$, the beating length in the y-direction is much larger than the period of the transverse interference pattern, and the overall effect is one of a comb of side lobes that offsets by half the period of the transverse interference pattern every half longitudinal beating length. Figure 3.11 shows the emerging lateral interference pattern as well as the longitudinal beating. In order to correctly resolve the side lobes, very wide PCs must be simulated. Because of computational limitations we reduced the discretization to 22 points per unit cell for this calculation. This computational change introduced a 1% frequency down shift of the bands (0.003 in units of normalized frequency) around $a/\lambda = 0.2596$.

It is important to take this beating pattern into account if self-collimation is to be used in real devices. For example, if a self-collimated beam is to be coupled to a waveguide, it is important to know that the field might have a minimum at the center of the self-collimated beam.

So far we have analyzed self-collimation in the $2^{\text{nd}}$ band of a square lattice PPC. However, light can also be self-collimated in the $1^{\text{st}}$ band of a square lattice PC, but in the ΓM direction instead of the ΓX direction. In the next subsection we will show that a self-collimated beam can even be transmitted at the interface between two different PCs so that it corresponds to the $1^{\text{st}}$ band in one and to the $2^{\text{nd}}$ band in the other. This transmission occurs with low losses and low distortion. We will investigate structural similarities (in reciprocal space) between self-collimation in the $1^{\text{st}}$ and the $2^{\text{nd}}$ bands that show self-collimation to be essentially identical in both bands.

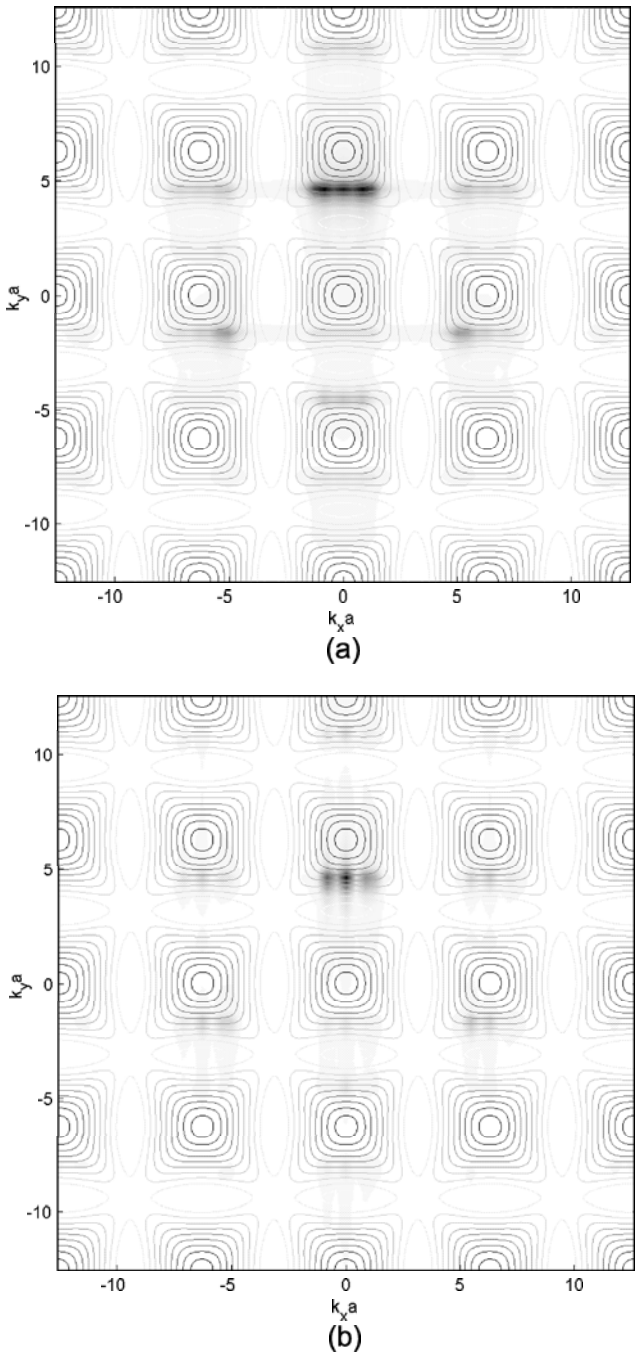


Figure 3.10: The spatial Fourier transform of a self-collimated beam at normalized frequency 0.2596 respectively 30 periods (a) and 400 periods (b) after launching it with a dipole source. Three discrete components become dominant. The EFCs are overlaid.

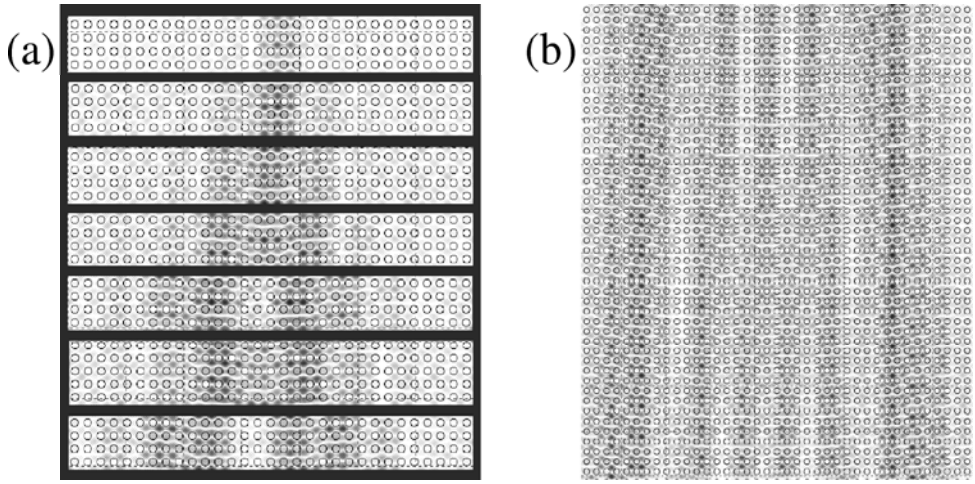


Figure 3.11: (a) Self-collimated beam ($a/\lambda = 0.2596$) after different propagation distances (top down: 30, 80, 130, 180, 230, 280 and 330 lattice periods). The self-collimated beam broadens, and a beating pattern appears. (b) Self-collimated beam ($a/\lambda = 0.25$) after propagation over 220 lattice periods. The beating pattern and the transverse interference pattern are clearly seen: the comb of lobes correspond to the transverse beating pattern; the offset of the comb between the top and the bottom of the figure is due to the longitudinal beating. Light on the sides of the beam corresponds to weakly self-collimated light that disperses out of the beam. It corresponds to the Fourier components of the continuum of k-vectors of the original beam that do not belong to the three remaining k-vector groups.

## 3.5 Comparative analysis of self-collimation in the first and second bands

The first and the second band of a square lattice PPC seem to have very different structures. Indeed, the group velocity points out of the EFCs in the first band, while in the second band it points inside. Also, self-collimation takes place in the ΓM direction in the first band and in the ΓX direction in the second band. However, we can show that the two bands are related by a simple transformation consisting of a 45° rotation and a rescaling. In particular, the regions where self-collimation takes place, where the sides of the EFCs are flat, have the same structure in both bands. Indeed the reciprocal space transformation maps these two regions one onto the other, except for a slight frequency offset (0.007 in units of normalized frequency).

In order to show this we will introduce a second PC lattice (PC2), that is in fact the same PC rescaled and rotated, and show similarities between the two PCs. The transformation in real space that maps PC1 onto PC2 is the equivalent of the inverse space transformation that maps the $1^{st}$ band onto the $2^{nd}$ band. By showing that the $1^{st}$ band of PC2 overlaps with the $2^{nd}$ band of PC1 we conclude that self-collimation in the $1^{st}$ and $2^{nd}$ bands has similar properties.

We define PC2 as a square lattice 2D PC with lattice constant $a/\sqrt{2}$ (where a is the lattice period of PC1), hole radius $r/\sqrt{2}$ (where r is the hole radius of PC1) and with a lattice rotated by

45° in respect to PC1. $r/a$ is conserved, the bands of PC2 are obtained by rotating the bands of PC1 by 45° and by rescaling both the frequencies and the k-vectors according to equations 3.7 and 3.8. The area of the 1st BZ of PC2 is then twice the area of the 1st BZ of PC1 [Figure 3.12(b)]. It contains both the 1st BZ and the 2nd BZ of PC1 (the 2nd BZ of PC1 is composed by the 4 "corners" of the BZ of PC2, that is, the white region in figure 3.12).

$$\vec{k_2} = \sqrt{2} \cdot \mathrm{rot}_{45^\circ}(\vec{k_1}) \tag{3.7}$$

$$(a/\lambda)_2 = \frac{(a/\lambda)_1}{\sqrt{2}} \tag{3.8}$$

Figures 3.12(a) and (b) show the EFC of the second band of PC1 and of the first band of PC2. The contours are almost identical in the white regions and differ in the grey shaded regions. Indeed the white region of PC2 corresponds to the second band of PC1, while the grey region of PC2 corresponds to the first band of PC1. The only significant difference between PC1 and PC2 is that PC2 does not have a PBG around $a/\lambda = 0.18$ (Figure 3.12(c)). This frequency region corresponds to the interface between the white and the grey zones in the band diagram of PC2 (figure 3.12(b)).

As already mentioned, the structural similarities between PC1 and PC2 correspond to structural similarities between the first and the second band of PC1. In other words, self-collimation in the first band will closely resemble self-collimation in the second band modulo a 45° rotation and a rescaling by $\sqrt{2}$.

There is a slight frequency offset as PC1 and PC2 overlay closely, but not perfectly. The EFC corresponding to the 2nd band of PC2 at $a/\lambda = 0.2596$ overlays the EFC of the 1st band of PC1 at $a/\lambda = 0.2526$ (2.7% offset). We can compensate this frequency offset for $a/\lambda = 0.2596$ by using a hole radius of $r/\sqrt{2} = 0.322 \cdot a/\sqrt{2}$ for PC2 instead of $0.3 \cdot a/\sqrt{2}$. In the following discussion this hole radius compensation is applied.

We compare the width of a beam of normalized frequency $a/\lambda = 0.2596$, self-collimated in the 2nd band of PC1 ($r/a = 0.3$), with the width of a beam of normalized frequency $a/\lambda = 0.2596/\sqrt{2} = 0.1836$, self-collimated in the 1st band of a PC of same lattice period a and with $r/a = 0.322$. The beams are excited by a dipole source predominantly radiating in ΓX ($a/\lambda = 0.2596$) and the ΓM ($a/\lambda = 0.1836$) directions and located in the center of one of the holes. The respective root mean square (rms) of the beams [Equation 3.9] are respectively $2.3060 \cdot a$ and $2.7881 \cdot \sqrt{2} \cdot a$.

$$\mathrm{rms} = \frac{\sqrt{\int x^2 B_z^2 dx}}{\sqrt{\int B_z^2 dx}} \tag{3.9}$$

$$\frac{\mathrm{rms}_{1^{\mathrm{st}}\mathrm{band}}}{\mathrm{rms}_{2^{\mathrm{nd}}\mathrm{band}}} = \sqrt{2} \cdot 1.21 \tag{3.10}$$

The ratio between the beam widths [Equation 3.10] could lead to the erroneous conclusion that self-

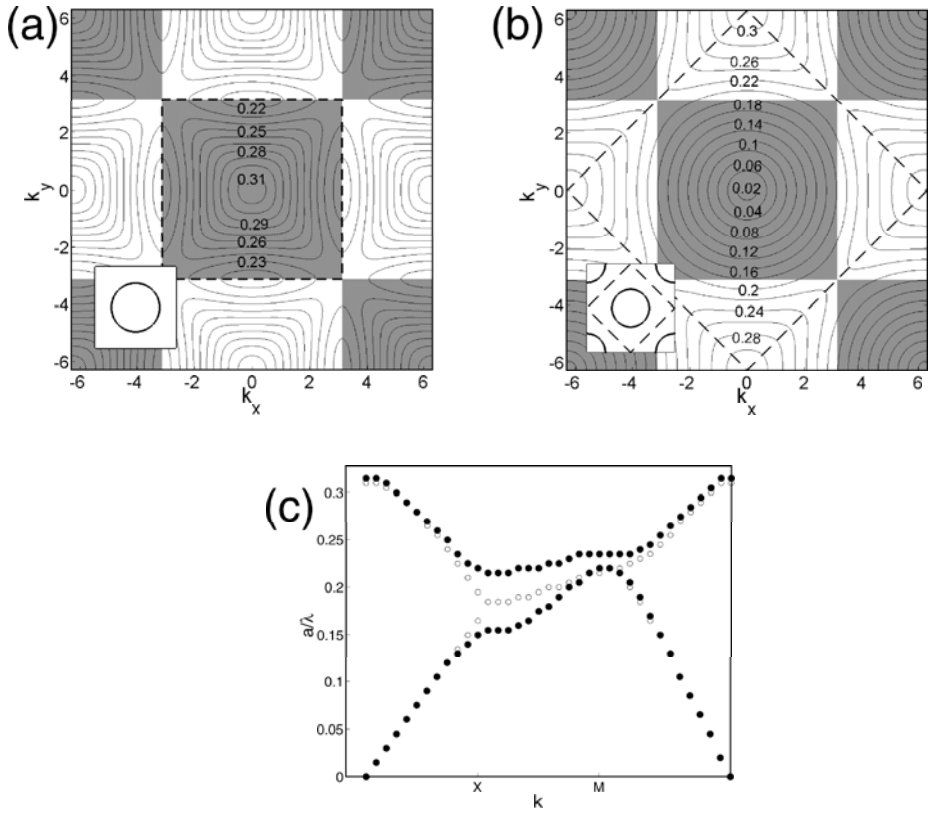


Figure 3.12: EFCs of the second band of PC1 (a) and of the first band of PC2 (b). The unit cells are shown in the insets. The dashed lines show the first BZs of PC1 and PC2. The shaded region corresponds to where the band structures differ, and the white region to where they are similar. (c) The $1^{st}$ and $2^{nd}$ bands of PC1 (dots) and the $1^{st}$ band of PC2 (circles). The $1^{st}$ band of PC2 is folded back into the first BZ of PC1. The labels X and M refer to the high symmetry points of PC1 (the labels would need to be interchanged for PC2, since it has been rotated). The band structures of the two EFCs are almost identical but for the frequency range of the PBG of PC1.

collimation is significantly stronger in the 2nd band. However, if a beam of normalized frequency $a/\lambda = 0.1836$ were to be self-collimated in the 2nd band instead of the 1st, the PC would need to be rescaled to a lattice constant of $a\sqrt{2}$, rescaling the rms by $\sqrt{2}$ at the same time. For a fixed frequency the beam width is thus similar independently whether the beam has been self-collimated in the first or in the second band. However it is easier to fabricate a PC so that a given frequency is self-collimated in the second band, as the lattice constant is $\sqrt{2}$ times larger, requiring less demanding lithography. However these conclusions can also be applied to a 3D PC: in Figure 3.1, we showed a self-collimated beam in the 2nd band at $a/\lambda = 0.295$ and in the 1st band at $a/\lambda = 0.295/\sqrt{2} = 0.2086$. However there is an additional constraint in the case of the 2nd band in that Bloch modes need be outside the light cone to avoid radiative losses. This problem is alleviated by using the 1st band.

The second practical consequence is that a self-collimated beam can be transmitted almost undistorted between PCs of type 1 and type 2. Indeed PC1 and PC2 have a lattice matched interface, as shown in Figure 3.14. As they also have a similar band structure, we could be tempted to conclude that they have similar Bloch modes, and thus a good interface. However, this cannot be directly concluded from the EFCs, since Bloch modes have more than one Fourier component [Figure 3.5]. They are indexed by the Fourier component inside the first BZ, but have Fourier components shifted from the "base" component by an integer number of reciprocal lattice vectors (defined in chapter 2). In fact the 1st BZ of PC2 has twice the size of the 1st BZ of PC1, so that the modes in PC2 have only one Fourier component where PC1 has two. The component inside the 1st BZ of PC2 is the same as the component inside the 2nd BZ of PC1. The component inside the 1st BZ of PC1 does not have an equivalent in PC2. However we evaluated that component to contain only 0.057 times the amount of power contained in the common, dominant component, so that it should only have a very minor impact on most applications.[2]

Due to the almost identical EFCs of PC1 and PC2 in the frequency region of interest for self-collimation, it would seem that a self-collimated beam should be transmitted with very small distortion from PC1 to PC2. This turns out to be true, although the analysis leading to this conclusion also has to take into account the Bloch-mode structure in PC1 and PC2. In fact, not only is the Fourier structure of the corresponding modes very similar, but the small component that is unique to PC1 projects onto the interface at the same position as the dominant component: If an interface is created between PC1 and PC2 such as in figure 3.14(a), the k-vectors of the components in the 1st and 2nd BZ of PC1 have the same projection onto the interface so that they can both couple to the same component in the 1st BZ of PC2. Thus it is not surprising that we were able to achieve very low loss transmission between the two types of PCs. The beam distortion is also expected to be very low due to the similarity of the EFCs.

[2] A counter example is given in chapter 4, where a waveguide coupling scheme is implemented that relies on this very component to achieve phase matching. There the presence or absence of the component is used to turn the coupling on or off.

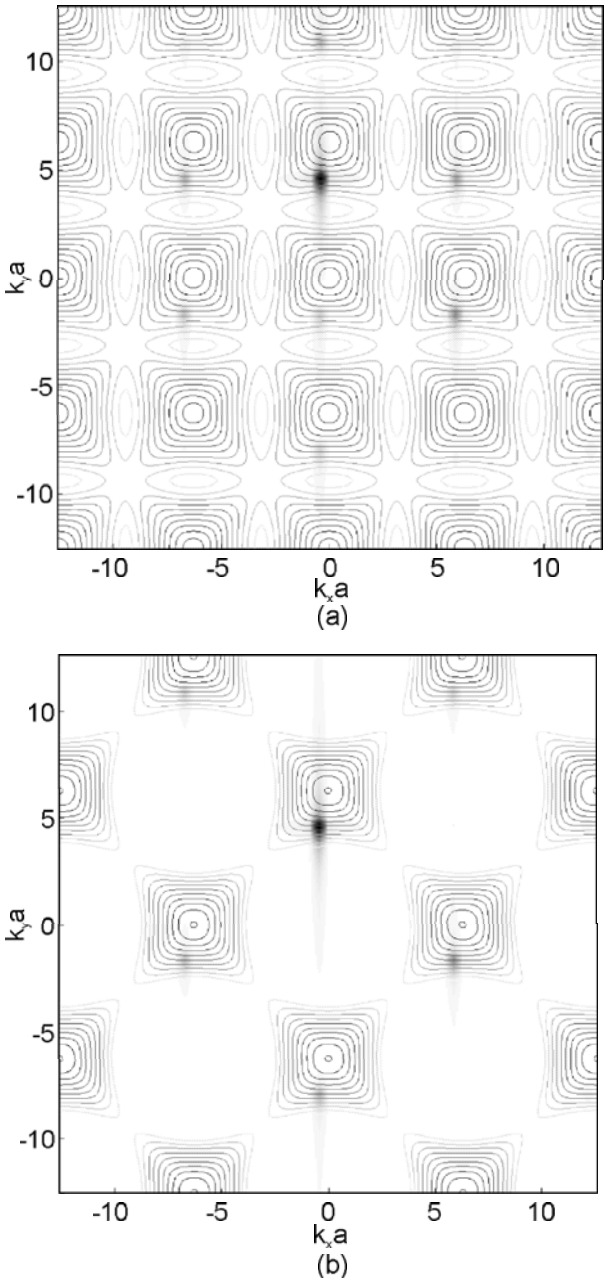


Figure 3.13: (a) Spatial Fourier transform of a Bloch mode of PC1 and (b) of the mode of PC2 that has the same normalized frequency and approximately the same extended $k$-vector. EFCs in the normalized frequency range 0.22 to 0.31 are overlaid. It can be seen that the Bloch mode of PC1 differs in that it has a weak but non zero component in the first BZ of PC1; however, this component only makes up a tiny fraction of the power of the Bloch mode.

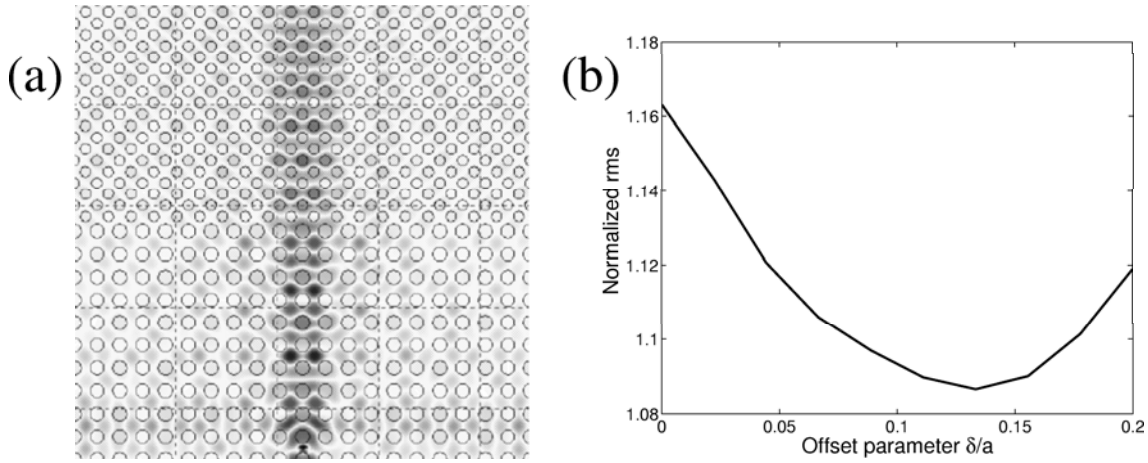


Figure 3.14: (a) Self-collimated beam at frequency $a/\lambda = 0.2596$ that propagates from PC1 (r/a=0.3) to PC2 ($r = 0.322/\sqrt{2}a$). (b) rms of the self-collimated beam in PC2 after crossing the boundary as a function of the line dislocation introduced at the interface. The rms of the beam is normalized by the rms before the interface.

In order to verify this, we simulated a beam propagating from PC1 to PC2. At the junction between PC1 and PC2 we introduced an extra line defect of width $\delta = 0.14a$ that optimized the rms of the transmitted beam, after crossing the interface. We found that in the best case the rms after the interface was 1.07 times the rms before the interface and that 94% of the power was transmitted. The interface between these two PCs could be adapted to triangular lattice PCs by using a 30° rotation and by rescaling the lattice period by $1/\sqrt{3}$.

In summary, we have conducted a 3D analysis of self-collimation and have given a range of parameters to experimentally explore self-collimation in a PPC. For the PC investigated in this chapter, minimum temporal and spatial distortion of self-collimated beams was found to take place at a k-space point slightly inside the light cone, and thus in an intrinsically lossy region. However by shifting the k-space point slightly outside the light cone a good compromise should be obtained. In-depth analysis of self-collimation, based on analysis in reciprocal space, was performed. We showed the occurrence of beating patterns and beam broadening that must be taken into account when designing devices based on self-collimation. Finally we showed that it is possible to make a low loss interface between two square lattice PCs with different orientations and scaling, again achieved by matching the Bloch-modes in reciprocal space. This interface might be used in integrated optics in order to build multi-functional PPC structures.

# Chapter 4

# Vertical coupling between a waveguide and a photonic crystal

There has been an ongoing effort to develop efficient methods to couple light in and out of PPC structures, either from other planar structures such as dielectric waveguides [24,76–78] or by coupling PC modes and PC waveguide modes to free space [20, 75]. Furthermore, there have been several investigations on how to combine PC based devices with more conventional integrated optics [77,78]. This chapter investigates how vertical coupling between a conventional dielectric waveguide and a PPC can be used to couple light between these two optical elements. A very similar method has been used experimentally to couple light from a tapered optical fiber to photonic crystal cavities and photonic crystal waveguides [79,80]. Here we couple to bulk photonic crystals for applications such as the self-collimation effect. In section 4.1 a self-collimated beam is launched inside the PPC from the waveguide. The waveguide-PPC system then operates in a very similar manner to a contradirectional coupler. In section 4.2 the orientation of the waveguide is changed so as to excite a single Bloch mode inside the PPC. In both sections the Bloch mode Fourier structure is used to obtain phase matching between the waveguide and individual Fourier components of the Bloch mode. In chapter 3 we have shown that a self-collimated beam can be transmitted almost distortionless through a heterojunction between two types of photonic lattices. In section 4.1 we use this heterojunction to switch on and off the coupling between the waveguide and the PPC, as the waveguide is only phase matched to one of the two lattices and thus is only coupled to one of them.

In both sections we consider a silicon slab (refractive index $n_{\mathrm{Si}} = 3.5$) of thickness $t = 0.57a$, where $a$ is the lattice constant of the PC. This slab is patterned with a 2D square lattice of holes of radius $r = 0.3a$. The slab is surrounded by a material of index $n_{\mathrm{clad}} = 1$ on both sides. In the photonic crystal literature, dimensions, frequencies and k-vectors are usually given in normalized units. However, we chose a particular set of dimensions, so that the phenomena described below are valid for $\lambda = 1.5$ $\mu$m and take place outside the light cone, and so that reported dimensions are realistic from a fabrication point of view ($a = 0.45$ $\mu$m, $r = 0.135$ $\mu$m, $t = 0.2565$ $\mu$m, where $a$ is

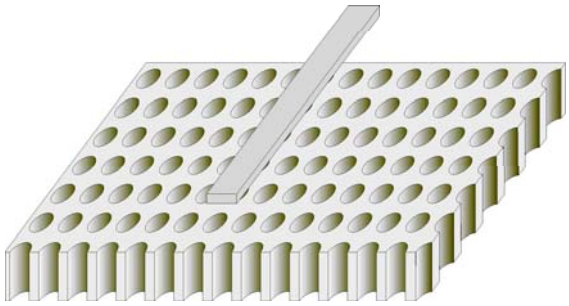

Figure 4.1: Schematic view of a planar PC and a waveguide oriented in the ΓX direction above the PPC. This waveguide orientation corresponds to the coupling mechanism described in section 4.1 that results in launching a self-collimated beam inside the PPC.

the lattice constant, $r$ the hole radius and $t$ the thickness of the slab). Furthermore $\lambda = 1.5$ $\mu$m corresponds to Bloch modes in the second band of the PC where EFCs are approximate squares, so that self-collimation takes place at this wavelength. Self-collimation has been described extensively in chapter 3. The dimensions of the waveguide are critical as they determine the phase velocity of the waveguide mode, and thus to which PPC modes the waveguide is coupled to.

A silicon waveguide is placed above the PC and is separated by a 200 nm vertical gap (figure 4.1). In section 4.1 the waveguide is oriented in the ΓX direction, whereas in section 4.2 it is aligned in the ΓM direction (the crystallographic directions are defined at the beginning of chapter 2). The cross-section of the waveguide varies in the different cases.

## 4.1 Coupling between a waveguide and a self-collimated beam

In this section a dielectric waveguide mode is coupled to a self-collimated beam that propagates inside the PPC. We locate a silicon waveguide of width = 350 nm and height = 100 nm above the PPC, with a spacing of 200 nm. The waveguide is oriented along the ΓX direction of the PC. This geometry is illustrated in figure 4.1.

The dimensions of the waveguide have been chosen so that the dispersion diagram of the waveguide crosses the $2^{\text{nd}}$ band of the PPC at $\lambda = 1.5$ $\mu$m. In other words, the waveguide is phase matched to the Fourier component of the Bloch mode located inside the $1^{\text{st}}$ BZ. The corresponding mode in the PPC is in the second band (folded back once). This has the crucial consequence that the PPC modes propagate in the opposite direction than the waveguide mode, since their group velocities ($v_g$) point inside the EFC. Light is self-collimated along the ΓX direction inside the PPC so that it stays in the vicinity of the waveguide. Furthermore, as the side of the EFC is approximately flat and all the modes located on that side have the same phase velocity in the direction of the waveguide, the waveguide is coupled to the whole side of the EFC and excites a continuum of modes inside the PPC. Because two contrapropagating waves are coupled together, anticrossing occurs and

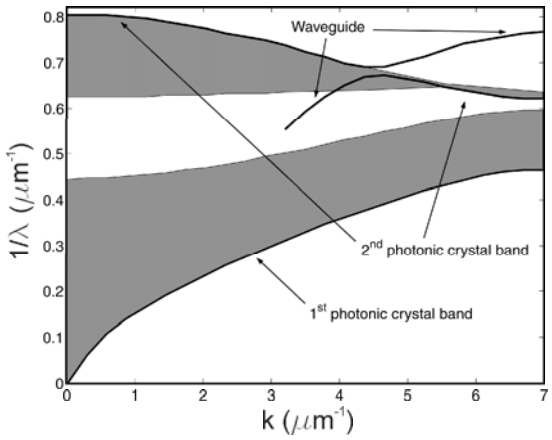


Figure 4.2: Band diagram of the coupled PPC waveguide system. The x-axis corresponds to the projection of the k-vector onto the ΓX direction (as imposed by the BBC) and the $y$-axis to the inverse wavelength $1/\lambda$ of the resulting modes. Modes are detected as resonances in time series recorded from the simulations. Labels indicate modes that correspond to the PC and to the waveguide. They are clearly defined far from the coupling region; however, the $2^{\text{nd}}$ band of the PC anticrosses with the waveguide.

a mini stop-band is opened in the coupled system (Figure 4.2). Of course the mini-stop band is only seen by the PPC in the immediate vicinity of the waveguide. Away from the waveguide, the PPC remains unperturbed and has no stop band. The Band diagram was obtained through FDTD calculations [3] with a 10 nm discretization. Bloch boundary conditions (BBC) were applied in the translation direction of the waveguide. The BBC impose the phase velocity of the recorded modes along the ΓX direction and act as a filter. Modes with the right phase velocity are then seen as resonances in the recorded spectrum (the Fourier transform of the recorded time-series). However modes can correspond to waveguide modes, PPC modes or supermodes of the coupled system in the frequency region where phase matching is achieved. In order to discriminate between these categories of modes several field probes are placed inside the computational domain, inside the waveguide, inside the PPC immediately below the waveguide and inside the PPC away from the waveguide. Mur absorbing boundary conditions (ABC) were applied on the other boundaries so that the k-vector component perpendicular to the waveguide direction was not determined (there is no third component as only bound modes concern us here). In figure 4.2, PC modes corresponding to the ΓX direction are plotted as thick lines ($1^{\text{st}}$ and $2^{\text{nd}}$ photonic bands). However, PC modes that propagate in arbitrary directions but with the same k-vector component on ΓX also appear in the simulations. The grey shaded regions correspond to those modes and result from projecting the first two photonic bands onto the ΓX direction.

If light in the frequency range of the mini stop-band is launched into the waveguide, it will exponentially decay in the coupled system. The light progressively couples into the PPC and back-

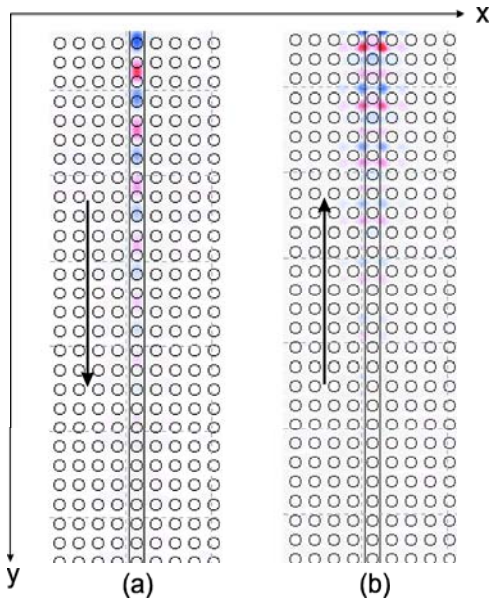


Figure 4.3: FDTD simulation of the decaying field in the frequency range of the mini stop-band ($\lambda = 1.48$ $\mu$m). The mode of the stand alone waveguide, previously obtained with a numerical mode solver, is launched into the waveguide. (a) shows $B_z$ in the waveguide and (b) shows $B_z$ on the center plane of the PPC. As light is transferred from the waveguide to the PPC, the decay of the field inside the waveguide as well as the build-up inside the PPC can be clearly seen. The field in the PPC propagates in the opposite direction than the field in the waveguide.

propagates (figure 4.3). If the waveguide starts where the pulse was launched, the light will propagate unperturbed inside the PPC behind the point of entry in the form of a self-collimated beam. This might be difficult to achieve, however, as coupling schemes such as grating couplers have a finite size. This is why we revert to a heterojunction between photonic crystals at a later point in this section.

We simulated the structure by FDTD with a 20 nm discretization step. The wavelength of the light source ($\lambda = 1.48$ $\mu$m) was chosen to correspond to the lower edge of the mini stop-band. Figure 4.3 shows the out of plane component of the B-field in two cross-sections of the device. Figure 4.3(a) shows the field inside the waveguide and figure 4.3(b) shows the field along the center plane of the PPC. In both cases it can clearly be seen that the field decreases in the y-direction as it gets progressively coupled from one optical element to the other. Also in figure 4.3(b) it can be seen that it forms a self-collimated beam inside the PPC.

Figure 4.4 shows a different cross-section of the device (along the centermost yz plane). It illustrates how the field couples from the waveguide to the PPC. The field in the PPC seems to have a different phase velocity than the field in the waveguide, as the apparent wavelength inside the PPC is shorter than the wavelength inside the waveguide. This might appear surprising as the waveguide and the PPC are coupled together without an additional phase matching mechanism. In fact the waveguide is coupled to the Bloch mode by means of the Bloch mode Fourier component located

inside the 1st BZ. As this component carries only a small fraction of the total power of the Bloch mode (sections 2.5 and 5.1), the wavefronts seen in the PPC correspond to the another, dominant Fourier component that is not phase matched to the waveguide.

To use this power transfer mechanism in a device, it is beneficial to have the ability to switch on and off the coupling between the PC and the waveguide. To this effect we introduce a second type of PC lattice, rotated by 45° and rescaled by $1/\sqrt{2}$, which we refer to as PC2. We refer to the original lattice as PC1. In chapter 3 we have shown that PC2 supports self-collimated beams and that a self-collimated beam can be transmitted between PC1 and PC2 with small distortion and small insertion losses. The corresponding modes in PC2 lack the Fourier component in the first Brillouin zone of PC1, which is the one that is coupled to the waveguide (figure 4.5). Thus no anticrossing will occur if the waveguide is positioned above PC2. By substituting PC2 by PC1, the coupling can be switched on. The power is then transferred into a self-collimated beam in PC1 that back-propagates and crosses again the boundary between PC1 and PC2, this time inside the PPC rather than inside the waveguide (figure 4.6).

The coupling scheme proposed in this section is very similar to a contradirectional coupler [81], where two waveguides are coupled by means of a corrugation of one or both of the waveguides. The mode of one of the waveguides is then coupled to the contrapropagating mode of the other waveguide. In a directional coupler full power transfer is only achieved through careful control of the coupling length. However in the case of a contradirectional coupler, the coupling efficiency is very robust to variations in the coupling length (the coupling length needs only to be long enough, rather than having exactly the right length as in a forward coupling scheme). This is of particular advantage with PCs where a small process bias modifying the hole size could severally impact the effective coupling length and thus the efficiency of a forward coupling scheme.

In a contradirectional coupler, the coupling condition is given by $\vec{k}_1 - \vec{k}_2 = m\vec{K}$, where $m$ is an integer and $\vec{K}$ is the reciprocal lattice vector given by the periodicity of the waveguide modulation ($K = 2\pi/\Lambda$ where $\Lambda$ is the modulation period). $m$ is usually chosen to be 1, as higher order back-reflections also induce radiative losses, in general. This coupled wave approach is intuitive in the limit of small corrugations (first order perturbation theory). In a similar way the 2D lattice of holes acts as a "perturbation" that couples the waveguide to the silicon slab. However, in this case the modulation is provided by a deeply etched lattice of holes, which no longer satisfies small perturbation assumptions. The slab modes are strongly modified by the lattice so that the original slab modes are not a satisfactory expansion basis to describe Bloch modes with coupled-mode theory. In that case it is a better approach to directly consider coupling between the waveguide mode and the PPC Bloch modes rather than between the waveguide mode and slab modes [82]. Thus the periodic modulation of the medium is already taken into account by the structures of the Bloch modes, that comprise several Fourier components. The coupling condition then translates into an

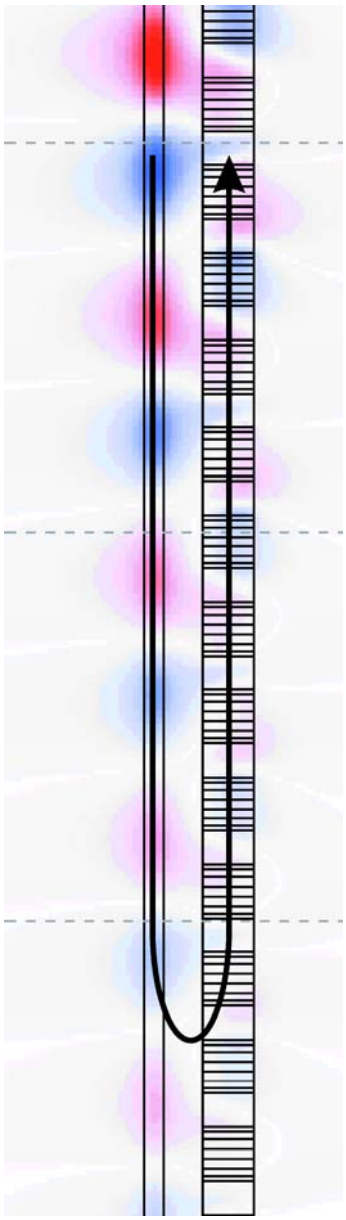

Figure 4.4: Field profile ($B_z$) in the coupled waveguide-PPC system recorded on the yz symmetry plane. Light is within the mini-stop band ($\lambda = 1.48$ $\mu$m) and decays. The field is coupled from the waveguide to the PPC and back-propagates in the opposite direction.

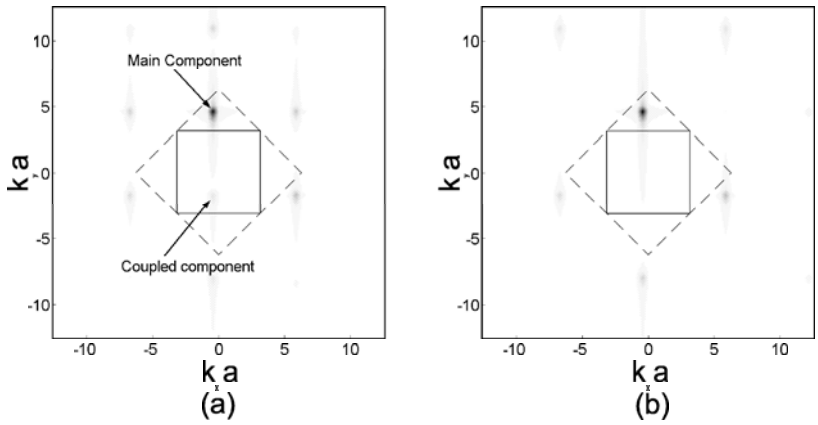


Figure 4.5: (a) Spatial Fourier transform of a typical Bloch mode of the second band of PC1 and (b) the spatial Fourier transform of the corresponding Bloch mode (same frequency and same main component k-vector) of PC2. The 1st Brillouin zone of PC1 is indicated by the continuous square, and the 2nd Brillouin zone is indicated by the dashed square. The Bloch mode of PC2 does not contain the Fourier component that is phase matched to the waveguide; thus by transmitting a beam from PC1 to PC2 the coupling to the waveguide can be switched on and off. Due to the fact that PC2 is rescaled and rotated relative to PC1, the 1st Brillouin zone of PC2 corresponds to both the 1st and the 2nd Brillouin zones of PC1. This explains why a Bloch mode of PC2 has only one Fourier component where a Bloch mode of PC1 has two. k-vector components are given in dimensionless units of $k \cdot a$, where $a$ is the lattice constant of PC1.

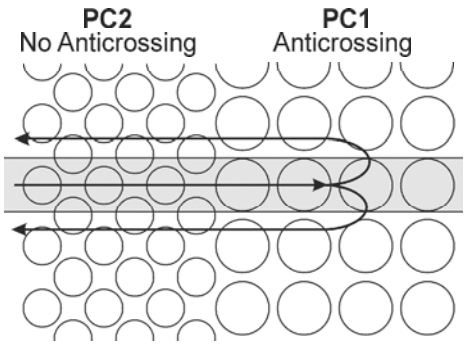


Figure 4.6: A waveguide is located above a heterojunction between lattices of type 1 and 2. This way the coupling between the PPC and the waveguide can be turned on and off and a self-collimated beam can be launched into PC2.

equality, $\vec{k}_{\mathrm{WG}} = \vec{k}_{\mathrm{PPC},i}$, where $\vec{k}_{\mathrm{WG}}$ is the k-vector of the waveguide mode and $\vec{k}_{\mathrm{PPC},i}$ the *extended* k-vector of *one* of the Fourier components of the coupled Bloch mode.

There is one important difference between the PPC coupler and a standard contradirectional coupler. In a contradirectional coupler, two waveguides are coupled together so that lateral confinement of light is provided by the waveguiding mechanism, whereas here a waveguide is coupled to a two-dimensional system. In both conventional and contradirectional couplers light coupled from one waveguide to the other interferes destructively with the remaining light when coupled back to the original waveguide. Usually, if a waveguide is coupled to a 2D system with no collimation mechanism, the field will diffract in the 2D system and not couple back to the original waveguide. Due to the lack of interference the light transfer mechanism will require a longer length to take place (for a given coupling strength). However, as the PC supports self-collimation along the orientation of the waveguide (ΓX), lateral confinement is still provided, even in the 2D system. The coupled system then behaves in every aspect as a contradirectional coupler. This is to be contrasted with the next section in which a waveguide is coupled to Bloch modes that propagate in a different direction than the waveguide. In that case the waveguide behaves rather like a leaky waveguide as there is no significant back-coupling mechanism.

In order to avoid constraints linked to the light cone, a self-collimated beam could be launched in the $1^{\mathrm{st}}$ band rather than in the $2^{\mathrm{nd}}$ band. However the coupling mechanism will then have to be a forward coupling scheme if light is coupled by means of the Fourier component inside the $1^{\mathrm{st}}$ BZ, as the group-velocity points outside the EFC in the case of the $1^{\mathrm{st}}$ band.

## 4.2 Selective excitation of a single Bloch mode

If the waveguide is oriented in the ΓM direction rather than in the ΓX direction, it is coupled to only a few Bloch modes rather than to a continuum of modes, as the latter relied on the flatness of the EFC associated to self-collimation. We will show that it is possible to selectively excite a single Bloch mode if the waveguide cross-section is adequately tailored. The Bloch modes excited in the PC have a propagation direction that is different than the waveguide direction. We again use FDTD to simulate the coupled system (10 nm discretization size).

In order to illustrate that the phase matching mechanism can lead to the excitation of one or more PC modes, we investigate two different waveguide geometries. First we will show a case where multiple Bloch modes are excited inside the PPC. We will then adjust the waveguide phase velocity by modifying the waveguide cross-section so as to target a single Bloch mode. In the first case, we took a waveguide of dimensions 520 nm × 100 nm, positioned above the PPC with a 200 nm vertical gap. When light couples into the PC, the projection of the k-vector onto ΓM is conserved (inside the $1^{\mathrm{st}}$ BZ) as the discrete translation symmetry along ΓM is not broken by the waveguide.

This conservation law selects the Bloch modes to which the waveguide can couple to. Figure 4.7(a) illustrates this. The squarish contours are an idealized form of the EFCs of the PC at $\lambda = 1.5$ $\mu$m. The waveguide k-vector is conserved, so only the modes that lie on the horizontal line (distant from $\Gamma$ by the magnitude of the k-vector) can be coupled to. In other words the intersection of the horizontal line and the EFCs corresponds to the set of excited PPC modes. It can be seen that only four PC modes are coupled to. Figure 4.7(b) shows the propagation directions of those modes in real space. The propagation direction is given by the group velocity $\nabla_k(\omega)$, which is perpendicular to the EFC and points inside the EFC in the case of the $2^{\text{nd}}$ band. Although 4 modes are excited, there are only two modes on either side of the waveguide. To show this, we perform a Fourier transform on the field on the left side and label each Fourier component with the corresponding Bloch mode (figure 4.8). To map out the transverse electric (TE) Bloch modes, we operate the spatial Fourier transform on the field recorded from the center plane of the PPC ($B_z$ recorded over a region of 15 by 15 periods). It should be noted that TM modes are marginally excited, although a TE mode was launched into the waveguide. Because the xy-plane symmetry is broken in the coupled system, the overlap integral between the TE waveguide mode and the TM PC mode can be non zero.

In order to obtain single mode excitation on each side of the waveguide, we changed the waveguide geometry to 400 nm $\times$ 200 nm. This waveguide has a larger effective index and a smaller k-vector, so that the situation shown in figure 4.9(a) is obtained. The waveguide was designed so that $k \cdot a = 0.4$ was barely smaller than $\sqrt{2} \cdot \pi = 4.44$, and thus the waveguide k-vector is slightly inside the $1^{\text{st}}$ Brillouin zone, near the corner. Again, we operated a Fourier transform of the field to the left of the waveguide (figure 4.10). It can be seen that all of the Fourier components belong to the same Bloch mode.

It should be noted that the decay of the waveguide mode leads to a Lorentzian broadening of the spatial Fourier spectrum. By increasing the separation between the waveguide and the PPC, the coupling strength can be reduced and the decay length inside the waveguide increased. Thus a wider beam can be obtained inside the PPC, with a narrower mode distribution.

In conclusion, we have shown that through out of plane coupling between a PPC and a waveguide, a self-collimated beam as well as a single Bloch mode can be launched inside the PPC. This mechanism might enable further integration of self-collimation based devices and conventional integrated optics.

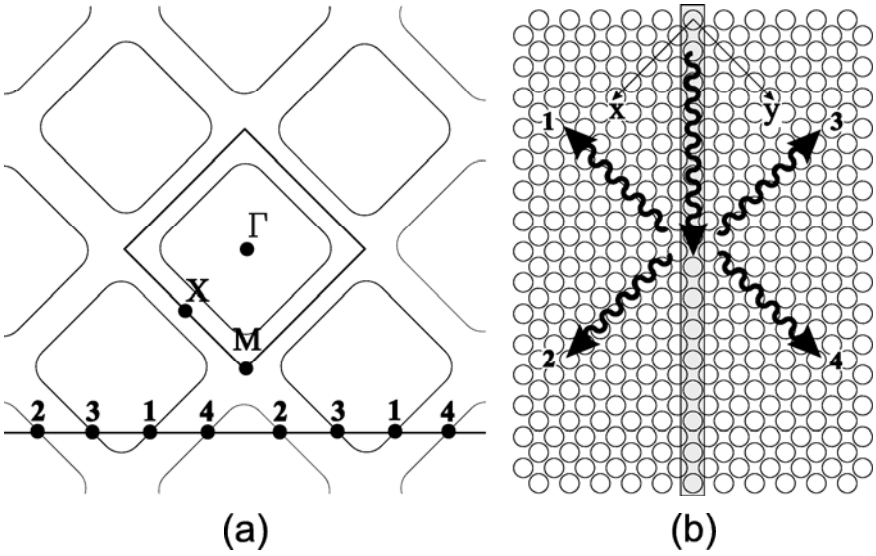


Figure 4.7: The modes excited inside the PPC by the waveguide can be determined by conservation of the k-vector component in the ΓM direction (modulo $2\pi/(\sqrt{2}a)$ due to the discrete translation symmetry of period $\sqrt{2}a$). (a) shows the idealized EFC inside the 1st Brillouin zone (dashed square), as well as higher order EFCs in extended Fourier space. The position of the horizontal line is determined by the k-vector of the waveguide mode and intersects all the PPC modes that are coupled to. Four modes are excited, labeled 1 to 4. The high-symmetry points are shown on the diagram (Γ, M and X). The directions of propagation (given by the group velocity) are indicated in (b) for each of the excited modes.

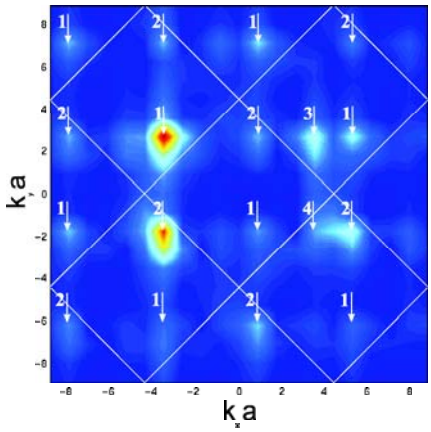


Figure 4.8: Spatial Fourier transform of the field inside the PPC, to the left of the waveguide ($B_z$ is recorded on the center plane of the PPC in a region of 15 by 15 lattice periods, and subsequently a Fourier transform is operated). Modes 1 and 2 propagate to the left of the waveguide and are present in the obtained spatial spectrum. The field was simulated by FDTD with a 10 nm discretization, waveguide dimensions are 520 nm × 100 nm and $\lambda = 1.54$ $\mu$m. The corresponding coupling process is illustrated in figure 4.7. The Fourier components are labeled in the same way as in figure 4.7. k-vector components are given in dimensionless units of $k \cdot a$, where $a$ is the lattice constant.

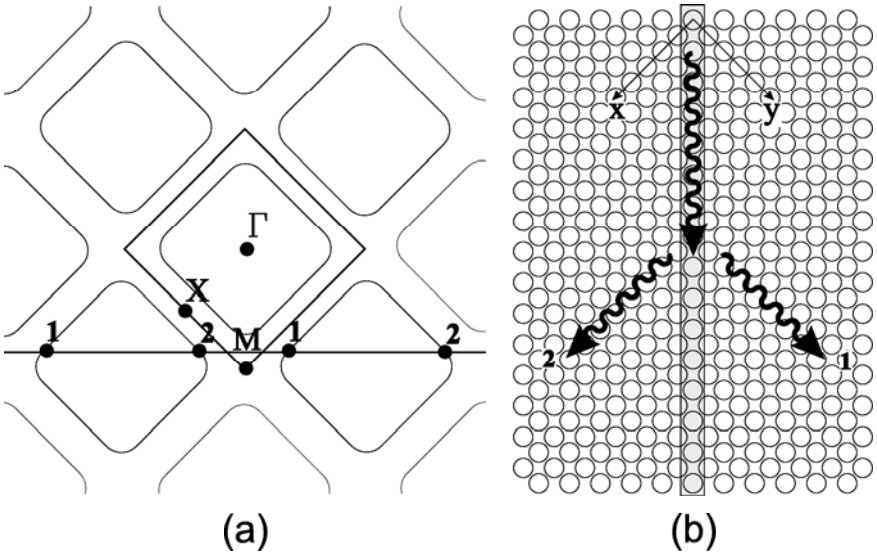


Figure 4.9: This is a similar diagram to figure 4.7. However the geometry of the waveguide has been modified so that different Bloch modes are targeted. In particular only two Bloch modes are coupled to, that propagate in opposite directions relative to the waveguide. This also illustrates the importance of considering *extended* Fourier space when investigating coupling mechanisms. Indeed the horizontal line does not intersect the EFC in the 1$^{st}$ BZ, but in higher order BZs.

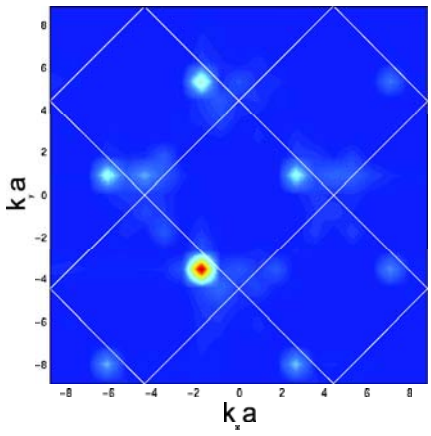


Figure 4.10: As in figure 4.8 a Fourier transform is taken of the field inside the PPC to the left of the waveguide. However this data corresponds to the situation schematized in figure 4.9. On each side of the waveguide, a single Bloch mode is coupled to.

# Chapter 5

# Mode-matching interfaces for the superprism

In this chapter we investigate methods to butt-couple a beam into a planar photonic crystal with high insertion efficiencies. In particular, we consider a PPC of finite extent, etched into a thin dielectric slab, and we address how to transfer a beam from the unpatterned slab to the PPC. We do not investigate how to initially transfer the light into the slab as efficient methods to do the latter can be found in the literature [83–92]. Two mode-matching interfaces with different underlying mechanisms are described. The mode-matching mechanisms described in this section could provide insight on how to couple light into photonic crystal waveguides (PCW); however, the primary target is to couple into bulk PCs. They were developed specifically to be applied to the demultiplexion of light by means of the superprism (SP). Indeed, one of the crucial difficulties in using the superprism effect for practical planar demultiplexers is the coupling of light into the photonic crystal with acceptable insertion losses. These insertion losses can be very high in the absence of mode-matching because of the complex structure of the Bloch modes involved in the superprism effect. This is a crucial difficulty and has received an increasing amount of attention in the literature [39–41].

The mode-matching difficulties are particularly stringent in the vicinity of sharp features of the EFCs, due to the complexity of the Bloch modes. In fact, this is quite a general problem as the sharp features in the EFCs correlate with brusk changes in the mode structure regardless of whether the PPC has a square or triangular lattice and independently of the photonic band that is used. However, these sharp features are very useful for devices such as the SP as beam steering relies on changes in the EFC. Thus there is a strong incentive to solve the mode-matching problem in these k-space regions.

In section 5.1 the Bloch mode structure is derived from band folding, and it is shown that it undergoes strong changes in the vicinity of the cusps. The large changes in propagation direction are linked to drastic changes in the mode structure and to high insertion losses in the absence of additional insertion mechanisms.

The mode-matching interface described in section 5.2 converts a "plane wave" (slab mode of infinite extent) into the previously derived Bloch mode structure by cascading a series of diffraction gratings. The distance between successive gratings is constrained by interference conditions (constructive build-up of the Bloch mode and anti-reflection conditions to suppress reflections induced by individual gratings). Individual gratings are defined as a row of holes into the dielectric slab so that the definition of the MLG does not create any additional fabrication steps. We refer to this interface as the "multilayered grating" (MLG). It has several limitations. As it relies on coherent interference between the cascaded gratings, the distance between the gratings has to be carefully calibrated, and the MLG has a limited pass-band for which these interference conditions hold. Furthermore it was designed to couple to a specific mode (the very center of the cusp). As already mentioned the difficulty of coupling into a PPC at the cusp is two-fold: the Bloch modes have a complex Fourier structure that needs to be reconstructed from a plane wave or a Gaussian beam by the mode-matching interface. This is adequately solved by the MLG. However, the Bloch mode structure also undergoes strong changes for small displacements along the EFC. For an application such as the SP it is particularly important to mode-match to modes on both sides of the cusp, so as to exploit the full steering potential of the cusp (that is the angular pass-band has also to be high).

These limitations are overcome in 5.3 with an adiabatic transition. The hole size is progressively ramped down at the boundary of the PPC so as to adiabatically convert Bloch modes to slab modes. Adiabatic mode conversion has been previously investigated in the context of PCWs [77, 93–95]. However, an adiabatic transition on its own is not sufficient to couple into bulk PCs *at the cusp of the EFC*. It needs to convert a Bloch mode into a single slab mode and a PC beam into a single slab beam (or in other words it needs to suppress higher diffraction orders of the PC emission). This is achieved by choosing the orientation of the PPC so as to break certain symmetries. For example, in the implementation shown in section 5.3, the orientation of the interface needs to break the symmetry by ΓM, otherwise the Bloch mode at the center of the cusp (on ΓM) will be converted to two rather than to a single slab mode. We show that this latter approach yields high insertion efficiencies for a wide range of k-vectors and frequencies and is thus suitable for the superprism effect.

## 5.1 Band folding and Bloch-mode Fourier-structure

We start the analysis with the Bloch theorem already introduced in chapter 2. Due to the periodic nature of photonic crystals, photonic crystal modes (Bloch modes) can be described by functions of the following form

$$f(\vec{r})e^{i\vec{k}\cdot\vec{r}} \tag{5.1}$$

where $\vec{r}$ is the position-vector, $\vec{k}$ is the reduced k-vector of the Bloch mode (in the 1$^{\text{st}}$ BZ) and $f$ is a function with the same periodicity as the photonic crystal. In the case of a PPC (2D periodicity) the Fourier transform of such a function takes the form

$$\sum_{a,b} f_{a,b} e^{i(\vec{k}+a\vec{K_1}+b\vec{K_2})\cdot\vec{r}} \tag{5.2}$$

where $\vec{K_1}$ and $\vec{K_2}$ are the inverse lattice vectors of the PPC and $a$ and $b$ are integers. We call the lattice vectors of the PPC $\vec{e_1}$ and $\vec{e_2}$. $\vec{K_1}$ and $\vec{K_2}$ verify $\vec{K_i}\cdot\vec{e_j} = \delta_{ij}2\pi$. When more than one of the Fourier components in equation 5.2 carries a significant portion of the mode's power, there can be a significant mode mismatch between the Bloch mode of the PPC and any incoming single "plane wave" (slab mode with planar wavefront), as the latter corresponds to a single Fourier component.

In a photonic crystal EFCs have features such as approximately flat sides and cusps (figure 5.1). This causes light to propagate in a PPC in a fundamentally different way than in an unpatterned slab (chapters 2 and 3) and enables the frequency selective steering of light inside the PC (SP effect, chapters 2, 6 and 7). These abrupt changes in the direction of propagation are accompanied by abrupt modifications of the mode structure that makes coupling into a SP particularly challenging.

The cusps in the EFC are due to coupling between two higher order Fourier components. This coupling is induced by the periodic array of holes. On either side of the cusp, the Bloch mode is dominated by one of the Fourier components, while at the cusp itself the two components are of equal magnitude. In the case of the 2$^{\text{nd}}$ band of a square lattice PPC, the EFCs have a cusp at their intersection with the ΓM direction, where Γ and M are the high-symmetry points shown in figure 5.1.

Before we numerically analyze the Bloch mode structure, we derive it from band folding so as to relate it to the presence of the cusp rather than to a particularity of the square lattice. As a thought experiment, we start with a homogeneous media and progressively turn on coupling between higher order Fourier components. This gives an adequate description of the mode structure in the limit of very small hole size. In the case of finite hole size the EFCs as well as the Bloch mode structure undergo further modification; however, the essential characteristics stay the same and can be intuitively understood with the weak coupling model. As an example we will derive the mode structure of the second band of a square lattice PPC etched into a 205 nm silicon film, with lattice constant $a = 0.5$ $\mu$m and hole radius $r = 0.15$ $\mu$m.

In figure 5.1 the circle centered on Γ represents the EFC of an unpatterned slab with a modified effective index $((a^2 - \pi r^2)n_{\text{slab}} + \pi r^2 n_{\text{SiO}_2}))/a^2$. The effective index is the weighted mean of the effective index of the unpatterned slab ($n_{\text{slab}} = 2.76$ at $\lambda = 1.54$ $\mu$m) and of the refractive index of the holes ($n_{\text{SiO}_2} = 1.46$). This corresponds to an isotropic media with a modified effective index that takes into account the lower refractive index of the holes, but where the anisotropy and the coupling

induced by the holes is ignored. This would be a good description of the PPC in the limit of long wavelengths, as shown by homogenization theory (see footnote 4 in chapter 2). However, for $\lambda$ of the order of the lattice period, coupling to higher order components and the resulting distortions of the EFC have to be taken into account. Thus we also represent the higher order Fourier components generated by the lattice (circles centered on $a\vec{K_1} + b\vec{K_2}$ where $a$ and $b$ are integers). At the k-space points where two of these circles cross, modes that were originally non-degenerate (located at different points on the circle centered on $\Gamma$) are coupled together and anti-cross. Fragments of the circles that were originally connected are disjoint in the modified contour, such as the green and red portions of the circles in figure 5.1. In order to obtain the complete band structure it is sufficient to identify such crossings in the 1$^{\text{st}}$ BZ as the circles tile the extended k-space in a periodic manner.

If the reduced k-vector of a Bloch mode is on a circle centered on $a\vec{K_1} + b\vec{K_2}$, it is also offset by $a\vec{K_1} + b\vec{K_2}$ from the initial, uncoupled component that is also the *dominant* component. In other words the dominant component is offset by $-a\vec{K_1} - b\vec{K_2}$ from the component in the 1$^{\text{st}}$ BZ. Thus when the reduced k-vector lies on a point where 2 circles cross, the Bloch mode has 2 dominant components, while if it is not at a crossing point the Bloch mode has only one dominant Fourier component. For example the circles centered on [1 0] and [0 1] intersect inside the 1$^{\text{st}}$ BZ on $\Gamma$M, at the upper right corner of the EFC of the second band. When the coupling between the Fourier components is "turned on" (small but non-vanishing hole size) the two circles anticross, and disjoint contours are formed. The resulting contours correspond to the second (red) and to the third (green) photonic bands. Anticrossing also gives rise to the rounded corners on the actual EFC (shown by the black contour). The corresponding Bloch mode thus has two dominant Fourier components respectively offset by [-1 0] and [0 -1] from the 1$^{\text{st}}$ BZ. When anticrossing occurs, the two-fold degeneracy is also removed by the creation of two disjoint contours belonging to separate bands. On $\Gamma$M, the Bloch modes of the second and third band are essentially composed of two Fourier components respectively offset from the 1$^{\text{st}}$ BZ by $-\vec{K_1}$ and by $-\vec{K_2}$; however, they differ by their symmetry in respect to $\Gamma$M. The cusp mode of the 2$^{\text{nd}}$ band has an even $B_3$ (out-of-plane B-field component $B_3 = \vec{B} \cdot \vec{e}_3$ with $\vec{e}_3 = \vec{e}_1 \times \vec{e}_2$) as shown in figure 5.2(a) while the cusp mode of the 3$^{\text{rd}}$ band has an odd B-field as shown in figure 5.2(b). In the case of a regular PPC with large hole size this leads to the large splitting between the two bands as the second band has a field maximum in a high index region while the third band has a field minimum. This large splitting explains why there is a significant frequency region for which the second band is unique (figure 6.1). The circles centered on [1 1] (or equivalent k-space points) also intersect $\Gamma$M inside the 1$^{\text{st}}$ BZ. They correspond to the 4$^{\text{th}}$ band that is thus composed of a single dominant Fourier component on $\Gamma$M.

In the case of a finite hole size there will also be other Fourier components in the Bloch mode structure, and the EFC has a slightly different shape (compare the true EFC in figure 5.1 to the red contour), but the Bloch mode is still dominated by the same two higher order components. As an

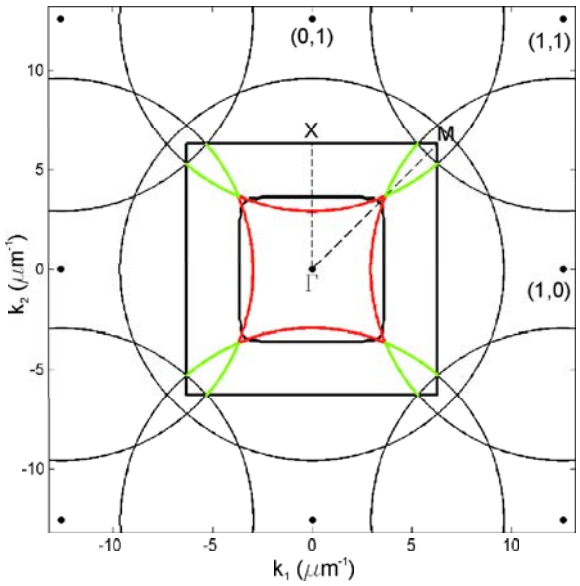


Figure 5.1: This figure illustrates how the structure of the 2nd band is formed by turning on coupling between higher order Fourier components. The circle centered on Γ is the EFC of an unpatterned slab of effective index $((a^2 - \pi r^2)n_{\text{slab}} + \pi r^2 n_{\text{SiO}_2})/a^2$ (at $\lambda = 1.54$ $\mu$m), where $a$ is the lattice constant of the PPC (0.5 $\mu$m). The effective index is the weighted mean of the effective index of the unpatterned slab and of the refractive index of silicon dioxide (holes) so that the finite holes are taken into account by the modified effective index; however, the coupling and the anisotropy induced by the holes is ignored. To modelize the latter we represent by circles centered on $a\vec{K_1} + b\vec{K_2}$ the generated higher order Fourier components, where a and b are integers. The circles centered on [1 0] and [0 1] intersect inside the 1st BZ (represented by the black square) and anticross when coupling is turned on. The red contour represents the 2nd band, and the green contour represents the 3rd band in the case of infinitesimal coupling. The real EFC of the 2nd band at $\lambda = 1.54$ $\mu$m is also represented (black squarish contour). Even though the structure is more complex in the case of finite coupling, the mode on the cusp is essentially composed of two Fourier components offset by $\vec{K_1}$ and $\vec{K_2}$ from the 1st BZ. The exact Fourier structure of such a mode is represented in figure 5.2. The axes are labeled with the projections of the k-vector on $\vec{e_1}$ and $\vec{e_2}$ ($k_1 = \vec{k} \cdot \vec{e_1}$ and $k_2 = \vec{k} \cdot \vec{e_2}$).

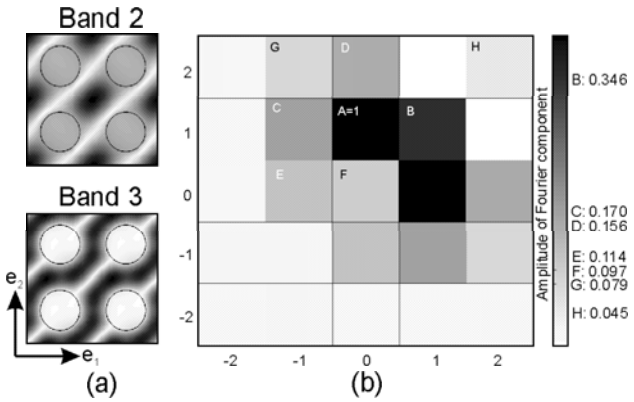


Figure 5.2: (a) Field profiles (amplitude of the out-of-plane component of the B-field, $B_3$, on the center plane of the PPC) of modes of the 2nd and 3rd bands located on ΓM (at $\lambda = 1.55$ $\mu$m). The mode of the 2nd band has a field maximum in the high index region at the center of the inset, where the mode of the 3rd band has a field minimum. (b) Fourier structure of the mode of the 2nd band obtained by taking the Fourier transform of $B_3$. The amplitudes of the Fourier components are shown. The Fourier components are represented in a checkerboard pattern and are labeled by integers $a$ and $b$. The Fourier components are respectively offset from the 1st BZ component (the [0 0] component) by $a\vec{K_1} + b\vec{K_2}$.

example, we operated a Fourier decomposition of an actual Bloch mode of the 2nd band located on ΓM at $\lambda = 1.55$ $\mu$m. Figure 5.2 shows the detailed Fourier structure of the mode. The power shared between the two main components is calculated to be 87%.

Most of the power of the Bloch modes is still contained in Fourier components close to the dispersion of the unpatterned slab, as schematically shown in figure 5.3. In particular when moving along the EFC from one side of the squarish contour to another side of the contour, through the cusp, the mode structure undergoes a sharp change. On the left side of the corner the [1 0] component is dominant (component $d$), while on the other side the [0 1] component is dominant (component $a$). The mode that is exactly on the ΓM direction has an equal fraction of its power in the [1 0] and in the [0 1] components. The mode structure can then be related to the direction of propagation. On the flat sides of the EFC the Bloch modes are dominated by a single Fourier component and the direction of propagation is almost collinear to the extended k-vector of this component. In the case of schematic 5.3 the group velocity is exactly collinear (this corresponds to the limit of small lattice induced coupling). In a real PPC the concavity of the sides of the EFC is modified as can be seen in figure 5.1 where the sides are flattened out. This leads to a small discrepancy between the two directions, which is accompanied by the emergence of additional weak Fourier components. In the case of the cusp the abrupt change of propagation direction corresponds to one Fourier component becoming dominant over the other.

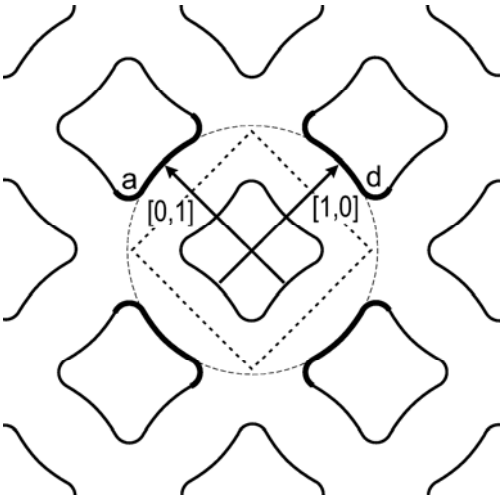


Figure 5.3: This schematic illustrates the Fourier structure of the Bloch modes. The squarish EFC originates from folding back the circular EFC of the slab into the 1$^{st}$ BZ. The 1$^{st}$ BZ is shown by the dashed square, and the dashed circle represents the dispersion characteristic of the unpatterned slab. Even after folding back the circle into the 1$^{st}$ BZ, most of the power of the mode is still contained in the higher-order components that are close to the original circle. These components are indicated by a thickened line along the higher-order contours and are labeled by $a$ and $d$ (this nomenclature is used in section 5.3, see figure 5.18). They are offset from the component in the 1$^{st}$ BZ by inverse lattice vectors represented by arrows and labeled by [0 1] and [1 0]. This model is a simplification, as the lattice of holes not only perturbs the contour at the anticrossing points, but also perturbs slightly the rest of the contour. For example, a flattening of the sides as is the case for the EFC shown in figure 5.1 leads to self-collimation.

## 5.2 Multilayered grating

Here we will use the Bloch mode structure derived in the previous section to design a mode-matching interface based on cascaded diffraction gratings. We aim to couple to the Bloch mode located on the cusp of the EFC. As the functionality that needs to be fulfilled by the interface is clearly defined (converting a plane wave into the known mode profile), it can be designed and simulated independently of the planar photonic crystal (PPC). In section 5.2.1 we introduce the multilayered grating (MLG) used to implement the mode-matching interface. In particular, the MLG relies on interference conditions between the individual gratings that will be derived in that section. In section 5.2.3 we optimize the stand alone MLG with a transfer matrix method. This method is considerably faster than FDTD so that design iterations can be accelerated. After characterizing the stand alone MLG, we evaluate the mode-matching efficiency by integrating the MLG with the PPC and by simulating the combined device with 3D FDTD (section 5.2.4). The data resulting from the simulations is analyzed by means of an inner product introduced in section 5.2.2 (the applicability of this inner product to Bloch modes is further investigated in appendix A). One of the conclusions of section 5.2.3 is that cascading a higher number of diffraction gratings with a reduced single grating efficiency is beneficial because it reduces out-of-plane scattering losses and enables a finer adjustment of the MLG (one of the degrees of freedom in the design is the number of cascaded gratings). However, when a Gaussian beam rather than a slab mode of infinite extent is coupled into the PPC, additional difficulties arise. In that case a more compact MLG with bigger holes and fewer cascaded gratings needs to be used (section 5.2.5). Indeed, the Fourier components created inside the MLG propagate in different directions and spatially separate if the MLG is too wide. Finally, we give experimental evidence of the Bloch mode structure by letting a Bloch mode diffract into the unpatterned slab and by imaging the diffraction pattern (section 5.2.6). This experiment is repeated both with a bare PPC (without mode-matched interfaces) and with a mode-matched PPC to show that the MLG suppresses higher diffraction orders.

Although the mode-matching interface could easily be adapted to a triangular crystal lattice (the Bloch mode structure at the cusps of the EFCs is essentially the same in that it is dominated by two Fourier components), we restrict ourselves to a square lattice PPC to compute quantitative results. A square lattice of holes (radius r=0.15 $\mu$m) is etched into a silicon slab of thickness t=205 nm. The holes are backfilled with silicon dioxide, and the slab is clad on both sides with silicon dioxide. The lattice constant is linked to the design of the MLG and varies slightly from case to case, but is kept between 0.47 $\mu$m and 0.5 $\mu$m. In the calculations the refractive index of silicon is assumed to be 3.43, and the refractive index of silicon dioxide to be 1.46. The effective index of the slab ($n_{\text{slab}}$) is equal to 2.77 at 1.52 $\mu$m. $\lambda$ is the free space wavelength.

The $\Gamma$M direction corresponds to $\vec{e_1} + \vec{e_2}$ in real space. The interface between the PPC and the

slab is chosen to be along $\vec{e_1} - \vec{e_2}$ so that a slab mode with a propagation direction perpendicular to the interface is coupled to a Bloch mode on the ΓM direction on the cusp of the EFC. For a graphical representation of the PC interface and of the unit vectors see figure 2.8 in chapter 2.

Before introducing the MLG in the next section we will define more precisely the functionality it needs to fulfill. When a Bloch mode crosses the interface from the PPC to the unpatterned slab it generates multiple diffraction orders. Conversely, in order to insert a slab mode (single Fourier component) into the PPC, these multiple Fourier components need to be generated from the slab mode by the mode-matching interface. In order to design the mode-matching interface, the relative strength and phase of these diffraction orders need to be evaluated from the structure of the Bloch mode. Thus we need to establish a correspondence between the Fourier components of the Bloch mode and the diffraction orders in the slab. We denote by $\vec{n}_\perp$ the normalized vector *along* the interface, $(\vec{e_1} - \vec{e_2})/\|\vec{e_1} - \vec{e_2}\|$. The projection of the k-vector of the Fourier components onto the interface, $k_\perp = \vec{k} \cdot \vec{n}_\perp$, indicates the diffraction orders to which the Fourier components contribute. The Fourier component [1 1] corresponds to the $0^{\text{th}}$ diffraction order, $k_\perp = \vec{k} \cdot \vec{n}_\perp = 0$. The projections of the two dominant components, [1 0] and [0 1], are $k_\perp = (\vec{k} + \vec{K_{1/2}}) \cdot \vec{n}_\perp = \pm 2\pi/A$. They contribute to higher diffraction orders. $A = \sqrt{2}a$ is the periodicity of the holes along the interface. The correspondence between the Fourier components in the Bloch mode structure and the amplitude of their contribution is exactly one to one only if we assume 100% transmission at the bare interface from the PPC to the slab. Otherwise, reflection and radiative losses of individual Fourier components creates a deviation from this ideal correspondence. The total transmission from the PPC to the slab is indeed very high (section 5.2.5) so that the Bloch mode structure provides an excellent design target. Here "total transmission" is used in the sense of transmission into multiple slab modes.

Furthermore, we can classify Bloch modes on the ΓM direction by their symmetry relative to ΓM (in real space the surface generated by $\vec{e_1} + \vec{e_2}$ and $\vec{e_3} = \vec{e_1} \wedge \vec{e_2}$). More precisely we consider the symmetry operator S defined by a surface generated by $\vec{e_1} + \vec{e_2}$ and $\vec{e_3}$ and passing through the center of a hole. Then $\sigma_S = -1$ for the second band (even B-field and odd E-field) and $\sigma_S = 1$ for the third band (odd B-field and even E-field). The mode profiles and their corresponding symmetries can be seen in figure 5.2. We consider quasi-TE modes so that the field intensity on the center plane of the slab is best described by $B_3 = \vec{B} \cdot \vec{e_3}$. There is a high index region on the symmetry plane S (at the center of the square defined by four adjacent holes, figure 5.2). For the $2^{\text{nd}}$ band, $B_3$ has a maximum in that region, while for the $3^{\text{rd}}$ band $B_3$ is antisymmetric and has an antinode on S. The different field overlaps with the low and the high index regions create the wide splitting between these two bands. For more details on symmetries in photonic crystals see ref. [2].

In conclusion, the MLG needs to create two dominant Fourier components with equal power, with k-vectors that project onto the interface as $\pm A/\sqrt{2}$ and which verify $\sigma_S = -1$. This model

can be refined, and we will show that due to the finite power contained in the [1 1] component this conversion should be slightly less than 100%.

### 5.2.1 Multilayered grating

A grating formed by a row of holes of pitch $A$, parallel to the edge of the PPC, diffracts an incoming plane wave to higher diffraction orders offset by $K_{\text{grating}} = \pm 2\pi/A$ and is as such suitable to generate the higher order components composing the Bloch mode. However, the diffraction efficiency of a single grating is insufficient (for example 15% diffraction efficiency was computed by FDTD for holes of radius $r = 0.15$ $\mu$m). Hence several gratings are cascaded. To improve efficiency, constructive interference conditions are imposed between the contributions of the successive gratings to the higher diffraction orders and destructive interference conditions are imposed between the reflections generated by the successive gratings (anti-reflection conditions). We will show that these interference conditions can be reduced to two independent equations and that it is possible to satisfy both conditions at the same time for certain values of the PPC lattice constant. In the following, "coupling efficiency" characterizes the stand-alone MLG and corresponds to the power transfer from the $0^{\text{th}}$ order into the $1^{\text{st}}$ order. On the other hand, "insertion efficiency" characterizes the MLG integrated with the PPC and corresponds to the insertion efficiency into the PPC.

For the range of lattice constants used in this investigation the only diffraction orders that are supported by the slab are -1, 0 and 1 (in order to correspond to a propagative field, the diffraction order $m$ has to verify $|2\pi m/A| < 2\pi n_{\text{slab}}/\lambda$). The correct field symmetry to couple into the $2^{\text{nd}}$ band ($\sigma_S = -1$) is obtained when the holes of the gratings are in front of the holes of the PPC, or when the holes of the gratings are offset by A/2. This can be seen by the fact that the incoming TE slab mode has the correct symmetry and that the symmetry along S is preserved by the gratings in these two cases. If the offset is different from 0 or $A/2$ (modulo A), the symmetry is broken. In the following the holes of the grating will be offset by A/2 (figure 5.7). The 1 and -1 diffraction orders have the same magnitude and have the same phase (defined as the phase of $B_3$ on S) so that they can be described by a single scalar, referred to as order 1 in the following (in other words, as the two higher diffraction orders have a fixed symmetry, they can be described by a single scalar). The characteristic of the grating then reduces to scattering between four slab modes of identical symmetry relative to S (order 0, order 1 and their counter-propagating counterparts) and to scattering to free space modes (out-of-plane scattering losses). Hence, the grating can be described by a four by four lossy scattering matrix.

We call $\theta$ the diffraction angle. It takes the value $\theta = \sin^{-1}(2\pi/(Ak))$, where $k = 2\pi n_{\text{slab}}/\lambda$ is the wave number of the slab modes. $\varphi_0 = \varphi_{0\to 0}$ is the phase accumulated by the $0^{\text{th}}$ order due to transmission through a single grating, $\varphi_1 = \varphi_{1\to 1}$ is the phase accumulated by the $1^{\text{st}}$ order and $\varphi_{0\to 1}$ is the phase acquired by the fraction of the $0^{\text{th}}$ order scattered into the $1^{\text{st}}$ order by a single

grating ($\varphi_0$, $\varphi_1$ and $\varphi_{0\to1}$ are the phases of elements of the scattering matrix of a single grating). $\lambda_0$ is the target wavelength, and $d$ is the spacing between successive gratings. The constructive interference condition between the two forward propagating modes (order 0 and order 1) is obtained when

$$\varphi_0 + dn_{\text{slab}}\frac{2\pi}{\lambda_0} = \varphi_1 + \cos(\theta)dn_{\text{slab}}\frac{2\pi}{\lambda_0} + 2\pi m_1 \tag{5.3}$$

where $m_1$ is an integer. The anti-reflection conditions, respectively for reflections from the $0^{\text{th}}$ order to the $0^{\text{th}}$ order (equation 5.4), from the $1^{\text{st}}$ order to the $1^{\text{st}}$ order (equation 5.5) and from the $0^{\text{th}}$ order to the $1^{\text{st}}$ order (equation 5.6) are given by

$$2\varphi_0 + 2dn_{\text{slab}}\frac{2\pi}{\lambda_0} = \pi + 2\pi m_2 \tag{5.4}$$

$$2\varphi_1 + 2\cos(\theta)dn_{\text{slab}}\frac{2\pi}{\lambda_0} = \pi + 2\pi m_3 \tag{5.5}$$

$$\varphi_0 + \varphi_1 + dn_{\text{slab}}\frac{2\pi}{\lambda_0}(1+\cos(\theta)) = \pi + 2\pi m_4 \tag{5.6}$$

where $m_2$, $m_3$ and $m_4$ are integers. Equation 5.6 is also the anti-reflection condition for reflections from the $1^{\text{st}}$ order to the $0^{\text{th}}$ order. Equation 5.3 implies that equations 5.4-5.6 are equivalent with $m_3 = m_2 - 2m_1$ and $m_4 = m_2 - m_1$ so that only equations 5.3 and 5.4 need to be satisfied to suppress all the types of reflections. Since $d$, $\theta$ and $a$ are functions of $m_1$, $m_2$ and $\lambda_0$, the lattice constant of the PPC is linked to the design of the MLG[1].

Equations 5.4-5.6 ensure that zero reflection is achievable in the limit of small MLG holes. The small holes are necessary because otherwise the reflection of the first grating can not be compensated. This is the same phenomenon as the reflections from a distributed Bragg reflector (DBR) at the anti-reflection condition, i.e., if the scattering efficiency of a single grate is too high [96] the reflections due to the first grate can not be compensated [97]. When the reflections vanish, the two forward traveling diffraction orders can be modeled as two forward traveling waves coupled by an effective two by two transfer matrix. The device behaves like a directional coupler with a coupling length that can only take a set of discrete values whose step is dependant on the hole size. In the limit of vanishing hole size the effective coupling length behaves like a continuous parameter. Equation 5.3 implies that the elements on the diagonal of the effective 2 by 2 transfer matrix have the same phase (i.e., the $0^{\text{th}}$ diffraction order and the $1^{\text{st}}$ diffraction order accumulate the same phase while propagating forward and are thus phase matched). $(2\varphi_{0\to1} - \varphi_0 - \varphi_1)/2$ is the phase difference

[1]If a specific value for $a$ is targeted, the right choice of $m_1$ and $m_2$ will result in a close approximation of the target value; however, large values of $m_2$ might lead to higher out-of-plane scattering losses as the higher order Bragg condition is matched to a large number of free space modes. The k-vector corresponding to the longitudinal periodicity of the MLG is $K_{\text{long}} = k/(1/4 + m_2/2)$. If $m_2 = 0$, $K_{\text{long}} = 4k$ and it can be seen that no free space mode satisfies the Bragg condition. However, for $m_2 > 0$ there are free space modes that verify the Bragg condition.

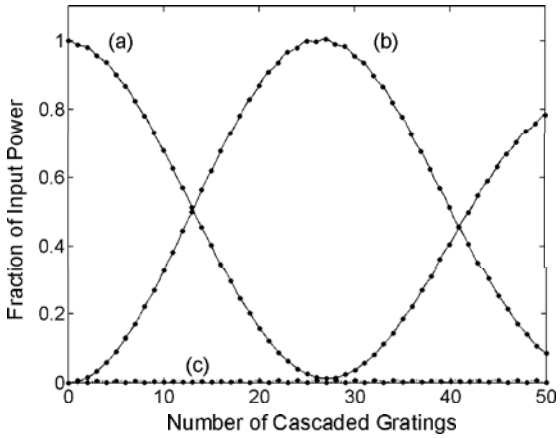


Figure 5.4: Transmission (a), coupling efficiency (b) and reflection (c) of the multilayered grating (hole size 40 nm) as computed by the transfer matrix method for $\lambda$=1.52 $\mu$m. The coupling efficiency is defined as the power transferred from the $0^{\text{th}}$ order into the $1^{\text{st}}$ order; the transmission is defined as the power remaining in the $1^{\text{st}}$ order. Optimum coupling is obtained with 27 layers.

between the coupling coefficient in the 2 by 2 transfer matrix and the diagonal terms.

There is one last condition that is necessary to achieve 100% extinction of the $0^{\text{th}}$ order (i.e., a coupling efficiency of the MLG uniquely limited by out-of-plane scattering losses). If $(2\varphi_{0\to1} - \varphi_0 - \varphi_1)/2 = \pm\pi/2$ the MLG behaves like a symmetric directional coupler, and 100% power transfer is possible if the adequate coupling length is chosen (power coupled from the $0^{\text{th}}$ order into the $1^{\text{st}}$ order and then back into the $0^{\text{th}}$ order interferes destructively with the field that stayed inside the $0^{\text{th}}$ order). If $(2\varphi_{0\to1} - \varphi_0 - \varphi_1)/2 \neq \pm\pi/2$ the maximum power transfer is less than 100%. It can be derived from first principles (power conservation and reciprocity imposed on the scattering matrix) that in the limit where individual holes constituting the grating have small coupling efficiency (small radius) this phase tends to $-\pi/2$. In that limit $\varphi_0 \to 0$ and $\varphi_1 \to 0$ (if the scattering efficiency of the holes is vanishing, a slab mode is transmitted unperturbed through the grating and does not accumulate an extra phase). It can then be derived from power conservation (unitarity of the transfer matrix) and from reciprocity that $\varphi_{0\to1} \to \pm\pi/2$.

The coupling efficiency is still limited by scattering losses. With numerical examples we will show that a structure with more layers of smaller holes has less scattering losses than a structure with fewer gratings of larger holes. The MLG described in section 5.2.3 (figure 5.4) is composed of 40 nm holes while the MLG described in section 5.2.5 (figure 5.12) is composed of 0.15 $\mu$m holes. With the bigger holes the maximum coupling efficiency is 70% and is limited by out-of-plane scattering losses.

In short, we showed that if the MLG is designed with small holes, reflections are suppressed and out-of-plane scattering losses reduced, and that the coupling efficiency of the MLG can be chosen between 0 and near 100 % on a quasi continuous scale. In section 5.2.3 we will implement an MLG with a hole size of 40 nm that verifies this.

### 5.2.2 Inner product

The analysis conducted in the next sections is based to a large extent on the decomposition of the electromagnetic field into modes of the unpatterned slab. This decomposition is performed with an inner product introduced in this section.

For waveguides with continuous translation symmetry, orthogonality conditions are well established [98]. In particular, for a non-absorbing waveguide with translation symmetry in the z-direction and two modes (bound or radiative) $\psi = (\mathbf{E}, \mathbf{H})$ and $(\bar{\psi} = \bar{\mathbf{E}}, \bar{\mathbf{H}})$ with the same implicit time dependence $exp(-i\omega t)$

$$\mathbf{E} = \mathbf{e}(x,y)e^{i\beta z} \qquad \mathbf{H} = \mathbf{h}(x,y)e^{i\beta z} \tag{5.7}$$

$$\bar{\mathbf{E}} = \bar{\mathbf{e}}(x,y)e^{i\bar{\beta} z} \qquad \bar{\mathbf{H}} = \bar{\mathbf{h}}(x,y)e^{i\bar{\beta} z} \tag{5.8}$$

The following holds if $\beta - \bar{\beta} \neq 0$

$$\int_A \{\mathbf{e} \times \bar{\mathbf{h}}^* + \bar{\mathbf{e}}^* \times \mathbf{h}\} \cdot \hat{\mathbf{z}} dA = 0 \tag{5.9}$$

where $\omega$ is the angular frequency, $\beta$ and $\bar{\beta}$ are the wave numbers and $A$ is a surface normal to the direction of propagation ($\hat{z}$).

This functional is taken as the inner product. We show in appendix A that Bloch modes also verify orthogonality conditions for this inner product [60], but we do not use this property here.

$|\phi\rangle$ is a field profile to be analyzed (field cross-section perpendicular to $\vec{e_1} + \vec{e_2}$) and $|\psi\rangle$ a normalized mode profile ($\langle\psi|\psi\rangle = \pm 1$, normalized to 1 if it is forward propagating and to -1 if it is backward propagating). Then

$$P = \langle\phi|\phi\rangle \tag{5.10}$$

$$P_\psi = \langle\psi|\phi\rangle^2 \text{sign}(\langle\psi|\psi\rangle) \tag{5.11}$$

where $P$ is the power carried by $|\phi\rangle$ and $P_\psi$ the power carried by the projection of $|\phi\rangle$ onto $|\psi\rangle$. Note that $P = \sum_i \langle\psi_i|\phi\rangle^2 \text{sign}(\langle\psi_i|\psi_i\rangle) = \sum_i P_{\psi_i}$, where the sum is taken over all the modes of the system. However, due to the fact that the inner product is not positive definite $P \leq \sum_i |\langle\psi_i|\phi\rangle|^2$.

The Bloch mode is decomposed into forward propagating modes of the unpatterned slab ($|\phi\rangle_{FP}$) and backward propagating modes of the unpatterned slab ($|\phi\rangle_{BP}$). These components correspond to the projection of the Bloch modes onto the propagative modes of the unpatterned slab (equations 5.12 and 5.13). We ignore the evanescent slab modes as the individual gratings are widely spaced ($\sim 1$ $\mu$m); this is a valid approximation due to the fact that the evanescent waves decay before reaching the next grating. By considering the effects of evanescent coupling between closely spaced rows of holes, a much more powerful mode-matching interface is designed in section 5.3 (adiabatic

coupling). The slab is single mode so that the TE-modes of the slab can be unambiguously referred to by the angle between $\vec{e_1} + \vec{e_2}$ and their direction of propagation. Furthermore, only slab modes with propagation directions corresponding to $\theta$, $0^o$ and $-\theta$ as well as their counter-propagating counterparts have a finite overlap with the Bloch mode and its diffraction pattern. The forward propagating modes are $|\psi_{-\theta}\rangle$, $|\psi_{0^\circ}\rangle$ and $|\psi_{\theta}\rangle$; the backward propagating modes are $|\psi_{180^\circ-\theta}\rangle$, $|\psi_{180^\circ}\rangle$ and $|\psi_{180^\circ+\theta}\rangle$. We couple to Bloch modes with a given symmetry ($\sigma_S$=-1) so that we only need to take into account $|\psi_1\rangle = 1/\sqrt{2}(|\psi_{-\theta}\rangle + |\psi_{\theta}\rangle)$, $|\psi_0\rangle = |\psi_{0^\circ}\rangle$, $|\bar{\psi_1}\rangle = 1/\sqrt{2}(|\psi_{180^\circ-\theta}\rangle + |\psi_{180^\circ+\theta}\rangle)$ and $|\bar{\psi_0}\rangle = |\psi_{180^\circ}\rangle$, where the relative phase between modes in the sums is chosen so as to satisfy $\sigma_S = -1$. $|\psi_0\rangle$ and $|\psi_1\rangle$ correspond to the $0^{\text{th}}$ and $1^{\text{st}}$ diffraction orders.

$$|\phi\rangle_{FP} = \langle\psi_0|\phi\rangle|\psi_0\rangle + \langle\psi_1|\phi\rangle|\psi_1\rangle \tag{5.12}$$

$$|\phi\rangle_{BP} = -\langle\bar{\psi_0}|\phi\rangle|\bar{\psi_0}\rangle - \langle\bar{\psi_1}|\phi\rangle|\bar{\psi_1}\rangle \tag{5.13}$$

The minus signs in equation 5.13 are due to the fact that the backwards propagating modes are normalized to -1.

### 5.2.3 Characterization of the stand-alone multilayered grating

We design an MLG with holes of radius 40 nm and with design parameters $\lambda_0 = 1.52$ $\mu$m, $m_1 = 1$ and $m_2 = 4$, which results in $a = 0.470$ $\mu$m and $d = 1.240$ $\mu$m.

First, the transfer matrix characterizing a single row of holes is computed by using FDTD with a spatial discretization of 20 nm and a time step $c_0 dt = 0.01143$ $\mu\text{m}^{-1}$ (where $c_0$ is the speed of light in vacuum). A silicon slab with a single hole (r=40 nm) is placed in a computational domain of dimensions $A \times 1.2$ $\mu$m $\times$ 100 $\mu$m (respectively x, y and z, where x is along the interface $\vec{e_1} - \vec{e_2}$, y is along the out-of-plane direction $\vec{e_3}$ and z is along the direction of propagation $\vec{e_1} + \vec{e_2}$). Bloch boundary conditions (BBC) with a 0 phase are applied in the x-direction so as to effectively simulate an infinite grating. Absorbing boundary conditions (ABC) are applied in the other directions. The zero phase is compatible with $|\psi_0\rangle$ ($k_x = k_\perp = 0$) and with the higher diffraction order $|\psi_1\rangle$ ($k_\perp = \pm 2\pi/A$ so that $k_\perp \cdot A = 0$ modulo $2\pi$).

$|\psi_0\rangle$ and $|\psi_1\rangle$ are successively launched and propagated through the hole. Probes store field profiles before and after the hole. By taking the inner products with $|\psi_0\rangle$, $|\psi_1\rangle$, $|\bar{\psi_0}\rangle$ and $|\bar{\psi_1}\rangle$ all the coefficients of the scattering matrix are extracted. The transfer matrix is then computed from the scattering matrix. By exponentiating the transfer matrix and imposing as a boundary condition only forward propagating waves at the output boundary of the MLG, the properties of MLGs with a variable number of cascaded gratings are computed.

Figure 5.4 shows the transmission ($0^{\text{th}}$ order to $0^{\text{th}}$ order), coupling ($0^{\text{th}}$ order to $1^{\text{st}}$ order) and

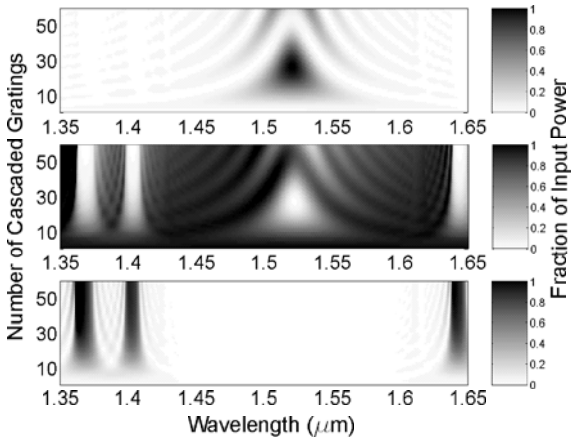


Figure 5.5: Coupling efficiency (upper plot), transmission (middle plot) and reflection (lower plot) of the MLG as a function of the wavelength and of the number of cascaded gratings. The optimum coupling efficiency is obtained with 27 layers at $\lambda$=1.52 $\mu$m; however, the passband of the MLG is higher for a smaller number of cascaded gratings.

reflections of the MLG as a function of the number of cascaded gratings at the target wavelength $\lambda_0$=1.52 $\mu$m, as computed by the transfer matrix method. It is apparent that the optimum coupling efficiency is reached with 27 layers. FDTD simulations of the full MLG are in good agreement with the transfer matrix method (at $\lambda$=1.51 $\mu$m, the optimum is computed to be 26 layers with the transfer matrix method and to be 23 layers with a full FDTD simulation). Figure 5.5 shows the results of the transfer matrix method as a function of both the number of cascaded gratings and of the wavelength. The triangular shape of the transmission shows that there is an inherent trade-off between the maximum coupling efficiency and the pass band (the maximum coupling efficiency is achieved with 27 layers; however, the pass band is higher for a smaller number of layers). This will be reflected in the insertion efficiency and pass band of the mode-matched photonic crystal shown in section 5.2.4 (figure 5.11).

### 5.2.4 Integration of the multilayered grating with the planar photonic crystal

In section 5.1 we have shown that the structure of the Bloch mode located on ΓM is dominated by $|\psi_1\rangle$ (the two dominant Fourier components with the correct symmetry). It was also mentioned that the [1 1] Fourier component contains a small but still significant amount of power. The [1 1] component couples to $|\psi_0\rangle$ so that the best overlap with the Bloch mode is achieved with $\alpha|\psi_1\rangle + \beta|\psi_0\rangle$, where $\alpha \simeq 1$ and $|\beta| << |\alpha|$. However, $|\beta| > 0$ so that the coupling efficiency of the MLG should be high but slightly below 100% in order to obtain the best insertion efficiency. We have shown in section 5.2.3 that the power distribution between $|\psi_0\rangle$ and $|\psi_1\rangle$ could be tailored by choosing adequately

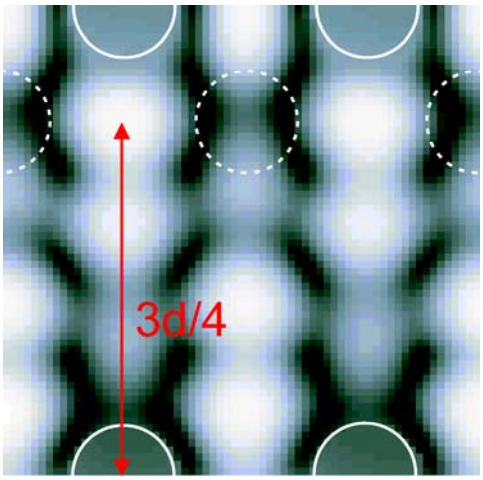


Figure 5.6: This figure shows the field distribution ($B_z$) inside the MLG (white is high intensity). The holes are shown with continuous circles. In this case the holes are large (0.15 $\mu$m), this corresponds to the geometry used in 5.2.5; however, it can also illustrate the derivations made in this section. The dashed circles indicate the position where the PPC would be placed. It can be seen that there is a field maxima in the high index region between the PPC holes and that this region is located 3d/4 away from the last row of the MLG.

the number of cascaded gratings inside the MLG. However, it was not mentioned how to tailor the relative phase between the two components. Fortunately, as there is only one phase that needs to be adjusted, the problem can be solved by choosing the distance $d_{MLG\to PPC}$ between the last row of the MLG and the first row of the PPC (figure 5.7). Indeed $|\psi_0\rangle$ and $|\psi_1\rangle$ propagate with different phase velocities inside the unpatterned slab so that their relative phase can be adjusted this way. In the following we will derive $d_{MLG\to PPC}$ so as to satisfy this constraint.

Inside the PPC, $|\psi_0\rangle$ and $|\psi_1\rangle$ are in phase in the high index region between four adjacent holes (figure 5.2a). This also holds for the first row of the PPC and constrains $d_{MLG\to PPC}$. For $m_1 = 1$ and $\varphi_{0\to 1} - \varphi_0 = -\pi/2$, this results in $d_{MLG\to PPC} = 3d/4$. Indeed the distance 3d/4 introduces a phase shift $\varphi_{|\psi_1\rangle} - \varphi_{|\psi_0\rangle} = -3/4 m_1 2\pi = -3\pi/2$. At the last row of the MLG $\varphi_{|\psi_1\rangle} - \varphi_{|\psi_0\rangle} = \varphi_{0\to 1} - \varphi_0 = -\pi/2$ so that the resulting phase difference at the 1$^{\text{st}}$ row of the PPC is $-3\pi/2 - \pi/2 = -2\pi$. Figure 5.6 illustrates this by showing the field distribution inside the MLG. It can be seen that there are field maxima displaced by 3d/4 (or -d/4) from the gratings.

We will now proceed by simulating the combined PPC and MLG with 3D FDTD. As for the calculation of the transfer matrix we apply BBC in the x-direction to a computational domain of dimensions A$\times$1.2 $\mu$m$\times$100 $\mu$m. The slab mode $|\psi_0\rangle$ is launched at the beginning of the MLG. After 40000 time steps the wave packet traveling inside the PPC reaches the absorbing boundary condition (ABC) at $+z$ (figure 5.8a). Between subsequent layers of the MLG, as well as inside the

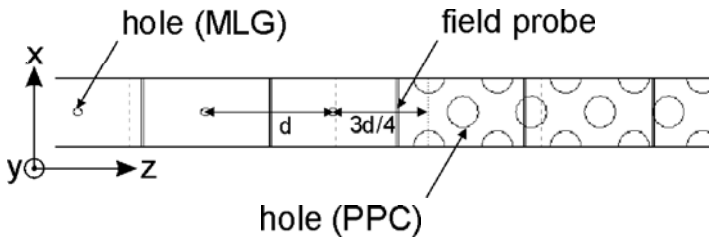


Figure 5.7: Configuration of the simulation. The width (x-direction) is A so that a single hole per cascaded grating is placed inside the computational domain. Bloch boundary conditions are applied (x-direction) so as to effectively simulate an MLG and a PPC with infinite lateral extent. The field is launched in the unpatterned slab, propagates through the MLG and is transmitted into the PPC. Field probes are periodically placed inside the MLG and inside the PPC (probes are also spaced by $d$). The distance between the MLG and the PPC is chosen so as to impose the correct phase relationship between the $0^{\text{th}}$ and the $1^{\text{st}}$ order for optimum insertion into the Bloch mode. This results in the distance 3d/4 between the last grating of the MLG and the $1^{\text{st}}$ row of the PPC (hole center to hole center).

PPC, probes store the field-profiles ($|\phi\rangle$). We stop all simulations after 50000 time steps so that the reflection of the Bloch mode at the $+z$ interface does not reach the field probes and biasing the data. The inner product is taken between the field profiles and $|\psi_0\rangle$, $|\psi_1\rangle$, $|\bar{\psi}_0\rangle$ and $|\bar{\psi}_1\rangle$ (see figures 5.8 and 5.9). The inner product is defined between field cross-sections of same implicit time dependence so that a temporal Fourier transform needs to be applied to the field profiles before the inner product can be calculated.

We compute throughout the MLG and the PPC the power carried by (i) the $0^{\text{th}}$ order ($|\langle\psi_0|\phi\rangle|^2$), (ii) the $1^{\text{st}}$ order ($|\langle\psi_1|\phi\rangle|^2$), (iii) the total power carried by forward propagating slab modes (i.e., the sum of the previous two) and (iv) the total power carried by backward propagating slab modes ($|\langle\bar{\psi}_0|\phi\rangle|^2+|\langle\bar{\psi}_1|\phi\rangle|^2$). We evaluate the insertion efficiency by

$$\frac{P_{fwd,PPC} - P_{bwd,PPC}}{P_0} \tag{5.14}$$

where $P_{fwd,PPC}$ is the power carried by forward propagating slab modes inside the PPC (iii) and $P_{bwd,PPC}$ is the absolute value of the power carried by backward propagating modes (iv). $P_0$ is the power that was initially launched. Forward propagating Bloch modes in a PPC have components that would correspond to backward propagating modes in the slab so that $P_{bwd,PPC}$ has to be taken into account in equation 5.14. This equation corresponds to the projection of the Bloch mode onto slab modes. It is an approximation as the Bloch modes also contains other components. Evanescent modes of the slab do not carry power; however, the Bloch mode probably has a non vanishing overlap with radiative modes of the cladding, even though the Bloch mode itself is below the light line and contained. This is a somewhat subtle point as the Bloch mode has zero overlap with radiative modes of the cladding with a *perforated* PPC membrane in its mist; however, it can have a finite overlap with the radiative modes of the cladding with an *unperturbed* membrane. Even though some

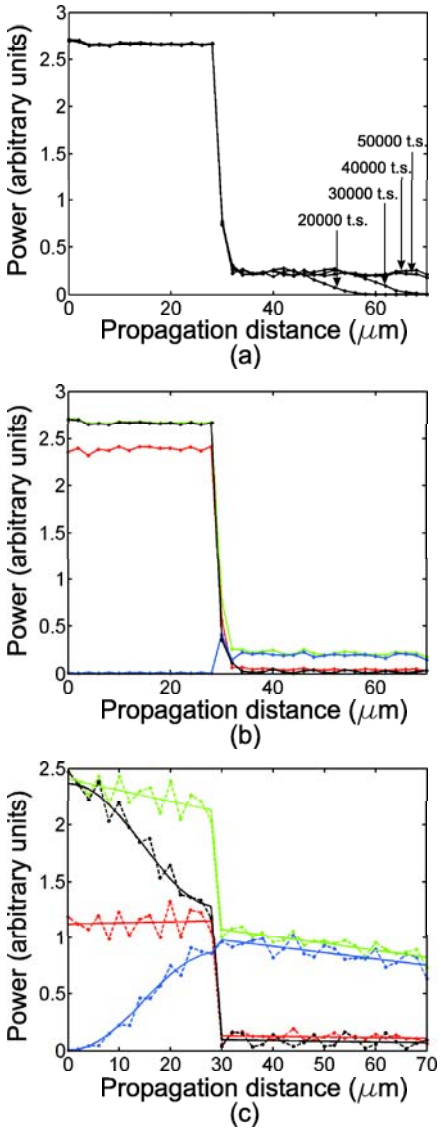


Figure 5.8: Field decomposition extracted from the field probes. (a) and (b) correspond to a non-mode-matched PPC ($\lambda = 1.51$ $\mu$m) and (c) corresponds to a PPC integrated with an MLG of 14 layers that operates partial mode-matching ($\lambda = 1.49$ $\mu$m). (c) corresponds to the same device as figure 5.9a, but the wavelength has been detuned from the optimum. In (a) $|\langle\psi_0|\phi\rangle|^2+|\langle\psi_1|\phi\rangle|^2$ is shown for various time steps after the start of the FDTD simulation. It can be seen that at 50000 time steps the Bloch mode has propagated all the way to the $+y$ interface. The ABC at $+y$ absorbs forward propagating plane waves, but Bloch modes are partially reflected. Thus we stop the other simulations at 50000 time steps to avoid these reflections bias the data. In (b) and (c) the black curve shows $|\langle\psi_0|\phi\rangle|^2$ (i in the text), the blue curve shows $|\langle\psi_1|\phi\rangle|^2$ (ii), the green curve shows $|\langle\psi_0|\phi\rangle|^2+|\langle\psi_1|\phi\rangle|^2$ (iii) and the red curve shows $|\langle\bar{\psi}_0|\phi\rangle|^2+|\langle\bar{\psi}_1|\phi\rangle|^2$ (iv). It is apparent in (b) that the $0^{\text{th}}$ order (black line) is reflected (red line). In (c) it is apparent that the $1^{\text{st}}$ order is transmitted (blue line). Inside the MLG the $0^{\text{th}}$ order is progressively transfered into the $1^{\text{st}}$ order (black to blue). The power remaining in the $0^{\text{th}}$ order is reflected at the interface (black to red).

components might be neglected, the slab modes make up for the quasi totality of the Bloch mode power and the obtained results are very compelling.

Figure 5.8 shows (i), (ii), (iii) and (iv) as a function of the propagation distance ($z$) for a bare PPC and for a PPC integrated with an MLG that operates partial mode-matching. In figure 5.8b the PPC is not mode-matched, and almost all the power is reflected (9% insertion efficiency). In figure 5.8c the MLG operates partial mode-matching. At the interface, the power remaining in the $0^{\text{th}}$ order is almost completely reflected, while the power in the $1^{\text{st}}$ order is transmitted into the photonic crystal.

This picture can be further refined. The Bloch modes have most of their power in the higher diffraction order, but there is still a finite amount of power in the $0^{\text{th}}$ order. Thus the optimum insertion efficiency is not at 100% coupling efficiency (defined as the power transfer from the $0^{\text{th}}$ to the $1^{\text{st}}$ order inside the MLG) but at a slightly lower coupling efficiency. This is illustrated by figure 5.9. In (a) the coupling into the $1^{\text{st}}$ order is insufficient, and there is a significant reflection at the interface due to the excess power carried by the $0^{\text{th}}$ order. In (c) the MLG has near 100% power transfer into the $1^{\text{st}}$ order but the situation is still sub-optimal, this time because the coupling efficiency is too high. At the interface, the power in the $0^{\text{th}}$ order increases while the power in the $1^{\text{st}}$ order decreases so that the ratio between the two components is modified. This corresponds to a mode mismatch, and there are additional reflections as compared to (b). The situation is optimum in (b) and the reflection is minimized. Note that both the powers in the $1^{\text{st}}$ and in the $0^{\text{th}}$ order increase at the interface. This does not contradict power conservation because the power carried in back propagating slab modes also increases.

We plotted the insertion efficiency at the target wavelength ($\lambda_0$=1.51 $\mu$m) as a function of the number of gratings composing the MLG (figure 5.10), i.e., the power transmitted into the PPC normalized by the power initially launched (a). We also plotted the power transmitted into the PPC normalized by the power contained in forward traveling modes at the interface between the MLG and the PPC (b). The latter normalizes out the losses incurred inside the MLG due to out-of-plane scattering and is a better characterization of the mode mismatch. It is apparent that mode mismatch is the main limiting factor (the maximum power transmission is 83.7%, versus 86.9% without out-of-plane scattering losses).

There are some limits to this coupling scheme that may explain the remaining insertion losses. Only the components of the Bloch mode that correspond to forward propagating modes of the slab ($|\psi_0\rangle$ and $|\psi_1\rangle$) are generated. However, the Bloch mode also contains components that would be back-propagating in the slab, such as component E in figure 5.2. This is not a fundamental limit of this coupling scheme but is rather a consequence of not having been taken into account in section 5.2.1. The transfer matrix method could be generalized to take it into account by modifying the output boundary condition to the Bloch mode profile rather than imposing uniquely outgoing waves.

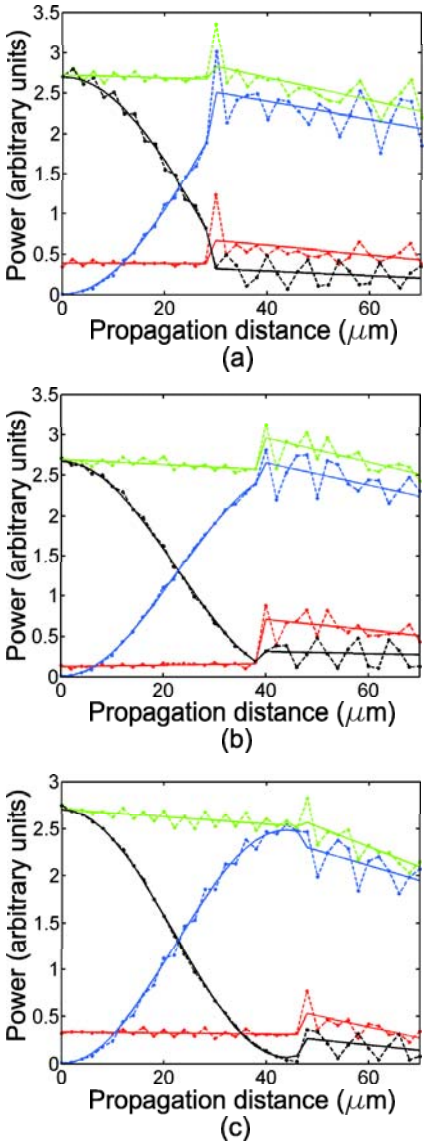


Figure 5.9: Field decomposition extracted from the field probes. The PPC is integrated with an MLG of (a) 14 layers, (b) 19 layers and (c) 23 layers ($\lambda = 1.51$ $\mu$m in all three cases). The MLG in (a) has less than the optimum number of layers (not enough power coupled into the $1^{st}$ order), (b) maximizes the insertion efficiency and (c) has too many layers. In (c) the coupling from the $0^{th}$ order into the $1^{st}$ order is maximized; however, the insertion efficiency into the PPC is suboptimum due to the small fraction of the Bloch mode contained inside the $0^{th}$ order ([1 1] Fourier component). The color conventions are the same as in figure 5.8.

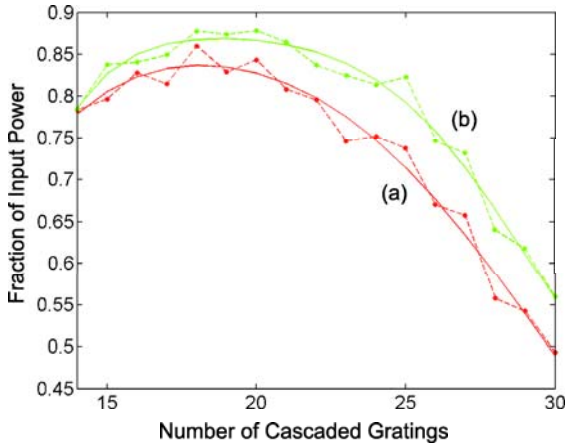


Figure 5.10: (a) Insertion efficiency as a function of the number of cascaded gratings in the MLG for $\lambda$=1.51 $\mu$m and (b) fraction of the output power of the MLG transmitted into the PPC. (b) normalizes out the losses due to out-of-plane scattering inside the MLG in order to evaluate the insertion losses uniquely due to mode mismatch.

There are also components orthogonal to the radiative modes of the slab, for example higher order Fourier components with $k_x > 2\pi n/\lambda$ that can not propagate in the unpatterned slab (for example components C and D in figure 5.2). This is a fundamental limit of this approach as evanescent waves cannot be regenerated from grating to grating, due to the large spacing.

In figure 5.11 we show the insertion efficiency as a function of wavelength. As predicted there is a tradeoff between the best peak efficiency (19 layer MLG) and the pass band. For a 19 layer MLG the peak efficiency is 84% (as compared to 9% without mode-matching interface), and the full width at half maximum (FWHM) is 28.5 nm. For a 14 layer MLG the peak efficiency is 79%, and the FWHM is 45 nm.

### 5.2.5 Compact design for Gaussian beams

In section 5.2.1 we have shown that if a slab mode of infinite extent is coupled into the PPC, an MLG composed of many layers of small holes is more efficient than an MLG with fewer cascaded gratings and larger holes. Reflections are suppressed, maximum achievable coupling efficiency is higher and out-of-plane scattering losses decrease. However, when a beam of finite width (e.g., a Gaussian beam) is coupled into the PPC, the higher diffraction orders generated inside the MLG propagate in different directions than the $0^{\text{th}}$ order so that the three beams separate. The MLG will only function as an efficient coupling scheme if the initial beam is much wider than the length of the MLG (number of cascaded gratings times d). Then the beam separation will only be a fringe effect.

We design an MLG with a hole size $r = 0.15$ $\mu$m and with design parameters $m_1 = 1$, $m_2 = 4$, $\lambda_0 = 1.52$ $\mu$m, which results in $a = 0.483$ $\mu$m and $d = 1.3141$ $\mu$m. Three cascaded layers are

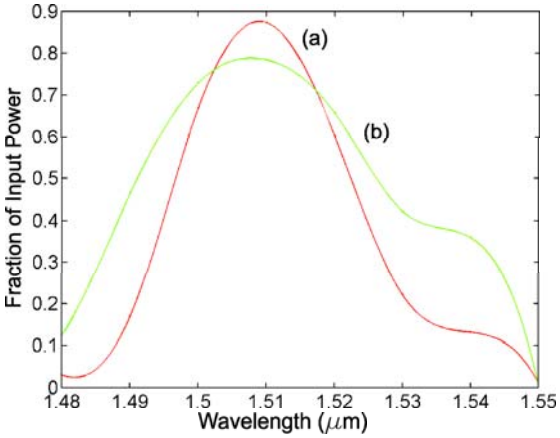


Figure 5.11: Insertion efficiency as a function of frequency for (a) 19 layers and (b) 14 layers. Optimum insertion efficiency is achieved in the case of 19 layers at 1.51 $\mu$m (84%); however, the bandpass is higher in the case of 14 layers (45 nm versus 28.5 nm).

sufficient to achieve optimum coupling, but this optimum is only 70% at 1.52 $\mu$m due to large out-of-plane scattering losses (figure 5.12). The insertion efficiency at the non-mode-matched interface is calculated to be $8\% \pm 2\%$, and the peak insertion efficiency with the mode-matched interface is calculated to be 58% at 1.54 $\mu$m.

We simulate by FDTD the transmission through a PPC of 31 rows. We compute both the case of a PPC with two mode-matched interfaces and the case of a non-mode-matched PPC (the "bare" PPC). We launch $|\psi_0\rangle$ and let it propagate through the structure. The transmission spectrum through the PPC (figure 5.13) results from the two interfaces, as well as Fabry-Perot resonances between interfaces, losses inside the PPC for modes above the light line and near zero transmission inside the band-gap. Both the total transmission through the PPC and the fraction of the transmitted power contained in $|\psi_0\rangle$ are shown. We attribute oscillations in the transmission spectrum to Fabry-Perot resonances between the interfaces.

In the absence of mode-matching the transmission suddenly increases at the onset of the $4^{\text{th}}$ band because Bloch modes of the $4^{\text{th}}$ band essentially correspond to $|\psi_0\rangle$, as explained in section 5.1. In the frequency range of the $2^{\text{nd}}$ band, the transmission through the PPC is enhanced by the MLG. The $3^{\text{rd}}$ band does not play any role in the transmission because it has the opposite symmetry ($\sigma_S = +1$). Also the fraction of the transmitted power contained in $|\psi_0\rangle$ is much higher in the mode-matched case than in the non-mode-matched case (respectively 81.45% and 8.6% at their peak transmission at 1.55 $\mu$m and 1.57 $\mu$m). This ratio also corresponds to the mode mismatch, and in the second case to the insertion efficiency. In the case of the mode-matched crystal, the insertion efficiency (58%) is actually smaller due to the out-of-plane scattering losses occuring inside the MLG.

The two interfaces of the PPC have a completely different transmission characteristic: in the case

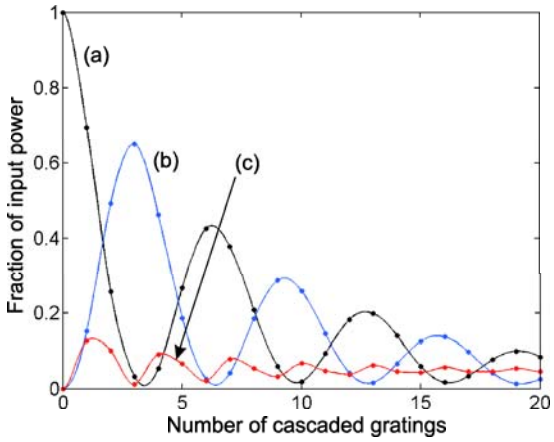


Figure 5.12: Transmission (a), coupling efficiency (b) and reflection (c) of the MLG as a function of the number of cascaded gratings. The data corresponds to the target wavelength $\lambda = 1.52$ $\mu$m, and the hole radius is 0.15 $\mu$m. The optimum coupling efficiency is achieved with 3 cascaded gratings. The coupling efficiency is limited by out-of-plane scattering losses. It can be seen that transmission and reflection of the 3-layer MLG are close to zero and are not limiting the coupling efficiency in a significant way. The envelope of (a) and (b) follows an exponential decay due to out-of-plane scattering losses.

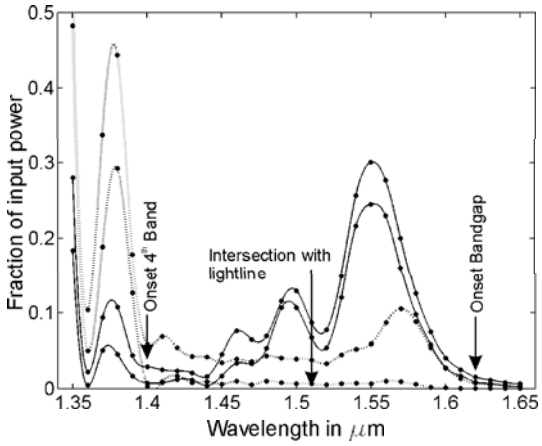


Figure 5.13: Transmission through the stand alone PPC (dashed) and through the mode-matched PPC (continuous). In both cases the upper curve is the total power transmission, and the lower curve is the power transmitted into the $0^{\text{th}}$ order. Points show computed data points. The oscillations in the transmission might be due to a Fabry-Perot resonance between the edges of the PPC. The $3^{\text{rd}}$ band has an antisymmetric B-field and is not excited so that the transmission between $\lambda = 1.4$ $\mu$m and $\lambda = 1.62$ $\mu$m corresponds uniquely to the $2^{\text{nd}}$ band.

of the bare PPC there is an almost total reflection at the 1st interface (8% transmission), but high transmission at the second because the Bloch mode is free to diffract in all diffraction orders. Thus the transmission through the bare PPC corresponds to the insertion efficiency at the 1st interface. However, in the case of the bare PPC the out-of-plane scattering losses due to the 3-layer MLG occur at both interfaces, and most of the transmission is contained inside the 0th order so that the insertion efficiency is expected to be of the order of the square root of the total transmission.

This can be formulated quantitatively: the insertion efficiency from the slab mode $|\psi_0\rangle$ into the PPC at the 1st interface is the same as the transmission efficiency from the PPC into $|\psi_0\rangle$ at the 2nd interface (reciprocity principle). Hence, the insertion efficiency can be calculated as the square root of the fraction of the power transmitted into the 0th order. This way the insertion efficiency is confirmed to be $8\% \pm 2\%$ for the non-mode-matched interface and is estimated to be 50% for the mode-matched interface at 1.55 $\mu$m, the wavelength of maximum transmission. The discrepancy from the previous estimate (58%) based on the same methodology as section 5.2.4 is easily taken into account by the Fabry-Perot effect.

The total power transmission through the PPC could be optimized by putting a mode-matching interface only at the first interface. However, for integrated optics applications it will usually be necessary to mode-match both interfaces, since the figure of merit will be the transmission into a particular slab mode if the PPC is interfaced with single mode optics.

In the case of the bare PPC, the insertion efficiency can also be evaluated by the ratio between the power transmitted into $|\psi_0\rangle$ and the total transmitted power. Indeed this ratio is calculated to be 8.6% and is in accordance with the insertion efficiency calculated previously. However, this is not a good estimate in the case of the mode-matched PPC because there are significant out-of-plane scattering losses. However, the ratio between the transmitted power contained in $|\psi_0\rangle$ and the total transmitted power can serve to estimate the mode-overlap, i.e., the insertion efficiency with the internal losses of the MLG normalized out (81%). This number is very close to the insertion efficiency obtained with the MLG composed of 40 nm holes that is not limited by out-of-plane scattering (84%). In other words, the compact 3-layer MLG creates almost the same mode overlap with the Bloch mode than the 40 nm holes MLG. The lower efficiency of the 3-layer MLG can be almost completely attributed to out-of-plane losses.

### 5.2.6 Experimental demonstration

We experimentally image the diffraction pattern of a Bloch mode after it propagates through the PPC and crosses the interface to the unpatterned slab. We compare the case of a non-mode-matched PPC and of a mode-matched PPC. In the latter case a three layer MLG with holes of radius $r = 0.15$ $\mu$m is added to the interface. In the absence of a mode-matching interface the Bloch mode gives rise to higher diffraction orders that are the signature of the higher order Fourier components in the Bloch

mode structure. When the MLG is added to the PPC, the higher diffraction orders are suppressed. Because of reciprocity, this is expected when the mode-matching efficiency is high.

In order to compensate for small variations in refractive indeces and film thickness, we fabricated several samples corresponding to variations in $\lambda_0$, the target wavelength of the MLG (varying $\lambda_0$ is equivalent to varying $n_{\text{slab}}$ in equations 5.3 and 5.4). The best suppression of the higher diffraction orders at the output of the mode-matched PPC was achieved for $\lambda_0 = 1.565$ $\mu$m. The lattice constant of the PPC is dependant on $\lambda_0$ as indicated in section 5.2.1 and varies slightly throughout the span. $\lambda_0 = 1.565$ $\mu$m leads to $a = 0.470$ $\mu$m and $d = 1.277$ $\mu$m. For a description of the fabrication procedure see chapter 7.

Polarized light is butt-coupled into a 10 $\mu$m wide waveguide with a 100X long working distance lens. The high magnification is necessary to get light into the thin, 205 nm thick silicon slab. In order to generate a wide beam, the waveguide is expanded with a parabolic taper [62] to the final width $W = 70$ $\mu$m. A microscope image of the taper can be seen in figure 5.15a. The local width of the taper is given by $W(y)^2 = (2\alpha\lambda_0/n)y + W_0^2$, where $\lambda_0 = 1.52$ $\mu$m and $W_0 = 10$ $\mu$m and $\alpha = 1$. The criterion to design the taper was for the local expansion angle of the waveguide to be smaller than the diffraction angle of a beam with the local waveguide width, so as to always constrain the field. In particular the expansion angle of the waveguide is chosen to be proportional to the beam expansion angle, with $\alpha$ being the proportionality factor. The smaller $\alpha$ is, the better the mode conversion (i.e., the smaller the cross talk to higher order modes of the wide waveguide). The conversion efficiency drops severely for $\alpha > 1$.

A PPC with 59 rows of holes (figure 5.15b), with bare or mode-matched interfaces, is placed at the end of the waveguide. The field then diffracts into the unpatterned slab. 325 $\mu$m away from the PPC an amorphous "crystal" (figures 5.14 and 5.15c) vertically extracts light that is subsequently imaged by an IR camera (Indigo systems, Merlin InGaAs NIR). The "crystal" is amorphous so that it has an isotropic in plane behavior, i.e., light guided by the slab is vertically extracted independently of its angle of incidence. The crystal is designed in such a way as to keep the distance between adjacent holes as close as possible to a predetermined mean ($\sim \lambda/n_{\text{eff}}$), but so that the relative orientation of two adjacent holes is random. The Fourier transform of such a structure is a circle rather than a set of discrete components. The positions of the holes are determined with a simple algorithm. They are placed into a computational domain and assigned an interaction potential. The positions are incremented each time step by updating them with a small displacement pointing in the opposite direction than the potential gradient. Circular boundary conditions are imposed on the computational domain, that is, if a hole is pushed out of the domain it reenters at the opposite boundary. The operation is repeated until the system achieves steady state. The potential associated

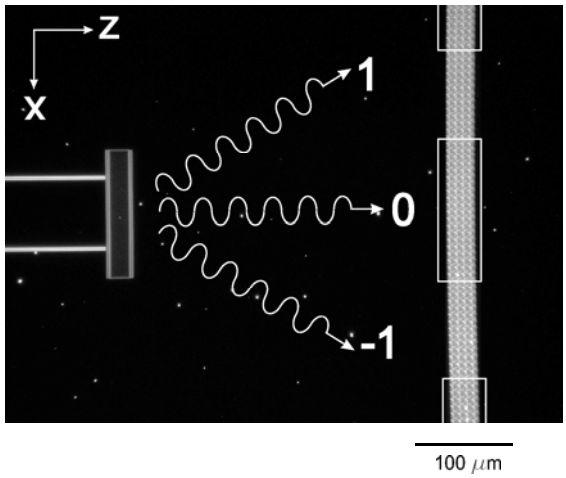


Figure 5.14: Device imaged with a dark field microscope. On the left, a waveguide is connected to a mode-matched PPC. The waveguide is delimited by 2 $\mu$m wide trenches etched into the silicon membrane. These trenches can be seen as white horizontal lines. An amorphous crystal is placed to the right. Diffraction orders are numbered and represented by arrows. The white boxes show the regions imaged by the IR camera (figure 5.16).

to "hole" $j$, $V_j$, and the corresponding displacement, $\vec{\pi_j}$, have the form

$$V_j = \sum_i \frac{\zeta^2}{d_{ij}^2} - \frac{\zeta}{d_{ij}} \tag{5.15}$$

$$\vec{\pi_j} = -\epsilon \vec{\nabla} V_j / \parallel \vec{\nabla} V_j \parallel \tag{5.16}$$

In the above equations $d_{ij}$ is the distance between holes $i$ and $j$, $\zeta$ is the characteristic length scale of the potential and $\epsilon$ is the magnitude of the small displacement. Even though the potential has a characteristic length scale, the mean distance between holes will be determined by the density of holes inside the computational domain. This density has to be high enough to avoid the holes forming a cluster in the center of the domain. They should be closely packed; maybe a good analogy would be a compressed gas with an interaction potential. Finally, for the light to see a truly homogeneous media, the penetration distance of the light inside the amorphous crystal should be large enough. In that respect, the hole size in figure 5.15(c) is rather on the large side.

Figure 5.16 shows the diffraction patterns as imaged by the IR camera. The diffraction orders -1, 0 and 1 have different propagation directions and separate into three separate beams inside the slab. These beams then impact on the amorphous crystal and get extracted out of the slab, thus three bright spots appear on the amorphous crystal. These spots are imaged by the IR camera and are shown in figure 5.16. The light is generated by a tunable laser and this measurement is repeated for free space wavelengths ranging from 1.5 $\mu$m to 1.58 $\mu$m. The white boxes in figure 5.14 correspond to the imaged regions shown in figure 5.16. It can be seen that the -1 and 1 diffraction

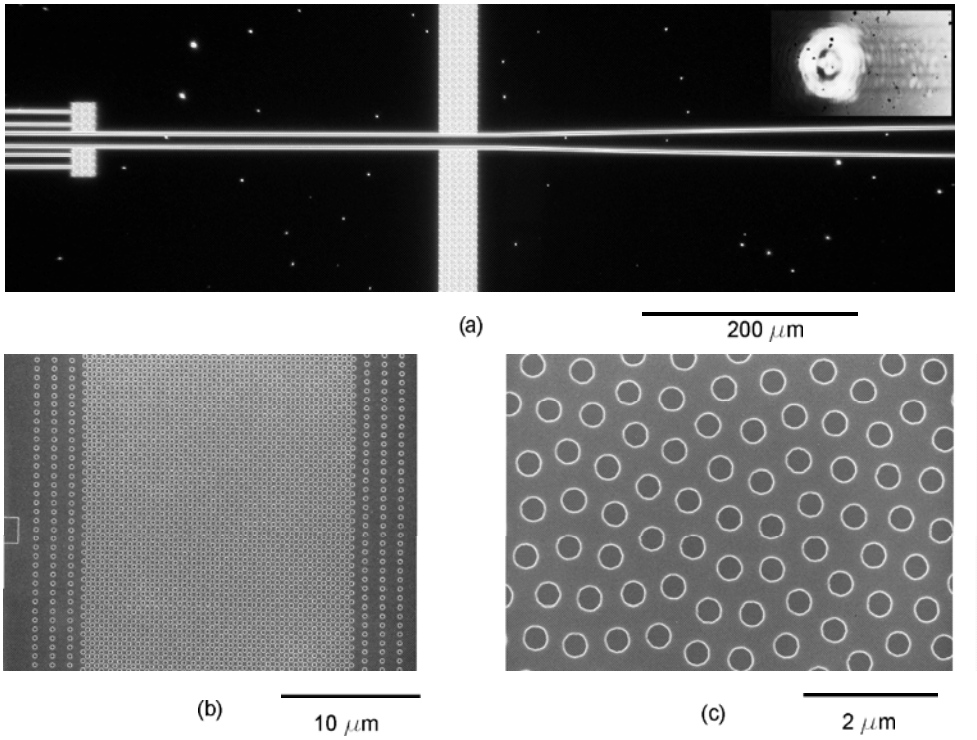


Figure 5.15: (a) Dark field microscope image of the waveguide region before the photonic crystal. On the left three waveguides are seen. The center one is tapered out and couples into the photonic crystal (figure 5.14). In the center of the image the white bar corresponds to an amorphous crystal that extracts stray light coupled from free space into the slab (outside of the waveguide). This ensures that the light imaged in the region of the PPC originates from the center waveguide. The upper and lower waveguides on the left of the picture are used as fiducials to optimize coupling from free space: in order to center the position of the spot from the focusing lens, we aimed to have an equal amount of light extracted by the amorphous crystals at the terminations of the two outer waveguides. The inset is a picture taken with the IR camera. The spot from the focusing lens can be seen as well as the three waveguides. (b) is a SEM micrograph of the mode-matched PPC, and (c) is a SEM view of the amorphous crystal.

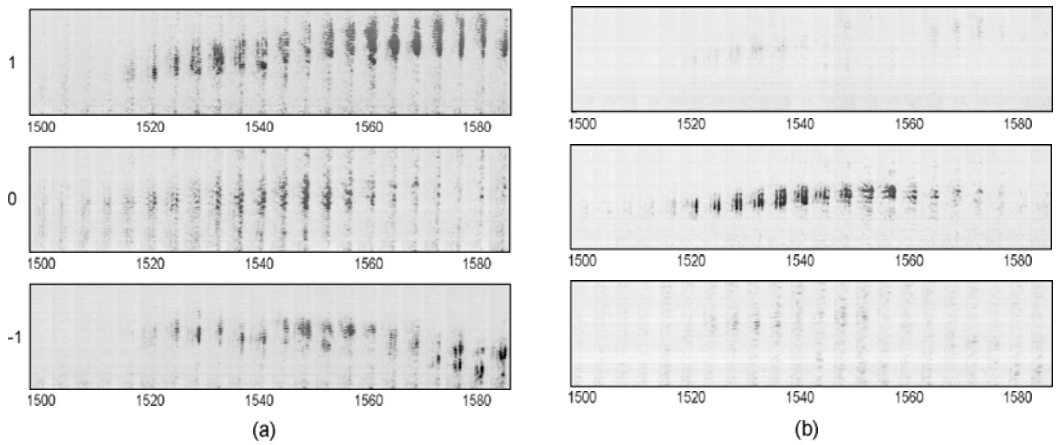


Figure 5.16: (a) Experimental results for the non-mode-matched PPC. The amorphous crystal is imaged with an IR camera for each subsequent wavelength. The intensities of all diffraction orders are shown. (b) Experimental results for the mode-matched PPC. The diffraction orders 1 and -1 are suppressed. In (a) and (b), the color scaling is the same for the three diffraction orders. The settings of the IR camera were the same, and the spots were imaged on the same region of the InGaAs diode array.

orders are suppressed in figure 5.16b. The pass band of the mode-matched device is 40 to 50 nm and corresponds to the pass band calculated in section 5.2.4.

In conclusion, we have shown that a diffraction grating composed of multiple rows of holes can be designed to mode-match an unpatterned slab to a planar photonic crystal. We achieved 84% insertion efficiency with a multilayered grating composed of 19 layers of holes with a radius of 40 nm, compared to 9% without mode-matching. It is possible to design more compact structures with bigger holes at the cost of significant out-of-plane scattering losses and a corresponding decrease in insertion efficiency. In particular 58% insertion was achieved with a multilayered grating composed of three rows of holes with a radius 0.15 $\mu$m. Despite their reduced insertion efficiency, these more compact structures are of interest because they enable coupling into a planar photonic crystal of beams with small widths.

## 5.3 Adiabatic transition

In this section we mode-match the slab to the PPC by introducing an adiabatic transition inside the PPC. This approach differs by several points from the MLG introduced in the last section. Indeed, the MLG could be designed with transfer matrices uniquely taking into account the propagative modes of the slab. The evanescent coupling between successive gratings could be ignored due to the fact that the individual gratings were separated by a fairly wide distance (greater than a micron). On the other hand, inside the adiabatic transition, the successive rows of holes are closely packed

so that evanescent coupling plays an essential part. This gives a much wider design freedom, but the underlying physics would also be much more difficult to modalize in a reductionist manner (that is by breaking down the adiabatic transition into individual rows). Fortunately the adiabatic transition can be modeled in different ways. Instead of breaking the transition down into individual rows, the transition is locally characterized by the band diagram of the local crystal lattice. In the previous section the transfer matrix of a single row was calculated by FDTD; subsequently the rows were assembled. Here, the bulk properties of the local lattice are calculated by FDTD, and then the light propagation properties derived from deformations of the local EFCs. The evanescent coupling between holes is taken into account by the FDTD calculation and hidden inside the band diagram. The adiabatic transition has compelling advantages over the MLG. For one, light inside the adiabatic transition corresponds to the local Bloch mode so that the problem incurred inside the MLG of various Fourier components spatially separating is alleviated. Furthermore, the adiabatic transition does not depend on strict interference conditions. As a consequence it has a wider pass-band. Most importantly, it has a wide angular pass-band, which makes it particularly compelling for the superprism. Finally, it does not rely on constructive and destructive interference condition such as the MLG. Thus the restrictions on the design are much more relaxed. It does not need to be carefully fine-tuned like the MLG and can be easily adapted to different lattices.

We are able to achieve a high insertion-efficiency on the order of 95% throughout a wide frequency range (1.47 $\mu$m to 1.68 $\mu$m) by adiabaticlly reducing the hole size at the PC interfaces. The two interfaces of the PC are along the [1 -2] crystallographic axis (figure 5.17(a)), and the hole size is adiabatically reduced along the direction orthogonal to the interface (the [2 1] direction). Inside the adiabatic transition region, holes that are offset by the [1 -2] vector have the same size. As will be explained in the next section, the orientation of the interface is crucial for the adiabatic transition to fulfill its function.

In section 5.3.1 we will show that the adiabatic transition projects the complex Bloch modes at the cusp of the EFCs onto modes located on the sides of the EFC. The latter have a single dominant Fourier component and are gradually converted into a single plane wave. We will also give a quantitative model for the insertion efficiency in the absence of mode-matching, and we will evaluate the efficiency of the adiabatic transition. All calculations are performed with 2D FDTD due to the large size of the devices. In the case of the MLG, 3D FDTD was crucial to take into account the out-of-plane radiation losses at the interface. In the case of the adiabatic transition, such losses should be suppressed if the transition is slow enough so that 2D FDTD is adequate. However, this only holds if the Bloch modes stay outside the light cone, both in the "bulk" PPC and in the adiabatic transition. The resulting design constraints are derived in section 5.3.3 and numerical examples for realistic lattices are given. In particular, it is shown that it is beneficial to chose the thickest possible slab thickness (before the PPC turns multi-mode). The problem can also

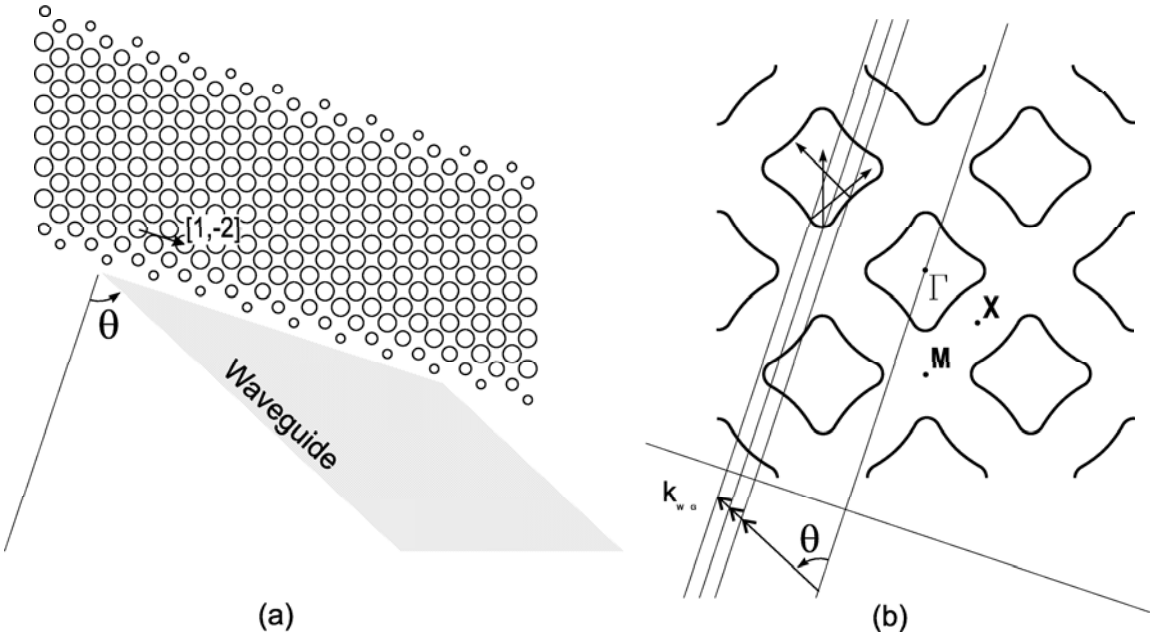


Figure 5.17: In (a) the superprism configuration is illustrated. The waveguide direction relative to the PC as well as the orientation of the PC interfaces are shown. The hole size is varied in the adiabatic transition regions. Holes offset by the [1 -2] vector have the same radius. (b) illustrates the coupling from the waveguide to the photonic crystal. The k-vector of the waveguide-mode $k_{WG}$ is projected onto the EFC of the PC, with a projection direction perpendicular to the interface. At wavelengths shorter (higher) than $\lambda = 1.54$ $\mu$m, $k_{WG}$ increases (decreases), and light is coupled to modes left (right) of the cusp. The direction of propagation is indicated by arrows inside the EFC. The Γ, M and X high symmetry points are also shown.

be completely avoided by working with the 1st rather than with the 2nd band.

### 5.3.1 Investigation with 2D FDTD

In the following we investigate a 2D square lattice PC with the 2D FDTD method. The refractive index of the slab is assumed to be 3.43 (silicon), and the holes are assumed to be backfilled with silicon dioxide (refractive index 1.46). The lattice-constant of the crystal ($a$) is 0.4 $\mu$m, and the radius of the holes in the bulk part of the crystal (that is outside the adiabatic transition) is 0.12 $\mu$m. All fields are transverse-electric (TE) with the B-field pointing out-of-plane. The discretization is 0.01 $\mu$m, and the time-step is $dtc_0 = 0.005$ $\mu$m (where $c_0$ is the speed of light in vacuum).

In a superprism, an angled waveguide is coupled to a PC. In order to predict to which Bloch mode the waveguide is going to couple, the conservation of the k-vector component parallel to the interface ($k_{||}$) is used (figure 5.17(b)). Due to the discrete translation symmetry along the PC interface, this conservation is only exact modulo $2\pi/A$ where $A$ is the periodicity of the PC along the interface. The PC we investigate in this section has both its interfaces along the [1 -2] direction so that in

this case $A = \sqrt{5}a$. $k_{\|}$ can be deduced from the waveguide geometry by $k_{\|} = \sin(\theta)2\pi n_{WG}/\lambda$, where $n_{WG}$ is the effective index of the waveguide and $\theta$ is the angle between the waveguide and the normal to the interface of the PC (figure 5.17(a)). $\theta$ is chosen in such a way as to couple light at $\lambda = 1.54$ $\mu$m to a Bloch mode located at the center of the cusp. This corresponds to the condition $k_{\|} = k_{\|,cusp} + m2\pi/A$, where $k_{\|,cusp}$ is the projection of the reduced k-vector (inside the 1$^{\text{st}}$ BZ) of the center of the cusp onto the interface, and $m$ is an integer. The projection of the various Fourier components of the Bloch mode onto the interface is shown in figure 5.18. $k_{\|,cusp}$ corresponds to the position of component $c$ in figure 5.18. Depending on the value of $m$, the light exciting the waveguide couples to the Bloch mode through a different Fourier component, respectively $m$ = -2, -1, 0 and 1 correspond to Fourier components $a$, $b$, $c$ and $d$ (the letters label the Fourier components, while the integer $m$ refers to a coupling condition, thus we keep the two separate notations). Here $m$ is chosen to be $-2$ so that we couple to a higher-order Fourier-component (component $a$ in figure 5.18) outside the first BZ. This results in $\theta = 60.95^{\text{o}}$.

It is useful to work with $m = -2$ because this leads to enhanced demultiplexion compared to $m = 0$ (see chapters 2 and 6). There is a second compelling reason to work with $m = -2$. Even in the absence of a mode-matching mechanism, much higher insertion efficiency is achievable this way. Indeed $m = -2$ corresponds to coupling to component $a$, which is one of the two dominant Fourier components of the Bloch mode on the cusp and which is the dominant component for modes to the right of the cusp. $m = 0$ however would correspond to couple to component $c$, which contains only a small fraction of the power of the Bloch mode. Later in this section we will show with numerical examples that in the absence of a mode-matching mechanism the insertion efficiency can be modeled as

$$I_x = P_x/(P_a + P_b + P_c + P_d) \tag{5.17}$$

where $I_x$ is the insertion efficiency corresponding to coupling through component $x$ and $P_x$ is the fraction of the Bloch mode contained in component $x$ ($x \in$\{a, b, c, d\}). This formula corresponds to a simple mode overlap integral. It is then apparent that the insertion efficiency is proportional to the fraction of the Bloch mode contained in the Fourier component that is coupled to by the waveguide. For the case $m = -2$ investigated in this paper, in the absence of mode-matching the insertion efficiency is high for modes to the right of the cusp; however, the insertion efficiency is low for modes to the left of the cusp that are dominated by component $d$ rather than component $a$ (figure 5.20b).

The principle of the adiabatic transition is illustrated in figure 5.19(a). The hole size is progressively decreased inside the adiabatic transition region. The main effect of decreasing the hole size is shrinking the EFC. This can be explained to the first order by an increase of the effecting index of the PC slab due to a higher volume ratio of high index material so that the unfolded contour

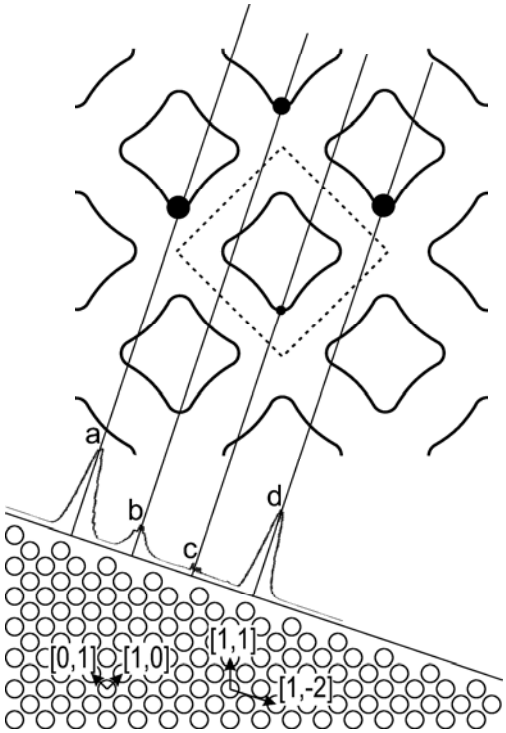


Figure 5.18: This schematic illustrates how the different components of the Bloch mode project onto the interface between the crystal and the slab. The squarish contours show the EFC inside the first BZ (shown by the dashed square) and in higher Brillouin zones (outside the dashed square). The four main Fourier components of the Bloch mode located on the lower cusp as well as their projection onto the interface of the crystal are shown by dots and by a curve along the interface. The curve corresponds to real data and gives an idea of the relative intensity of these components. They are spaced by $2\pi/(a\sqrt{5})$ and labeled for reference in the text. Components $a$, $b$, $c$ and $d$ correspond to $m$=-2, -1, 0 and 1. It is apparent that component $a$, which we are coupling to as we chose $m$=-2, is one of the two dominant components. We also show the real-space lattice-vectors, the unit-vector of the interface, [1 -2], and the direction of propagation of light at $\lambda = 1.54$, [1 1].

(dashed circle in figure 5.3) is enlarged. After folding back the contour into the 1$^{st}$ BZ the resulting squarish contour is smaller. In other words, due to the fact that the 2$^{nd}$ band is folded back once, the dependence of the size of the contour on the index of the materials constituting the slab is the opposite of what would be expected from an unpatterned slab. Due to the slanted orientation of the interface, the Bloch modes originally in the vicinity of the cusp are not projected onto the cusp of the smaller contour (as would happen if the interface had been along the [1 -1] direction and the hole size varied along the [1 1] direction). Rather, while propagating through the adiabatic region, the Bloch modes originally in the vicinity of the cusp are progressively projected onto the side of the smaller squarish contours corresponding to the local band structure. On the sides of the contour, the Bloch modes are dominated by a single Fourier-component and are easy to couple to. Furthermore, with decreasing hole size this single Fourier-component dominates more and more the overall Fourier structure until 100% of the mode is contained in this single component. In order to simplify the diagram, figure 5.19(a) shows a step change of the hole radius instead of a continuous change over a large number of layers. Such a brusk change would induce reflections as well as out-of-plane scattering losses in a planar PC defined in a finite thickness slab. The slow transition from the full hole size to the small holes in figure 5.19(b) suppresses these loss mechanisms. It is essential for the interface to be along an orientation other than [1 -1] when modes on both side of the cusp are being mode-matched. Indeed, if the orientation were [1 -1], the mode on the center of the cusp would stay at the center of the cusp throughout the mode-matching interface and would finally be converted to two distinct plane waves.

Figure 5.19(b) illustrates the real-space behavior of light in the slab, superprism and adiabatic transition region. In the latter, the direction of propagation progressively undergoes a change in direction. This is an additional advantage over the MLG introduced in section 5.2. Indeed inside the MLG the two Fourier-components containing most of the power of the Bloch mode were progressively generated, but had different directions of propagation so that the MLG had to be compact to avoid the two components spatially separating. In the adiabatic transition region, the light corresponds to the local Bloch mode at each point of the transition so that all the generated components copropagate in the same direction. In particular in the case of the MLG there was a tradeoff between compactness and insertion-efficiency, which is not an issue in the present design, as there is no disadvantage in increasing the size of the adiabatic transition other than a slight loss of real estate on the chip.

We evaluated the insertion-efficiency of the adiabatic transition by 2D FDTD computation. In the following simulations we adiabatically reduced the hole radius from 0.12 $\mu$m to 0.06 $\mu$m. We did not go all the way to zero for practical reasons, both due to limitations of the FDTD method (discretization) and due to the resolution limitations of lithography in a fabricated device. We transmit light through PCs with both interfaces oriented along the [2 -1] direction, in one case the PC consists in a "bulk" PC and in the other case by a PC with adiabatic transitions at the input and

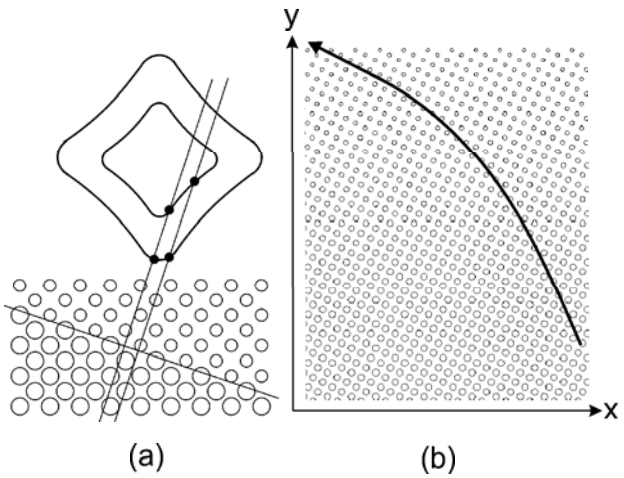


Figure 5.19: (a) illustrates the mechanism underlying the adiabatic transition. To simplify the schematic we show a step in hole radius rather than a continuous change, but the general idea is the same. Due to the change in hole size, the contour is deformed. In particular, for the same wavelength, the contour in the region of smaller holes is smaller. Because the translation invariance is conserved along the [1 -2] direction, it is straightforward to predict how a Bloch mode couples from one crystal to the other by projecting it along the [2 1] direction. Modes that were in the vicinity of the cusp in the "bulk" PC (with larger holes) couple to modes on the side of the contour in the PC with smaller holes. Those modes have a dominant Fourier-component and are easy to couple to. When the transition is made adiabatic, rather than stepwise, the reflections induced at the interface are suppressed. (b) illustrates the real-space behavior of the light propagation. In the adiabatic transition region, the group-velocity is progressively deflected. The interface of the PC is along the x-direction (the coordinate frame of (b) is rotated relative to the other figures).

at the output facets (the "adiabatic PC"). The bulk PC is 150 layers wide, where "layer" refers to a row of holes along the [2 -1] direction (for example the PC in figure 5.17(a) would correspond to 23 rows). The adiabatic PC consists of 150 layers, where the hole radius is ramped up from $r = 0.06$ $\mu$m to $r = 0.12$ $\mu$m in the $1^{\text{st}}$ 50 layers, kept constant in the next 50 layers, and finally ramped back down to $r = 0.06$ $\mu$m in the last 50 layers. In figure 5.20 we show data for a wide range of k-vectors but for a fixed wavelength $\lambda = 1.54$ $\mu$m. A transform-limited Gaussian beam is launched in the unpatterned slab before the PC, with an angle $\theta = 60.95^{\text{o}}$ relative to the normal to the interface of the PC. However, the waist of the beam is chosen to be narrow; due to the small waist the light source contains a wide range of k-vectors centered on $k_{\|,cusp} + m2\pi/A$ (with $m = -2$), rather than a narrow k-vector distribution generated by a wider light-source so that data can be collected for a wide range of k-vectors. The field at the output facet of the PC is Fourier-transformed, and the component of the Poynting-vector along the y-direction $P_y(k_\|)$ is calculated as a function of $k_\|$. Three items are confirmed by this data: first that the Bloch mode structure indeed undergoes the predicted transition from one Fourier-component to the other, second that equation 5.17 is adequate to predict the insertion-losses in the vicinity of the cusp and in the absence of an adiabatic transition, and third that the adiabatic transition does solve the insertion problem for a wide range of k-vectors. In order to evaluate the insertion-efficiency, in both cases we compare the incoming power to the transmitted power. In order to show the Bloch mode structure, we decompose the transmitted power into the various Fourier-components. Finally, to verify the validity of equation 5.17, we compare the actual transmitted power to the transmitted power predicted by equation 5.17.

Figures 5.20(a) and 5.20(c) show the raw data respectively for the bulk PC and for the adiabatic PC. Figures 5.20(b) and 5.20(d) show the actual transmission through the PC as well as the predicted transmission. In figure 5.18 we can see that there are 4 peaks in the k-space transmission spectrum, three of which, $a$, $b$ and $d$, are significant. In figure 5.20(a) and 5.20(c) we show peaks $a$ (rightmost dash-pointed curve), $b$ (pointed curve) and $d$ (leftmost dash-pointed curve) as a function of their reduced k-vector so that all the components corresponding to the same Bloch mode share the same abscissa. In other words the Fourier components corresponding to $k_\| + p2\pi/A$ with $p \in \{$-2 -1 0 1$\}$ are all plotted with the abscissa $k_\|$. In all four figures the zero abscissa corresponds to the intersection of the contour with the ΓM direction, the center of the cusp. The total outgoing power is the sum of those three components and is shown by the lower continuous curve. The incoming power is shown by the upper continuous curve. The dashed curve, almost identical to the outgoing power, corresponds to the outgoing power predicted by equation 5.17 from the power distribution in components $a$, $b$ and $d$. In figures 5.20(b) and 5.20(d), the continuous curve is the actual transmission, that is, the outgoing power divided by the incoming power, while the dashed curve is the predicted transmission.

There are some comments that can be made on this data. In figure 5.20(a) the Bloch mode structure predicted by the model shown in figure 5.3 can be clearly seen. Modes to the left of

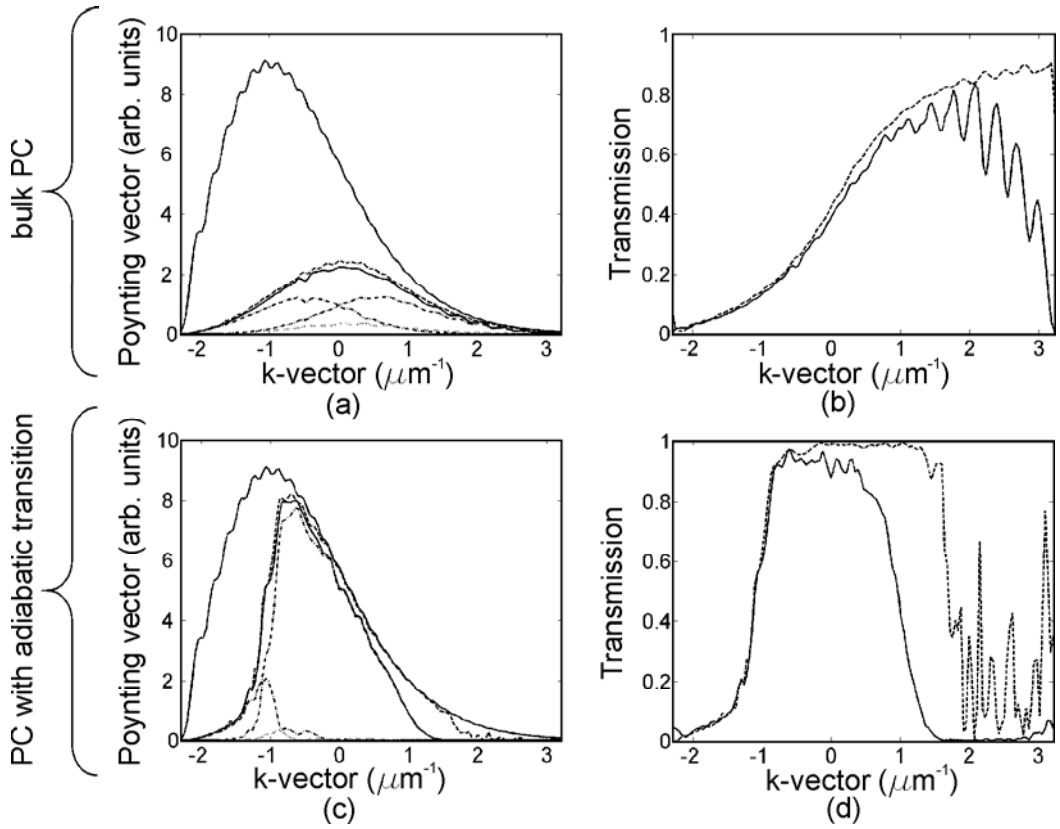


Figure 5.20: We propagate light at $\lambda = 1.54$ $\mu$m through a bulk PC ((a) and (b)) and through an adiabatic PC ((c) and (d)). The abscissae correspond to the projection onto the interface of the reduced k-vector of the Bloch mode (the zero abscissa has been shifted so that it corresponds to the mode on the $\Gamma$M direction). In (a) and (c) the upper continuous curve is the incoming power, and the lower continuous curve is the outgoing power. The dashed curve is the prediction of the output power based on equation 5.17. The left dash-point curve corresponds to component $d$ (figure 5.18), the right dash-point curve to component $a$ and the pointed curve to component $b$. All the Fourier-components corresponding to the same Bloch mode are represented at the same abscissa. In (b) and (d) we show both the actual insertion-efficiency (continuous curve) and the predicted insertion-efficiency based on equation 5.17 (dashed curve). In (a) and (c), the trailing edge of the incoming Gaussian beam is due to the fact that the interface of the PC is rotated in respect to the direction of propagation of the beam.

the cusp, with a negative abscissa, propagate to the right, and the dominant component is $d$. Conversely, modes to the right of the cusp, with a positive abscissa, propagate to the left, and the dominant component is $a$. In figure 5.20(b) it can be seen that the predicted insertion-efficiency is S-shaped, where modes with a higher abscissa, that are dominated by component $a$, have a higher insertion-efficiency because component $a$ is provided by the light source in the slab. The actual insertion-efficiency is close to the predicted one for a large range of k-vectors. At positive abscissae there is also another limiting mechanism on the insertion-efficiency that we did not investigate. In the case of the adiabatic PC, as predicted, component $a$ is heavily dominant in the transmission spectrum around the zero abscissa. This leads to an insertion-efficiency above 90% for a large range of k-vectors on both sides of the cusp (i.e., with positive and negative abscissae). Also, it can be seen that the transition point from one dominant Fourier-component to the other is shifted from $k_{\|} = 0$ to $k_{\|} = -1.12\ \mu\text{m}^{-1}$. That is to be expected from the model shown in figure 5.19(a), where a mode originally left of the cusp (with $k_{\|} = -1.12\ \mu\text{m}^{-1}$) gets projected onto the cusp of the smaller contour, while all the mode to its right, including the mode originally on the cusp (with $k_{\|} = 0$), get projected on the side of the contour where $a$ is dominant. Finally, in the case of the adiabatic PC, the transition from one Fourier-component to the next is much more abrupt, as visualized by the slope at $k_{\|} = -1.12\ \mu\text{m}^{-1}$ in figure 5.20(d). This is due to the fact that the field at the output of the crystal corresponds to the modes of the PC with reduced hole size ($r = 0.06\ \mu$m), where the coupling strength between Fourier-components as well as the extent in k-space over which anticrossing occurs are reduced.

As explained in detail in chapter 6, for an angled waveguide coupled to a PC, there is a one-to-one relationship between the wavelength and the k-vector of the Bloch mode that is coupled to. The true figure of merit of a mode-matching interface used in conjunction with a superprism is the insertion-efficiency at each of these frequency/k-vector points that determines the frequency dependent coupling-efficiency of the complete system. We show this data in figure 5.21. The field is launched from a much wider Gaussian beam, the full width at half minimum (FWHM) is 3 $\mu$m so that a narrow range of k-vectors is targeted at each frequency, rather than averaging the insertion-efficiency over a wide range of k-vectors. The Gaussian beam approximates the mode profile of the waveguide leading to the superprism in a real device. It can be seen that the insertion-efficiency (transmittance through two interfaces with adiabatic transition) is above 90% for a range of wavelengths (1.47 $\mu$m to 1.68 $\mu$m) including the telecommunication C-band (1.528 $\mu$m to 1.570 $\mu$m) and L-band (1.570 $\mu$m to 1.605 $\mu$m).

### 5.3.2 Effect of higher order bands

The numerical study presented in the last section was restricted to a design and a frequency domain where a unique photonic band was present, the second band. However, it is an important question

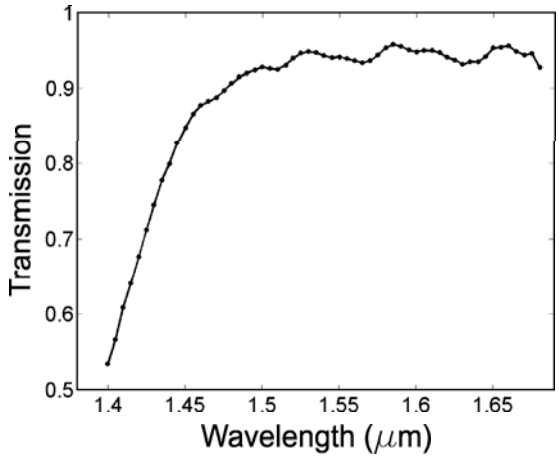


Figure 5.21: Power transmission through the "adiabatic crystal". A Gaussian beam with a FWHM of 3 $\mu$m and an angle $\theta = 60.95^{\circ}$ is launched into the slab and coupled to the crystal (150 layers, 100 of which are split between the adiabatic transitions on both interfaces). $\theta$ is chosen so that light at $\lambda = 1.54$ $\mu$m propagates along the [1 1] direction. The transmission is in excess of 90% over the wavelength range 1.47 $\mu$m to 1.68 $\mu$m.

how the mode-matching mechanism would be modified by the presence of a higher order band in the same frequency range. This is also a relevant question for the design described above as in the adiabatic transition region the splitting between the second and third band decreases as the hole size decreases. Thus even though in the bulk PPC only the second band is present, the second and third bands coexist in the transition region. We did not do numerical simulations to verify what happens; however, by using the same techniques that led to the initial design, that is, by considering deformations of the EFC and projections from the original EFC to the modified EFC along preferential directions imposed by the orientation of the interface, a fairly precise picture can be derived. We will show that the third band does not perturb the mode-matching mechanism as modes of the third band get converted to a different slab mode.

As shown in section 5.1, the modes of the second and of the third band take the form $1/\sqrt{2}(a \pm b)$ at the cusp, where $a$ and $b$ are the [1 0] and [0 1] Fourier components. We have already shown for the previous design, where only the second band is present, that the mode of the second band $1/\sqrt{2}(a + b)$ gets converted into a single plane wave, $\bar{a}$ (where $\bar{a}$ is the diffraction order that would be generated in the unpatterned slab at the interface to the PPC if the Bloch mode were uniquely composed of $a$[2]). From the discrete translational symmetry of the system and from the conservation of the lateral k-vector component we conclude that the mode of the third band has to be converted to a field of the form $\alpha\bar{a} + \beta\bar{b}$. Since the two Bloch modes $1/\sqrt{2}(a \pm b)$ are orthogonal we expect them to be converted into orthogonal fields (due to conservation of the flux, appendix A) so that

[2] $a$ is distinguished from $\bar{a}$ because even though they have the same k-vector along the interface, their k-vector component perpendicular to the interface is different.

the third band should be converted into $\bar{b}$. The effect of the adiabatic transition then takes the form of a change of base. Without the transition, a single plane wave would excite both bands with limited efficiency. With the adiabatic transition a single plane wave will excite a single band, with an insertion efficiency close to 1. This is confirmed by the band diagrams (figure 5.22).

### 5.3.3 Constraints due to the light cone

The calculations in the last section were made with 2D FDTD that does not account for radiative losses of modes inside the light cone. Thus, in order to apply the calculations to a real device, an additional constraint has to be added to ensure that the modes are outside the light cone. For a given lattice constant ($a$), slab thickness ($t$), minimum hole size ($r_{\min}$) and maximum hole size ($r_{\max}$), we derive the frequency range in which modes are *outside the light cone* at any point of the adiabatic transition and in which *the EFCs of the second band are closed contours* with corners inside of the $1^{\text{st}}$ BZ. Ideally one would like to ramp down the hole size from $r_{\max}$ to zero inside the adiabatic transition. This is not realistic from a fabrication point of view. Also we found that for $r_{\min} = 0$ and $r_{\max} = 0.3a$ it is extremely difficult to find geometries for which the useful frequency range is not empty. In the numerical examples shown below we assume $r_{\min} = 0.1a$ and $r_{\max} = 0.2a$.

First, we derive the constraint that ensures Bloch modes are below the light line. This constraint is the most restrictive for the highest frequency at which the demultiplexer is utilized ($f_{\max} = c_0/\lambda_1$), at which the light cone has the widest cross section and the EFC is the smallest. Furthermore this constraint is also the most restrictive in the region of the adiabatic transition where the hole size is the smallest. This is due to the fact the size of the EFC shrinks with decreasing hole size ($2^{\text{nd}}$ Band). The radius of the light cone is then $2\pi n_{\text{cladd}}/\lambda_1$ (where $n_{\text{cladd}}$ is the refractive index of the cladding). The radius of the EFC *before folding back* into the $1^{\text{st}}$ BZ is $2\pi n_{\text{eff}}/\lambda_1$. Here $n_{\text{eff}}$ is the modified effective index corresponding to the smallest hole size $(1-\pi(r_{\min}/a)^2)n_{\text{slab}}+\pi(r_{\min}/a)^2 n_{\text{cladd}}$ (where $n_{\text{slab}}$ is the effective index of the unperturbed slab). The condition for the cusp of the folded-back EFC to be on the light cone can then be obtained after some derivations as

$$\lambda > \lambda_1 = \frac{a}{\sqrt{2}}\left(\sqrt{2n_{\text{eff}}^2 - n_{\text{cladd}}^2} + n_{\text{cladd}}\right) \tag{5.18}$$

This corresponds to the cusp of the EFC to be exactly on the light cone and to the rest of the EFC to be inside the light cone. As modes on the side of the EFC are also used (in particular at $\lambda_1$ and at $\lambda_2$, the extremum of the demultiplexion range) this restriction needs to be reinforced a little, depending on how far the modes deviate from the center of the cusp. Furthermore this relation assumes that the EFC is derived from a simple umklapp process and ignores higher order deformations of the EFC. In particular it ignores the rounding of the cusp induced by anticrossing. This is another reason why relation 5.18 is an optimistic estimate.

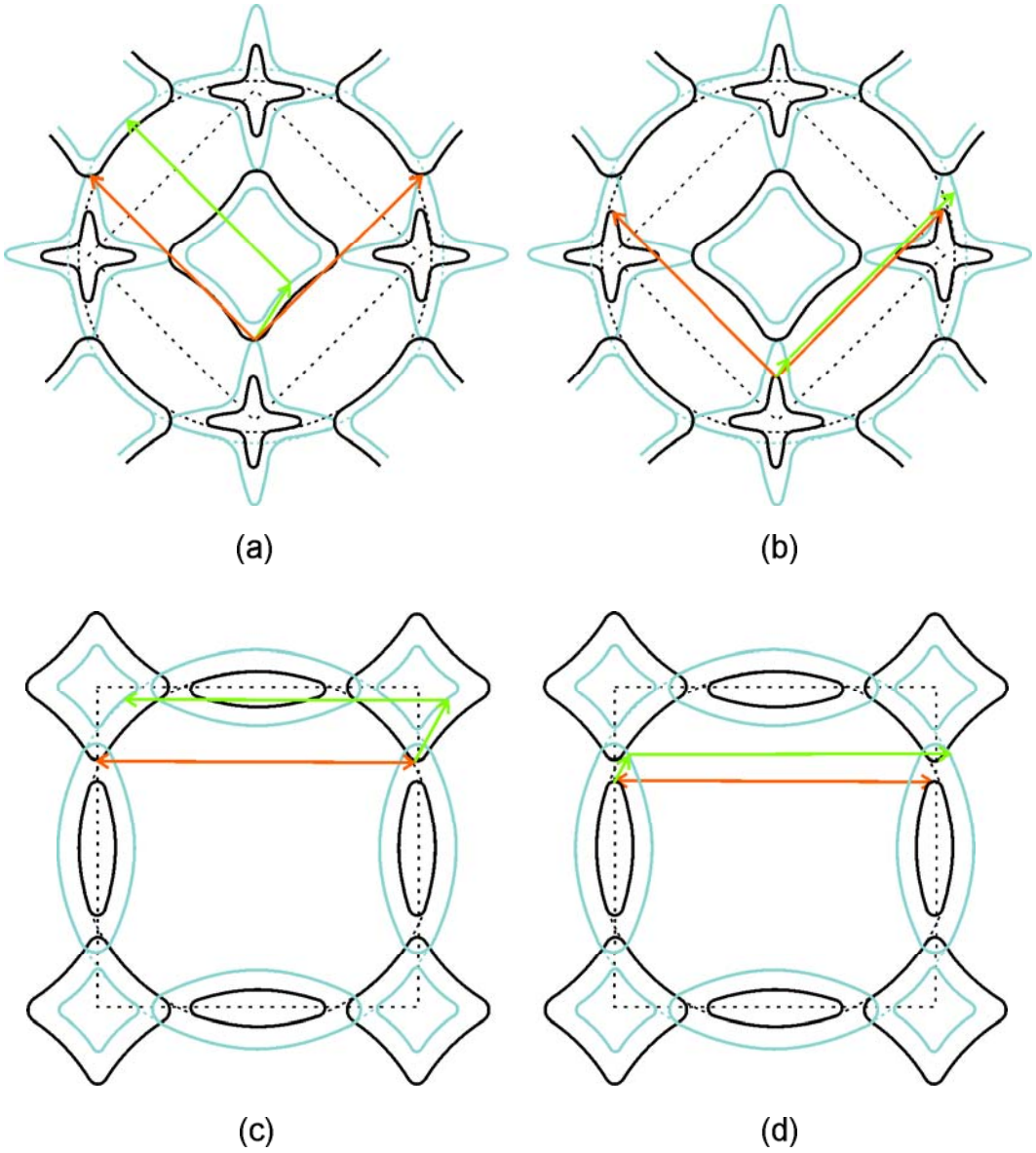


Figure 5.22: These schematics illustrate how the adiabatic transition behaves when several photonic bands are present in the same frequency range, which is for example the case when the holes defining the crystal are small. (a) and (b) illustrate the case when the $2^{nd}$ and $3^{rd}$ bands are present, while (c) and (d) illustrate the case when the $1^{st}$ and $2^{nd}$ bands are present. The black contours represent the EFC of the bulk crystal, while the grey contours represent the EFC for smaller holes, at some point inside the adiabatic transition. The red arrows indicate the dominant Fourier components of the cusp modes of the bulk crystal. In all the illustrated cases there are two dominant components that carry an equal fraction of the total power. The green arrows illustrate the mechanism underlying the adiabatic transition. The first green arrow represents the slanted projection from the bulk EFC to the modified EFC. The cusp modes are projected onto modes of the modified crystal that have a single dominant Fourier component. This Fourier component is indicated by the second green arrow. (a) and (b) show the mechanism respectively for the $2^{nd}$ and $3^{rd}$ band (in the frequency range where both bands are present), and (c) and (d) show the mechanism respectively for the $1^{st}$ and $2^{nd}$ band, for a lower frequency range where these latter bands are present. The situation shown by (c) and (d) is not encountered in a bulk crystal with a complete band gap; however, it will occur inside the adiabatic transition. For all the depicted examples, when there are two bands present that are mode-matched at the same time, these bands are converted to different plane waves so that cross talk between the photonic bands is not an issue.

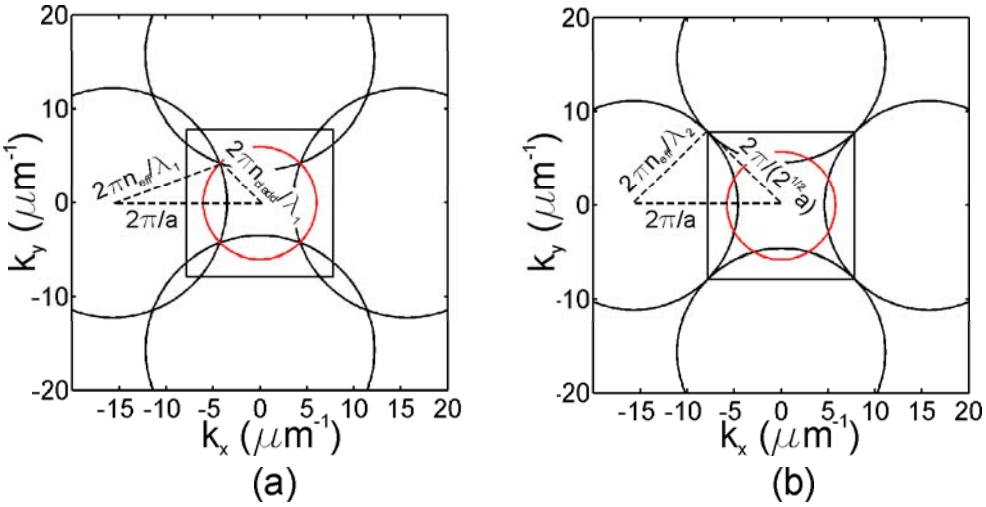


Figure 5.23: These schematics show the geometric constructions that lead to equations 5.18 and 5.19. In both (a) and (b) the black circles represent the higher order Fourier components generated by the periodic array of holes (see section 5.1). The EFC of the 2$^{\text{nd}}$ band is assumed to be the squarish shape formed by the intersection of those circles inside the 1$^{\text{st}}$ BZ (the latter is represented by a black square). This approximation ignores higher order deformations of the EFC, in particular the rounding of the corners induced by anticrossing. In (a) the corner of the EFC is on the light cone (shown in red) so that any further frequency increase would lead the corner to be inside the light cone. In (b) the corner of the EFC is at the corner of the 1$^{\text{st}}$ BZ so that any further frequency decrease would transform the EFC into four disconnected contours.

A second constraint enforces that the EFC is a closed contour inside the 1$^{\text{st}}$ BZ and has a cusp. This time the constraint is the most restrictive at the lowest frequency $f_{\min} = c_0/\lambda_2$ and for the biggest hole size. We obtain

$$\lambda < \lambda_2 = a\bar{n}_{\text{eff}}\sqrt{2} \tag{5.19}$$

where $\bar{n}_{\text{eff}}$ is the modified effective index corresponding to the biggest hole size $(1-\pi(r_{\max}/a)^2)n_{\text{eff}} + \pi(r_{\max}/a)^2 n_{\text{cladd}}$. For example for a square lattice PPC with parameters $a = 0.46$ $\mu$m, $\mathbf{t = 205\ nm}$, $r_{\min} = 0.1a$, $r_{\max} = 0.2a$ etched into a silicon slab cladd by silicon dioxide, $n_{\text{slab}} = 2.757$ at 1.54 $\mu$m, $\boldsymbol{\lambda_1 = 1.542\ \mu m}$ and $\boldsymbol{\lambda_2 = 1.584\ \mu m}$. For a square lattice PPC with parameters $a =$ 0.4 $\mu$m, $\mathbf{t = 300\ nm}$, $r_{\min} = 0.1a$, $r_{\max} = 0.2a$, $n_{\text{slab}} = 3.006$ at 1.54 $\mu$m, $\boldsymbol{\lambda_1 = 1.519\ \mu m}$ and $\boldsymbol{\lambda_2 = 1.587\ \mu m}$. The useful frequency range is 1.6 times wider for the thicker slab. Thus it is preferable to design a SP in the thickest possible slab that still results in a single mode PPC when the second band is used.

Figure 5.23 shows the geometrical constructions that lead to constraints 5.18 and 5.19. The formulas derived above hold for a square lattice PPC and need to be modified for a triangular lattice.

In chapter 7 a superprism that incorporates the adiabatic transition is implemented and experimentally characterized. To avoid the stringent constraints derived above, the 1$^{\text{st}}$ band rather than

the $2^{nd}$ photonic band will be used. In fact all the concepts derived so far can also be applied to the third band. This is illustrated by figure 5.22 for the adiabatic transition. We have also shown in chapter **3** that in the "bulk" region of the bands, i.e., away from the band-gap, the first and second band have a very similar structure given the right geometric transformation (rotation and rescaling).

# Chapter 6

# Enhancing the frequency resolution of the superprism

In this chapter we address the issue of superprism compactness versus frequency resolution. In section 6.1 we describe the limitations first derived by T. Baba and T. Matsumoto in ref. [38]. In the following two sections we show an alternate geometry that overcomes these limitations [41]. In the analysis conducted in section 6.1, beam broadening inside the PC is in competition with beam steering and limits the frequency resolution. Indeed, the criterion to demultiplex two frequencies is for the corresponding beams to be spatially separated at the output edge of the PC. If the beams broaden inside the PC, more beam steering is necessary to separate them. In the geometry introduced in section 6.3, instead of terminating the incoming waveguide right at the boundary of the PC, the waveguide is terminated some distance before the PC. Thus the beam broadens in the unpatterned slab before entering the PPC. The PPC is designed for the beam to propagate with a negative effective refractive index [58]. Thus, instead of further broadening inside the PPC, the beam can be refocused. The expansion distance in the unpatterned slab (the distance between the end of the waveguide and the beginning of the PPC) is chosen so that the positive refraction in the slab and the negative refraction in the PPC can compensate each other. If the SP is laid out in such a way, beam broadening inside the PPC does not limit the SP resolution, and the limitations introduced in section 6.1 do not hold. In particular, compensating for the beam broadening modifies the scaling law of the resolution. While the model derived in 6.1 predicts $(\Delta\lambda/\lambda)^{-1} \propto \sqrt{L}$, the modified geometry leads to $(\Delta\lambda/\lambda)^{-1} \propto L$. In sections 6.2 and 6.3 we use the same PPC geometry as in section 5.3. In section 6.2 we show under which conditions this crystal supports quasi-negative refraction, and in section 6.3 we show how negative refraction inside the PPC can be used to enhance the SP resolution.

## 6.1 Usual limitations of the frequency resolution

In this section we derive limitations of the SP resolution that were first derived by T. Baba and T. Matsumoto in [38]. It describes in a formal way the competition between beam broadening and beam steering inside the PPC. The derivation assumes that the beam is transform limited at the input boundary of the PPC. It is important to keep this assumption in mind, as we will show that it does not necessarily lead to the best resolution for certain PPC geometries. Indeed we will show in section 6.3 that better resolution can be achieved in certain cases by first broadening the beam in the unpatterned slab prior to the PPC.

First we will define "transform limited". This concept is most often found in relation to the time domain, i.e., references to "transform limited pulses" is often found. If a train of pulses is analyzed with an optical spectrum analyzer, the *power* spectrum of the pulses is available; however, the *phase information* is lost. That is, we know how the power is distributed between wavelengths; however, the relative phase between the various frequencies is not accessible. Due to this missing phase information, we cannot directly deduce the temporal pulse width without making additional assumptions. However, there are assumptions on the phases that minimizes the pulse width. That minimum pulse width is called the transform limited width because it is not limited by the relative phases but by the distribution of the power spectrum. This concept can also be applied to beam widths and *spatial* Fourier transforms. The cross section of a beam can be Fourier transformed, and the power spectrum of the Fourier transform can be derived. A beam width is said to be transform limited if it is the minimum beam width for all possible assumptions on the relative phases. The concept of transform limitation is very powerful for the analysis of the SP. Indeed in all the geometries investigated below, the SP has two parallel interfaces. The discrete translation symmetry along these interfaces is never broken so that the power spectrum of the k-vector distribution is conserved throughout the device (modulo $2\pi/A$, where $A$ is the periodicity of the interface). This conservation law corresponds to a generalized Snell's law introduced in chapter 2. Beam broadening, beam refocusing and beam steering are only a function of the relative phases. This is for example not the case with conventional lenses that have curved interfaces. Indeed a lens can focus a plane wave (as such transform limited) to a tiny spot.

In order to predict how light coupled from the waveguide propagates inside the PPC the generalized Snell's law is applied, i.e., the projection of the k-vector onto the interface is conserved modulo $2\pi/A$ (chapter 2). The incoming light has a finite beam width. Thus it corresponds to a finite-width distribution of k-vectors. We start by considering uniquely the center component of the k-vector distribution, i.e., we start out the analysis by ignoring beam broadening. In a configuration as in figure 2.8, the projection of the k-vector of the incoming beam is $2\pi n_{\mathrm{WG}}\sin(\theta)/\lambda$, where $\theta$ corresponds to the waveguide orientation and $n_{\mathrm{WG}}$ is the effective index of the waveguide. As explained

in chapter 2, the Bloch mode that is coupled to can be determined from the fact that the projection of its k-vector onto the interface has to take the same value modulo $2\pi/A$. The correspondence between the frequency and the reduced k-vector of the Bloch mode can be represented by a curve $\vec{k}(\omega)$ inside the 1$^{\text{st}}$ BZ of the PPC. The Bloch modes along that curve have varying group velocities, which in turn leads to the frequency dependent direction of propagation and to the SP effect. In the following, we will refer to $\vec{k}(\omega)$ as the "coupling point".

The frequency dependence of the group velocity can be broken down into two factors. On the one hand, the magnitude of the k-vector of the incoming light changes, i.e., the magnitude of $2\pi n_{\text{WG}}\sin(\theta)/\lambda$ is modified. This would lead to another portion of the EFC to be coupled to, even if the shape of the EFC had not any frequency dependence. This can be referred to as a "frequency dependent sampling" the EFC. On the other hand, the EFC changes shape with frequency. This could lead to a change of the group velocity even if the magnitude of $2\pi n_{\text{WG}}\sin(\theta)/\lambda$ stayed constant. Of course both effects occur at the same time, and it might seem a bit arbitrary to separate them. However, as shown below, there are cases where one of them is dominant. In the context of this chapter it is important to distinguish between them. Indeed, we will show that if sampling of the EFC is the dominant effect, beam broadening necessarily also has an important role. In this case the analysis of sections 6.2 and 6.3 is very relevant as it shows how to compensate for beam broadening. If the deformation of the EFC is dominant, and if it consists in the change of orientation of an otherwise flat portion of the EFC, there can be frequency dependent beam steering and self-collimation at the same time so that beam broadening is not an issue. Nevertheless, the 1$^{\text{st}}$ case can be very attractive because of very strong beam steering and because the beam broadening can be compensated, as we will show in 6.3.

We will now proceed by explaining how beam broadening has been taken into account in reference [38]. The derivations assume that the waveguide is terminated right at the boundary of the PC. Waveguide modes are often approximated by a transform limited Gaussian (or more precisely the cross section of a waveguide mode is often approximated by the waist of a Gaussian beam). Thus in the following it is assumed that a transform limited Gaussian beam is coupled into the PC.

We assume the *amplitude* of the beam to have a cross section of the form $A \cdot \exp(-x^2/\sigma^2)$ at the input boundary of the PC. The width of the beam is then defined as $W_0 = 2\sigma$. As already mentioned in chapter 2, the beam would then have an angular divergence $2\lambda/\pi n_{\text{slab}} W_0$ inside the unpatterned slab. As explained above, for a given frequency, the angle of propagation inside the PC ($\alpha_{\text{PC}}$) can be determined from the angle of propagation inside the unpatterned slab ($\alpha_{\text{slab}}$). In order to relate the beam broadening inside the PC to the beam broadening inside the slab we introduce the parameter $p$ defined as $p \equiv \partial\alpha_{\text{PC}}/\partial\alpha_{\text{slab}}$. After propagation for a distance $L$ through the PC, the beam is broadened to the width

$$W = \frac{4\lambda L}{\pi n_{\text{slab}} W_0} p \tag{6.1}$$

This corresponds to the beam broadening that would have occured in the slab, multiplied by $p$ to take into account the modified propagation inside the PPC. It is valid if the propagation length inside the PPC is longer than the Raleigh length (in other words, this formula describes the broadening correctly if the final width is significantly larger than the initial width). This is given by the condition

$$L > \frac{\pi n_{\text{slab}} {W_0}^2}{4\lambda} \frac{1}{p} \tag{6.2}$$

In order to achieve demultiplexion, the displacement due to beam steering has to be larger than beam broadening. The displacement due to beam steering is given by $\partial\alpha_{\text{PC}}/\partial(a/\lambda) \cdot a\Delta\lambda/\lambda^2 \cdot L = qaL\Delta\lambda/\lambda^2$ where $q \equiv \partial\alpha_{\text{PC}}/\partial(a/\lambda)$. The resolution $(\Delta\lambda/\lambda)^{-1}$ then takes the form[1]

$$\left(\frac{\Delta\lambda}{\lambda}\right)^{-1} = \frac{\pi a n_{\text{slab}} W_0}{4\lambda^2} \frac{q}{p} \tag{6.3}$$

The analysis given in ref. [38] stops at this point. However the resolution is given in terms of $W_0$, rather than in terms of the SP dimension ($L$). The latter is an important relation as it gives the *scaling law* of the resolution of the SP as a function of its size. In order to resolve $\Delta\lambda/\lambda$ the beam steering has to be at least wider than the initial beam width $W_0$. This leads to

$$\frac{qaL}{\lambda}\left(\frac{\Delta\lambda}{\lambda}\right) > W_0 \tag{6.4}$$

By combining equations 6.3 and 6.4 we obtain

$$\left(\frac{\Delta\lambda}{\lambda}\right)^{-2} = \frac{\pi a^2 n_{\text{slab}}}{4\lambda^3} \frac{q^2}{p} L \tag{6.5}$$

Thus the resolution of the SP goes as the square root of its length. The beam displacement does increase in a linear fashion with the length of the SP; however, in order to increase the resolution $W_0$ has also to be increased. This is why the linear increase of the beam displacement does not lead to a linear increase of the resolution. The object of this chapter is to design a geometry where the beam is refocused, and where beam broadening is thus not an issue. We will show that in this way a *linear* scaling law of the resolution can be recovered.

The SP described in section 5.3 relies on the cusp of the EFC to achieve demultiplexion (as shown in figure 5.17(b)). Light is coupled to different points of the cusp depending on the frequency. In particular light is first coupled to one side of the cusp and then to the other side. In the process, the direction of propagation undergoes a near to $90^o$ change. This scheme relies mostly on sampling the EFC at different points rather than on a deformation of the EFC (in this case the

[1] There is a difference in notations compared to ref. [38] because we defined $W_0$ as $2\sigma$ in order to keep coherent notations with the rest of this thesis and with ref. [41].

deformation of the EFC even works against the dominant beam steering mechanism, see chapter 7). The sampling of the EFC is accelerated by the steep injection angle $\theta = 60.95^o$ of the incoming waveguide ($dk = 2\pi n_{\mathrm{WG}} \sin(\theta) d(1/\lambda) \propto \sin(\theta)$). This is another benefit of coupling through higher order BZs as it leads to a higher injection angle.

A superprism where the frequency dependence of the group velocity is dominated by the deformation of the EFC can be found in [35]. Compared to the previous case, light stays much more collimated inside the PC due to the fact that it is coupled to a rather flat section of the EFC. The direction of the group velocity changes with frequency because the orientation of the EFC changes. However in this case the available angular swing is of the order of $20^o$ and is much smaller than the swing available in the region of the cusp ($\sim 90^o$ for a square lattice). This would make the latter type of SP very attractive if the difficulties related to beam broadening could be resolved. This is the topic of the next two sections.

## 6.2 Negative effective index of the superprism

In the following two sections computations are made for the same lattice as in section 5.3, that is, a square lattice 2D PC etched into silicon with silicon dioxide backfilling the holes, a lattice constant of 0.4 $\mu$m and a hole radius of 0.12 $\mu$m. In this section we examine under which conditions quasi-negative refraction (chapter 2) can be associated to the cusp of the EFC.

Figure 6.1(a) shows the band-diagram for this crystal along the $\Gamma$M direction, and figure 6.1(b) shows the EFC of the 2$^{\mathrm{nd}}$ photonic band at the free-space wavelength $\lambda = 1.54$ $\mu$m. In the corner-region, the group-velocity $\vec{\nabla}_{\vec{k}}\omega$, perpendicular to the contour, undergoes a strong shift in direction. In a small k-space region around the cusp this shift in direction can be characterized by a single number. The rounded corner can be approximated as an arc of a circle as shown in figure 6.1(b). The radius of that circle is approximately $0.3 \cdot 2\pi/1.54$ so that the diffraction of a Gaussian beam can be predicted inside the PC by an effective index of $-0.3$, provided the range of k-vectors of the beam is restricted to the corner-region approximated by the arc. The negative sign in the effective index comes from the fact that the group velocity points inside the circle. Negative refraction and superlensing have been experimentally investigated in a similar geometry by E. Cubucku et al. in ref. [58].

In the next section we will show that negative refraction in the PC and positive refraction in the unpatterned slab can compensate each other so that a beam diffracting in the slab can be deflected and refocused at the same time inside the PC. In such a way cross talk induced by beam broadening is suppressed.

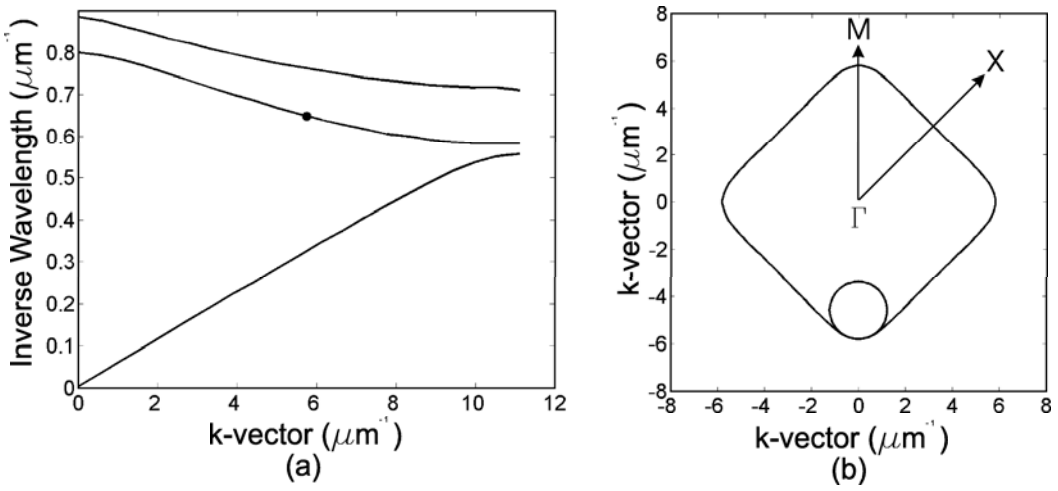


Figure 6.1: (a) Band-diagram showing the first three TE photonic bands along the ΓM direction. The black dot corresponds to $\lambda = 1.54$ $\mu$m. The lattice-constant of the PC was chosen for the 2$^{\text{nd}}$ band to be the only one present in the frequency range of interest (C-band). (b) shows the EFC of the 2$^{\text{nd}}$ band for $\lambda = 1.54$ $\mu$m. The contour has a squarish shape with rounded corners. The corners can be approximated by the arc of a circle with a radius of $0.3 \cdot 2\pi/1.54$. Thus Gaussian beams with a distribution of k-vectors restricted to that k-space region diffract inside the PC as if they were in a material of refractive index -0.3.

## 6.3 Resolution enhancement with help of negative refraction

Here we examine the situation where the waveguide stops some distance before the interface so that the beam diffracts inside the unpatterned slab before coupling into the PC. As shown in the previous section, the propagation inside the PC is determined by a quasi-negative index of refraction so that diffraction inside the unpatterned slab and inside the PC can compensate each other. If the diffraction length in the unpatterned slab is adequately chosen, the beam can be nearly transform-limited at the output facet of the PC. The impact of beam-broadening on the superprism resolution can then be neglected. There is still a price to pay in the form of chip space necessary to expand the beam. However the chip space needed to expand the beam is of the same order as the chip space needed for the PC (see chapter 7 and figure 7.1 for a concrete example). Furthermore we will show that with this scheme the resolution scales linearly with the device size (comprising both the PC and the slab region), while without it the resolution scales with the square root of the device size.

In the following we derive the diffraction length in the slab ($d_{\text{slab}}$) necessary to compensate for the diffraction inside the PC ($d_{\text{PC}}$). If the PC is mode matched with the adiabatic transition introduced in section 5.3, the width of the transition has to be split in some way between $d_{\text{slab}}$ and $d_{\text{PC}}$ that we do not quantify here; however, in a real device the width of the adiabatic transition would be much smaller than both the width of the bulk part of the PC and the diffraction length inside the slab so that it can be neglected. As shown in figure 6.2, $d_{\text{PC}}$ is the width of the PC (because we

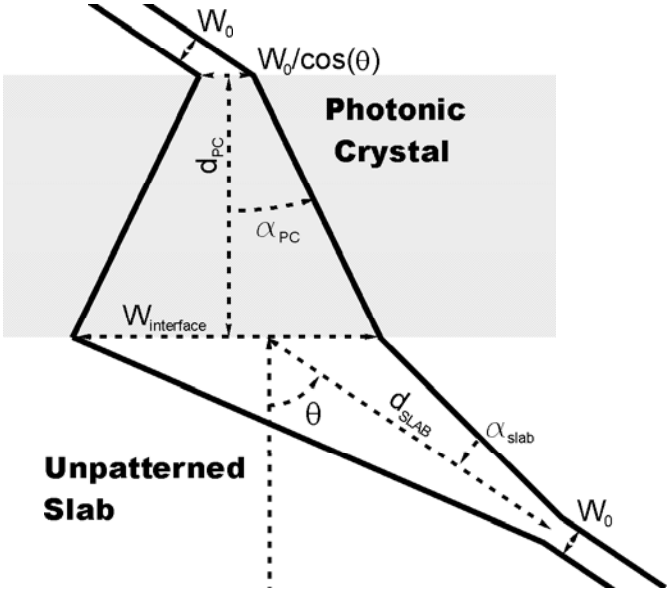


Figure 6.2: This figure is a schematic of the beam-expansion inside the unpatterned slab and inside the PC. The lengths and angles are labeled for reference in the text.

optimize $d_{\text{slab}}$ for the wavelength at which light propagates in the [2 1] direction normal to the [1 -2] interface), and $d_{\text{slab}}$ is the distance over which the beam is propagated inside the slab. We assume the beam to be a transform-limited Gaussian beam at the output edge of the waveguide and we aim for a transform-limited Gaussian beam at the exit of the superprism. The width of the beam at the end of the waveguide is $W_0$ (as in 6.1 the width of the beam is defined as $2\sigma$, where the functional dependence of the amplitude along the cross-section of the beam is given by $\exp(-x^2/\sigma^2)$). The diffraction angle inside the unpatterned slab is $\alpha_{\text{slab}} = 2\lambda/(\pi n_{\text{slab}} W_0)$ so that the width of the beam at the input interface of the superprism is $W_{\text{interface}} = 2tan(\alpha_{\text{slab}}) d_{\text{slab}}/\cos(\theta)$. The additional $1/\cos(\theta)$ factor comes from the fact that the interface of the PC makes an angle $\pi/2 + \theta$ with the direction of propagation of the beam (instead of $\pi/2$ as would usually be expected for a cross section). The width of the transform-limited beam at the output facet of the PC should also be $W_0$ as the power spectrum is conserved throughout the device. The width of the beam *along* the output facet should then be $W_0/\cos(\theta)$. The beam propagates along the normal to the interface inside the PC so that the relevant width to evaluate the diffraction angle inside the PC is $W_0/\cos(\theta)$ and not $W_0$. The diffraction angle inside the PC is then derived to be $\alpha_{\text{PC}} = 2\lambda\cos(\theta)/(\pi n_{\text{PC}} W_0)$. The size of the beam at the input facet of the PC can also be expressed as $W_{\text{interface}} = 2tan(\alpha_{\text{PC}}) d_{\text{PC}}$. By

equating the two expressions for $W_{\text{interface}}$ we obtain the equation

$$\tan(\frac{2\lambda\cos(\theta)}{\pi n_{\text{PC}} W_0}) d_{\text{PC}} = \tan(\frac{2\lambda}{\pi n_{\text{slab}} W_0}) d_{\text{slab}} \frac{1}{\cos(\theta)} \tag{6.6}$$

Because the Gaussian beam expanding in the slab is cut at an angle $\theta$, the beam-profile along the interface of the PC is not exactly Gaussian. As a consequence the beam is not exactly Gaussian inside the PC. Thus the model exposed above is an approximation in that it derives the expansion angle inside the PC as if the beam were Gaussian. To further validate equation 6.6, we investigated the dependence of the width of the beam exiting the PC as a function of $d_{\text{slab}}$ without making this approximation. We use a simple beam propagation code based on a scalar description of the field and an effective index approximation inside the PC. As above, the effective index approximation is only valid for a beam with a small enough k-vector distribution to be completely contained within the rounded part of the cusp. At the boundaries of the PC an extra transformation has to be operated on the field. Indeed, inside the PC light is described by an effective k-vector that corresponds to the offset between the center of the circle approximating the cusp of the EFC and the reduced k-vector of the Bloch-mode. Light with a lateral k-vector of $k_{\text{cusp},\|} + m2\pi/A$ is in fact at the center of the cusp and propagates inside the PC as if it had a 0 lateral k-vector in a material of index $n_{\text{PC}}$. At the input boundary $m2\pi/A$ (where $m$ is the coupling parameter introduced in 5.3) has to be subtracted from the lateral k-vector ($k_{\|}$) in order to convert the k-vector into the *reduced* k-vector. Then the projection of the cusp onto the interface, $k_{\text{cusp},\|}$, has to be subtracted to compute the offset from the center of the circle. At the output boundary $m2\pi/A + k_{\text{cusp},\|}$ has to be added again before further propagation in the slab.

This model is a little more sophisticated than the simple considerations that led to equation 6.6; for example it takes into account the exact Fourier spectrum of the field rather than making Gaussian beam approximations throughout the structure. For the numerical results shown in figure 6.3 the PC is assumed to be 300 $\mu$m thick, and the FWHM of the waveguide is assumed to be 5 $\mu$m. The optimum diffraction length in the slab is then calculated to be 655 $\mu$m with equation 6.6. In figure 6.3 we show the beam profile at the input boundary and at the output boundary of the PC, as a function of $d_{\text{slab}}$. It can be seen that in this model the optimum expansion length is still given by equation 6.6.

As mentioned in the first section, the diffraction of the beam inside the PC is described by an effective index $n_{\text{PC}} = -0.3$ that is much smaller than the index of the silicon slab ($n_{\text{slab}} = 3.43$). As a consequence the beam needs to propagate a longer distance in the slab than in the PC in order for the diffraction lengths to compensate each other (section 2.3). However, due to the fact that the beam propagates inside the slab along a slanted direction, the distance between the waveguide edge and the edge of the PC ($655 \cdot \cos(\theta) = 318\mu m$) is of the same order as the width of the PC (300 $\mu$m).

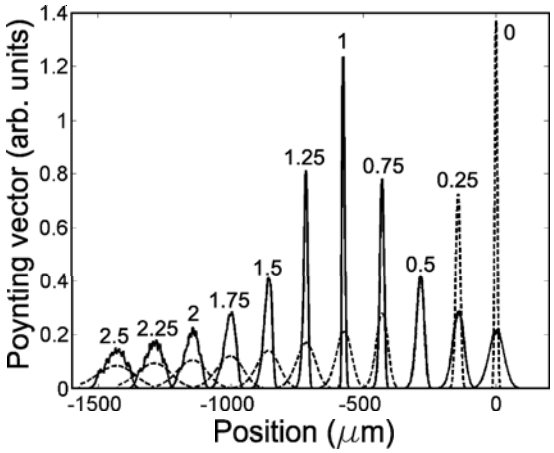


Figure 6.3: This figure shows the dependence on the expansion length inside the unpatterned slab ($d_{\text{slab}}$) of the beam width at the input (dashed line) and output (continuous line) boundaries of the PC. The beam profiles are labeled by $d_{\text{slab}}/d_0$, where $d_0$ is the optimum expansion length predicted by equation 6.6. The beam is assumed to propagate perpendicular to the PC interface inside the PC. At $d_{\text{slab}} = 0$ (that is, the waveguide terminates directly in front of the PC interface) the beam is significantly broadened at the output edge of the PC. At the optimum expansion length $d_0$ the diffraction inside the slab and inside the PC compensate each other, and the beam recovers its transform limited width at the PC output interface.

By applying equation 6.6 we also got convincing results with a full 2D FDTD simulation. We simulated the transmission through the adiabatic PC introduced in the previous section (same PC as in figures 5.20 and 5.21). We use a transform-limited beam as a light source at the input-interface of the PC in (a) and a beam that has been propagated 80 $\mu$m before hitting the interface in (b). The results are shown in figure 6.4. It can be seen that the separation between beams corresponding to different frequencies at the output of the superprism is much better in the second case. It can also be seen in the second case that the beam-profile at the output interface is very close to the transform-limited beam-profile, while it is significantly broadened in (a).

## 6.4 Modified scaling law of resolution versus device size

The frequency resolution shown in figure 6.4 is 60 nm and is quite low due to the small size of the simulated device (the PC is only 26.8 $\mu$m wide). However this can be easily resolved by making a larger device. In particular in this case the resolution scales linearly with the size of the SP rather than the square root scaling derived in section 6.1 due to the fact that beam broadening is alleviated. The difference between the case depicted here and the case depicted in section 6.1 is that here the waveguide width does not need to be increased when the SP is scaled up and the resolution increased. In both cases, for a given wavelength change the beam deflection scales linearly with the PC size. However in the case depicted in 6.1 the spacing between output waveguides becomes larger at higher

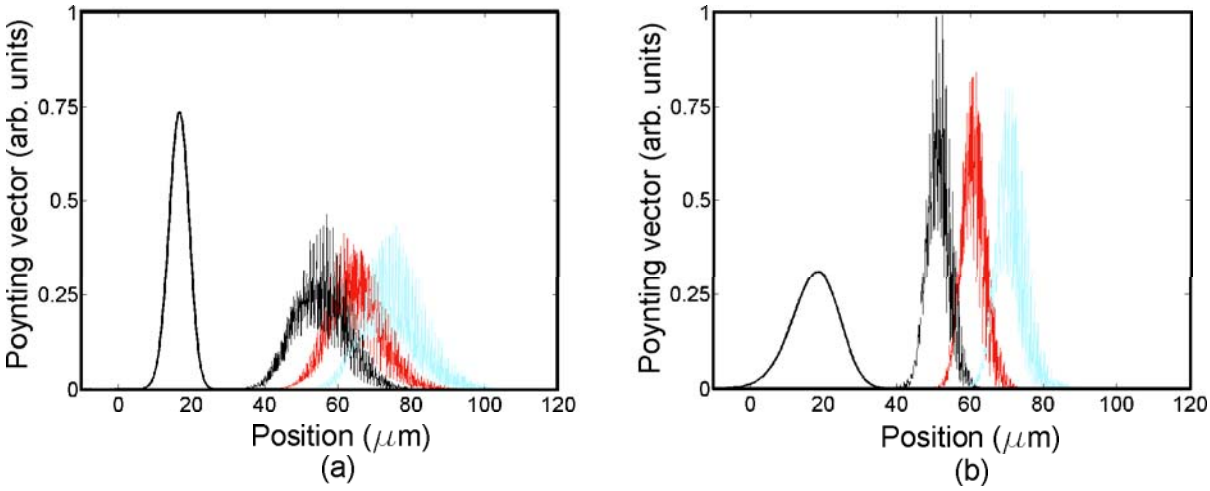


Figure 6.4: In (a) a transform-limited beam (leftmost beam) is launched inside the PC. The shape of the beam at the output of the PC is shown for the free-space wavelengths 1.6 $\mu$m, 1.54 $\mu$m and 1.48 $\mu$m (left to right). (b) shows the same data for a beam that has been propagated 80 $\mu$m inside the slab before being coupled to the PC. The leftmost beam is the cross-section of the beam at the input edge of the PC after propagation through the slab. In this case the beam is approximately transform-limited at the output of the PC. Both in (a) and in (b) the relative positions of the output beams are correct, but the input beams have been separated out, so as not to overlay too many plots.

resolutions so that the needed deflection also increases (6.3). In the case depicted in this section the length of the PC goes as $L \propto (\Delta\lambda/\lambda)^{-1}$, while in the case depicted in 6.1 we obtain $L \propto (\Delta\lambda/\lambda)^{-2}$.

In chapter 7 a particular implementation of the superprism incorporating the mechanisms depicted in this and in the previous chapter is described in detail. In particular the figure of merit for the resolution versus size is derived as a function of the frequency dependent effective index of the SP and of the deformation of the EFC, i.e., of the position of the center of the cusp and of the radius of curvature of the cusp.

# Chapter 7

# Experimental characterization of the superprism

In this chapter a superprism (SP) is designed, fabricated and measured. It incorporates the design ameliorations introduced in previous chapters. It uses an adiabatic transition to reduce insertion losses (chapter 5) [41], and the resolution of the superprism is enhanced by compensating beam broadening with the technique described in chapter 6 [41]. The only fundamental difference is that here we use the first photonic band of a square lattice photonic crystal instead of the second, in order to avoid the very limiting constraints imposed by the light cone. Indeed we have shown in chapter 3, section 3.5, that away from the photonic band gap (PBG), the band structure of the first band is almost identical (figure 7.2(a)), provided the crystal is adequately rotated and rescaled [40]. Also, the photonic crystal can be mode matched with the same adiabatic mechanism as when the $2^{nd}$ band is used (figure 5.22). Furthermore, instead of expanding the field in the slab only on one side of the PPC as in chapter 6, the expansion distance is equally split to both sides (figure 7.1(a)) as this reduces the necessary lateral extent of the PPC. Finally, the orientation of the PPC interface is taken to be along a different crystallographic orientation as in chapter 5, resulting from a trade off between pass band of the adiabatic interface and frequency sensitivity of the device. In section 7.1 we derive adequate values for all the critical design parameters from analytical expressions and from a full band diagram of the PPC. Section 7.2 describes the fabrication process used for silicon on insulator (SOI) based SPs. Next, we describe the measurement method and the on-chip grating couplers used to fiber couple light on and off the chip (section 7.3). Finally the experimental results are shown in section 7.4. The devices are etched into a 205 nm thick SOI silicon membrane (refractive index 3.43) and are clad by $SiO_2$ and polymethylmetacrilate (PMMA) (with respective refractive indeces 1.46 and 1.5). In the bulk of the PPC, the normalized hole radius is $r/a = 0.3$. $\lambda_0 = 1.538$ $\mu$m is the center wavelength of the demultiplexed wavelength range, and we aim for a 10 nm resolution, 4 channels demultiplexer.

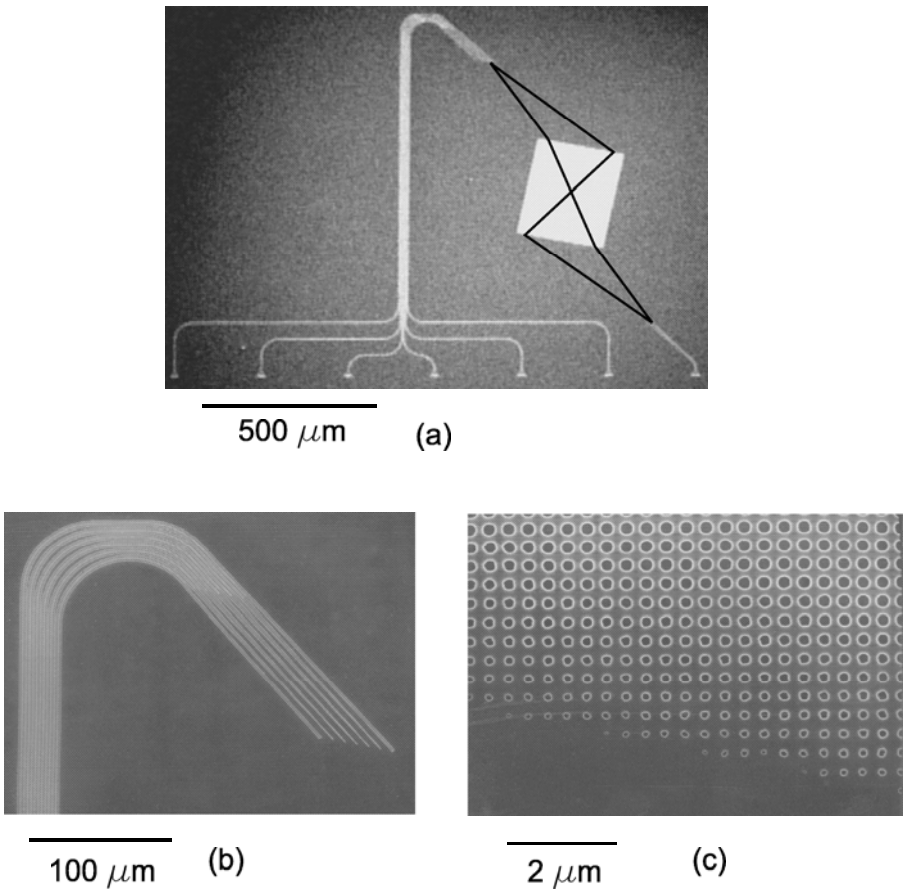


Figure 7.1: SEM micrographs of a fabricated superprism. (a) shows an overview of the device. At the bottom of the picture, seven grating couplers couple light to single mode waveguides. The rightmost grating coupler is the input port, while the six grating couplers to the left are the output ports for the various demultiplexed frequencies. The output waveguides are bundled into a tree-like structure. At the top the waveguide bundle is bent, and each individual waveguide is adiabatically tapered to the width $W_{\mathrm{WG}}$ (b). The input waveguide is also tapered to the same width. The photonic crystal can be recognized in (a) as a rotated white square. (c) shows a detailed view of the adiabatic transition at the input edge of the PC. It can be seen that the interface makes an angle $\varphi = \mathrm{atan}(1/5)$ relative to the [1 0] crystallographic direction.

## 7.1 Design parameters

In this section we will derive numerical values for the critical design parameters that determine the device geometry. The last two chapters were aimed at demonstrating the concepts involved in the SP design, while this section only briefly goes through the calculations for the specific implementation demonstrated in this chapter. However the constraints on the SP design are exhaustively covered. The reader will find this section useful when attempting to reproduce or improve the experimental results. The important design parameters are

- The lattice constant (**a**).
- The incident angle of the waveguides onto the SP ($\theta$).
- The (tapered) width of the waveguides[1] ($\mathbf{W_{WG}}$).
- The width of the PPC ($\mathbf{d_{PC}}$).
- The expansion length ($\mathbf{d_{slab}}$).
- The width of the adiabatic transition.

**Lattice constant:** $\theta$, $d_{\mathrm{PC}}$ and $d_{\mathrm{slab}}$ are represented in figure 6.2. As in the previous chapter, $n_{\mathrm{WG}}$ and $n_{\mathrm{PC}}$ denote the effective indeces of the waveguide and of the PPC, where $n_{\mathrm{PC}}$ is derived from the curvature of the rounded EFC corner. For the beam to be correctly refocused into the outgoing waveguides, equation 6.6 has to hold over the whole demultiplexed frequency range. To the first order (by linearizing the tangents), this imposes

$$\frac{dn_{\mathrm{PC}}}{n_{\mathrm{PC}}} = \frac{dn_{\mathrm{slab}}}{n_{\mathrm{slab}}} \tag{7.1}$$

We derived the frequency dependence of $n_{\mathrm{PC}}$ from a full band diagram and found that it has very high derivatives near the M and $\Gamma$ high symmetry points, but has a maximum at a k-space point near the center of $\Gamma$M (figure 7.2(b)). We found that for a lattice periodicity $a = 0.37$ $\mu$m, $n_{\mathrm{PC}}/n_{\mathrm{slab}}$ stayed within half a percent of its mean value in the wavelength range $\lambda \in [1.5\ \mu\mathrm{m},\ 1.58\ \mu\mathrm{m}]$.

**Incident waveguide angle:** As we use the first band in this chapter, the crystallographic directions reported in chapters 5 and 6 have to be rotated by 45° to apply (this transformation is introduced in section 3.5). In chapter 5 we have shown that for the adiabatic transition to work, the interface of the PPC cannot be along the "natural" crystallographic direction. Here the interface of the PPC has to be rotated away from the [1 0] direction. We chose the interface to

[1] The waveguide width $W_{\mathrm{WG}}$ corresponds to the width of the waveguide as drawn, while the notation $W_0$ used in previous chapters corresponds to $2\sigma$, see equations 2.9 to 2.11. As the FWHM of the first mode of wide dielectric rectangular waveguides is close to $W_{\mathrm{WG}}/2$ (figure 7.6) they can be related by $W_{\mathrm{WG}} = \sqrt{2\log(2)}W_0$.

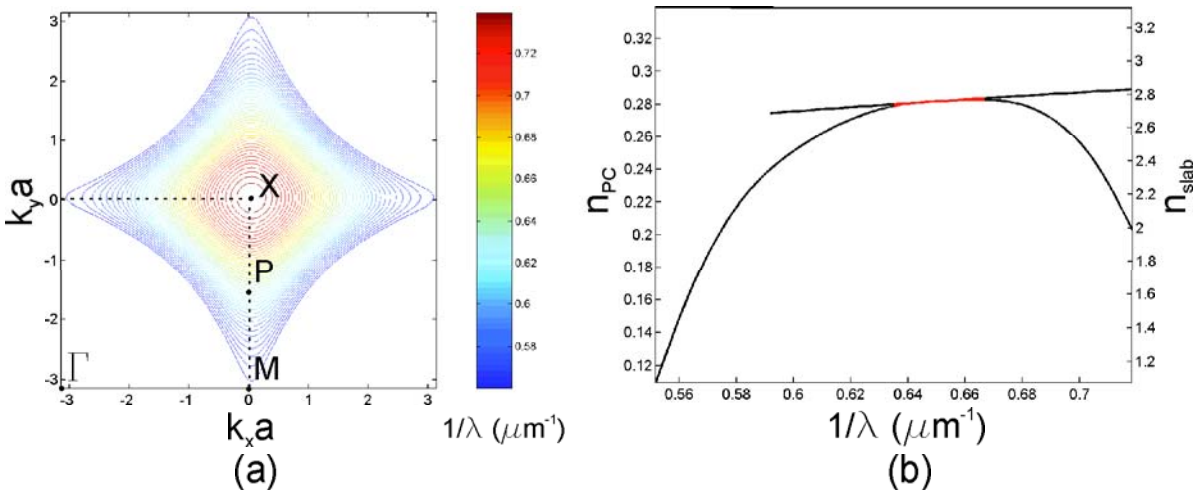


Figure 7.2: (a) shows the EFCs of the first band of the PPC, in the wavelength range [1.34 $\mu$m 1.78 $\mu$m] for which they feature a squarish shape. To show the similarities with the EFCs of the second band we didn't represent the contours in the 1$^{st}$ BZ, but in a section of Fourier space centered on the high symmetry point X (the lower left corner of the diagram delimited by the dashed lines belongs to the 1$^{st}$ BZ). P is the k-space point to which light from the waveguide couples at the wavelength $\lambda_0$. It is located on XM. (b) shows the effective index of the waveguide (upper curve, right axis) and of the PPC (lower curve, left axis). The red section of the curves corresponds to the wavelength range $\lambda \in$ [1.45 $\mu$m, 1.64 $\mu$m]. It can be seen that although the PC negative effective index undergoes strong variations, it stays roughly proportional to the slab index in that frequency range.

be along [5 -1] so that it makes an angle $\varphi = \text{atan}(1/5)$ with the [1 0] direction[2]. The adequate incident waveguide angle can then be deduced by projecting the cusp of the EFC (P) at the center frequency $c/\lambda_0$ onto the interface ($k_{||}$) and by matching it to the projection of the waveguide k-vector. The interface is oriented along the [cos($\varphi$) -sin($\varphi$)] crystallographic direction. $\vec{\Gamma P} = \vec{\Gamma M} + \vec{MP} = \pi/a \cdot [-1\ 0] + \text{MP} \cdot [0\ 1]$, which results in $k_{||} = -\cos(\varphi)\pi/a - \text{MP}\sin(\varphi)$. By projecting the k-vector of the incoming waveguide mode onto the interface we obtain $k_{||} = -2\pi n_{\text{slab}}\sin(\theta)/\lambda_0$. The value of MP is derived from the full band diagram to be $5.32\mu m^{-1}$ (figure 7.2(a)) so that we obtain $\theta = 55^{\text{o}}$. This procedure is described in detail in chapter 5, in particular the reader will find a graphical representation of the projections.

**Orientation of the PPC interface:** The choice of $\varphi$ is not arbitrary, but is also carefully optimized. As the mode matching mechanism inside the adiabatic transition relies on a slanted projection of the k-vector (chapter 5), its frequency and angular pass bands are wider if $\varphi$ is bigger. However a large $\varphi$ reduces the resolution of the superprism. Indeed the wavelength dependence of the projection of the waveguide k-vector onto the interface is given by $2\pi n_{\text{slab}}\delta\lambda\sin(\theta)/\lambda^2$, while the wavelength dependence of the projection of the cusp of the EFC is given by $-\sin(\varphi)(\partial\text{MP}/\partial\lambda)\delta\lambda$. To

[2]Here $\phi$ is smaller than the angle used in chapter 5 for the reason that in the latter the focus was on the optimization of the adiabatic transition, while here a compromise is being made between frequency resolution and the pass band of the mode matching mechanism

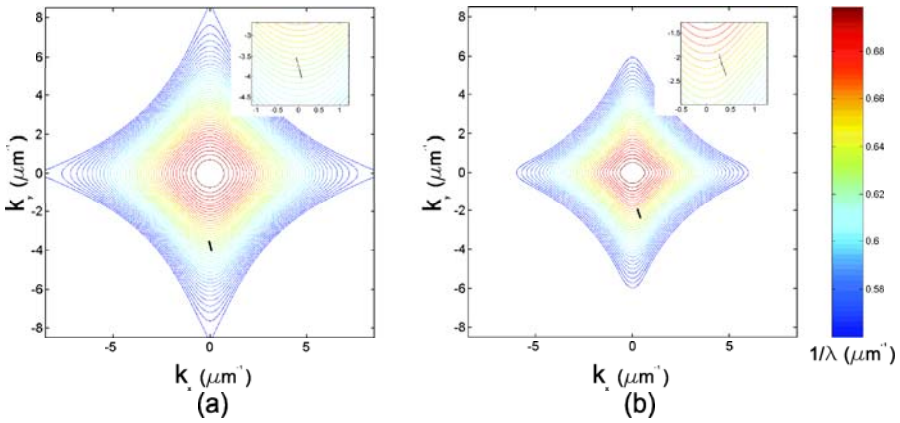


Figure 7.3: (a) EFCs for the bulk PPC ($r/a = 0.3$) for $\lambda \in$[1.34 $\mu$m 1.78 $\mu$m]. The black line shows the modes to which the waveguide couples to for $\lambda \in$[1.518 $\mu$m 1.558 $\mu$m]. (b) shows the same data for the lattice with the smallest hole size ($r/a = 0.15$). The EFCs are smaller, and the black line is completely to the right of the cusp, so that the pass band of the adiabatic transition should encompass the four channels. $\varphi$ =atan(1/5) and $\theta = 55^{\circ}$.

demultiplex light, the projection of the waveguide k-vector has to be displaced relative to the projection of the cusp when the wavelength is varied. The displacement is given by $2\pi n_{\text{slab}}\delta\lambda\sin(\theta)/\lambda^2 + \sin(\varphi)(\partial\text{MP}/\partial\lambda)\delta\lambda$. As $\partial\text{MP}/\partial\lambda$ is negative, the second term tends to reduce the resolution. As it is proportional to $\sin(\varphi)$, it is better to keep $\varphi$ as small as possible while maintaining the smallest necessary mode matching pass band.[3] The adiabatic transition is chosen to ramp the hole radius from $r/a = 0.15$ to $r/a = 0.3$. From the full band diagrams of the bulk PPC ($r/a = 0.3$) and of the full band diagram of the lattice corresponding to the smallest local hole size at the onset of the adiabatic transition ($r/a = 0.15$) we deduced that $\varphi = \text{atan}(1/5)$ is a good estimate (figure 7.3). $\varphi$ has to take the form $\text{atan}(1/N)$ with $N$ a positive integer, so that the interface has a well-defined periodicity. The adiabatic interface is chosen to ramp the radius up over 25 layers of holes. The width of each adiabatic transition is then given by $25 \cdot 3a/10/\cos(\varphi) = 2.83$ $\mu$m.

**Figure of merit for lateral beam steering per PPC size:** The frequency dependent angle of propagation inside the PPC ($\alpha$) can be calculated from the frequency dependent effective index of the PPC $n_{\text{PC}}$, from the incident waveguide angle $\theta$ and from the frequency dependence of MP. The lateral displacement of the beam position at the output edge of the PPC can then be determined to be $\tan(\alpha)d_{\text{PC}}$. Figure 7.4 shows $\tan(\alpha)$ as a function of the wavelength. It can be seen that the dependency is extremely close to linear in the considered wavelength range. Thus equal spacing between the output waveguides should result into equal spectral spacing between the demultiplexed channels. The figure of merit to determine the required PPC thickness for a given lateral beam

[3] An exact optimization of $\phi$ would also need to take into account the dependence of $\theta$ on $\phi$.

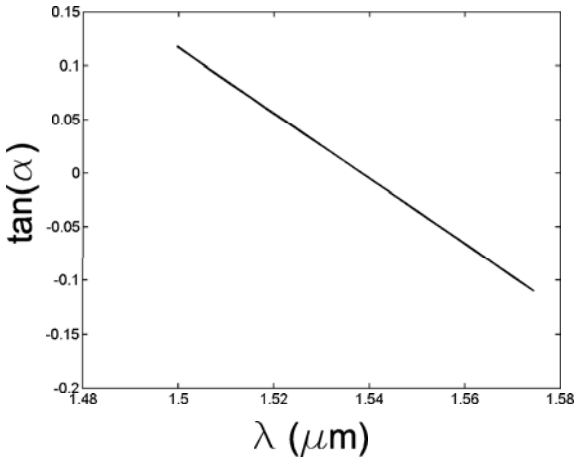


Figure 7.4: Dependance of the propagation angle inside the PPC ($\alpha$) on the wavelength. $\tan(\alpha)$ is shown rather than $\alpha$, as it is the tangent that determines the lateral beam steering.

steering is

$$\eta = \frac{\partial \tan(\alpha)}{\partial \lambda} = -3.0\ \mu\mathrm{m}^{-1} \tag{7.2}$$

As we operate in the frequency range where the radius of curvature of the cusp is almost constant (figure 7.2), $\eta$ can also be approximated as

$$\eta \simeq -\Big(\frac{2\pi n_{\mathrm{slab}}}{\lambda^2}\sin(\theta) + \frac{\partial \mathrm{MP}}{\partial \lambda}\sin(\varphi)\Big)\frac{\lambda}{2\pi n_{\mathrm{PC}}} \tag{7.3}$$

$\partial \mathrm{MP}/\partial\lambda = -13.4\ \mu\mathrm{m}^{-2}$, which results in $\eta = -2.95\ \mu\mathrm{m}^{-1}$.

**Waveguide width:** For a channel spacing $\delta\lambda$, the lateral beam steering is $\delta\lambda\eta d_{\mathrm{PC}}$ and should be equal to the spacing between the outgoing waveguides that pick up the signal at the output facet of the PPC. This spacing is of the order of $W_{\mathrm{WG}}/\cos(\theta)$ (in fact the spacing has to be a little wider to provide room for some separation between the waveguides). This is shown in figure 7.5.

The k-vector distribution of light coupled to the PPC has to be contained within the rounded part of the EFC cusp. This constrains the minimum waveguide width ($W_{\mathrm{WG}}$). The width of the cusp is extracted from the EFC to be $\delta k = 1.2\ \mu\mathrm{m}^{-1}$. When projected onto the interface this results in $\delta k_{\parallel} = \delta k\cos(\varphi)$. On the waveguide side the broadening of the k-vector distribution has two sources. One is the finite width of the waveguide ($\delta k_1$), the other is the frequency dependent position of the center of the distribution ($\delta k_2$). The incoming light is assumed to be a Gaussian beam. The Fourier amplitude distribution is then given by $\exp(-k_1^2/\sigma_k^2)$ where $\sigma_k = 2/\sigma_x = 2\sqrt{2\log(2)}/\mathrm{FWHM}$. Setting $\delta k_1 = 2 \cdot 0.8\sigma_k$ leads to $\mathrm{erf}(\sqrt{2} \cdot 0.8) = 89\%$ of the power to be taken into account, where erf is the error function $\mathrm{erf}(x) = \int_0^x \exp(-t^2)dt$ (there is a factor $\sqrt{2}$ inside erf due to the fact that the power corresponds to the squared amplitude). $\delta k_2 = 2\pi n_{\mathrm{slab}}\delta(1/\lambda) = 0.2933\ \mu\mathrm{m}^{-1}$ for

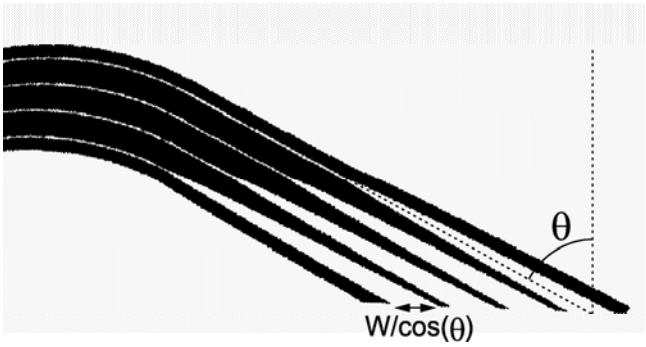


Figure 7.5: Screen shot of the electron beam lithography mask showing the tapered outgoing waveguides. They are oriented with an angle $\theta$ relative to the edge of the PPC. At the end of the taper the waveguide width is $W_{\mathrm{WG}}$, which results in a width $W_{\mathrm{WG}}/\cos(\theta)$ along the interface direction. Black corresponds to the region that is etched into the silicon film.

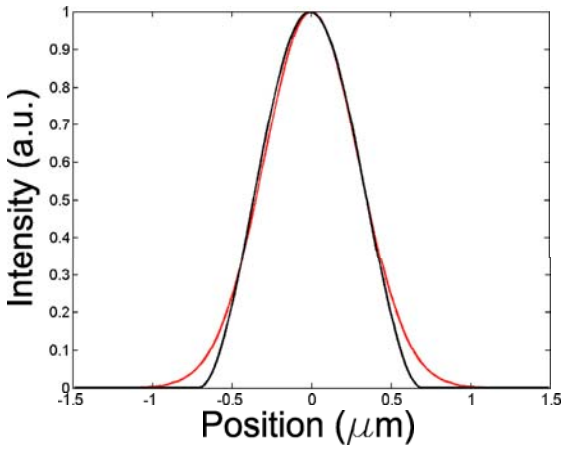


Figure 7.6: Comparison of a Gaussian beam with a FWHM of 0.7 $\mu$m (red curve) and the mode profile of a 1.4 $\mu$m wide dielectric waveguide etched into the silicon film (black curve). The squared B-field on the center plane of the dielectric waveguide is represented in the latter case.

$\lambda \in [1.518\ \mu\mathrm{m}\ 1.558\ \mu\mathrm{m}]$ (we aim at 4 channels with a 10 nm channel spacing). By equating $\cos(\varphi)\delta k = \cos(\theta)\delta k_1 + \sin(\theta)\delta k_2$ we obtain FWHM=2.3 $\mu$m and $W_{\mathrm{WG}} \simeq 4.6\ \mu$m (the cosine and sine factors come from projecting the k-vector distributions onto the interface of the crystal). Large, multimode dielectric waveguides tend to have a FWHM of about $W_{\mathrm{WG}}/2$ (figure 7.6). We also checked that a separation of 600 nm between the *wide* waveguides was sufficient for waveguide coupling to be negligible over the length of the tapered region (elsewhere the waveguides are thinner and the evanescent field penetrates deeper into the cladding, but the waveguide separation is also much wider).

**PPC dimensions:** The minimum dimensions of the PPC can now be determined. The spacing between waveguides along the direction of the PPC edge is $(W_{\mathrm{WG}} + 0.6\ \mu\mathrm{m})/\cos(\theta) = 9\ \mu$m. For a resolution $\delta\lambda = 10$ nm, this leads to a minimum PPC width $d_{\mathrm{PC}} = 9/\delta\lambda/\eta = 300\ \mu$m. With equation

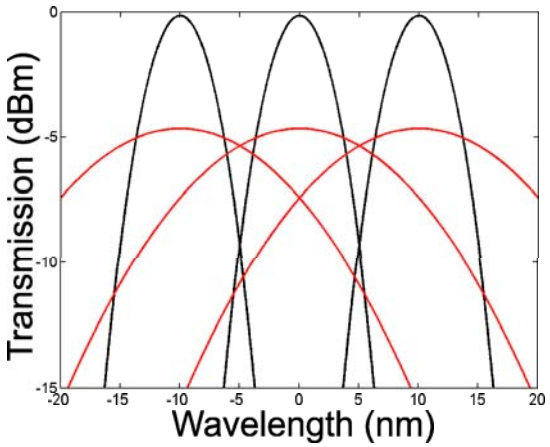


Figure 7.7: This figure shows the transmission through the demultiplexer as evaluated with Gaussian overlap integrals. Three channels are shown. In one case (black lines), $d_{\text{slab}}$ is assumed to take its ideal value, while in the other case it is assumed to be off by a 100 $\mu$m. This is an extremely simplified model, but it is useful to evaluate the tolerance on the beam expansion length.

6.6 we determine $d_{\text{slab}}$ to be 3.5 $d_{\text{PC}}$ (in equation 6.6 $W_0$ refers to $2\sigma_x$ while in this chapter $W_{\text{WG}}$ refers to the waveguide width). The lateral extent of the PPC must be enough to accommodate the lateral extent of the beam, that has been broadened after propagating for $d_{\text{slab}}/2$ through the unpatterned slab ($d_{\text{slab}}$ is equally split before and after the PPC). It must also accommodate the lateral displacement induced by beam steering, although the latter is much smaller than beam broadening. FWHM=2.3 $\mu$m corresponds to a diffraction angle of $\sqrt{2\log(2)}\lambda/(n_{\text{slab}}\pi\text{FWHM}) = 5.2^{\text{o}}$. The beam width at the interface is then $2\tan(5.2^{\text{o}})(d_{\text{slab}}/2)/\cos(\theta) = 167$ $\mu$m.

**Tolerance on incident waveguide angle:** The most critical parameter is the incidence angle of the waveguides. The devices are fiber coupled with grating couplers with a relatively low pass band ($\sim$ 50 nm if -6 dB from maximum coupling is used as a cutoff criterion) so that only relatively small deviations of $\theta$ can be compensated by shifting the channel frequencies. Here we evaluate the tolerance on $\theta$ to obtain a rationale for the parameter space exploration (small variations in slab thickness and material indeces have to be experimentally compensated). When setting the deviation of $k_{||}$ from its target value to zero, i.e., $\left(\delta\lambda(\partial/\partial\lambda) + \delta\theta(\partial/\partial\theta)\right)\left(2\pi n_{\text{slab}}\sin(\theta)/\lambda\right) = 0$, we obtain $\delta\theta = tan(\theta)\delta\lambda/\lambda$. $\delta\theta = 0.5^{\text{o}}$ then results in shifting the frequency comb by one channel ($\delta\lambda = 10$ nm).

**Tolerance on beam expansion length:** The tolerance on $d_{\text{slab}}$, $\delta d$, verifies $\tan(5.2^{\text{o}})\delta d = \sigma_x = \text{FWHM}/\sqrt{2\log(2)}$. This results in $\delta d = 21$ $\mu$m. Figure 7.7 evaluates the transmission through the demultiplexer with simple Gaussian overlap integrals. It is a highly simplified model, but provides an estimate of the impact of deviations of $d_{\text{slab}}$. It shows both the case of zero deviation and of a deviation of 100 $\mu$m.

## 7.2 Fabrication process

The PPC as well as the waveguides leading to and from the PPC are defined in a 205 nm silicon film. The film is surrounded by silicon dioxide ($n = 1.46$) and PMMA ($n = 1.5$) that act as the cladding materials. The fabrication process starts with silicon on insulator (SOI) material, with a 3 $\mu$m thick silicon dioxide layer below the silicon film. The oxide layer is chosen large so as to optically isolate the silicon film from the silicon substrate and to avoid losses due to coupling to the substrate. A silicon dioxide layer is then deposited on top of the SOI to act as a hard mask layer for the subsequent etch step. We use spin on glass (Spintronics 15A) spun at 3000 rpm for 1 min. and subsequently baked on a hot plate (1 min. at 80 °C, 1 min. at 180 °C and 1 min. at 250 °C). This results in a 120 nm thick silica layer. 4% 495K PMMA is spun 1 min. at 3000 rpm and baked for 1 min. 30 sec. at 180 °C. The PMMA is exposed by e-beam lithography with the LEICA 5000+ e-beam writer at 100 keV and 1000 $\mu$C/cm$^2$ and subsequently developed for 1 min. in a 1:3 mixture of MIBK:IPA (methyl isobutyl ketone and isopropanol alcohol). Subsequently, an oxygen reactive ion plasma (RIE) descum process is applied for 5 sec. (90 W, 90 sccm, 30 mTorr chamber pressure). The pattern is then transfered from the PMMA into the silicon dioxide with a $CHF_3$ RIE process (4 min. 30 sec. at 40 mTorr, 20 sccm, and 100 W) followed by a 5 min. $O_2$ descum in an inductively coupled plasma reactive ion etch (ICPRIE) to remove residues formed during the $CHF_3$ etching process (100 sccm $O_2$, 5 W forward power, 800 W ICP power, 20 mTorr chamber pressure and 10 mTorr strike pressure, cooled with 20$^o$ water). The $SiO_2$ etch rate in the $CHF_3$ RIE process is 50 to 60 nm per minute (figure 7.8). The residues formed during the $CHF_3$ process are quite resistant and act as a mask during subsequent Si etching, which leads to the formation of micro pillars (figure 7.9). The residues might be a form of fluo-carbon as both elements are provided by the etching gas. The oxygen descum successively removes them in most cases (there was still a little bit of variability from chip to chip).

Finally the pattern is transferred from the silicon dioxide into the silicon film with a Cl ICPRIE process (1 min. 45 sec., 80 sccm Cl, 50 W fwd power, 800 W ICP power, 12 mTorr chamber pressure, 10 mTorr strike pressure, cooled with 20$^o$ water). After the final etching step 950K PMMA is spun on top of the structure to backfill the holes and act as the top cladding layer (the layer is several microns thick). We use PMMA as a top cladding layer as it has a refractive index very close to the index of $SiO_2$ so that the PPC conserves a vertical symmetry. Furthermore it has been shown that PMMA has very low absorption in the infrared [69, 125].

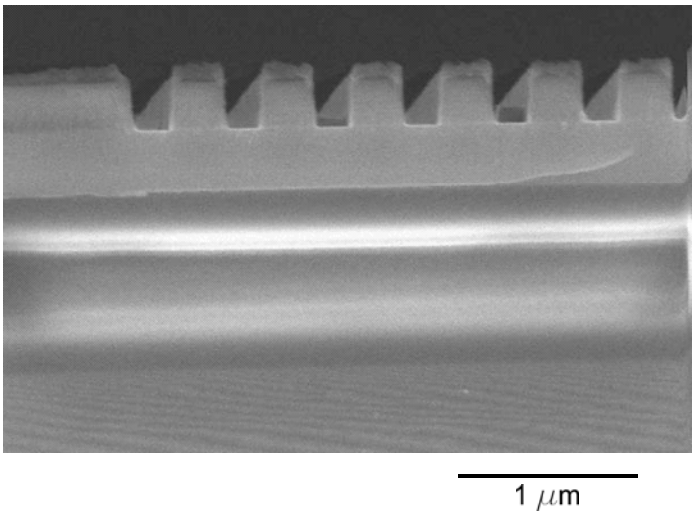


Figure 7.8: SEM micrograph of a cleaved sample after etching of a test pattern into the spin-on glass layer. It can be seen that the side walls are fairly straight with the optimized process parameters.

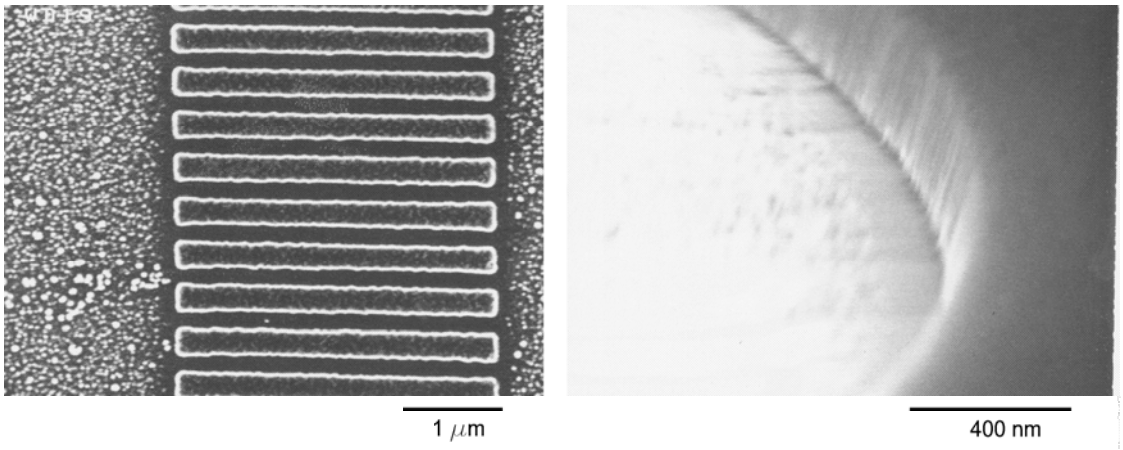


Figure 7.9: SEM micrographs of samples after etching the Si layer. In this instance the oxygen descum was not applied after the $CHF_3$ etch, and the residue deposition was particularly disruptive. In most cases the residue redeposition was much weaker (less than a particle per $\mu m^2$) and could be removed with an oxygen plasma.

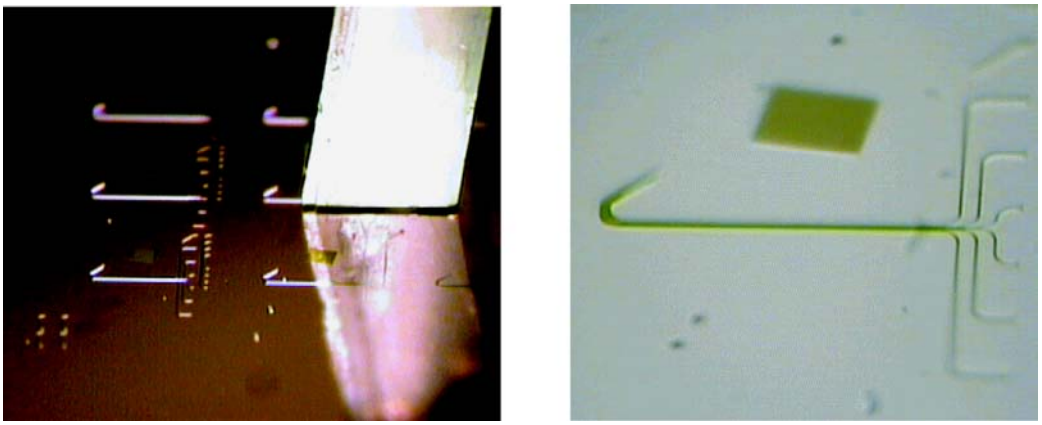


Figure 7.10: (a) Snapshot of a chip aligned to a fiber array. Several superprisms can be seen. The right side of the tree-like structure corresponds to multiple grating couplers separated by a fixed pitch (250 $\mu$m) corresponding to the pitch of the fiber array. The waveguides are bundled, bent (on the left side of the structure) and oriented towards the photonic crystal (rotated square). (b) shows a detailed view of a device. After bending the fiber bundle the waveguides are tapered on the left side of the device. On the right side of the device, the topmost isolated structure corresponds to the in port, while the fiber bundle corresponds to the output ports.

## 7.3 Grating couplers

The chips are grating coupled [83–92] to polarization maintaining single mode fiber arrays (figure 7.10). A tunable laser and a photodetector are then used to obtain a spectrum from the devices. The grating couplers consist of grates completely etched through the 205 nm thick silicon membrane. Two improvements are applied to the grating coupler as compared to the most basic design, variable grate strength and curved grate geometry. Indeed constant grate strength limits the overlap between the fiber mode and the grating coupler emission. The constant decay rate of the waveguide mode inside the grating coupler leads to an exponentially decaying intensity profile inside the waveguide, and in turn to an exponential shape of the grating coupler emission. A variable grate strength can lead to a Gaussian shaped emission profile with a higher overlap with the fiber mode [83, 84]. In particular it has been shown that a grating coupler with linearly tapered grates leads to an approximately Gaussian field emission [83].

The grating coupler couples an optical fiber to a much smaller single mode waveguide and needs thus to focus the field [85–89]. Compared to the size of the fiber mode the on-chip waveguide size can be approximated as a point source. Thus the phase matching condition is operated between the circular wavefronts of the point source (the edge of the on-chip waveguide) and the linear wavefronts of the fiber (cleaved along an angled plane). This leads to elliptic grates [89]. Most optical fibers are cleaved along an 8° angle to minimize back reflections. This shallow angle leads to elliptic grates with an eccentricity close to 1, so that circular grates are an appropriate approximation. Other

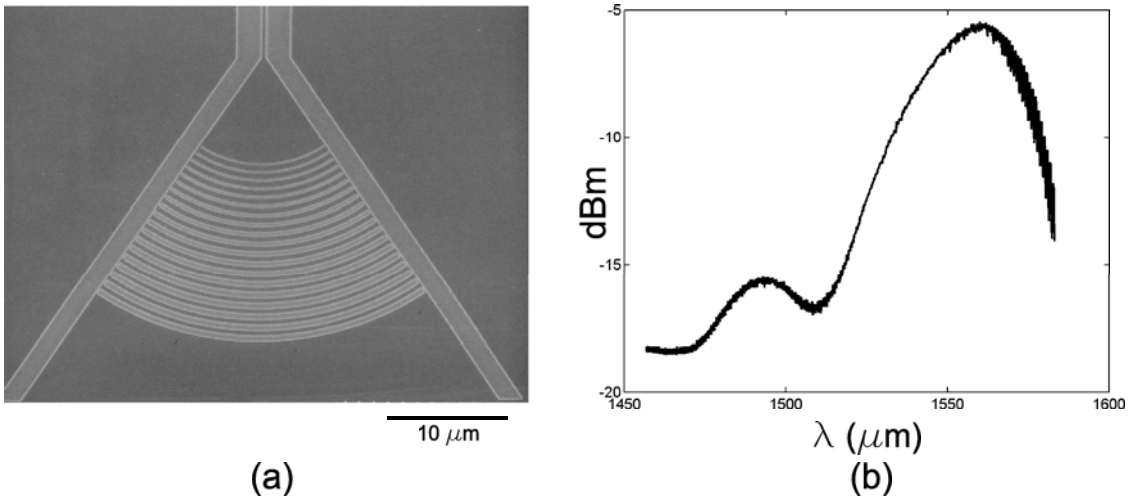


Figure 7.11: (a) shows a SEM micrograph of a fabricated grating coupler, and (b) is a typical coupling spectrum for a single grating coupler.

techniques, such as multilayer stacks below the grating coupler can be used to further enhance the efficiency [89, 90]. Here however we worked with the geometry of the available SOI material and did not attempt to optimize this last aspect.

We designed grating couplers with linearly tapered circular grates. The rate at which the grate strength is ramped up was experimentally optimized by parameter space exploration. Figure 7.11 shows a fabricated grating coupler as well as the coupling efficiency of a typical structure. We found that a 5 nm increment of grate width per grate and starting from a lithography limited smallest grate size gave good results (figure 7.11(b)).

## 7.4 Experimental results

We fabricated and measured devices with various incident waveguide angle ($\theta \in \{53^o,\ 55^o,\ 57^o\}$) and a range of expansion distances ($d_{\text{slab}} \in \{d_0 - 200\ \mu\text{m},\ d_0,\ d_0 + 200\ \mu\text{m}\}$, where $d_0$ is the calculated optimum $d_{\text{slab}}$). The best devices corresponded to $\theta = 57^o$ and had a maximum transmission at 1565 nm for the $6^{th}$ output channel (rightmost taper in figure 7.1(b)). The spectrum is shown in figure 7.12(b) (black curve). In the last section we calculated that a deviation of the incident waveguide angle of $\delta\theta = 0.5^o$ corresponds to a wavelength shift of about 10 nm at fixed output waveguide position. From this and from the spectral position of the $\theta = 57^o$ device we conclude that the maximum transmission should have occured at $\lambda = 1525$ nm for $\theta = 55^o$. This is outside the pass band of the grating coupler used for this experiment (figure 7.12(a)) this is why no useful data was recorded for the other devices. Furthermore we only obtained useful data for the fourth and sixth output channels (with tapers numbered from left to right), as the fourth channel was already

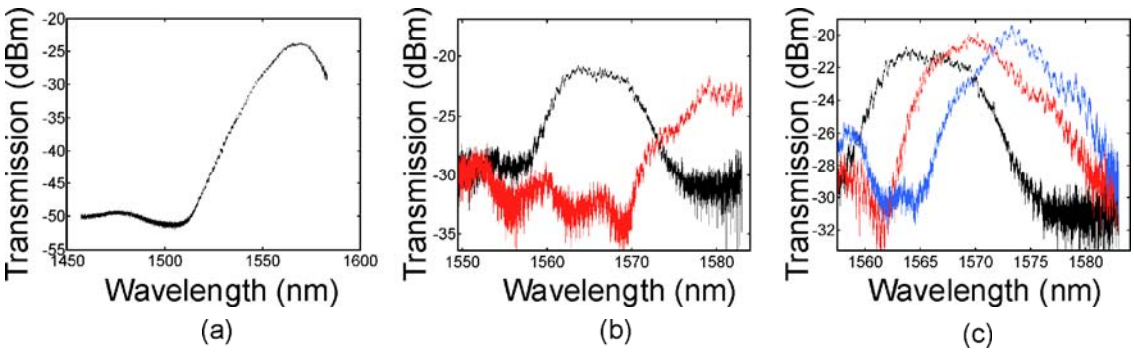


Figure 7.12: Experimentally obtained transmission spectra for the characterized superprisms. (a) shows the transmission spectrum for a loop fiber coupled with two grating couplers, including losses incurred elsewhere in the measurement setup. This spectrum has been subtracted from the device spectra shown in (b) and (c) so as to normalize out the effect of both the finite grating coupler efficiency and additional losses in the measurement setup (of about 5.5 dB). (b) shows the transmission spectra for a device with $\theta = 57^{\circ}$ and for the sixth (black curve) and fourth (red curve) output channels. Output channels are numbered by the position of their output taper, from left to right. $d_{\text{slab}} = d_0 - 200\ \mu$m. (c) shows spectra recorded for the sixth output channel of devices with $\theta = 57^{\circ}$ and $d_{\text{slab}} = d_0 - 200\ \mu$m (black curve), $d_0$ (red curve) and $d_0 + 200\ \mu$m (blue curve).

halfway out of the range of the tunable laser, and the transmission through the fifth channel was very low, probably due to some defect in the waveguide. Had there been additional tapers to the right, more channels would have been recorded.

However the obtained data is in good agreement with the design targets. The fourth channel is shifted by 20 nm from the sixth channel, which corresponds exactly to the targeted resolution of 10 nm per channel, as shown in figure 7.12(b). This figure corresponds to $\theta = 57^{\circ}$ and $d_{\text{slab}} = d_0 - 200\ \mu$m. In figure 7.12(c) we show the dependency of the spectrum on the expansion length $d_{\text{slab}}$. $\theta$ is fixed at $57^{\circ}$ but $d_{\text{slab}}$ is varied. It can be seen that the spectrum shifts to higher wavelengths when $d_{\text{slab}}$ is lengthened. This might seem surprising at first as the position of the spectrum of the devices was meant to stay unchanged, only the width of the spectrum should change as shown by figure 7.7. However it was assumed that the Gaussian beam propagates inside the unpatterned slab in the direction given by the orientation of the taper of the input channel (figures 7.1(a) and 6.3). This is indeed a very good approximation, but not exactly true as the effective index of the wide dielectric waveguide at the end of the taper is close but not exactly equal to the effective index of the slab, as the tapers are not terminated perpendicular to the direction of propagation of the waveguide, but along an angle $\theta$ relative to the direction of propagation (figures 7.1(b) and 7.5). In order to evaluate the effective index of the lowest mode of the tapered waveguide we used a one dimensional approximation, where we solved for a waveguide with the effective index of the slab ($n_{\text{slab}}$) in the core and the $SiO_2$ index in the cladding (effective index or Marcatelli approximation). Of course the Marcatelli approximation [99] is not really appropriate here as it is only applicable for low index contrast geometries, but we use it to obtain an order of magnitude of

the expected spectrum shift. By setting $n_{\text{slab}} = 2.76$ we obtain $n_{\text{WG}} = 2.7554$. By applying Snell's law, $n_{\text{WG}}\sin(\theta) = n_{\text{slab}}\sin(\bar{\theta})$, where $\bar{\theta}$ is the direction of propagation inside the unperturbed slab, we obtain $\bar{\theta} = 56.85^{\text{o}}$. As $d_{\text{slab}}$ is incremented by 200 $\mu$m, this would correspond to a lateral position shift of $200 \cdot (\tan(\bar{\theta}) - \tan(\theta)) = 1.72$ $\mu$m, or about 2 nm spectral shift for a fixed output waveguide position. The experimentally obtained spectral shift is more around 3.5 nm, but it is in the expected direction and is well within the right order of magnitude.

# Chapter 8

# Monolithic integration of vertical-cavity surface-emitting lasers with in-plane waveguides

The ability to couple light from a vertical-cavity surface-emitting laser (VCSEL) [100–103] into a planar, on-chip waveguide creates new opportunities for achieving higher levels of integration and functionality [66, 68]. For example it enables the monolithic integration of VCSELs, p-i-n photodetectors and lithographically defined planar photonic devices in a single chip. Previously, VCSELs have been coupled to on-chip, planar waveguides by introducing a weak grating within the internal waveguide [68]. However, it is advantageous to be able to define the grating coupler (GC) in the top layer of the structure rather than inside the vertical cavity because this removes the necessity for regrowth. In addition, this decouples the growth process from the lithography so that a variety of planar devices can be subsequently etched into the top layer. Such an external grating could also be used to transfer light from a VCSEL to a silicon on insulator (SOI) chip for applications such as optical clocking in CMOS technology. The VCSEL could be defined in a III-V chip flip-chip bonded to the SOI chip, and the GC located in the top silicon film of the SOI chip.

However, coupling light through a ninety degree bend with a strong external grating presents difficulties due to the fact that the Bragg condition of the grating also corresponds to its second order bandgap. In previous designs where the GC was inside the VCSEL cavity, the efficiency of the GC was not an issue because non-coupled light stayed inside the cavity. However an external GC needs to have a high efficiency. Here these coupling difficulties are overcome by introducing a defect into the grating and defining a horizontal cavity [66]. There are numerous examples in the literature of designs where bending of light is modified by resonant mechanisms, such as resonantly enhanced sharp waveguide bends [104] or waveguide crossings with suppressed cross talk [105]. In section 8.1 we derive the diffractive optics related to this device, and we evaluate the efficiency of the GC with FDTD. We achieve 40% coupling efficiency between the waveguide and the vertical laser cavity. We

also show that polarization control of the VCSEL can be enhanced by coupling to the defect mode, provided the vertical spacing between the VCSEL and the GC is adequately chosen. Section 8.2 briefly introduces VCSELs based on ion implantation and gain guiding. In section 8.3 we fabricate and measure gain guided VCSELs that incorporate the coupler.

## 8.1 Design and FDTD calculations

We investigate with the finite-difference time-domain method (FDTD) a vertical cavity defined by a multilayer stack of alternating GaAs and $Al_{0.866}GaAs$ $\lambda/4$ films, where $\lambda$=0.959 $\mu$m is the lasing wavelength of the VCSEL. The refractive indeces of the thin films are $n_{\mathrm{GaAs}} = 3.52$ and $n_{\mathrm{AlGaAs}} = 3.02$. A defect is introduced in the thin film stack by increasing the thickness of one of the AlGaAs layers to $\lambda/2/n_{\mathrm{AlGaAs}}$. Above the stack an 807 nm thick oxidized $Al_{0.98}GaAs$ buffer layer separates the top GaAs waveguiding layer from the VCSEL. The refractive index of the oxide ($n_{\mathrm{oxide}}$) is assumed to be 1.56, and the thickness of the top GaAs layer is $\lambda/2/n_{\mathrm{GaAs}}$ (140 nm). A grating is etched into the top GaAs layer to transfer the light emitted by the VCSEL into the waveguide. The individual grates consist of 60 nm wide, 50 nm deep trenches. A defect is introduced into the GC by locally changing the distance between two successive grates (the "grating defect" as opposed to the vertical-cavity defect). Finally, an $SiO_2$ cladding layer is assumed to be deposited on top of the grating after etching, in order to symmetrize the refractive index around the GaAs waveguiding layer ($n_{SiO_2} = 1.46$). The geometry of the device as well as the emitted E-field are shown in figure 8.1. For the purpose of FDTD simulations a small lateral index contrast is introduced in the defect layer of the vertical stack so as to force the vertical cavity mode to have a Gaussian cross section (the FWHM is 4.67 $\mu$m). In a real device this function is taken over by gain guiding.

First, the grating is optimized in such a way as to maximize the coupling between the transverse electric (TE) mode of the waveguide (E-field along the z-axis and B-field along the y-axis) and a Gaussian beam propagating normal to the waveguide (E-field along the z-axis and B-field along the x-axis). The axes are defined in figure 8.1. Then the coupling between the grating defect and the vertical cavity is investigated. One of the limitations of the GC is that it only couples TE polarized light; thus it is necessary to control the polarization of the VCSEL. The thickness of the AlGaAs oxide buffer layer determines the feedback from the grating defect into the vertical cavity. This feedback is used to enhance the quality factor (Q) of the TE vertical-cavity mode. FDTD calculations are performed with a spatial resolution of 0.01 $\mu$m and a time step of $c_0 dt = 0.005$ $\mu\mathrm{m}^{-1}$, where $c_0$ is the speed of light in vacuum.

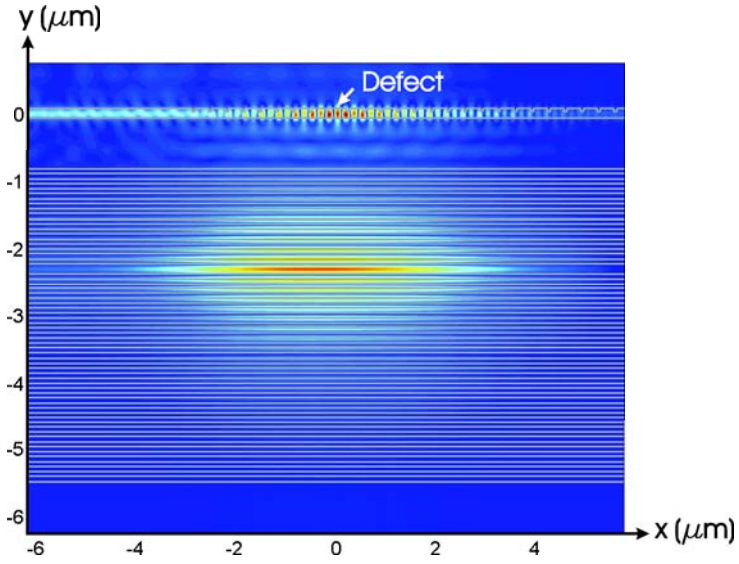


Figure 8.1: E-field ($|E_z|$) in the vertical cavity and in the GC (red corresponds to high intensity and blue to low intensity). The gray lines show interfaces between films of different refractive index. Alternating GaAs and AlGaAs layers define the VCSEL. Above the multilayer stack, an oxidized AlGaAs layer separates the waveguiding GaAs layer (with the grates) from the VCSEL.

### 8.1.1 Resonant grating coupler with defect mode

First, we consider a defectless, homogeneous grating, defined by etching trenches into the GaAs waveguiding layer. To outline the difficulties linked to the ninety degree bend, it is convenient to consider the converse problem that consists in coupling from the waveguide into the vertical cavity. The Bragg condition to couple light out of the waveguide at a ninety degree angle also corresponds to the second order bandgap of the grating so that most of the power incoming from the waveguide is reflected back instead of coupled out. In this particular geometry, the effective index of the waveguide is $n_{\mathrm{WG}} = 2.92$, and the grating period is $\Lambda$=0.336 $\mu$m. In order to compensate for these reflections, a second mirror is needed to recycle them, i.e., we need a cavity in the waveguide plane. Thus we introduced a defect into the grating by increasing locally the distance between two successive grates. The number of grates on the right side of the defect is chosen to be very large (20 grates) so that almost no power is transmitted to that side of the cavity; the number of grates left of the defect are chosen so as to minimize reflections (9 grates). In order to efficiently couple into a Gaussian field the displacement has to be carefully chosen. Indeed the fractions of the grating before and after the defect may scatter the field out of the waveguide with different phases. However, in order to couple into a single lobe Gaussian beam, the fields extracted on the two sides of the defect have to be in phase. Here we form a defect by increasing the separation by $\lambda/4/n_{\mathrm{WG}}$ that corresponds to a defect mode with even $E_z$. Defects have been previously used in horizontal-cavity, surface emitting distributed feedback (DFB) lasers to obtain a single lobe far field radiation pattern [106].

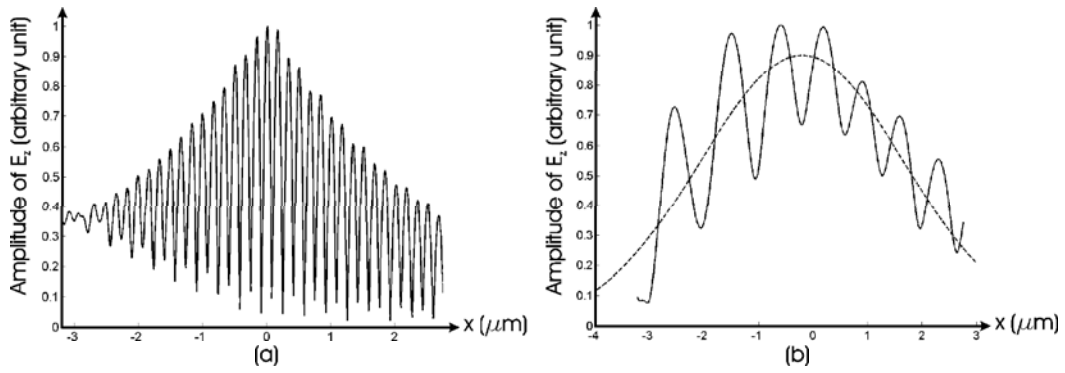


Figure 8.2: (a) Amplitude of $E_z$ along the center of the topmost (waveguiding) GaAs layer, in the region of the grating. The field enters from the left and reaches a maximum at the defect. In the region of the grating the field has nodes and antinodes due to the standing wave. (b) Amplitude of $E_z$ inside the oxidized AlGaAs cladding layer 4 $\mu$m below the stand-alone GC (continuous line). The best Gaussian fit (FWHM=3.1 $\mu$m) is also shown (dashed line). Due to the profile of the grating defect mode, the emitted field has a naturally "humped" shape with a good overlap with a Gaussian beam.

The definition of a defect inside the grating has the additional benefit of enhancing the overlap of the far field pattern of the grating with the VCSEL emission idealized as a Gaussian beam (figure 8.2). Indeed the field intensity has a naturally "humped" shape around the defect that has a bigger overlap with a Gaussian beam than the decaying exponential obtained with homogeneous gratings. Usually, the field overlap with a Gaussian is enhanced by varying the scattering strength of the grates throughout the grating [83, 84]. However, we found this to be impractical in the case of a 90 degree coupling angle. Due to the strong back-reflections induced by the grating, the field penetration into the grating is very short. In order to compensate for this, we chose the grates to be as weak as we estimated reasonable for standard fabrication techniques (60 nm wide with a very shallow etch), leaving no degree of freedom for additional tailoring. We calculated the overlap of the grating far-field pattern 4 $\mu$m away from the waveguide with Gaussian beams of varying width (vectorial calculation) and found that the best overlap was with a Gaussian with a full width at half maximum (FWHM) of 3.1 $\mu$m (93% overlap).

Figure 8.3 shows the efficiency of the stand alone coupler over a range of wavelengths. By stand alone we mean that the coupler is not combined with the vertical cavity, but merely clad by $SiO_2$ on the patterned side and AlGaAs oxide on the other side. In such a configuration, we found that the extracted field had the same intensity and profile in the +y and -y directions, even though the structure is slightly asymmetric (this may be linked to the fact that the thickness of the waveguiding GaAs layer is chosen to be $\lambda/2/n_{\mathrm{GaAs}}$ and has a resonance in the y-direction). In figure 8.3, we plotted the sum of the power extracted to +y and -y, or equivalently two times the power extracted towards -y. Due to the resonant nature of the coupling mechanism, the pass-band is quite small

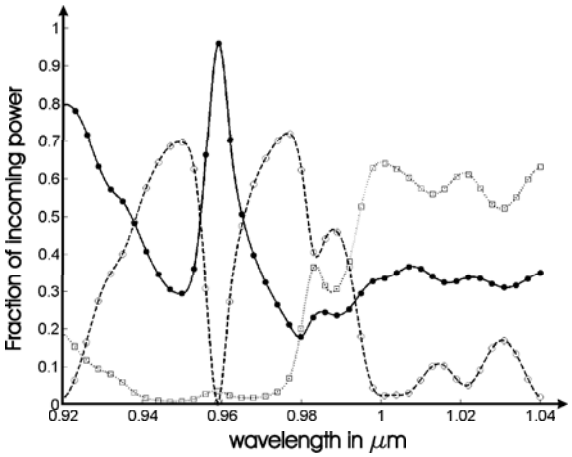


Figure 8.3: Coupling efficiency (dots), back-reflection into the waveguide (circles) and transmission to the other side of the grating (squares) as a function of wavelength. This data corresponds to a stand-alone GC. The plotted coupling efficiency is the sum of the coupling efficiency in the +y and in the -y directions.

compared to non-resonant GCs, but it is still wider than the line width of a VCSEL. The coupling efficiency of the stand-alone GC is 46% in each direction.

### 8.1.2 Feedback and polarization control of the VCSEL

In this section, we investigate the interaction between the grating defect and the VCSEL cavity. When the Gaussian beam is coupled from the oxidized AlGaAs layer into the waveguide, there is also a strong grating induced back-reflection (26%)[1] [107]. The reflected power is not lost but

[1]The 26% reflection has been calculated with FDTD; however, it could also have been easily derived from first principles that the anomalous reflection should be close to 25%. Indeed we have shown that the waveguide to free-space process is very efficient and almost 100% at resonance. The waveguide mode couples to a free-space mode propagating in the +y direction with a phase $\exp(iky+\varphi_+)$ and a free-space mode propagating in the -y direction with the phase $\exp(-iky+\varphi_-)$. Due to reciprocity, if two free-space modes impact the grating, one propagating in the -y direction with the phase $\exp(-iky-\varphi_+)$ and the other propagating in the +y direction with the phase $\exp(iky-\varphi_-)$, the converse coupling occurs, and the coupling efficiency is close to 100%. The light generated from the VCSEL corresponds to light propagating in the +y direction; however, it can be described as the sum of two fields: The same as previously described (a beam propagating in the -y direction with the prefactor $1/2\cdot\exp(-iky-\varphi_+)$ and a beam propagating in the +y direction with the prefactor $1/2\cdot\exp(iky-\varphi_-)$) plus a second field composed of a beam propagating in the -y direction with the prefactor $-1/2\cdot\exp(-iky-\varphi_+)$ and a beam propagating in the +y direction with the phase $+1/2\cdot\exp(iky-\varphi_-)$. The down-propagating components of the two films then cancel each other so that the resulting field corresponds to the VCSEL emission. As already mentioned, the first of the two fields is coupled into the waveguide; however, the second is orthogonal to the coupled field and is either reflected or transmitted through the thin film. We can assume that the grating itself has very little effect on the second field so that it essentially sees a thin film with a vertical resonance. We can then conclude that the field resulting from the scattering of the second field has equal amplitude on both sides of the thin film, 1/2. The reflection thus carries 1/4 of the total power.

recycled inside the VCSEL cavity, thus increasing the Q-factor of the VCSEL provided the thickness of the oxidized AlGaAs layer is chosen so that the reflection adds constructively to the VCSEL mode. Also the reflection induced by the grating has a different phase than the reflection from a plain dielectric interface so that the thickness of the AlGaAs oxide layer has to be modified from $\lambda/4/n_{oxide}$ to compensate for the extra phase. In the final design we obtained a 40% coupling efficiency from the vertical cavity to the waveguide.

The TM-mode of the waveguide (B-field along the z-axis) has a different effective index than the TE-mode (E-field along the z-axis) so that the TM-polarization is not resonant at $\lambda$=0.959 $\mu$m and does not verify the Bragg condition for the second bandgap. As a consequence, the strong grating-induced reflection does not occur for the TM-polarized vertical-cavity modes; it is actually quite small because the thin film had a vertical resonance before the grating was etched, and the grating has a small effect on the TM-mode. The reflection of the TM-mode was evaluated to be (8%). This can be used to enhance polarization control inside the VCSEL by tailoring the vertical-cavity Q-factors of the TE and the TM polarizations. In particular, the presence of the grating has only a small effect on the Q-factor of the TM-polarization, while the Q-factor of the TE-polarization is strongly enhanced. We simulated a device with 19 layers stacked between the vertical-cavity defect and the oxidized AlGaAs layer (10 layers of GaAs and 9 layers of AlGaAs, interleaved). This cavity had a Q-factor of 450 without the GC. After the unpatterned waveguiding layer was added, the Q-factor of the TE-mode stayed roughly unchanged (Q=555) due to the fact that this layer has a resonance in the y-direction (thickness $\lambda/2/n_{\mathrm{GaAs}}$) and hardly induces any reflections. When the grating was included, the Q-factor of the TE-mode was enhanced to 1520 while the Q-factor of the TM mode stayed quite low (600). The enhancement of the Q-factor of the TE-mode is slightly more than what would be expected from the 26% reflection (1400). This might be due to a folded cavity effect (i.e., the effective pathlength of the cavity is enhanced). On the other hand the enhancement of the Q-factor of the TM-mode is lower than what would be expected from the 8% reflection (800). This is due to the fact that the reflection adds a different phase increment to the TM field than to the TE field so that the AlGaAs oxide layer does not have the correct thickness to optimally enhance the Q-factor of the TM-mode.

The relative enhancement of the Q-factor of the TE-mode will facilitate polarization control in the VCSEL and might remove the need for more complex polarization splitting GCs [91, 92]. The strong reflection induced by a GC defined on top of a VCSEL has been previously used to reduce the Q-factor of one of the modes for polarization-control, but in that case the goal was not to outcouple into a waveguide, and the Q-factor of the grating-coupled mode was reduced rather than enhanced [108].

In conclusion, we have shown theoretically that by introducing a defect into a GC, light can be efficiently coupled around a ninety degree bend. We obtained 40% coupling efficiency from a

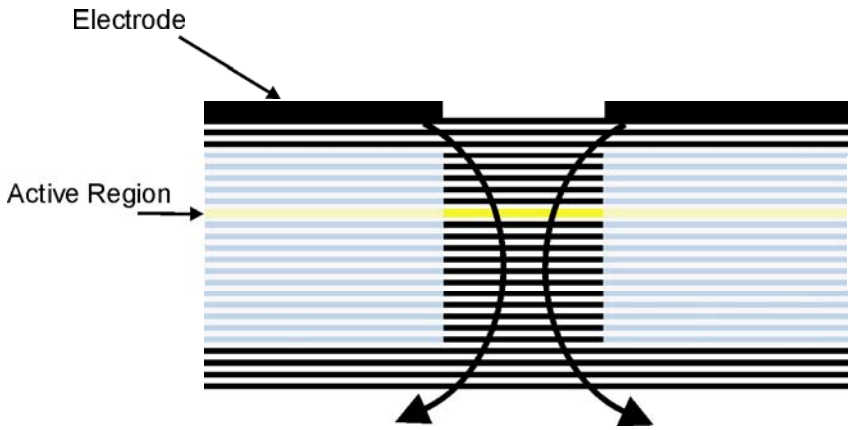


Figure 8.4: Schematic representation of lateral electrical confinement by means of an implantation induced resistivity profile. The electrical current flow is shown with bent arrows, and the implanted region is shown by grey shading.

vertical cavity to an in-plane waveguide defined in the topmost layer of the same chip. Furthermore, feedback from the defect mode of the GC to the vertical cavity enhances polarization-control of the VCSEL.

## 8.2 Gain guided vertical-cavity surface-emitting lasers

The design shown in the previous section will be implemented with electrically pumped gain guided VCSELs in the next section. Here we briefly discuss such VCSELs. The electrical current is laterally confined in the VCSEL by selective ion implantation (typically hydrogen). The ion implantation creates lattice defects and locally increases the resistivity of the material so that the current is constrained to pass in the non-implanted regions (typically a circular aperture of $\sim 10$ $\mu$m radius). Typical implantation doses are $2.5 \cdot 10^{14}$ cm$^{-2}$ at 300 keV. The implantation energy should be large enough to reach the quantum well (QW) as the lateral carrier diffusion in the QW can be quite high due to the vertical carrier confinement. A schematic of such a structure is shown in figure 8.4.

Lateral confinement of the light is obtained by gain guiding, that is, the gain in the electrically pumped region confines the field so that the optical mode profile automatically overlaps with the electrically pumped quantum well region. In the following we will derive gain guiding in a slab geometry. It is relatively straightforward to extend the model to the cylindrical VCSEL geometry by replacing cosines and exponentials by Bessel functions and modified Bessel functions.

In the presence of gain the evolution of the electrical field is given by

$$E(z) = e^{-i\frac{2\pi}{\lambda}\left(n+i\frac{\lambda}{2\pi}\alpha\right)z} \tag{8.1}$$

where $n$ is the refractive index of the media and $\alpha$ the gain coefficient (typically of the order of 1

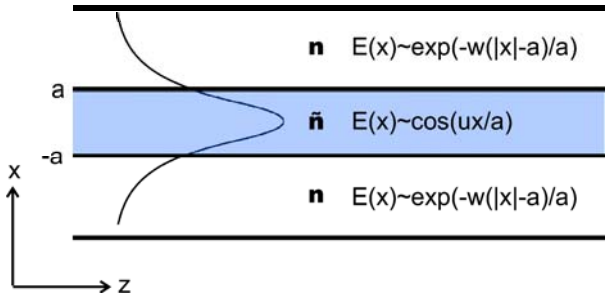


Figure 8.5: Schematic of a slab waveguide with gain guiding. The refractive index of the cladding is $n$, and the refractive index of the core is $\tilde{n}$. In the case of gain guiding $\Delta n = \tilde{n} - n$ is complex. The functional dependence of the *lateral* field profile is indicated.

$\mathrm{cm}^{-1}$ for a heavily pumped laser medium). The complex valued refractive index is then defined as $\tilde{n} \equiv n + i\lambda\alpha/2\pi$. As in the case of a conventional slab waveguide we describe the field independently in spatial regions with a given index and then proceed by solving the continuity equations. As shown in figure 8.5, the functional dependence of the field is $\cos(ux/a)$ in the core and $\exp(-w(|x| - a)/a)$ in the cladding (as in the case of index guiding). Phase matching at the interface between media leads to

$$w^2 + u^2 = \left(\frac{2\pi a}{\lambda}\right)^2(\tilde{n}^2 - n^2) = \left(\frac{2\pi a}{\lambda}\right)^2 2n[\mathrm{Re}(\Delta n) + i\frac{\lambda}{2\pi}\alpha] \tag{8.2}$$

$\mathrm{Re}(\Delta n)$ might be non zero as thermal effects or carrier density effects might modify the refractive index. The continuity equations further impose $w = u \cdot \tan(u)$ for even modes and $w = -u/\tan(u)$ for odd modes. In the case of gain guiding, $u$ and $w$ are complex numbers. Positive gain leads to gain guiding that is robust to perturbations.

It has been experimentally determined in the case of circular aperture VCSELs (10 $\mu$m radius) that the $1/e^2$ intensity point of the emitted Gaussian beam is about half the aperture radius [102].

## 8.3 Fabrication and measurements

In this section we will describe how electrically pumped VCSELs can be fabricated in conjunction with the in-plane waveguides and the defect mode GC. One of the difficulties is to selectively oxidize the AlGaAs buffer layer below the waveguides and above the VCSELs, but without oxidizing it below the electrodes. Indeed the buffer layer has to be oxidized in the immediate vicinity of the optical structure in order to provide the high index contrast relative to the GaAs layer. However it has to remain unoxidized for electrical conduction below the electrodes. In order to achieve this the VCSELs are defined by hydrogen implantation [101], and the waveguides are delimited by trenches etched into the topmost, waveguiding GaAs layer. The AlGaAs buffer layer can then be locally oxidized around the waveguides, as the AlGaAs buffer layer is only exposed to the thermal oxidation

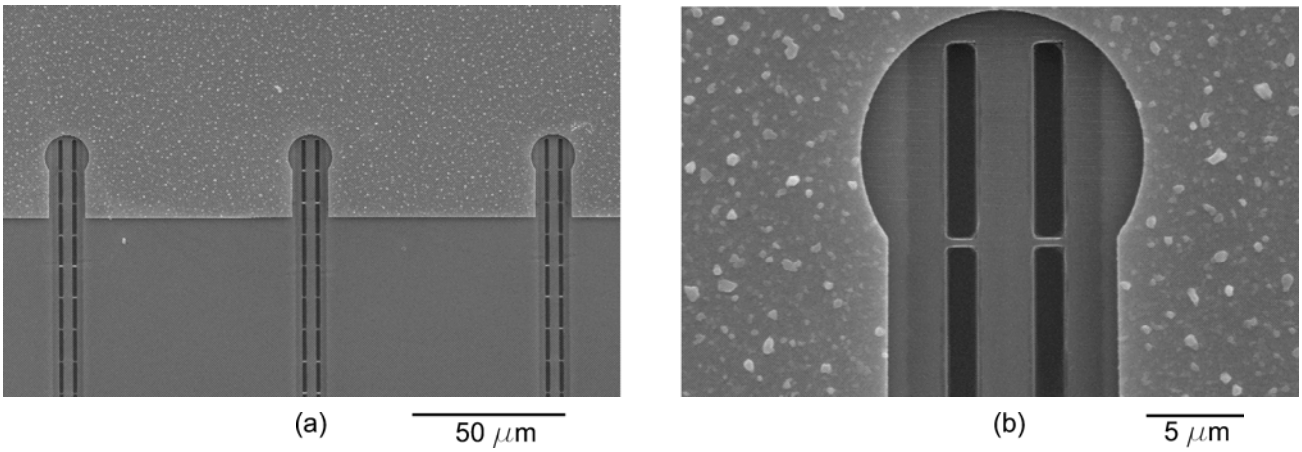


Figure 8.6: (a) shows three fabricated devices that share a common electrode. The TiAu electrode can be seen at the top of the image. The VCSELs are coupled to segmented waveguides that run in the vertical direction (in the image). (b) is a detailed micrograph of a single VCSEL. A circular aperture is left unmetalized above the VCSEL, and a rectangular aperture is left unmetalized above the segmented waveguide. The waveguide is defined by two trenches etched into the topmost GaAs layer. The trenches are periodically interrupted by small "bridges" to prevent the waveguide from peeling off. The AlGaAs buffer layer is selectively oxidized around the waveguide and can be seen as a rectangular shaded region.

process by means of these trenches. In the following the individual processing steps will be described in detail, and the emission of the electrically pumped VCSELs characterized.

Figure 8.6 shows fabricated devices. The VCSELs are defined by selective hydrogen implantation and gain guiding. Circular apertures are left unmetalized at the location of the VCSELs and rectangular apertures are left unmetalized around the segmented waveguides [109, 110]. Trenches etched into the GaAs layer define the segmented waveguides. The trenches are interrupted to prevent the waveguides from peeling off. In order to electrically pump the VCSELs, the AlGaAs buffer layer is only selectively oxidized through the trenches (the oxidized region can be recognized as the shaded region around the waveguides). Below the TiAu electrode the AlGaAs buffer layer is not oxidized and stays conductive (p-doped) so that the current can pass through. The grates are etched above the VCSELs in the circular apertures; however, the grates are not resolved in these micrographs. The images were taken before deposition of the top $SiO_2$ cladding layer.

The VCSEL fabrication starts with an epitaxial wafer grown by molecular beam epitaxy (MBE). A defect is placed inside a vertical stack of alternating $Al_{0.866}GaAs$ ($n$=3.02) and GaAs ($n$=3.52) $\lambda/4$ films that form a distributed Bragg reflector (DBR). An InGaAs quantum well (QW) is grown in the center of the defect. The DBR, defect and QW are optimized for emission at 980 nm. 18 pairs of $Al_{0.866}GaAs$ and GaAs $\lambda/4$ layers are grown above the defect. Many more layers are grown below as the VCSELs are aimed to be top emitting. A 735 nm thick $Al_{0.95}GaAs$ layer and a 140 nm GaAs layer (topmost) are grown on top of the multilayer stack. The former corresponds to

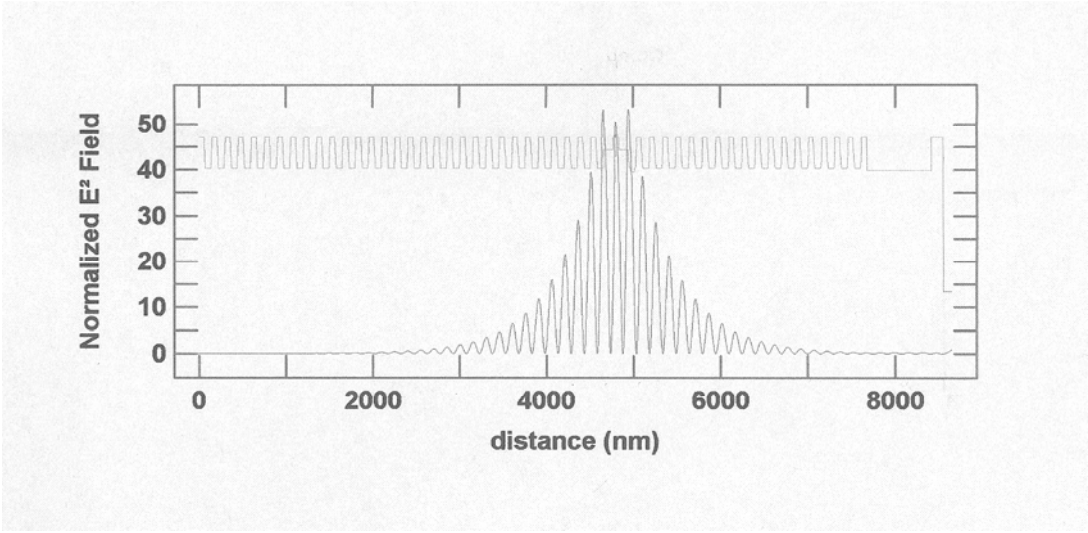


Figure 8.7: This figure shows the structure of the epitaxially grown wafer. The "humped" curve shows the field distribution inside the cavity (square of the E-field in arbitrary units). The other curve shows the refractive index distribution. From right to left the following layers can be identified: the waveguiding GaAs layer (weakly p-doped), the AlGaAs buffer layer (weakly p-doped) followed by 18 pairs of $\lambda/4$ layers (p-doped), the defect with the QW (intrinsic) and finally n-doped $\lambda/4$ films.

the (to be oxidized) buffer layer that optically isolates the topmost GaAs waveguiding layer from the rest of the structure. For subsequent electrical contacting the layers above the QW are grown p-doped, while the substrate and the layers below the QW were chosen to be n-doped. The wafer does not have exactly the structure assumed in the theoretical section of this chapter. For one, the AlGaAs oxide layer is thinner. Indeed oxidation of high aluminum content AlGaAs leads to about 6% contraction of the layer thickness, resulting in $\sim 691$ nm rather than 807 nm (this discrepancy was not deliberate but was due to constraints on the available material). Furthermore the AlGaAs buffer layer has a 95% aluminum content rather than 98%. This resulted in relatively high oxidation temperatures (480 °C) that led to a degradation of the QW efficiency (the growth temperature of the QW is 550 °C and gives an idea of the temperatures at which intermixing starts to occur). As a consequence the optimization of the oxidation process was critical (see below). It is beneficial to have some Ga in the AlGaAs layer as pure AlAs layers tend to form granularities during oxidation, but the Ga content should be kept below 2% when thermal budget is an issue. Figure 8.7 shows the structure of the wafer.

The first fabrication step consists in H ion implantation to define the gain guided VCSELs (section 8.2). The implantation profile typically consists in leaving out 10 $\mu$m diameter circles or 12 $\mu$m by 8 $\mu$m rectangles. For circular VCSELs, the $1/e^2$ radius is about half the radius of the implantation profile ($R$) [102] so that the FWHM of the laser beam is $\sqrt{2\log(2)}R/2 = 5.88$ $\mu$m.

It has been reported that the polarization of gain guided VCSELs with InGaAs QWs tends to

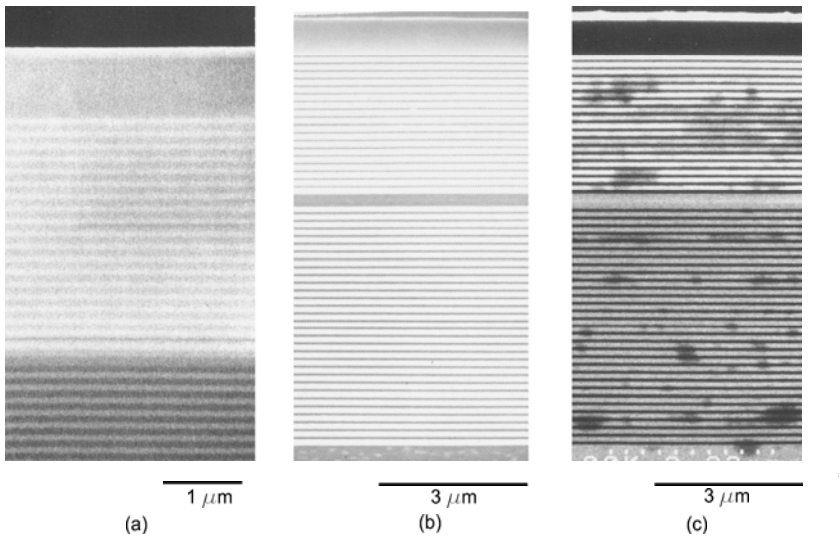


Figure 8.8: SEM micrographs of the wafer structure. In (a) the structure has been imaged with a low acceleration voltage (10 keV). Under these conditions the individual layers of the multilayer stack can be well resolved. Also the doping profile can be seen as the n-type region is imaged with a darker shade (bottom of the picture). In (b) the GaAs layers have been selectively etched to increase the contrast after cleaving. A mixture of citric acid and hydrogen peroxide was used ($C_6H_8O_7$:$H_2O_2$:$H_20$) [111]. In (c) the AlGaAs layers have been selectively oxidized after cleaving. High aluminum contents significantly decrease oxidation temperatures.

be along the cleaving axes (<110>) in the absence of other anisotropies [102]. In order to increase polarization control, the rectangular VCSELs are oriented along the <110> axes. However both possible orientations (long side by short side and short side by long side) are implemented. Indeed the polarization of rectangular VCSELs can depend on the relative spectral position of the maximum QW gain and the ground and higher order modes of the rectangular cavity so that it can be hard to predict in which mode the VCSEL is going to lase. In particular it has been observed that thermal tuning of the QW emission can switch the polarization of the VCSEL emission [103].

In order to selectively implant hydrogen an 8 $\mu$m thick implantation stop photoresist (PR) mask is deposited and patterned. First a hexamethyldisilizane (HMDS) layer is deposited for adhesion promotion. Then SPR 220-7 PR is spun at 3000 rounds per minute (rpm) for 40 seconds and soft baked for 10 minutes at 90 °C. It is exposed for 3 minutes, developed for 1 minute in MF 319 and finally hard baked 20 minutes at 115 °C.

Table 8.1 shows the implantation recipe. Due to the additional AlGaAs buffer layer and the waveguiding GaAs layer, the QW is buried deeper inside the chip than in typical ion implanted VCSELs (3.7 $\mu$m). The implantation energies have to be quite high to reach the QW (400 keV). In this design we were not concerned in electrical cross talk between the structures so that the topmost material (depth < 100 nm) could be left with low implantation. In order to reduce ion channeling

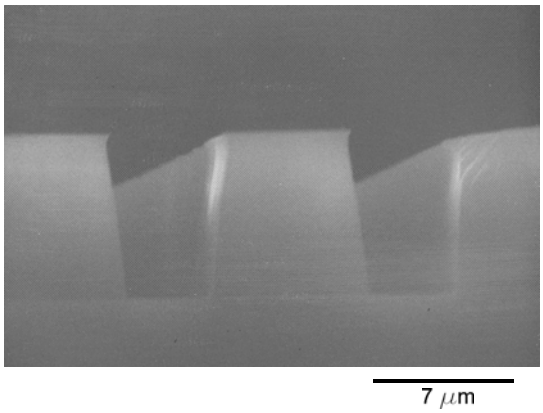


Figure 8.9: Cross-section of photoresist structures used to optimize the photoresist process needed to define the implantation stop. The photoresist film is 8 $\mu$m thick in order to provide an adequate stopping layer for the high velocity hydrogen ions.

Table 8.1: Implantation Recipe

| Energy (keV) | Dose ($cm^{-2}$) | Implantation depth (nm) |
|---|---|---|
| 150 | 1.5e14 | 1180 |
| 200 | 1.5e14 | 1610 |
| 260 | 1.5e14 | 2117 |
| 330 | 1.7e14 | 2751 |
| 400 | 2e14 | 3417 |

the implantation was made at a 7 $^{o}$ angle.

After implantation the PR is removed with an $O_2$ plasma in an ICPRIE (same process as in chapter 7). We prefer the ICPRIE to the RIE process described in chapter 7 due to the ability to decouple the plasma energy from the acceleration voltage. This way minimum acceleration voltage is achieved and surface damage is minimized.

The top electrodes are defined with a lift-off process using a bi-layer PMMA film. Bi-layer PMMA is used to achieve a slight undercut of the PMMA during development. This way the metal films deposited directly on the surface of the chip are disconnected from the metal films on top of the PMMA and lift-off is facilitated. First a layer of 4% 495K PMMA is spun at 4000 rpm for 1 minute and baked 30 minutes at 180 $^{o}$C. Then a second layer of 4% 950K PMMA is spun at 4000 rpm for 1 minute and baked 8 minutes at 150 $^{o}$C. The PMMA is exposed with a dose of 650 $\mu C/cm^{-2}$ at a 100 keV. The dose is fairly low due to the fact that large areas are exposed that lead to a significant proximity effect. The PMMA is developed for 5 minutes in a 1:3 solution of methyl-isobutyl-ketone (MIBK) and isopropyl alcohol (IPA). 10 nm of titanium is e-beam evaporated, followed by the thermal evaporation of 100 nm of gold. The backside n-type contacts are made of 5 to 10 nm of

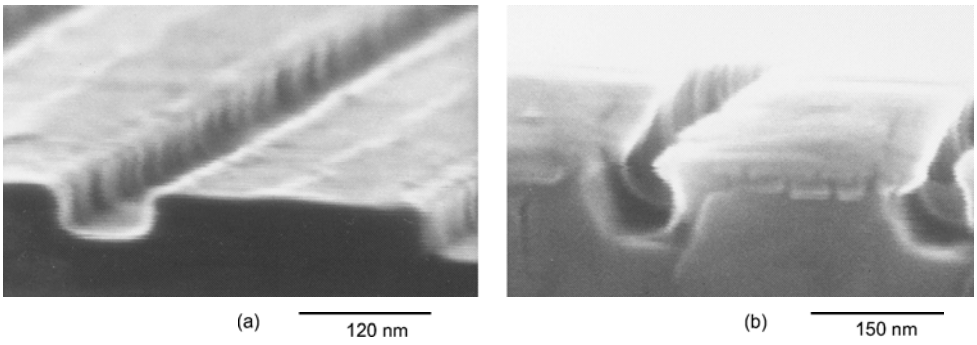


Figure 8.10: SEM micrographs of Ag/Cl etches on GaAs. In both (a) and (b) process parameters were 200 W ICP power, 50 W forward (acceleration) power, 5 mTorr chamber pressure. In (a) the chlorine made up for 20% of the gas flow, and in (b) it made up for 50% of the gas flow. It can be seen that in (a) the side walls are fairly straight while in (b) the GaAs is undercut. In (a) the side wall roughness might be due to underexposure of the PMMA mask. In (b) the PMMA can be recognized as the topmost layer.

Nickel followed by 200 nm of AuGe. Finally the chip is left in a chloroform bath for a few minutes, blow dried and put in an acetone ultrasound bath to operate the lift-off. The gold alloys (TiAu and AuGe) are chosen to delta-dope the surface in order to overcome the Schottky contacts at the metal semiconductor interface. The role of the nickel in the n-type contact is to penetrate the surface during annealing and to induce lattice defects that promote the diffusion of AuGe. It also acts as a sticking layer to prevent the AuGe contact peeling off. For the p-type contact titanium acts both as a delta-dopant and as a sticking layer.

Next the trenches defining the GC are etched into the topmost GaAs film. 4% 495K PMMA is used as a mask for a Cl/Ag ICPRIE etch. The argon is used to dilute the chemical action of the chlorine and to obtain the correct ratio between overcutting and undercutting for straight side walls (the more chlorine, the more undercutting). Figure 8.10 shows etches with different Ag/Cl ratios. In one case straight side walls are obtained while in the other case the film is undercut. In the optimized process, 20% chlorine versus 80% argon is used, the ICP power is 200 W, the forward power 50 W and the chamber pressure 5 mTorr. The chip is placed on a cooled wafer. The heat transfer is obtained with a helium flow between the wafer and waterlines cooled to 20 $^{o}$C. The etch rate is approximately 200 nm per minute.

The GC is composed of shallow grates that do not go all the way through the GaAs film. Before proceeding to thermal oxidation, trenches have to be defined in the GaAs film for the water vapor to access the AlGaAs film (pure GaAs acts as an efficient oxidation stop; during oxidation we found that even the thin $\lambda/4$ film below the buffer layer was enough to stop diffusion of water vapor and to prevent the next AlGaAs layer to be oxidized). These trenches define the segmented waveguides

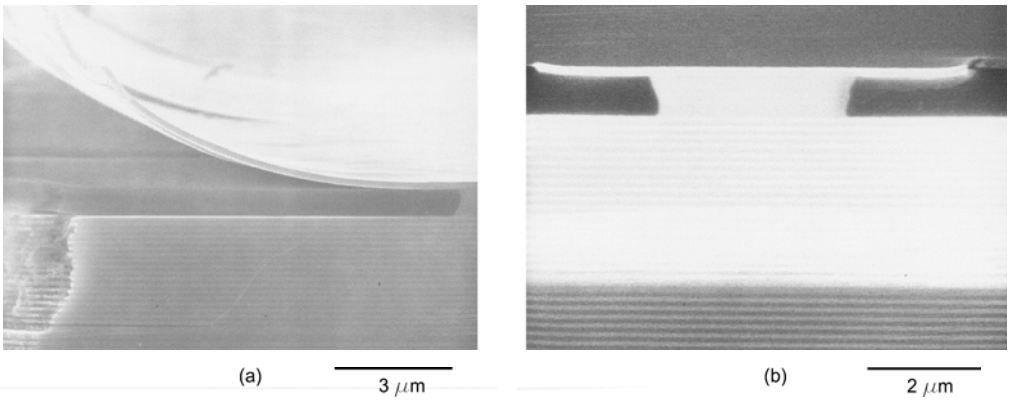


Figure 8.11: (a) shows the cross-section of an oxidized chip where delamination took place (delamination actually took place before cleaving). (b) was oxidized for 5 minutes at 550 °C. It shows how selective oxidation can be achieved by defining local openings in the topmost GaAs film.

at the same time (figure 8.6). The same etching recipe is used with a shorter etching time to define the GCs after another e-beam lithography step.

After etching the trenches the $Al_{0.95}GaAs$ layer is thermally oxidized in a furnace. Nitrogen flows through a bubbler with boiling water before being led through the furnace tube (200 sccm). The temperature of the furnace is maintained at 480 °C, and the sample is oxidized for 20 minutes. The timing of the oxidation is crucial as the oxidized region should only minimally overlap with the region below the electrodes. Otherwise an increased current path would lead to inefficient current injection. More importantly the thermal threshold for QW damage is already reached so that unnecessarily prolonged oxidation times would lead to a deterioration of the VCSEL efficiency and to an increase of the lasing threshold. The oxidation step also serves as an indiffusion and annealing step for the contacts. This is an important step as the germanium and titanium have to penetrate the GaAs lattice in order to overcome the Schottky barrier. Longer oxidation at lower temperature (which might result in less deterioration of the QWs) led to delamination of the topmost GaAs layer (figure 8.11(a)). This might be prevented in later designs by digitally growing the AlGaAs layer (that is one atomic layer at a time). This would lead to better material quality and would make delamination during the oxidation process less likely. In this case the AlGaAs layer was not digitally grown as it was originally meant as a sacrificial layer.

The VCSELs were characterized with an emission spectrum and an LL curve (LL stands for light in, light out; here the input is characterized by the current used to pump the VCSELs and the analog voltage output of a photodetector).

In order to measure the VCSELs we built a measurement setup by retrofitting a probe station. A beam splitter was added to the camera port of the microscope. One port of the beam splitter is connected to a charge-coupled device (CCD) camera for imaging (inset of figure 8.13(b)). A fiber

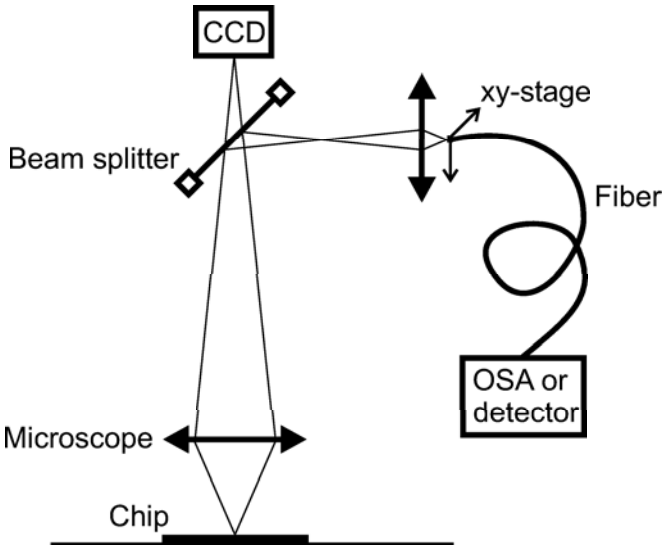


Figure 8.12: Schematic of the measurement setup. A beam splitter is added to the camera port of the microscope so that both a CCD camera and a fiber can be connected to the port. The procedure used to align both the fiber and the camera to the sample is described in the text.

coupler was added to the other port. The fiber coupler is composed of a lens that can be translated on a rail system. An xy-stage is also affixed to the rail system, and the fiber is attached to the xy-stage. Both the CCD camera and the fiber have to project their focal point onto the surface of the VCSEL so that the structure can be imaged and a spectrum or an LL curve taken at the same time. In order to achieve this, the focal adjustment of the microscope is first adjusted so as to obtain a sharp image from the CCD camera. Then a fiber coupled diode laser is connected to the xy stage. The emission of the laser diode is reflected by the chip and imaged by the CCD camera. Next, the position of the lens in the fiber coupler setup is adjusted to focus the laser beam to the smallest possible spot on the chip (the spot is imaged by the CCD during this procedure). The xy-stage is then adjusted to center the spot on the VCSEL. Finally the laser diode is detached from the xy-stage and replaced by a multi-mode fiber leading to the detector (to obtain the LL curve) or to the optical spectrum analyzer (OSA) to obtain a spectrum. A schematic of the measurement setup is shown in figure 8.12

Figure 8.13 shows both the spectrum and the LL curve of a VCSEL. The LL curve features the characteristic onset of lasing at 10 mA (or at 2 mA per VCSEL as 5 VCSEL share a common electrode and all 5 started lasing within a very narrow current range) in continuous wave (CW) operation. For currents higher then 11 mA the emitted power is reduced.

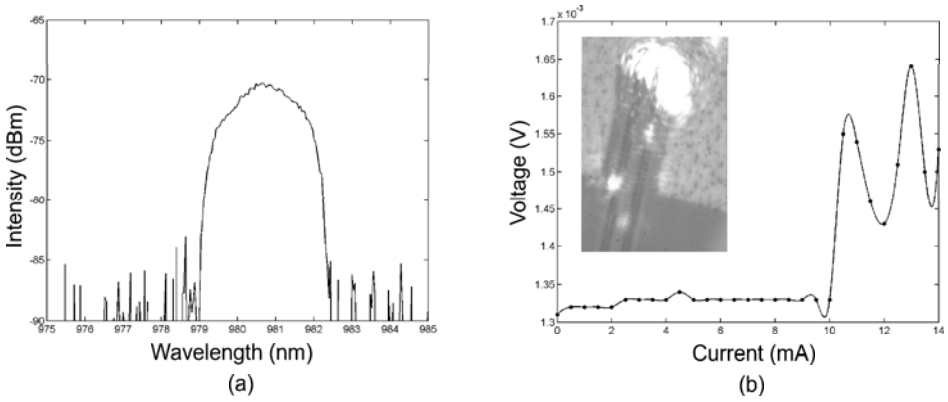


Figure 8.13: (a) shows the emission spectrum of a fabricated VCSEL. The FWHM is 2.1 nm. (b) LL curve for 5 VCSELs operated by a single top electrode. The threshold current is 2 mA per VCSEL. The power is measured with a photodiode, and the output voltage of the photodiode is plotted on the y-axis. The inset shows a picture taken of the VCSEL with a CCD camera. The bright spot corresponds to the VCSEL emission. The electrode and the GaAs waveguide can also be seen in the picture.

# Appendix A

# Orthogonality between Bloch modes and computation of intrinsic photonic crystal waveguide losses

In this appendix we show how advanced data analysis can be used in conjunction with FDTD simulations to evaluate intrinsic losses of corrugated waveguides, photonic crystal waveguides (PCW) and segmented waveguides. In most cases, by using this method we can both shrink the necessary computational domain and increase the accuracy of the extracted waveguide losses. Complications arise when Bloch modes with very low group velocity are investigated.

Line-defects formed in a PPC by changing the properties of one or several rows of holes [3–5] can be used for waveguiding. In such a system the guided wave is confined in the vertical direction by total internal reflection and in the lateral direction by distributed Bragg reflection or by effective index confinement. Recently, propagation losses as low as 11dB/mm have been reported for silicon on insulator (SOI) based photonic crystal waveguides [5]. Losses can be due to material absorption, surface roughness, random variations due to finite fabrication tolerances or intrinsic losses due to coupling to free space. The latter only occurs when the Bloch modes have Fourier components inside the light cone. The coupling to free space from PPC modes and PCW modes has been used for light extraction [20] and experimental mode mapping [75, 127]. Several experimental [127, 128] and theoretical [127–134] investigations of the intrinsic losses of photonic crystal waveguides have been published. In this appendix we show a novel method for evaluating intrinsic losses with FDTD simulations [61]. Intrinsic PCW losses have previously been investigated by FDTD [127, 133], but previous methods were based on evaluating the power transmission through a device [134] or the intensity decay along the waveguide [127, 133]. In both cases the separation of insertion losses due to mode mismatch from propagation losses is problematic. In the first case, several simulations need to be done to find the asymptotic value of losses versus device length (and to ensure that there is no tunneling). In the second case the field needs to be propagated for a long enough distance to ensure

that it has converged to a waveguide mode. Both methods require computational domains with a longitudinal dimension on the order of the length scale required for the field to converge to a mode. In ref. [133], mode profiles are calculated, but are not used for the propagation loss calculations.

In order to shorten the computational domain necessary to evaluate waveguide losses, the ability to extract the power contained in a given Bloch mode from the raw FDTD data is crucial. If the spatial dependence of the power is taken without previous filtering, reflected Bloch modes, radiative free space modes or tunneling of waves that would be reflected in a longer simulation can make the data difficult to exploit. It is then necessary to propagate the field for a longer distance for these waves to decay (in the case of spurious free space modes and tunneling). Reflected Bloch modes are always present as existing FDTD implementations of absorbing boundary conditions (ABCs) are not adapted to Bloch waves. However, if the simulated waveguide is long enough (on the order of 1.5 times the $1/e^2$ intensity decay length) the field is dominated by the forward propagating wave in the beginning of the waveguide (section A.3, figure A.9). To circumvent these difficulties and to shrink the computational domain to a few lattice periods, we have developed a method to extract the power carried by specific Bloch modes from the recorded fields. This is done with an inner product that verifies orthogonality conditions for Bloch modes [60]. Prior to the actual filtering, the mode profile of the Bloch modes has to be obtained by FDTD [3] or with a numerical mode solver. It is then possible to revert to very small FDTD computational domains and to propagate the field only for a few lattice constants, as the relevant energy flux can be extracted from the other fields. In section A.1 we will introduce the inner product and show that in the absence of absorption losses it verifies orthogonality for Bloch modes. Moreover, this inner product only necessitates data over a field cross section rather than over an extended volume. This makes it particularly practical for the computation of waveguide losses that require the evaluation of the *local* intensity of the Bloch mode. In section A.2 we develop the methodology to extract intrinsic waveguide losses with the concrete example of an W1 PCW (the W1 geometry will be defined below). This also provides additional validation of the arguments derived in section A.1. The results are compared with waveguide losses reported in the literature that were computed with different methods, and the data are found to be in good agreement. However, we observe that the numerical accuracy decreases when the method is applied to Bloch modes with very low group velocities. In section A.2 we argue that the problems arise from the fact that the inner product is not positive definite. In particular the inner product is related to the *energy flux* so that at fixed energy density the value of the inner product decreases with the group velocity. To further exemplify these limitations, the corrugated waveguide is investigated in section A.3. In this case analytical expressions for the Bloch mode structure and for the reflection of Bloch modes at the boundary of the media can be derived with coupled mode theory. These expressions will be used in the following section to illustrate the limitations of the method with explicit analytical examples.

## A.1 Inner product

In this section we will show that an inner product commonly used for continuous waveguides can also be applied to PCWs and segmented waveguides when there is no material absorption. The quadratic function associated to the inner product corresponds to the energy flux and is as such a conserved quantity in a system without absorption or gain. From the conservation of the quadratic function (power conservation) and from the discrete translation invariance of the mode structure (Bloch theorem), we conclude that Bloch modes verify orthogonality conditions for this inner product. This inner product is particularly attractive as it only needs data across a field *cross section* rather than over an *extended volume*.

For waveguides with continuous symmetry, orthogonality conditions between bound modes and between bound modes and radiative modes are well established [98]. In particular for a non absorbing waveguide with translation symmetry in the y-direction, and two modes (bound or radiative) $\psi_j = (\mathbf{E}, \mathbf{H})$ and $(\bar{\psi_k} = \bar{\mathbf{E}}, \bar{\mathbf{H}})$ with the same implicit time dependence $\exp(-i\omega t)$

$$\begin{array}{rclcrcl} \mathbf{E} & = & \mathbf{e_j}(x,z)e^{-i\beta_j y} & & \mathbf{H} & = & \mathbf{h_j}(x,z)e^{-i\beta_j y} \\ \bar{\mathbf{E}} & = & \mathbf{e_k}(x,z)e^{-i\beta_k y} & & \bar{\mathbf{H}} & = & \mathbf{h_k}(x,z)e^{-i\beta_k y} \end{array} \tag{A.1}$$

where $\omega$ is the angular frequency and $\beta_{j/k}$ are the propagation constants (wave numbers), the following holds

$$(\beta_j - \beta_k) \int_S \{\mathbf{e_j} \times \mathbf{h_k^*} + \mathbf{e_k^*} \times \mathbf{h_j}\} \cdot \hat{\mathbf{y}} dS = 0 \tag{A.2}$$

where $\hat{\mathbf{y}}$ is the unit vector in the y-direction and $S$ is an xz plane. PCW modes can be written as

$$\begin{array}{rclcrcl} \mathbf{E} & = & \mathbf{e_j}(x,y,z)e^{-i\beta_j y} & & \mathbf{H} & = & \mathbf{h_j}(x,y,z)e^{-i\beta_j y} \\ \bar{\mathbf{E}} & = & \mathbf{e_k}(x,y,z)e^{-i\beta_k y} & & \bar{\mathbf{H}} & = & \mathbf{h_k}(x,y,z)e^{-i\beta_k y} \end{array} \tag{A.3}$$

where $\beta_j$ and $\beta_k$ are the reduced wave numbers in the first Brillouin zone and $\mathbf{e_{j/k}}$ and $\mathbf{h_{j/k}}$ verify the same periodicity in the y-direction as the waveguide ($\Lambda$), for example $\mathbf{e_j}(x, y+\Lambda, z) = \mathbf{e_j}(x,y,z)$. We use functional A.2 as an inner product for photonic crystal waveguides

$$\langle \psi, \bar{\psi} \rangle_{y_0} = \frac{1}{4} \int_{S\{y=y_0\}} \{\mathbf{e_j} \times \mathbf{h_k^*} + \mathbf{e_k^*} \times \mathbf{h_j}\} \cdot \hat{\mathbf{y}} dS \tag{A.4}$$

This inner product will be denoted as $\langle ., . \rangle_{y_0}$ in the following, where $y_0$ refers to the xz plane $S\{y = y_0\}$ over which the field cross sections are taken. It corresponds to a symmetrized version of the time averaged Poynting vector, integrated over the field cross section. It is not a scalar product as backward propagating modes have a negative square product and standing waves are null vectors.[1] For this choice of inner product, the square of a steady state field $\psi$, $\langle \psi, \psi \rangle_{y_0}$, is the

[1] "Null vector" refers to the fact that the square of a standing wave is zero, as it transports no

time averaged energy flux propagating in the y-direction and is thus independent of the position of the reference plane provided its *orientation* is conserved (we assumed non-absorbing materials and S is an infinite plane). In particular the transfer matrix $T_{y_0 \to y_0+\delta y} = T_{\delta y}$ that maps the field from one cross section $S_1\{y = y_0\}$ to another cross section $S_2\{y = y_0+\delta y\}$ offset by $\delta y$ conserves $\langle \psi, \psi \rangle$. From the conservation of the quadratic function we conclude on the conservation of the inner product

$$\begin{aligned}
\langle \psi_1 + \alpha\psi_2, \psi_1 + \alpha\psi_2 \rangle_{y_0} &= \langle \psi_1 + \alpha\psi_2, \psi_1 + \alpha\psi_2 \rangle_{y_0+\delta y} && \text{(A.5)} \\
\langle \psi_1, \psi_1 \rangle_{y_0} + |\alpha|^2 \langle \psi_2, \psi_2 \rangle_{y_0} + 2\mathrm{Re}\big(\alpha \langle \psi_1, \psi_2 \rangle_{y_0}\big) & \\
&= \langle \psi_1, \psi_1 \rangle_{y_0+\delta y} + |\alpha|^2 \langle \psi_2, \psi_2 \rangle_{y_0+\delta y} + 2\mathrm{Re}\big(\alpha \langle \psi_1, \psi_2 \rangle_{y_0+\delta y}\big) & \\
&= \langle \psi_1, \psi_1 \rangle_{y_0} + |\alpha|^2 \langle \psi_2, \psi_2 \rangle_{y_0} + 2\mathrm{Re}\big(\alpha \langle \psi_1, \psi_2 \rangle_{y_0+\delta y}\big) && \text{(A.6)} \\
\langle \psi_1, \psi_2 \rangle_{y_0} &= \langle \psi_1, \psi_2 \rangle_{y_0+\delta y} & \\
&= \langle \psi_1 T_{\delta y}^{+}, T_{\delta y} \psi_2 \rangle_{y_0} && \text{(A.7)}
\end{aligned}$$

In the above $\alpha$ is an arbitrary complex number. We choose $\delta y$ to be the period of the waveguide ($\Lambda$). The EM-field can be decomposed into eigenmodes of operator $T_\Lambda$ (Bloch modes) because of the periodicity of the PCW (Bloch theorem). $T_\Lambda$ then conserves the inner product *and* is diagonal in the basis given by the Bloch modes.[2] This is sufficient to prove that Bloch modes with different *reduced* wave numbers and same implicit time dependence are orthogonal. For two modes $\psi_1$ and $\psi_2$ satisfying $T_\Lambda \psi_1 = e^{i\beta_1 \Lambda}\psi_1$ and $T_\Lambda \psi_2 = e^{i\beta_2 \Lambda}\psi_2$, we have

$$\langle \psi_1 T_\Lambda^{+}, T_\Lambda \psi_2 \rangle = e^{-i(\beta_2 - \beta_1)\Lambda} \langle \psi_1, \psi_2 \rangle \qquad \text{(A.8)}$$

From equations A.7 and A.8 we conclude that $\langle \psi_1, \psi_2 \rangle = 0$ if $\beta 1 \neq \beta 2$ (that is, when the

energy and the quadratic function associated to this inner product is the energy flux. This does not necessarily imply that it is in the kernel of the inner product as the cross product between a standing wave and another field can be non zero. For example if $\psi_+$ and $\psi_-$ are the forward and backward propagating modes of a waveguide, $\langle [\psi_+ + \psi_-]/\sqrt{2}, [\psi_+ + \psi_-]/\sqrt{2} \rangle = 0$, but $\langle [\psi_+ + \psi_-]/\sqrt{2}, \psi_+ \rangle = 1/\sqrt{2}$. Evanescent waves belong to the kernel of the inner product, as well as Bloch modes with zero group velocity of the inner product which is *restricted* to fields that are physical solutions of a specific waveguide geometry.

[2] This is a similar situation as for the standard scalar product used in quantum mechanics that is derived from the conservation of the probability density, $\psi_1 \cdot \psi_2 = \int \psi_1 \psi_2^* d^3r$. "Modes" are then defined as energy eigenstates and are eigenmodes of the Hamiltonian $H$. The time evolution operator, $\exp(iHt)$, both conserves the probability density *and* is diagonal in the basis given by these modes. As a consequence the energy eigenstates verify orthogonality with that particular scalar product. In electromagnetics the scalar product can also be derived from the energy density as $1/4 \cdot \int (\epsilon E E^* + \mu H H^*) d^3r$. It has the advantage of being positive definite. However, the integral needs to be taken over the whole universe (or over the whole mode volume in the case of bound modes). This is due to the fact that the energy is only *globally* conserved due to mode beating and interference effects. For this reason this scalar product is not practical for the computation of waveguide losses.

Bloch modes are *nondegenerate*). When two bands cross we can conclude from the continuity of the photonic bands (or more precisely, the continuity of the Bloch mode structure for adjacent modes on a given band) that $\langle \psi_1, \psi_2 \rangle = 0$ also holds at the crossover point. This is a somewhat subtle point as there is a degree of freedom to choose the basis at the cross-over point. It means that orthogonality is verified provided the basis is chosen to be the "natural" one, which verifies continuity of the photonic bands. Whether orthogonality will indeed hold at the cross-over point in a numerical application depends on the mode solving method and whether it provides a field decomposition in the natural basis. This is for example not the case with FDTD iterations of a unit cell, with Bloch boundary conditions (BBC) and Fourier filtering, as it doesn't distinguish between two degenerate modes and returns a superposition of the two modes dependent on their overlap with the initial field launched inside the simulation.

In the next section the inner product will be used to calculate intrinsic PCW losses, which might seem contradictory as the orthogonality has been derived in this section for strictly lossless PCW modes. However it seems natural to assume that for small losses the deviation from orthogonality should be small. In the next section we will proceed directly to the application of the inner product to the computation of intrinsic PCW losses.

## A.2 Computation of intrinsic photonic crystal waveguide losses

In this section we evaluate PCW losses with help of the inner product. The obtained results are in good agreement with the literature. In A.2.1 we describe how raw data is generated by FDTD and in A.2.2 we filter the data with the inner product. It is observed that the obtained numerical accuracy decreases for Bloch modes with very low group velocities.

### A.2.1 Setup of the simulations

We analyze a W1 waveguide formed by leaving out 1 row of holes in a triangular lattice PPC of lattice constant $a$, radius $r = 0.3a$ and slab thickness $t = 0.577a$ [127]. In this case the period of the waveguide $\Lambda$ is equal to one lattice constant $a$. The slab is made out of silicon (refractive index 3.43); the holes and the cladding have an index of 1. The photonic crystal is in the xy plane, and the direction of propagation is y. We evaluate the losses for the e1 mode, which has an even symmetry relative to the xy plane ($\sigma_{xy} = +1$) and an odd symmetry relative to the yz plane ($\sigma_{yz} = -1$). All simulations are performed with 3D FDTD with a discretization of 26 points per lattice constant. In order to get stable simulations with Bloch boundary conditions (BBC), the time step $dt$ was reduced to $dx/(4c_0)$, where $dx$ is the spatial discretization and $c_0$ is the speed of light in vacuum. Results are given in normalized frequency $a/\lambda$ and normalized wave number $a\beta$, where $\lambda$ is the free space wavelength and $\beta$ the reduced wave number.

In order to obtain the modal profiles of the PCW, we simulate one unit cell of the waveguide with a BBC applied in the direction of propagation (y-axis) [3]. The BBC forces the field on the $y = a$ boundary to be $\exp(i\phi)$ times the field on the $y = 0$ boundary, where $\phi$ is a fixed phase. By applying a discrete Fourier transform to a time series collected by a field probe, the spectral resonances are found. The simulation is then run a second time, with the field stored over an entire cross section. In order to reduce the amount of stored data, the field is directly Fourier transformed during the simulation. The Fourier transformed field is stored and updated at each time step. As the resonant frequencies are already known from the previous simulation, the size of the array that has to be stored is the number of points of the cross section multiplied by the number of investigated resonances, rather than the number of points times the number of time steps. The obtained field is already Fourier transformed and thus corresponds to a steady state field with an implicit time dependence so that the assumptions of section A.1 are satisfied. This way, modes and leaky modes of the PCW are obtained. These simulations will further be referred to as "mode solving". We store the modal field profile along an xz plane (the "mode profile"). For all that follows the specific position of the xz plane is not important as long as it is consistent. In order to obtain the forward propagating mode, the BBC is set to a phase $-\beta a$, as the dispersion diagram has a negative slope (the group velocity points in the opposite direction than $\beta$). Alternatively, the field could also be solved with a BBC set to $\beta a$, followed by a field transformation that inverts the direction of propagation with respect to $y$ [98].

$$(E_x, E_y, E_z) \longrightarrow (E_x, -E_y, E_z)^* \qquad (B_x, B_y, B_z) \longrightarrow (-B_x, B_y, -B_z)^* \tag{A.9}$$

We then simulate the field propagation along 10 photonic crystal periods. Fig. A.1 shows the computational domain. We use a dipole source to launch a pulse into the PCW and save the field profile every second lattice period, at the same position relative to the unit cell than in the mode solving procedure. As before, the field is directly Fourier transformed during the simulation by updating a finite number of monitored frequencies at each time step. In the following this simulation will be simply referred to as "the simulation", as opposed to the mode solving procedure.

In the next subsection we will proceed with the data analysis. We use the inner product to filter out the portion of the field that corresponds to the e1 mode, and we evaluate the waveguide losses.

### A.2.2 Computational results

The computational domain is $7\sqrt{3}a \times 3.84a$ in the xz plane and $10a$ in the y direction. The properties of the inner product (orthogonality and flux conservation) have been derived for an integral over an infinite plane. When taking an inner product between an arbitrary field cross section and a *bound* mode, the integration domain can be reduced to a finite cross section due to the exponential decay

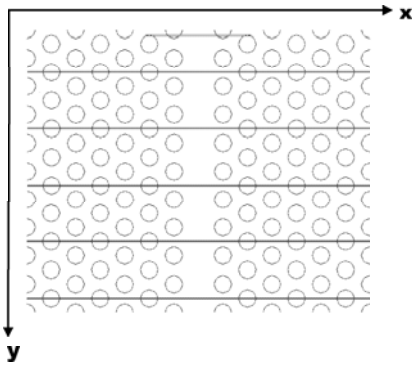


Figure A.1: Cross section of the computational domain. A dipole source launches a field with symmetries $\sigma_{xy} = -1$, $\sigma_{yz} = +1$. Every second lattice period a field probe saves the field.

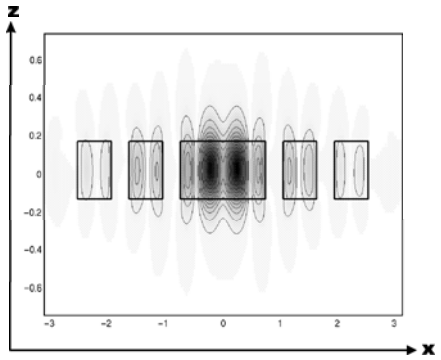


Figure A.2: Mode profile for $\beta a = 0.07\pi$ (lower band of e1). The colormap shows $|B_z|$. The thick black lines delimit the high index region ($n = 3.43$). The two maxima have the same phase (i.e., $B_z$ is even). Units are in microns for a lattice constant of $a = 0.52\mu$m.

of the bound modes in the evanescent field region. However, this does not hold when radiative modes are present on both sides of the inner product. In particular, the total energy flux $\langle \phi, \phi \rangle$ is not conserved along the y-direction because radiative modes are absorbed by the perfectly matched layer absorbing boundary condition (PML ABC). In the following, $\phi$ is used to refer to field cross sections recorded from the simulation while $\psi$ refers to cross sections of bound PCW modes.

The same simulation could have been performed with Bloch boundary conditions (BBC) with a phase of 0 applied to the xy and yz boundaries. This would create a supercell, and bound modes of the several mirror PCWs would be coupled to each other. However, if the computational domain is big enough in the x and z dimensions the induced band splittings are negligible. In such a case we would expect $\langle \phi, \phi \rangle$ to be conserved.

We analyze losses for the first band of the e1 mode between the light line and the $\Gamma$ point ($\beta = 0$). At that point a mini stop-band opens, and the group velocity goes to zero [127]. Indeed, it can be seen in figure A.5(a) that the dispersion diagram flattens out. Figure A.2 shows $|B_z|$ for the e1 mode at $a/\lambda = 0.3383$ ($\beta a = 0.07\pi$). The field amplitude has two maxima, but they have the same

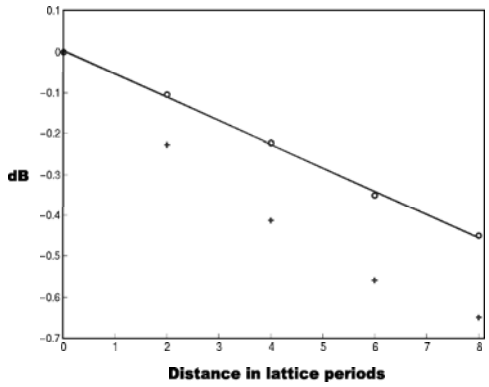


Figure A.3: $20\log_{10}(|\langle\phi^l, \psi_{\beta a=0.07\pi}\rangle|)$ is plotted with circles, where $\phi^l$ is the field profile at the $l^{th}$ probe and $\psi_{\beta a=0.07\pi}$ is the field cross section of the PCW Bloch mode with reduced wave number $\beta a = 0.07\pi$. $10\log_{10}(|\langle\phi^l, \phi^l\rangle|)$ is plotted with crosses. Probes are spaced by two lattice constants. It can be seen that the unfiltered energy flux decreases faster than the flux carried by the mode.

phase (i.e., $B_z$ is even and $\sigma_{yz} = -1$). Fig. A.3 shows $20\log_{10}(|\langle\psi_{\beta a=0.07\pi}, \phi^l\rangle|)$, where $\psi_{\beta a=0.07\pi}$ is a PCW mode and $\phi^l$ is the field profile at the $l_{th}$ probe (subscripts label modes by their reduced wave number, and superscripts label the real space position of the field cross sections). In both cases $a/\lambda = 0.3383$. The field intensity features the expected exponential decrease. On the same plot the unfiltered energy flux $10\log_{10}(|\langle\phi^l, \phi^l\rangle|)$ is also shown. It can be seen that using the latter would result in an overestimate of the losses because the field has not yet converged to the PCW mode. The additional field decay is due to insertion losses, to absorption of free space modes by the PML ABC and to the reflected Bloch wave. If the lattice constant $a$ is chosen to be $0.52\mu$m, the intrinsic losses are 110 dB/mm at that frequency. The very high losses are due to the fact that the frequency was chosen to be near the band edge for this example.

As an additional test we plotted the phase of $\langle\psi_{\beta a=0.07\pi}, \phi^l\rangle$ [Fig. A.4]. It can be seen that it has the expected linear behavior. The wave number is determined to be $0.0698\pi$ from the slope of the curve. This is very close to the wave number initially fixed in the mode solving procedure ($0.07\pi$).

Fig. A.5 shows the computed waveguide losses and the dispersion diagram of the lower band of the e1 mode. Losses first increase away from the light line, but then decrease again in the vicinity of the mini stop-band before diverging at the stop-band.

This numerical method should be very accurate in the region of high group velocity (from $a/\lambda = 0.28$ to $a/\lambda = 0.33$). However, this method cannot be used to calculate the quality factor of zero group velocity modes as they are null vectors of the inner product. For modes of decreasing group velocity, numerical inaccuracies in the mode profile become dominant and lead to inaccurate results. To illustrate this, we compared for each data point the wave number extracted from the inner products to the wave number initially fixed in the mode solve procedure [Fig. A.6]. It is seen that these values correspond for modes away from the mini-stop band. However, the first 8 data points

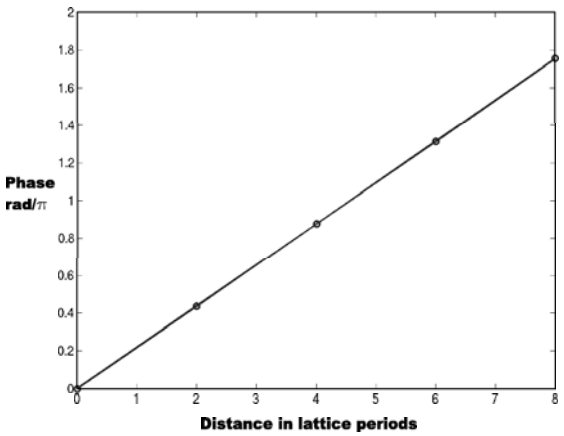


Figure A.4: The phase of $\langle \phi^l, \psi_{\beta a=0.07\pi} \rangle$ is plotted. The expected linear behavior is seen.

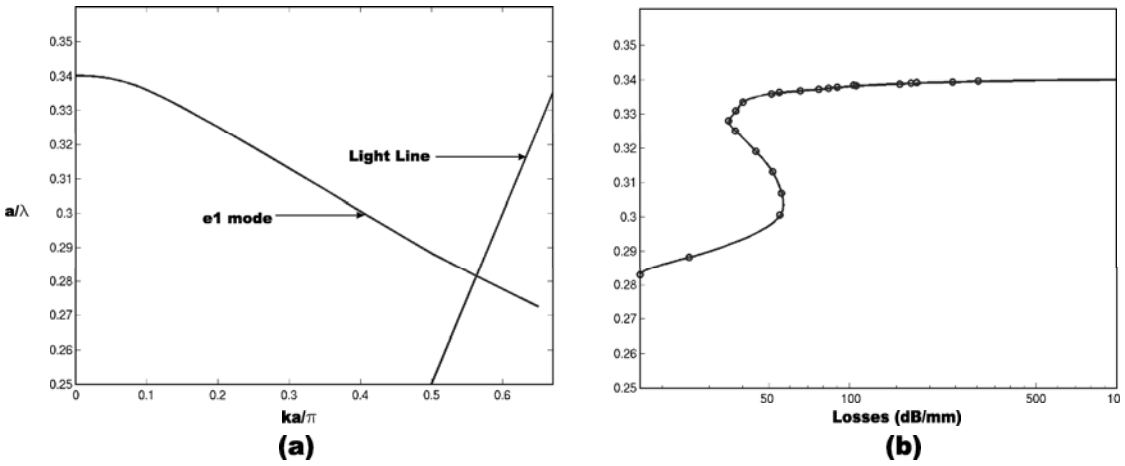


Figure A.5: (a) Dispersion diagram of the lower band of e1, and (b) losses of the lower band of e1. The straight line in (a) represents the light line. Losses in dB/mm correspond to a lattice constant of $a = 0.52\mu$m.

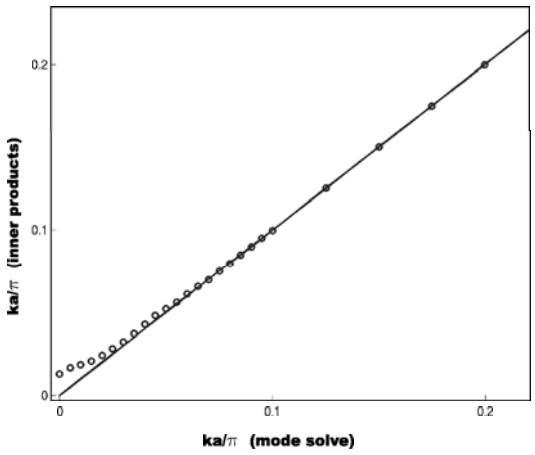


Figure A.6: $\beta a$ as set by the BBC during the mode solving is compared to the $\beta a$ extracted from the phases of $\langle \phi^l, \psi_{\beta a} \rangle$. Away from the mini-stop band, in the high group velocity regime, there is a good correspondence. However, near the mini-stop band the spatial evolution of the phase of $\langle \phi^l, \psi_{\beta a} \rangle$ differs from what would be expected from the dispersion diagram due to the fact that numerical errors in the mode profile dominate the values returned by the inner product.

from $\beta a = 0$ to $\beta a = 0.04\pi$ show a discrepancy. While the field profiles of the computed modes look good (comparable to Fig. A.2), the numerical error that is associated with forward propagating power dominates the inner products. Consequently we didn't plot these 8 data points on Fig. A.5.

The decrease of radiative losses of the lower band of e1 when approaching the mini-stop band has been experimentally observed [127] and theoretically investigated by other methods [132]. Ref. [132] is based on a 2D, effective index analysis combined with a variational estimation of radiative losses based on Fermi's golden rule. In that model, an upturn of losses in the immediate vicinity of the mini-stop band is also observed, but in a frequency range too narrow to be experimentally resolved, while in our analysis the upturn occurs between $a/\lambda = 0.33$ and $a/\lambda = 0.34$. It is not completely clear whether this is an artifact of the low group velocity and of the limitations of the inner product or whether this is due to 3D behavior not contained in the other model.

## A.3 Corrugated waveguide

A corrugated waveguide is the simplest case of waveguide with discrete translation symmetry. When the corrugation is weak, the propagation of light in the corrugated waveguide can be described by coupled mode theory with analytical expressions. In this section we derive the analytical expressions for the Bloch mode structure as well as the reflections of Bloch modes occurring at the end of the corrugation. This gives some insight about the difficulties encountered when analyzing waveguide losses without additional filtering mechanisms. In particular the effect of the reflected Bloch wave on the unfiltered power flux is quantified. It is important to take this into account as existing

implementations of ABCs for the FDTD method cannot absorb certain types of Bloch waves and induce reflections at the boundary of the computational domain. The coupled mode equations are first exactly solved in the absence of free space coupling, and the Bloch modes of the corrugated waveguide are calculated. The effect of radiative losses is then heuristically added to the model by adding an exponentially decreasing prefactor to the spatial evolution of the Bloch modes. Finally the outgoing boundary condition (that leads to reflections) is solved again with the modified Bloch modes. Numerical examples of field distributions within the corrugated waveguide are given.

We assume a weak corrugation so that the Bloch modes of the corrugated waveguide can be expressed within a very high degree of accuracy by coupled mode theory. We call $\psi_+$ and $\psi_-$ the forward and backward propagating modes of the unperturbed waveguide. They are coupled by the corrugation so that the supermodes of the complete system take the form $a(z)\psi_+ + b(z)\psi_-$ where $a(z)$ and $b(z)$ are complex functions with constant magnitude but varying phase. We note by $k$ the reduced wave number of the Bloch mode and by $\beta$ the reduced wave number of the uncorrugated waveguide. In order for the Bloch mode to satisfy the Bloch theorem, $a(z)$ and $b(z)$ have to take the form

$$a(z) = |a|e^{-i(k-\beta+m_a 2\pi/\Lambda)} \tag{A.10}$$

$$b(z) = |b|e^{-i(k+\beta+m_b 2\pi/\Lambda)} \tag{A.11}$$

where $m_a$ and $m_b$ are integers and $\Lambda$ is the period of the corrugation. This can be exemplified by explicitly calculating $a(z)$ and $b(z)$ with coupled mode theory.

We will now proceed by solving the coupled mode equations for the corrugated waveguide and by decomposing the obtained field distribution into Bloch modes. The amplitudes of the forward and backward propagating unperturbed waveguide modes are described by the envelope functions $A(z)$ and $B(z)$. Along the propagation direction $z$ they have the dependency $A(z)\exp(-i\beta z)$ and $B(z)\exp(+i\beta z)$. The coupled mode equations are [81]

$$\frac{dA}{dz} = -i\kappa^* B e^{i\left(2\beta-\frac{2\pi}{\Lambda}\right)z} \tag{A.12}$$

$$\frac{dB}{dz} = i\kappa A e^{-i\left(2\beta-\frac{2\pi}{\Lambda}\right)z} \tag{A.13}$$

where $\kappa$ is the coupling coefficient. We define $\varphi$ as $\beta - \pi/\Lambda$ and $\rho$ as $\sqrt{\varphi^2 - \kappa^2}$. Equations A.12 and A.13 are solved with the adequate boundary conditions (only outgoing waves at the end of the waveguide at $z = L$, i.e., $B(L) = 0$). We only consider light outside the bandgap where there are

propagative Bloch modes ($|\varphi| > \kappa$). This leads to

$$A(z)e^{-i\beta z} = A_0\big(\rho\cos[\rho(z-L)] - i\varphi\sin[\rho(z-L)]\big)e^{-i\frac{\pi}{\Lambda}z} \quad (A.14)$$

$$B(z)e^{i\beta z} = iA_0\kappa\sin[\rho(z-L)]e^{i\frac{\pi}{\Lambda}z} \quad (A.15)$$

where $A_0$ is proportional to the amplitude of the forward propagating unperturbed waveguide mode initially launched into the corrugated waveguide (the exact amplitude is $(\rho\cos(\rho L) + i\varphi\sin(\rho L))A_0$). This field distribution has Fourier components with wave numbers $\pi/\Lambda \pm \rho$ or equivalently (by folding back inside the 1st BZ) with reduced wave numbers $\pm(\pi/\Lambda - \rho)$. By decomposing the sines and cosines in exponentials, the field can be decomposed into two contrapropagating Bloch modes.

$$\begin{pmatrix} A(z)e^{-i\beta z} \\ B(z)e^{i\beta z} \end{pmatrix} = \frac{A_0}{2}\begin{pmatrix} (\rho-\varphi)e^{-i\frac{\pi}{\Lambda}z} \\ \kappa e^{i\frac{\pi}{\Lambda}z} \end{pmatrix} e^{i\rho(z-L)} + \frac{A_0}{2}\begin{pmatrix} (\rho+\varphi)e^{-i\frac{\pi}{\Lambda}z} \\ -\kappa e^{i\frac{\pi}{\Lambda}z} \end{pmatrix} e^{-i\rho(z-L)} \quad (A.16)$$

If $\varphi > 0$ (upper band)

$$\begin{pmatrix} A(z)e^{-i\beta z} \\ B(z)e^{i\beta z} \end{pmatrix} \propto \sqrt{\varphi-\rho}\begin{pmatrix} -\sqrt{\varphi-\rho}e^{-i\frac{\pi}{\Lambda}z} \\ \sqrt{\varphi+\rho}e^{i\frac{\pi}{\Lambda}z} \end{pmatrix} e^{i\rho(z-L)} + \sqrt{\varphi+\rho}\begin{pmatrix} \sqrt{\varphi+\rho}e^{-i\frac{\pi}{\Lambda}z} \\ -\sqrt{\varphi-\rho}e^{i\frac{\pi}{\Lambda}z} \end{pmatrix} e^{-i\rho(z-L)} \quad (A.17)$$

If $\varphi < 0$ (lower band)

$$\begin{pmatrix} A(z)e^{-i\beta z} \\ B(z)e^{i\beta z} \end{pmatrix} \propto \sqrt{|\varphi|+\rho}\begin{pmatrix} \sqrt{|\varphi|+\rho}e^{-i\frac{\pi}{\Lambda}z} \\ \sqrt{|\varphi|-\rho}e^{i\frac{\pi}{\Lambda}z} \end{pmatrix} e^{i\rho(z-L)} - \sqrt{|\varphi|-\rho}\begin{pmatrix} \sqrt{|\varphi|-\rho}e^{-i\frac{\pi}{\Lambda}z} \\ \sqrt{|\varphi|+\rho}e^{i\frac{\pi}{\Lambda}z} \end{pmatrix} e^{-i\rho(z-L)} \quad (A.18)$$

It can be seen that the field is decomposed into two Bloch modes (1st and 2nd terms of the sum). The $a(z)$ and $b(z)$ coefficients of the Bloch modes can be extracted from these formulas. For example in the case of the forward propagating Bloch mode of the upper band (second term in equation A.17), the coefficients are

$$a_{\text{fwd}}(z) = \sqrt{\frac{\varphi+\rho}{2\rho}}e^{-i(\rho+\frac{\pi}{\Lambda}-\beta)z} = \sqrt{\frac{\varphi+\rho}{2\rho}}e^{-i(k+\frac{2\pi}{\Lambda}-\beta)z} \quad (A.19)$$

$$b_{\text{fwd}}(z) = -\sqrt{\frac{\varphi-\rho}{2\rho}}e^{-i(\rho-\frac{\pi}{\Lambda}+\beta)z} = -\sqrt{\frac{\varphi-\rho}{2\rho}}e^{-i(k+\beta)z} \quad (A.20)$$

where $k = -\pi/\Lambda + \rho$. They take the form predicted by equations A.10 and A.11 with $m_a = 1$ and $m_b = 0$. The extra $1/\sqrt{2\rho}$ term is due to normalization. The coefficients of the backward propagating Bloch mode (first term in equation A.17) are $a_{\text{back}}(z) = b_{\text{fwd}}(z)^*$ and $b_{\text{back}}(z) = a_{\text{fwd}}(z)^*$. This

transformation corresponds to time reversal; thus they are each other's contrapropagating counterparts. We can also verify that they are orthogonal as $\langle a_{\text{fwd}}\psi_+ + b_{\text{fwd}}\psi_-, a_{\text{bwd}}\psi_+ + b_{\text{bwd}}\psi_-\rangle = a(b^*)^*\langle\psi_+,\psi_+\rangle + b(a^*)^*\langle\psi_-,\psi_-\rangle = a(b^*)^* - b(a^*)^* = 0$ (in the following $a$ and $b$ will refer to $a_{\text{fwd}}$ and $b_{\text{fwd}}$). We call $\Psi_+$ and $\Psi_-$ the forward and backward propagating Bloch modes. The transformation from unperturbed waveguide modes to Bloch modes is then given by

$$\begin{pmatrix}\Psi_+\\ \Psi_-\end{pmatrix} = \begin{pmatrix}a(z) & b(z)\\ b(z)^* & a(z)^*\end{pmatrix}\begin{pmatrix}\psi_+\\ \psi_-\end{pmatrix} \tag{A.21}$$

Radiative losses can be heuristically added to the system by introducing the loss coefficient $\gamma$ and by replacing $a(z)$ and $b(z)$ by $a(z)\exp(-\gamma z)$ and $b(z)\exp(-\gamma z)$ for the forward propagating Bloch mode, and by $a(z)\exp(\gamma z)$ and $b(z)\exp(\gamma z)$ for the backward propagating Bloch mode. This is an adequate description if the coupling length $\kappa^{-1}$ is significantly smaller than the characteristic length for radiative losses $\gamma^{-1}$. This assumption is necessary as the description assumes that light has *locally* the unperturbed Bloch mode structure. The field inside the lossy corrugated waveguide can then be solved for by assuming a superposition of Bloch modes and verifying the outgoing boundary condition (no back-propagating unperturbed waveguide mode at the end of the corrugation). If we call $F(z)$ the amplitude of the forward propagating Bloch mode and $R(z)$ the amplitude of the reflected (backward propagating) Bloch mode, the boundary condition translates into $B(L) = F(L)b(L) + R(L)a^*(L) = 0$

$$\frac{R(z)}{F(z)} = \sqrt{\frac{\varphi-\rho}{\varphi+\rho}}e^{-2(i\rho+\gamma)(L-z)} \tag{A.22}$$

It can be seen that the reflection at the end of the corrugation is the same as in the case without attenuation. The $\exp(-2\gamma(L-z))$ multiplicative factor takes into account the attenuation over a round trip. The field inside the waveguide then takes the form

$$\begin{pmatrix}A(z)\\ B(z)\end{pmatrix} = \begin{pmatrix}a(z) & b(z)^*\\ b(z) & a(z)^*\end{pmatrix}\begin{pmatrix}F(z)\\ R(z)\end{pmatrix} \tag{A.23}$$

which leads to

$$\begin{pmatrix}A(z)e^{-i\beta z}\\ B(z)e^{i\beta z}\end{pmatrix} \propto \sqrt{\varphi-\rho}\begin{pmatrix}-\sqrt{\varphi-\rho}e^{-i\frac{\pi}{\Lambda}z}\\ \sqrt{\varphi+\rho}e^{i\frac{\pi}{\Lambda}z}\end{pmatrix}e^{(i\rho+\gamma)(z-L)} + \sqrt{\varphi+\rho}\begin{pmatrix}\sqrt{\varphi+\rho}e^{-i\frac{\pi}{\Lambda}z}\\ -\sqrt{\varphi-\rho}e^{i\frac{\pi}{\Lambda}z}\end{pmatrix}e^{-(i\rho+\gamma)(z-L)} \tag{A.24}$$

Figure A.7 shows the field evolution inside a corrugated waveguide and compares the evolution of the total power $A(z)^2 - B(z)^2$ to the evolution of the power contained in the forward propagation unperturbed waveguide mode $A(z)^2$ and the power contained in the forward propagating Bloch mode $F(z)^2$. Two different boundary conditions are applied. In (a) the corrugation stops after 15 $\mu m$

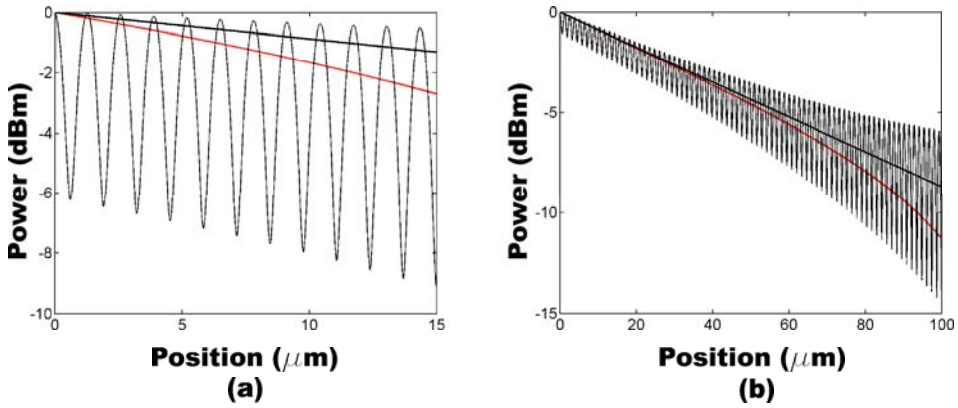


Figure A.7: Field evolution inside a corrugated waveguide. In (a) the corrugation stops after 15 $\mu$m and in (b) the corrugation stops after 100 $\mu$m. The different boundary conditions lead to a different field evolution. In particular, in the case of the short waveguide the losses of the total energy flux are almost twice those expected from the Bloch mode, due to the negative flux carried by the reflected Bloch wave, while in the second case the field evolution at the beginning of the waveguide is close to the losses expected from the Bloch mode (the reflected Bloch mode is almost completely decayed at that point). The parameters were assumed to be $\beta = 2\pi n_{WG}/\lambda$, $\kappa = 6$ $\mu$m$^{-1}$, $\Lambda = \lambda_0/n_{WG}$, $\gamma = 0.01$ $\mu$m$^{-1}$, $n_{WG} = 2.7$, $\lambda = 1.4$ $\mu$m and $\lambda_0 = 1.5$ $\mu$m. The red curve shows the total power, the straight black curve shows the power contained in the forward propagating Bloch mode and the oscillating black curve shows the power contained in the forward propagating unpatterned waveguide mode.

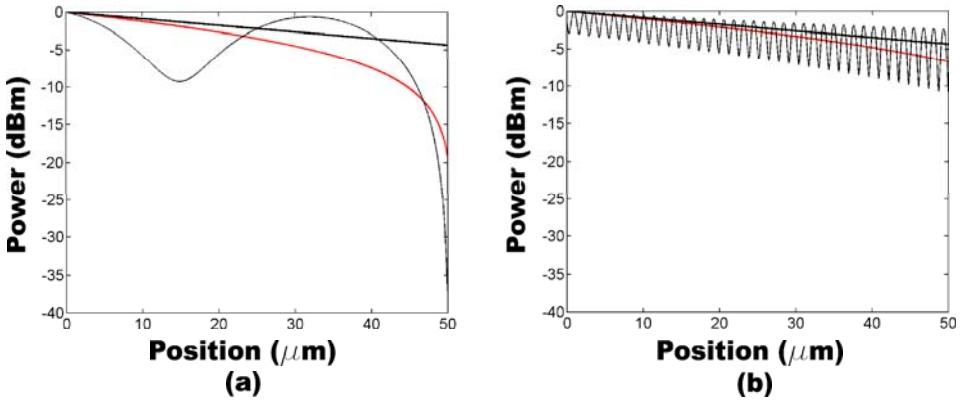


Figure A.8: This figure shows the field distribution inside the same corrugated waveguide (same parameters as in figure A.7, with a corrugation length of 50 $\mu$m) for different wavelengths. In (a) $\lambda = 1.4555$ $\mu$m is very close to the band edge, while in (b) $\lambda = 1.4$ $\mu$m. As in figure A.7 the black straight line is $F(z)^2$, the red line is $A(z)^2 - B(z)^2$ and the curvy black line is $A(z)^2$.

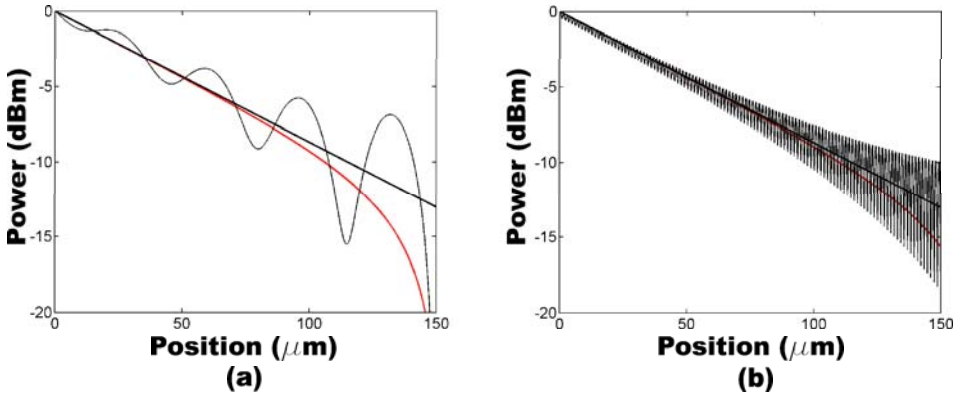


Figure A.9: This figure shows the field distribution inside the corrugated waveguide (same parameters as in figure A.7, with a corrugation length of 150 $\mu$m) for $\lambda = 1.4555$ $\mu$m (a) and $\lambda = 1.4$ $\mu$m (b). It can be seen that when the length of the waveguide is longer than the $1/e^2$ intensity decay length, the field evolution at the beginning of the waveguide is dominated by the forward propagating Bloch mode, and the beating pattern has a small amplitude. This is to be put in contrast with short waveguides as in figure A.7(a), where the logarithm of the field intensity is almost linear, but where the waveguide losses would be overestimated by a factor 2 if directly evaluated from that slope.

and in (b) the corrugation stops after 100 $\mu m$. The parameters were assumed to be $\beta = 2\pi n_{WG}/\lambda$, $\kappa = 6$ $\mu$m$^{-1}$, $\Lambda = \lambda_0/n_{WG}$, $\gamma = 0.01$ $\mu$m$^{-1}$, $n_{WG} = 2.7$, $\lambda = 1.4$ $\mu$m and $\lambda_0 = 1.5$ $\mu$m. Figure A.8 shows the effect of changing the offset of the wavelength relative to the band edge. It can be seen that using the total power to evaluate the waveguide losses can be very misleading if the waveguide length is short. In this situation the problem only arises from the partial reflection of the Bloch wave at the end of the corrugation, and it is possible to fit the total power as the difference of two exponentials (with opposite decay directions) to extract waveguide losses. In a real FDTD simulation the situation will be much more complex as the field at the beginning of the waveguide will not be exactly a waveguide mode but may contain radiative modes that need to be filtered out. In the case of a PCW, the situation is also more complex due to the fact that the Bloch mode cannot be completely decomposed into slab modes. Furthermore tunneling may occur in PCWs, which also does not occur in the case of the corrugated waveguide *outside the bandgap*. In these situations it is very helpful to be able to extract directly the intensity of the forward propagating Bloch wave by using the inner product.

In conclusion we have shown that an inner product usually applied to waveguides of continuous symmetry also verifies the orthogonality condition between PCW modes. The inner product was used to analyze data from an FDTD simulation and to evaluate losses of an W1 waveguide. General trends exposed in the literature are verified. However, the accuracy of the method is reduced when modes with a very low group velocity are analyzed. The numerical inaccuracy has at least two sources. Mode orthogonality was derived for lossless Bloch modes ("true" modes). When radiative losses are high, numerical cross talk between Bloch modes can become significant. Also, when the

group velocity of the analyzed Bloch mode is low, numerical cross talk with noise in the reference mode profile can become dominant.

# Bibliography

[1] E. Yablonovitch, "Inhibited spontaneous emission in solid-state physics and electronics", Phys. Rev. Lett. **58**, 2059-2062 (1987).

[2] J. D. Joannopoulos, R. D. Meade, and J. N. Winn, *Photonic Crystals, Molding the Flow of Light* (Princeton University Press, Princeton, New Jersey, 1995).

[3] M. Lončar, T. Doll, J. Vuckovic, and A. Scherer, "Design and Fabrication of Silicon Photonic Crystal Optical Waveguides", J. Lightwave Technol. **18**, 1402-1411 (2000).

[4] M. Lončar, J. Vuckovic, and A. Scherer, "Methods for controlling positions of guided modes of photonic-crystal waveguides", J. Opt. Soc. Am. B **18**, 1362-1368 (2001).

[5] T. Baba, A. Motegi, T. Iwai, N. Fukaya, Y. Watanabe, and A. Sakai, "Light Propagation Characteristics of Straight Single-Line-Defect Waveguides in Photonic Crystal Slabs Fabricated into a Silicon-on-Insulator Substrate", IEEE J. Quant. Electron., 38, 743-752 (2002).

[6] J. Vučković, M. Lončar, H. Mabuchi, and A. Scherer, "Optimization of the Q Factor in Photonic Crystal Microcavities", IEEE J. Quant. Electron. **38**, 850-856 (2002).

[7] K. Srinivasan and O. Painter, "Momentum space design of high-Q photonic crystal optical cavities", Opt. Express **10**, 670-684 (2002).

[8] Y. Akhahane, T. Asano, B.-S. Song, and S. Noda, "High-Q photonic nanocavity in a two-dimensional photonic crystal", Nature **425**, 944-947 (2003).

[9] O. Painter, R. K. Lee, A. Scherer, A. Yariv, J. D. O'Brien, P. D. Dapkus, and I. Kim, "Two-Dimensional Photonic Band-Gap Defect Mode Laser", Science **284**, 1819-1821 (1999).

[10] M. Lončar, T. Yoshie, P. Gogna, Y. Qiu, and A. Scherer, "Low-threshold photonic crystal laser", Appl. Phys. Lett. **81**, 2680-2682 (2002).

[11] T. Yoshie, O. B. Shchekin, H. Chen, D. G. Deppe, and A. Scherer, "Quantum dot photonic crystal laser", Electron. Lett. **38**, 967-968 (2002).

[12] T. Yoshie, M. Lončar, and A. Scherer, "High frequency oscillation in photonic crystal nanolasers", Appl. Phys. Lett. **84**, 3543-3545 (2004).

[13] H. G. Park, S. H. Kim, S. H. Kwon, Y. G. Ju, J. K. Yang, J. H. Baek, S. B. Kim, and Y. H. Lee, "Electrically driven single-cell photonic crystal laser", Science **305**, 1444-1447 (2004).

[14] R. Colombelli, K. Srinivasan, M. Troccoli, O. Painter, C. F. Gmachl, D. M. Tennant, A. M. Sergent, D. L. Sivco, A. Y. Cho, and F. Capasso, "Quantum Cascade Surface-Emitting Photonic Crystal Laser", Science **302**, 1374-1377 (2003).

[15] K. Srinivasan, O. Painter, R. Colombelli, C. Gmachl, D. M. Tennant, A. M. Sergent, D. L. Sivco, A. Y. Cho, M. Troccoli, and F. Capasso, "Lasing mode pattern of a quantum cascade photonic crystal surface-emitting microcavity laser", Appl. Phys. Lett. **84**, 4164-4166 (2004).

[16] C. J. M. Smith, R. M. De La Rue, M. Rattier, et al., "Coupled guide and cavity in a two-dimensional photonic crystal", Appl. Phys. Lett. **78**, 1487-1489 (2001).

[17] S. Noda, A. Chutinan, and M. Imada, "Trapping and emission of photons by a single defect in a photonic bandgap structure", Nature **407**, 608-610 (2000).

[18] Y. A. Vlasov, K. Luterova, I. Pelant, B. Honerlage, and V. N. Astratov, "Enhancement of optical gain of semiconductors embedded in three-dimensional photonic crystals", Appl. Phys. Lett. **71**, 1616-1618 (1997).

[19] E. P. Petrov, V. N. Bogomolov, I. I. Kalosha, and S. V. Gaponenko, "Spontaneous emission of organic molecules embedded in a photonic crystal", Phys. Rev. Lett. **81**, 77-80 (1998).

[20] M. Boroditsky, R. Vrijen, T. F. Krauss, R. Coccioli, R. Bhat, and E. Yablonovitch, "Spontaneous Emission Extraction and Purcell Enhancement from Thin-Film 2D Photonic Crystalls", J. Lightwave Technol. **17**, 2096-2112 (1999).

[21] T. Yoshie, A. Scherer, J. Hendrickson, G. Khitrova, H. M. Gibbs, G. Rupper, C. Ell, O. B. Shchekin, and D. G. Deppe, "Vacuum Rabi splitting with a single quantum dot in a photonic crystal nanocavity", Nature **432**, 200-203 (2004).

[22] S. Ogawa, M. Imada, S. Yoshimoto, M. Okano, and S. Noda, "Control of Light Emission by 3D Photonic Crystals", Science **305**, 227-229 (2004).

[23] P. Lodahl, A. F. van Driel, I. S. Nikolaev, A. Irman, K. Overgaag, D. Vanmaekelbergh, and W. L. Vos, "Controlling the dynamics of spontaneous emission from quantum dots by photonic crystals", Nature **430**, 654-657 (2004).

[24] H. Kosaka, T. Kawashima, A. Tomita, T. Sato, and S. Kawakami, "Photonic-crystal spot-size converter", Appl. Phys. Lett. **76**, 268-270 (2000).

[25] H. Kosaka, T. Kawashima, A. Tomita, M. Notomi, T. Tamamura, T. Sato, and S. Kawakami, "Self-collimating phenomena in photonic crystals", Appl. Phys. Lett. **74**, 1212-1214 (1999).

[26] D. N. Chigrin, S. Enoch, C. M. Sotomayor Torres, and G. Tayeb, "Self-guiding in two-dimensional photonic crystals", Opt. Express **11**, 1203-1211 (2003).

[27] J. Witzens, M. Lončar, and A. Scherer, "Self-Collimation in Planar Photonic Crystals", IEEE J. Sel. Top. Quant. Electron. **8**, 1246-1257 (2002).

[28] J. Witzens and A. Scherer, "Efficient excitation of self-collimated beams and single Bloch modes in planar photonic crystals", J. Opt. Soc. Am. A **20**, 935-940 (2003).

[29] L. Wu, M. Mazilu, and T. F. Krauss, "Optimizing bending efficiency of self-collimated beams in non-channel planar photonic crystal waveguides", Opt. Express **11**, 3153-3159 (2003).

[30] X. Yu and S. Fan, "Bends and splitters for self-collimated beams in photonic crystals", Appl. Phys. Lett. **83**, 3251-3253 (2003).

[31] H. Kosaka, T. Kawashima, A. Tomita, M. Notomi, T. Tamamura, T. Sato, and S. Kawakami, "Superprism phenomena in photonic crystals", Phys. Rev. B **58**, R10096-R10099 (1998).

[32] H. Kosaka, T. Kawashima, A. Tomita, M. Notomi, T. Tamamura, T. Sato, and S. Kawakami, "Photonic crystals for micro lightwave circuits using wavelength-dependent angular beam", Appl. Phys. Lett. **74**, 1370-1372 (1999).

[33] T. Baba and M. Nakamura, "Photonic crystal light deflection devices using the superprism effect", IEEE J. Quant. Electron. **38**, 909-914 (2002).

[34] L. J. Wu, M. Mazilu, T. Karle, and T. F. Krauss, "Superprism phenomena in planar photonic crystals", IEEE J. Quant. Electron. **38**, 915-918 (2002).

[35] L. Wu, M. Mazilu, and T. F. Krauss, "Beam Steering in Planar-Photonic Crystals: From Superprism to Supercollimator", J. Lightwave Technol. **21**, 561-566 (2003).

[36] T. Matsumoto and T. Baba, "Photonic Crystal k-vector Superprism", J. Lightwave Technol. **22**, 917-922 (2004).

[37] M. Gerken and D. A. B. Miller, "Multilayer Thin-Film Stacks With Steplike Spatial Beam Shifting", J. Lightwave Technol. **22**, 612-618 (2004).

[38] T. Baba and T. Matsumoto, "Resolution of photonic crystal superprism", Appl. Phys. Lett. **81**, 2325-2327 (2002).

[39] T. Baba and D. Ohsaki, "Interfaces of photonic crystals for high efficiency light transmission", Jpn. J. Appl. Phys. **40**, Part 1, 5920-5924 (2001).

[40] J. Witzens, M. Hochberg, T. Baehr-Jones, and A. Scherer, "Mode matching interface for efficient coupling of light into planar photonic crystals", Phys. Rev. E **69**, 046609 1-046609 12 (2004).

[41] J. Witzens, T. Baehr-Jones, and A. Scherer, "Hybrid superprism with low insertion losses and suppressed cross-talk", Phys. Rev. E **71**, 026604 1-026604 9 (2005).

[42] M. Lončar and A. Scherer, "Photonic crystal laser sources for chemical detection", Appl. Phys. Lett. **82**, 4648-4650 (2003).

[43] B. Maune, M. Lončar, J. Witzens, M. Hochberg, T. Baehr-Jones, D. Psaltis, Y. Qiu, and A. Scherer, "Liquid-crystal electric tuning of a photonic crystal laser", Appl. Phys. Lett. **85**, 360-362 (2004).

[44] B. Maune, J. Witzens, T. Baehr-Jones, M. Kolodrubetz, H. Atwater, R. Hagen, Y. Qiu, and A. Scherer, "An optically triggered Q-switched photonic crystal laser", *in review.*

[45] C. Cheng, V. Arbet-Engels, A. Scherer, and E. Yablonovitch, "Nanofabricated three dimensional photonic crystals operating at optical wavelengths", Physica Scripta **T68**, 17-20 (1996).

[46] S. Kawakami, "Fabrication of submicrometer 3D periodic structures composed of $Si/SiO_2$", Electron. Lett. **33**, 1620-1621 (1997).

[47] S. Kennedy, M. Brett, O. Toader, and S. John, "Optical Properties of a Silicon Square Spiral Photonic Crystal", J. Photon. and Nanostruct. **1**, 37-43 (2003).

[48] J. Schilling, J. White, A. Scherer, G. Stupian, R. Hillebrand, and U. Gosele, "Three-dimensional macroporous silicon photonic crystal with large photonic band gap", Appl. Phys. Lett. **86**, 011101 1-011101 3 (2005).

[49] M. Campbell, D. N. Sharp, M. T. Harrison, R. G. Denning, and A. J. Turberfield, "Fabrication of photonic crystals for the visible spectrum by holographic lithography", Nature **404**, 53-56 (2000).

[50] H.-B. Sun, S. Matsuo, and H. Misawa, "Three-dimensional photonic crystal structures achieved with two-photon-absorption photopolymerization of resin", Appl. Phys. Lett. **74**, 786-788 (1999).

[51] T. F. Krauss, R. M. De La Rue, and S. Brand, "Two-dimensional photonic-bandgap structures operating at near infrared wavelengths", Nature **383**, 699-702 (1996).

[52] S. G. Johnson, S. H. Fan, P. R. Villeneuve, J. D. Joannopoulos, and L. A. Kolodziejski, "Guided modes in photonic crystal slabs", Phys. Rev. B **60**, 5751-5758 (1999).

[53] Labilloy D., Benisty H., Weisbuch C., et al., "Quantitative measurement of transmission, reflection, and diffraction of two-dimensional photonic band gap structures at near-infrared wavelengths", Phys. Rev. Lett. **79**, 4147-4150 (1997).

[54] J. B. Pendry, "Negative refraction makes a perfect lens", Phys. Rev. Lett. **18**, 3966-3969 (2000).

[55] D. R. Smith, W. J. Padilla, D. C. Vier, S. C. Nemat-Nasser, and S. Schultz, "Composite Medium with Simultaneously Negative Permeability and Permittivity", Phys. Rev. Lett. **84**, 4184-4187 (2000).

[56] R. A. Shelby, D. R. Smith, S. C. Nemat-Nasser, and S. Schultz, "Microwave transmission through a two-dimensional, isotropic, left-handed metamaterial", Appl. Phys. Lett. **78**, 489-491 (2001).

[57] C. Luo, S. G. Johnson, and J. D. Joannopoulos, "Subwavelength imaging in photonic crystals", Phys. Rev. B **68**, 045115 1-045115 15 (2003).

[58] E. Cubukcu, K. Aydin, E. Ozbay, S. Foteinopolou, and C. M. Soukoulis, "Subwavelength Resolution in a Two-Dimensional Photonic-Crystal-Based Superlens", Phys. Rev. Lett. **91**, 207401 1-207401 4 (2003).

[59] A. Berrier, M. Mulot, M. Swillo, M. Qiu, L. Thylén, A. Talneau, and S. Anand, "Negative Refraction at Infrared Wavelengths in a Two-Dimensional Photonic Crystal", Phys. Rev. Lett. **93**, 073902 1-073902 4 (2004).

[60] J. Witzens, T. Baehr-Jones, M. Hochberg, M. Lončar, and A. Scherer, "Photonic crystal waveguide-mode orthogonality conditions and computation of intrinsic waveguide losses", J. Opt. Soc. Am. A **20**, 1963-1968 (2003).

[61] A. Taflove, *Computational Electrodynamics: the Finite-Difference Time-Domain Method* (Artech House, Norwood, Massachusetts, 1995).

[62] W. K. Burns, A. F. Milton, and A. B. Lee, "Optical waveguide parabolic coupling horns", Appl. Phys. Lett. **30**, 28-30 (1977).

[63] P. Gidon, S. Valette, and P. Mottier, "Integrated lenses on silicon nitride waveguides", Opt. Engineering **24**, 235-240 (1985).

[64] L. B. Soldano and E. C. M. Pennings, "Optical Multi-Mode Interference Devices Based on Self-Imaging: Principles and Applications", J. Lightwave Technol. **13**, 615-627 (1995).

[65] T. Fukazawa, F. Ohno, and T. Baba, "Very Compact Arrayed-Waveguide-Grating Demultiplexer Using Si Photonic Wire Waveguides", Japan. J. Appl. Phys. **43**, L673-L675 (2004).

[66] J. Witzens, G. Pickrell, D. Louderback, P. Guilfoyle, and A. Scherer, "Monolithic integration of vertical-cavity surface-emitting lasers", Appl. Phys. Lett. **86**, 101105 1-101105 3 (2005).

[67] D. Marcuse, "Mode Conversion Caused by Imperfections of a Dielectric Slab Waveguide", Bell Syst. Tech. J. **48**, 3187-3215 (1969).

[68] D. A. Louderback, G. W. Pickrell, M. A. Fish, J. J. Hindi, H. C. Lin, M. C. Simpson, T. J. Eustis, and P. S. Guilfoyle, "VCSELs with Monolithic Coupling to Internal In-Plane Waveguides using Integrated Diffraction Gratings", Electron. Lett. **40** 1064-1065 (2004).

[69] J. Witzens, T. J. Kippenberg, C. Walker, K. J. Vahala, and A. Scherer, "Scattering in ring resonators", *in review.*

[70] T. J. Kippenberg, A. L. Tchebotareva, J. Kalkman, A. Polman, and K. J. Vahala, "Purcell factor enhanced scattering efficiency in silicon nanocrystal doped microcavities", *in review.*

[71] B. E. A. Saleh, and M. C. Teich, *Fundamentals of Photonics* (Wiley Series in Pure and Applied Optics, Wiley Interscience, New York, 1991).

[72] M. Notomi, "Theory of light propagation in strongly modulated photonic crystals: Refractionlike behavior in the vicinity of the photonic bandgap", Phys. Rev. B **62**, 10696 1-10696 10 (2000).

[73] P. Halevi, A. A. Krokhin, and J. Arriaga, "Photonic Crystal Optics and Homogenization of 2D Periodic Composites", Phys. Rev. Lett. **82**, 719-722 (1999).

[74] G. P. Agrawal, *Nonlinear Fiber Optics* (Optics and Photonics, Academic Press, New York, 1989).

[75] V. N. Astratov, I. S. Culshaw, R. M. Stevenson, D. M. Whittaker, M. S. Skolnick, T. F. Krauss, and R. M. De la Rue, "Resonant Coupling of Near-Infrared Radiation to Photonic Band Structure Waveguides", J. Lightwave Technol., 17, 2050-2057 (1999)

[76] P. Lalanne and A. Talneau, "Modal conversion with artificial materials for photonic-crystal waveguides", Opt. Express **19**, 354-359 (2002).

[77] Y. Xu, R. K. Lee, and A. Yariv, "Adiabatic coupling between conventional dielectric waveguides and waveguides with discrete translational symmetry", Opt. Lett. **25**, 755-757 (2000).

[78] A. Mekis and J. D. Joannopulos, "Tapered couplers for efficient interfacing between dielectric and photonic crystal waveguides", J. Lightwave technol. **19**, 861-865 (2001).

[79] K. Srinivasan, P. E. Barclay, M. Borselli, and O. Painter, "Optical-fiber-based measurement of an ultrasmall volume high-Q photonic crystal microcavity", Phys. Rev. B **70**, 081306 1-081306 4 (2004).

[80] P. E. Barclay, K. Srinivasan, M. Borselli, and O. Painter, "Probing the dispersive and spatial properties of photonic crystal waveguides via highly efficient coupling from fiber tapers", Appl. Phys. Lett. **85**, 4-6 (2004).

[81] K. Okamoto, *Fundamentals of Optical Waveguides* (Academic Press, San Diego, California, 2000).

[82] C. M. de Sterke, D. Salinas, and J. E. Sipe, "Coupled-mode theory for light propagation through deep nonlinear gratings", Phys. Rev. E **54**, 1969-1989 (1996).

[83] S. Miyanaga and T. Asakura, "Intensity profile of outgoing beams from uniform and linearly tapered grating couplers", Appl. Opt. **20**, 688-695 (1981).

[84] K. A. Bates, L. Li, R. L. Roncone, and J. J. Burke, "Gaussian beams from variable groove depth grating couplers in planar waveguides", Appl. Opt. **32**, 2112-2116 (1993).

[85] M. Miler and M. Skalsky, "Chirped and Curved Grating Coupler Focusing Both Outgoing Beam and Guided wave", Opt. Commun. **33**, 13 (1980).

[86] D. Heitmann and C. Ortiz, "Calculation and Experimental Verification of Two-Dimensional Focusing Grating Coupler", IEEE J. Quant. Electron. **QE-17**, 1257-1263 (1981).

[87] L. Li and M. C. Gupta, "Effects of beam focusing on the efficiency of planar waveguide grating couplers", Appl. Opt. **29**, 5320-5325 (1990).

[88] T. Suhara, K. Okada, T. Saso, and H. Nishihara, "Focusing Grating Coupler in AlGaAs", IEEE Photon. Technol. Lett. **4**, 903-905 (1992).

[89] L. C. Gunn, T. J. Pinguet, M. J. Rattier, "Optical Waveguide Grating Coupler", United States Patent Application (2004).

[90] D. Taillaert, P. Bienstam, and R. Baets, "Compact efficient broadband grating coupler for silicon-on-insulator waveguides", Opt. Lett. **29**, 2749-2751 (2004).

[91] D. Taillaert, H. Chong, P. I. Borel, L. H. Frandsen, R. M. De La Rue, and R. Baets, "A Compact Two-Dimensional Grating Coupler used as a Polarization Splitter", IEEE Photon. Technol. Lett. **15**, 1249-1251 (2003).

[92] L. C. Gunn, T. J. Pinguet, M. J. Rattier, J. Witzens, "Polarization Splitting Grating Coupler", United States Patent Application (2004).

[93] M. Palamaru and Ph. Lalanne, "Photonic crystal waveguides: Out-of-plane losses and adiabatic modal conversion", Appl. Phys. Lett. **78**, 1466-1468 (2001).

[94] A. Talneau, Ph. Lalanne, M. Agio, and C. M. Soukoulis, "Low-reflection photonic-crystal taper for efficient coupling between guide sections of arbitrary widths", Opt. Lett. **27**, 1522-1524 (2002).

[95] S. G. Johnson, P. Bienstman, M. A. Skorobogatiy, M. Ibanescu, E. Lidorikis, and J. D. Joannopoulos, "Adiabatic theorem and continuous coupled-mode theory for efficient taper transitions in photonic crystals", Phys. Rev. E **66**, 066608 1-066608 15 (2002).

[96] C. F. Bohren and D. R. Huffman, *Absorption and Scattering of Light by Small Particles* (Wiley, New York, 1991).

[97] A. Yariv, *Optical Electronics in Modern Communications* (Oxford University Press, New York, 1991).

[98] A. W. Snyder and J. D. Love, *Optical Waveguide Theory* (Chapman & Hall, Australian National University, Canberra, Australia).

[99] E. A. J. Marcatilli, "Dielectric rectangular waveguide and directional coupler for integrated optics", Bell Syst. Tech. J. **48**, 2071-2102 (1969).

[100] J. L. Jewell, S. L. McCall, Y. H. Lee, A. Scherer, A. C. Gossard, and J. H. English, "Lasing Characteristics of GaAs microresonators", Appl. Phys. Lett. **54**, 1400-1402 (1989).

[101] B. Tell, Y. H. Lee, K. F. Brown-Goebeler, J. L. Jewell, R. E. Leibenguth, M. T. Asom, G. Livescu, L. Luther, and V. D. Mattera, "High-Power cw vertical-cavity top surface-emitting GaAs quantum well lasers", Appl. Phys. Lett. **57**, 1855-1857 (1990).

[102] J. L. Jewell, J. P. Harbison, A. Scherer, Y. H. Lee, and L. T. Florez, "Vertical-Cavity Surface-Emitting Lasers: Design, Growth, Fabrication, Characterization", IEEE J. Quantum Electron. **27**, 1332-1346 (1991).

[103] K. D. Choquette, D. A. Richie, and R. E. Leibenguth, "Temperature dependence of gain-guided vertical-cavity surface emitting laser polarization", Appl. Phys. Lett. **64**, 2062-2064 (1994).

[104] S. Olivier, H. Benisty, M. Rattier, C. Weisbuch, M. Qiu, A. Karlsson, C. J. M. Smith, R. Houdré, and U. Oesterle, "Resonant and nonresonant transmission through waveguide bends in a planar photonic crystal", Appl. Phys. Lett. **79**, 2514-2516 (2001).

[105] S. G. Johnson, C. Manolatou, S. Fan, P. R. Villeneuve, J. D. Joannopoulos, and H. A. Haus, "Elimination of cross talk in waveguide intersections", Opt. Lett. **23**, 1855-1857 (1998).

[106] S. Li, G. Witjaksono, S. Macomber, and D. Botez, "Analysis of Surface-Emitting Second-Order Distributed Feedback Lasers with Central Grating Phaseshift", IEEE J. Selec. Top. Quant. Electron. **9**, 1153-1165 (2003).

[107] G. A. Golubenko, A. S. Svakhin, V. A. Sychugov, and A. V. Tishchenko, "Total reflection of light from a corrugated surface of a dielectric waveguide", Sov. J. Quant. Electron. **15**, 886 (1985).

[108] M. A. Ahmed, F. Pigeon, A. V. Tishchenko, O. Parriaux, Y. Ouerdane, S. Reynaud, J.-C. Pommier, and H.J. Fuchs, "Polarizing Grating Coupler for High Q Laser Cavities", IEEE J. Quant. Electron. **39**, 614-619 (2003).

[109] L. Li and J. J. Burke, "Linear propagation characteristics of periodically segmented waveguides", Opt. Lett. **17**, 1195-1197 (1992).

[110] T. Baehr-Jones, M. Hochberg, C. Walker, J. Witzens, L. Gunn, and A. Scherer, "Segmented Waveguides in thin Silicon-on-Insulator", J. Opt. Soc. Am. B (2005).

[111] K. Hjort, "Sacrificial etching of III-V compounds for micromechanical devices", J. Micromech. Microeng. **6**, 370-375 (1996).

[112] E. A. J. Marcatilli, "Bends in optical dielectric guides", Bell Syst. Tech. J. **48**, 2103-2132 (1969).

[113] B. E. Little, S. T. Chu, H. A. Haus, J. Foresi, and J.-P. Laine, "Microring Resonator Channel Dropping Filters", J. Lightwave Technol. **15**, 998-1005 (1997).

[114] H. A. Haus, *Waves and Fields in Optoelectronics* (Prentice-Hall, Englewood Cliffs, New Jersey, 1984).

[115] M. Cai, O. Painter, and K. J. Vahala, "Observation of critical coupling in a fiber taper to a silica-microsphere whispering-gallery mode system", Phys. Rev. Lett. **85**, 74-77 (2000).

[116] P. W. Milonni, *The Quantum Vacuum* (Academic Press, New York, 1994).

[117] P. W. Milonni and P. L. Knight, "Spontaneous emission between mirrors", Opt. Commun. **9**, 119-122 (1973).

[118] M. L. Gorodetsky, A. D. Pryamikov, and V. S. Ilchenko, "Rayleigh scattering in high-Q microspheres ", J. Opt. Soc. Am. B **17**, 1051-1057 (2000).

[119] D. S. Weiss, V. Sandoghar, J. Hare, V. Lefevreseguin, J. M. Raimond, and S. Haroche, "Splitting of high-Q Mie modes induced by light backscattering in silica microspheres", Opt. Lett. **20**, 1835-1837 (1995).

[120] T. J. Kippenberg, S. M. Spillane, and K. J. Vahala, "Modal coupling in traveling-wave resonators", Opt. Lett. **27**, 1669-1671 (2002).

[121] E. M. Purcell, "Spontaneous emission probabilities at radio frequencies", Phys. Rev. **69**, 681-681 (1946).

[122] J.-M. Gérard and B. Gayral, "Strong Purcell Effect for InAs Quantum Boxes in Three-Dimensional Solid-State Microcavities", J. Lightwave Technol. **17**, 2089-2095 (1999).

[123] L. Weinstein, *Open Resonators and Open Waveguides* (The Golem Press, Boulder, Colorado, 1996).

[124] M. Heiblum and J. H. Harris, "Analysis of Curved Optical Waveguides by Conformal Transformation", IEEE J. Quantum Electron. **QE-11**, 75-83 (1975).

[125] T Baehr-Jones, M. Hochberg, C. Walker, and A. Scherer, "High-Q ring resonators in thin silicon-on-insulator", Appl. Phys. Lett. **85**, 3346-3347 (2004).

[126] E. Snoeks, A. Lagendijk, and A. Polman, "Measuring and Modifying the Spontaneous Emission Rate of Erbium near an Interface", Phys. Rev. Lett. **74**, 2459-2462 (1995).

[127] M. Lončar, D. Nedeljković, T. P. Pearsall, J. Vučković, A. Scherer, S. Kuchinsky, and D. C. Allan, "Experimental and theoretical confirmation of Bloch-Mode light propagation in planar photonic crystal waveguides", Appl. Phys. Lett., 80, 1689-1691 (2002).

[128] H. Benisty, P. Lalanne, S. Olivier, M. Rattier, C. J. M. Smith, T. F. Krauss, C. Jouanin, and D. Cassagne, "Finite-depth and intrinsic losses in vertically etched two-dimensional photonic crystals", Opt. Quantum Electron., 35, 205-215 (2002).

[129] P. Lalanne, "Electromagnetic Analysis of Photonic Crystal Waveguides Operating above the Light Cone", IEEE J. Quantum Elec., 38, 800-804 (2002).

[130] P. Lalanne and H. Benisty, "Out-of-plane losses of two-dimensional photonic crystals waveguides: Electromagnetic analysis", J. Appl. Phys., 89, 1512-1514 (2001).

[131] G. R. Hadley, "Out-of-plane Losses of Line Defect Photonic Crystal Waveguides", IEEE Photonics Technol. Lett., 14, 642-644 (2002).

[132] L. C. Andreani and M. Agio, "Intrinsic diffraction losses in photonic crystal waveguides with line defects", Appl. Phys. Lett., 82, 2011-2013 (2003).

[133] Y. Désières, T. Benyattou, R. Orobtchouk, A. Morand, P. Benech, C. Grillet, C. Seassal, X. Letartre, P. Rojo-Romeo, and P. Viktorovitch, "Propagation losses of the fundamental mode in a

single line-defect photonic crystal waveguide on an InP membrane", J. Appl. Phys., 92, 2227-2234 (2002).

[134] M. Qiu, B. Jaskorzynska, M. Swillo, and H. Benisty, "Time-Domain 2D Modeling of Slab-Waveguide-based Photonic-Crystal Devices in the presence of Radiation Losses", Microwave and Opt. Technol. Lett., 34, 387-393 (2002).

[135] K. K. Lee, D. R. Lim, H.-C. Luan, A. Agarwal, J. Foresi, and L. C. Kimerling, "Effect of size and roughness on light transmission in a $Si/SiO_2$ waveguide: Experiments and model", Appl. Phys. Lett. **77**, 1617-1619 (2000).

[136] K. K. Lee, D. R. Lim, L. C. Kimerling, J. Shin, and F. Cerrina, "Fabrication of ultralow-loss $Si/SiO_2$ waveguides by roughness reduction", Opt. Lett. **26**, 1888-1890 (2001).